The Fractal Nature of Fault Slip and its Incorporation into Earthquake Slip Inversions

Ruth Mary Joy Amey

Submitted in accordance with the requirements for the degree of
Doctor of Philosophy

The University of Leeds
School of Earth and Environment

September 2018

The candidate confirms that the work submitted is her own, except where work which has formed part of jointly authored publications has been included. The contribution of the candidate and the other authors to this work has been explicitly indicated below. The candidate confirms that appropriate credit has been given within the thesis where reference has been made to the work of others.

The work in Chapter 2 of this thesis is a manuscript to be submitted to Earth and Planetary Science Letters as follows:
Amey, R.M.J., L. Gregory, L. Wedmore, A. Hooper, H. Goodall, J. Woodman, M. Wilkinson, K.J.W. McCaffrey (in prep), *Fractal properties of the Campo Felice fault in the Italian Apennines.*

The idea for this paper was developed by myself and the co-authors, and methodology was developed by myself using published literature. Some terrestrial laser scans were collected by myself and co-authors during fieldwork in Italy, and some scans were provided by the other co-authors. I processed the results, wrote and produced all figures for the manuscript, which was improved by suggestions and comments from all co-authors and Jessica Hawthorne. The data and codes from this chapter can be found here: `https://doi.org/10.5518/443`

An edited version of Chapter 3 was published by AGU, Copyright (2018) American Geophysical Union:
Amey, R.M.J., A.J. Hooper, and R. Walters (2018), *A Bayesian Method for Incorporating Self-Similarity into Earthquake Slip Inversions*, Journal of Geophysical Research Solid Earth, 123, `doi:10.1029/2017JB015316`

The idea and methodology in this paper was developed by Andy Hooper and the data used is from Richard Walters and co-authors of *Floyd et al.* (2016). I wrote a code to develop this methodology and implemented it on data from the Napa Valley earthquake. Additionally I wrote the manuscript and produced all figures for it, which was improved by comments from the co-authors and Laura Gregory. The code developed in this chapter can be found here: `https://doi.org/10.5518/444`
The data required to run this codes and models outputs from this chapter can be found here: `https://doi.org/10.5518/445`

The work in Chapter 4 of this thesis has been submitted for publication in the Journal of Geophysical Research as follows:
Amey, R.M.J., A.J. Hooper, and Y. Morishita (2018), *Going to Any Lengths: Solving for Fault Size and Fractal Slip for the 2016, Mw 6.2 Central Tottori Earthquake, Japan, using a Trans-dimensional Inversion Scheme*, Journal of Geophysical Research Solid Earth

The idea and methodology was developed by myself and Andy Hooper. I up-

dated and implemented the code and processed the Sentinel-1 data. The ALOS-2 and GNSS data was provided by Yu Morishita. All authors and Huw Goodall read the manuscript and made improvements. The code developed in this chapter can be found here: `https://doi.org/10.5518/444`
The data required to run this code and models outputs from this chapter can be found here: `https://doi.org/10.5518/446`

References

Floyd, M. A., R. J. Walters, J. R. Elliott, G. J. Funning, J. L. Svarc, J. R. Murray, A. J. Hooper, Y. Larsen, P. Marinkovic, R. Bürgmann, I. A. Johanson, and T. J. Wright (2016), Spatial variations in fault friction related to lithology from rupture and afterslip of the 2014 South Napa, California, earthquake, *Geophysical Research Letters*, *43*(13), 6808–6816, doi:10.1002/2016GL069428. (document)

Acknowledgements

PhDs are difficult, and there's a lot that goes into them that no one ever sees. For anyone reading this shiny, finished version, particularly anyone who's still in the middle of their PhD, don't forget that success is an iceberg. Here I'd like to take the opportunity to thank everyone who's helped me along the way.

Many thanks to my supervisor Andy Hooper, for teaching me many new things, for your ongoing patience and for reading every thing that I sent to you. To Laura Gregory and Luke Wedmore for taking me on fieldwork and your enthusiasm about Chapter 2 of this thesis. To Jessica Hawthorne for making me want to be a scientist, rather than just a person with a PhD. To Tim Wright and many other IGT folk past and present for the science and the laughs, particularly John Elliott for giving me a postdoc. To Richard Rigby for your ability to fix any computer problem and do so with a smile, Pre Carbo for all the fun I've had doing outreach and seeing the bees, to Debbie Rosen for cake chat at COMET meetings and Graham Blyth for your patience in helping me make the online data repository that accompanies this thesis.

Figure 1: Figure credit to Sylvia Duckworth `https://sylviaduckworth.com`

Where would I be without everyone in office 8.125? What a lovely bunch of people to work with. Wishing everyone good things and a painless write-up. Thanks also to those I started with, the tectonics folk I kept bumping into at conferences those I have lunch with. With particular mention to Tom, my first Leeds buddy, who helped me with almost every thing I've done in this PhD, to Claire for every time you rolled your chair across the office to talk to me, to Ben for the memes and your terrible puns and to Lauren, and because we are both worriers and perfectionists, but we both made it. I couldn't have done it without you guys, and even if I could have, it wouldn't have been any fun.

With many, many thanks to my family, to Sher, Jacqui and Erin and especially my parents, who have all provided me with unending love and support at the low points of this PhD.

And finally to Huw, for reminding me every day at 5pm that there is life beyond my PhD. For some reason we thought it'd be a good idea to buy a house at the same time as I finish this thesis, and whilst moving in the month before hand-in has been hectic, it has been fun. Now that this is handed in, I promise to stop being boring so we can go on some adventures (at least until you write-up).

It is not the critic who counts; not the man who points out how the strong man stumbles, or where the doer of deeds could have done them better. The credit belongs to the man who is actually in the arena, whose face is marred by dust and sweat and blood; who strives valiantly; who errs, who comes short again and again, because there is no effort without error and shortcoming; but who does actually strive to do the deeds; who knows great enthusiasms, the great devotions; who spends himself in a worthy cause; who at the best knows in the end the triumph of high achievement, and who at the worst, if he fails, at least fails while daring greatly, so that his place shall never be with those cold and timid souls who neither know victory nor defeat.

- Theodore Roosevelt

Abstract

In order to understand how earthquakes nucleate, propagate and terminate it is essential to understand the properties and stress conditions of the surfaces upon which earthquakes occur. Fault surfaces control frictional properties and by measuring exhumed faults we can better understand earthquake propagation and how this may be linked to fault structure. In order to forecast areas of a fault likely to be at risk from future failure it is necessary to accurately model the slip that occurs during each measured earthquake.

In recent years many lines of evidence suggest that fault surfaces and earthquake slip show fractal properties. This includes high resolution scans of fault surfaces, observations of coseismic surface slip and analysis of published slip distributions. In this thesis I investigate how fault structure may affect the fractal properties of fault surface roughness, by investigating the along-strike changes in properties of the Campo Felice fault in the Italian Apennines. I then incorporate observations of fractal properties into earthquake slip inversions through a new form of regularisation, which I develop using Bayesian methods. Through this I aim to improve our understanding of the surfaces upon which earthquakes occur, how this links to fault structure and to improve our coseismic slip models, that provide the basis of stress models and hazard analysis.

Fault surfaces displaying fractal properties mean that there is a power-law relationship between the topography of a fault and the wavelength of this topography: the magnitude of height fluctuations depends upon the scale at which they are observed. Whilst many studies have investigated fault roughness properties, here I present the first study of how fault roughness varies along the strike of a fault. I use terrestrial laser scans and laser profilometer scans at 14 locations along the length of the Campo Felice normal fault in the Italian Apennines, as well as a scan encompassing several hundred meters along the length of the fault. These scans show that the Campo Felice fault displays fractal properties over at least six orders of magnitude perpendicular to slip and at least three orders of magnitude parallel to slip. But, contrary to previous findings on other faults, I find that the Hurst parameter, which controls the fractal nature of the fault surface, changes considerably and unpredictably along the length of the fault, even between observations tens of metres apart. I suggest that this variability may be due to the variation of slip vector along the length of the fault, as is frequently observed in earthquakes. This variability could, additionally, be linked to fault asperities halting or impeding rupture, such that some areas of the fault experience more earthquakes, or experience different stress conditions during the same earthquake. I also find that the magnitude of topography displayed by Campo Felice fault is low compared to previous studies, suggesting it may be at risk of larger earthquakes.

Observations of fractal fault surfaces suggest that earthquake slip should be fractal too. By using geodetic data taken at the surface before and after an earthquake we can perform slip inversions to give a model of how much slip occurred underground, on the fault surface. This is routinely performed for large, continental earthquakes. Due to noise and lack of data these inversions are frequently regularised to produce a stable solution, but the standard regularisation techniques have little physical basis. I incorporate fractal properties of earthquake slip into slip inversions by introducing a new regularisation technique: von Karman regularisation. I use a Bayesian method to fully explore parameter space and better understand uncertainties on the model parameters. From synthetic tests I find that this regularisation performs comparably, if not better, than other frequently used methods upon both fractal and Laplacian input slip distributions. Using InSAR (Interferometric Synthetic Aperture Radar) and GPS (Global Positioning System) data from the 2014 M_w 6.0 Napa Valley earthquake, I invert for slip using a two-segment fault model. I find that the choice of regularisation changes the location and magnitude of slip, which could have important implications for stress transfer and our understanding of the so-called shallow slip deficit.

Through its incorporation of fractal properties, von Karman regularisation represents a more physical regularisation of earthquake slip along a fault plane. However, some bias can be introduced by incorrectly choosing the length and width of the fault plane. If a fault plane is too large, the regularisation can cause slip smearing, particularly at depth where the model is poorly constrained by the data, in order to improve the von Karman probability. To eliminate this bias I modify my Bayesian inversion scheme to solve for the size of the fault plane during the inversion, along with slip, rake and a hyperparameter controlling slip variance. This makes the inversion trans-dimensional, and aims to reduce the bias caused by an incorrect model. I apply it to the M_w 6.2 Central Tottori earthquake, Japan, using InSAR and GNSS (Global Navigation Satellite System) data. My model shows that the earthquake ruptured most of the seismogenic zone, in contrast to seismological studies.

My results in this thesis further confirm that fault surface roughness shows fractal properties, and that fault structure may play an important role in the exact relationship between fault topography and the lengthscale of observation. Further investigation of exhumed fault surfaces can help inform earthquake models, including earthquake slip inversions, particularly if an earthquake were to occur on a fault upon which surface roughness measurements had already been taken. By incorporating observed fractal properties into earthquake slip inversions I aim to introduce less bias than other, less physical regularisations. With the European Space Agency's new satellites Sentinel-1a/b providing regular observations of the Earth's deforming regions, we are in a position to model earthquake slip better than ever before. I hope that by incorporating more realistic observations and using Bayesian methods to fully understand uncertainties, we can produce better, more realistic models. These models help our understanding of earthquakes, and, most importantly, earthquake hazard.

Contents

List of Figures

List of Tables

Nomenclature

List of acronyms

ABIC	Akaike's Bayesian Information Criterion
DEM	Digital Elevation Model
ESA	European Space Agency
GMT	Generic Mapping Tools
GNSS	Global Navigation Satellite System
GPS	Global Positioning System
InSAR	Interferometric Synthetic Aperture Radar
LOS	Line Of Sight
MAP	Maximum A posteriori
MCMC	Markov chain Monte Carlo
NERC	Natural Environmental Research Council
OMG	Oh my God
PCA	Principal Component Analysis
PDF	Probability Density Function
PGA	Peak Ground Acceleration
RMS	Root Mean Square
SAR	Synthetic Aperture Radar
SRTM	Shuttle Radar Topography Mision (DEM)
TLS	Terrestrial Laser Scan

List of symbols

α^2	Hyperparameter controlling slip variance	[-]
λ	Lamé's first parameter	[Pa]
μ	Lamé's second parameter, shear modulus	[Pa]
a_{as}	Correlation length along-strike	[m]
a_{dd}	Correlation length down-dip	[m]
C	Pre-factor	$[m^3]$
D	Fractal dimension	[-]
H	Hurst parameter	[-]
$H_{\parallel}$	Hurst parameter parallel to slip	[-]
$H_{\perp}$	Hurst parameter perpendicular to slip	[-]
M_w	Moment magnitude	[-]

Chapter 1

Introduction

Earthquakes pose a significant risk to life, and whilst earthquakes affect many countries in the world, the vulnerability to earthquakes (and all hazards) is significantly increased in developing countries (*Schneiderbauer and Ehrlich*, 2004). Wealthier countries incur significant economic costs from earthquake, but there are disproportionately more deaths in poorer countries (Figure 1.1, *Bilham* 2013). How much slip occurs on a fault, at what depth and whether this slip can continue on nearby or connecting faults, is fundamental to our understanding of seismic hazard (*Elliott et al.*, 2016). Currently one of our best methods for forecasting future earthquakes is to measure and model earthquakes that occur, and use these results to infer properties such as stress transfer, to identify regions of the fault that have been brought closer to failure (*Walters et al.*, 2009). But most current slip modelling methods are riddled with assumptions and often subjective choices that, if incorrect, will impact the slip solution (*Minson et al.*, 2013) and consequently any conclusions taken from it.

The amount of slip that occurs during an earthquake is controlled by roughness of a fault surface (*Candela et al.*, 2011a). Thus understanding a fault surface, its

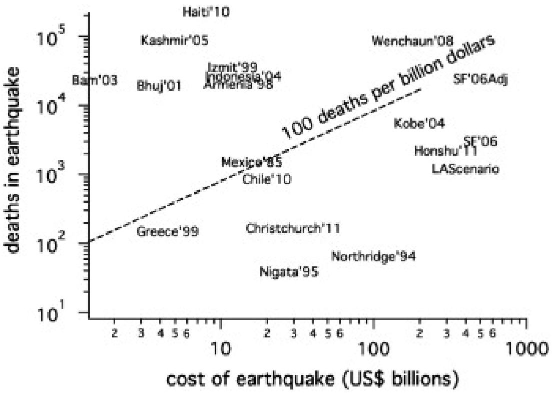

Figure 1.1: Countries with low per capita income (above the dotted line) suffer from large number of fatalities during earthquakes, whereas wealthier countries (below dotted line) incur greater reconstruction costs, yet relatively few people die. From *Bilham* (2013)

topography and behaviour over a large scale, is essential to understanding how faults slip. If we can parameterise fault surfaces correctly then we can incorporate the correct prior assumptions into earthquake models. This could help us understand earthquake friction on a fault surface (*Biegel et al.*, 1992), how earthquakes nucleate (*Harbord et al.*, 2017, *Tal et al.*, 2018), how they propagate (*Bruhat et al.*, 2016, *Fang and Dunham*, 2013, *Shi and Day*, 2013), how much moment is released (*Zielke et al.*, 2017), how much slip occurs (*Amey et al.*, 2018) and how they stop (*Parsons and Minasian*, 2015). These are all fundamental to seismic hazard assessment.

This thesis will focus on the observations that fault surfaces and earthquake slip, along with many features of earthquakes, show self-similar properties (*Ben-Zion*, 2008). Fractal properties, or self-similarity, means that a feature is similar at all scales, or mathematically, that a feature can be described by a power law (*Mandelbrot*, 1967). This long-scale structure of slip provides properties to help constrain earthquake slip distribution. It is important to properly characterise fractal fault properties using observations from fault and earthquakes, to then incorporate these features into models of earthquakes. In light of this, this thesis is concerned with two aspects of fractal slip. Chapter 2 focuses on the observed fractal nature of fault surface roughness and how it varies along-strike of a fault, and Chapters 3 and 4 introduce methodologies to incorporate this as a prior assumption into earthquake slip inversions.

In this chapter I will provide background on fault surfaces and earthquake slip showing self-similarity, or self-affinity (*Mai and Beroza*, 2002, *Sagy et al.*, 2007, *Milliner et al.*, 2015). I will then provide details on slip inversions and regularisation techniques, and how self-affinity can be incorporated. Finally I will lay out my aims and objectives and present a roadmap for this thesis.

1.1 Fractal fault roughness

1.1.1 Observations and context

Exhumed fault surfaces, whilst on first look seem remarkably planar, actually display topography at all scales. Early work found that this topography showed fractal (self-similar) properties (*Brown and Scholz*, 1985, *Poon et al.*, 1992, *Power and Tullis*, 1995). This means that root-mean-square height fluctuations are proportional to the profile length (*Fang and Dunham*, 2013) and that fault topography cannot be described by one value: the magnitude of topography depends upon the scale of observation. Mathematically a fractal relationship means that a feature can be described by a power law (*Mandelbrot*, 1967). This is a common feature of earthquake behaviour, including the Gutenberg-Richter frequency magnitude scale (*Gutenberg and Richter*, 1955, *Kanamori and Anderson*, 1975), the Omori decay of aftershocks (*Omori*, 1894), the decay of postseismic velocities (*Ingleby and Wright*, 2017) as well as many others (see

Ben-Zion 2008).

More recent work, aided by the availability of higher-resolution scanners, has quantified this relationship further and found that the topography of fault surfaces is self-affine, rather than self-similar (*Renard et al.*, 2006, *Sagy et al.*, 2007, *Brodsky et al.*, 2011, *Candela et al.*, 2012). Whereas a self-similar feature remains statistically identical at larger or smaller scales, a self-affine feature requires a different scaling in one direction. In the context of fault surfaces, if a profile perpendicular to slip, δx, underwent the transformation $\delta x \rightarrow \gamma \delta x$ by the scaling factor γ, then the fault topography, δz would undergo the transformation $\delta z \rightarrow \gamma^H \delta z$, where H is the Hurst parameter. Different values of H are found in the along-slip and perpendicular to slip directions (*Candela et al.*, 2012).

Whilst a large number of faults have been studied with multiple scans at various scales, no roughness study has quantified the change in self-affine properties along-strike of a fault. This is vital to understanding the role of fault structure and asperities in earthquake propagation and termination. In Chapter 2 of this thesis I present an investigation of the along-strike properties of fault roughness and investigate its relationship to fault structure on the Campo Felice fault, Italy.

1.1.2 Methodology of investigating fault roughness

Data in previous studies has been taken by numerous different methods, at different scales. At the very smallest scale, white light interferometers and laser profilometers have measured micro-meter topography (e.g. *Candela et al.* 2012, *Brodsky et al.* 2016, *Candela and Brodsky* 2016). Observations at these scales led to suggestions that the minimum scale of grooving is linked to the scale at which deformation mechanisms change (*Brodsky et al.*, 2016, *Candela and Brodsky*, 2016). At the largest scale, digitised surface rupture maps give data over hundreds of kilometers (*Klinger*, 2010, *Candela et al.*, 2012). In between these, terrestrial laser scanners or LiDAR can provide scans on meter to hundreds of meter scale (*Renard et al.*, 2006, *Sagy et al.*, 2007, *Candela et al.*, 2009, 2012). Photogrammetry has also proved a useful tool for scales inbetween terrestrial laser scanners and laser profilometers (*Bistacchi et al.*, 2011, *Corradetti et al.*, 2017). A combination of these data allows fractal properties to be constrained over many orders of magnitude (Figure 2.4).

Processing methods vary depending on exact techniques employed, but an example is shown in Figure 1.2. Common to all processing steps is the first in which grass, bushes and highly weathered areas are removed from the raw scans. The point clouds must then be orientated such that the fault plane lies approximately in the x, y plane, where one axis is orientated in the slip parallel direction, another in the slip perpendicular direction and z is topography of the fault. This orientation has been done a variety of ways, with Principal Component Analysis (PCA) proving a useful tool to fit the plane, as unlike a linear least-squares plane fitting method, principal component analysis takes

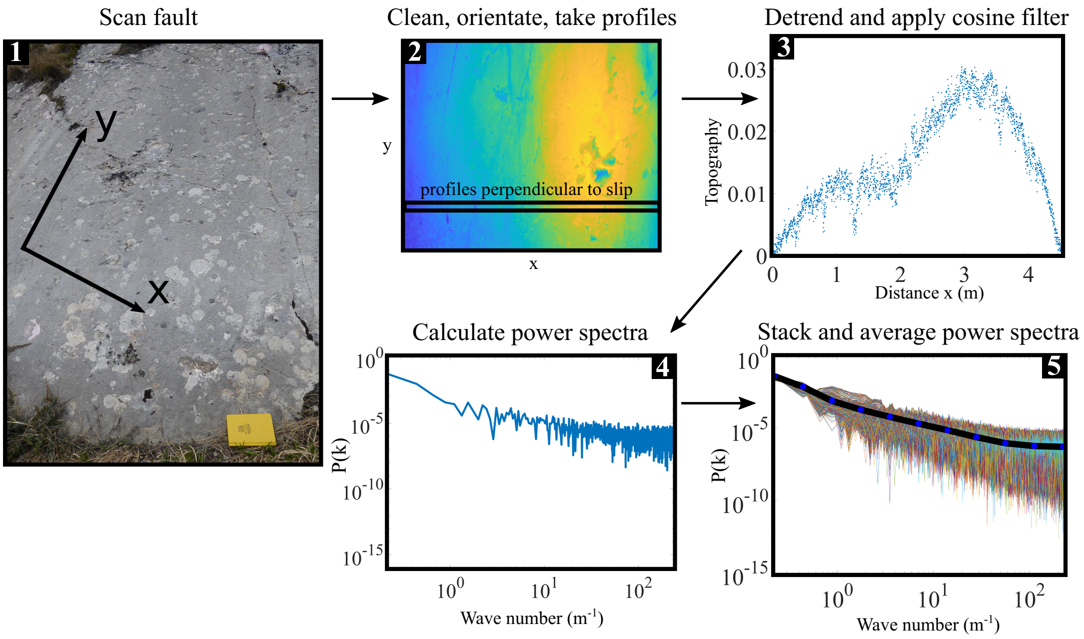

Figure 1.2: Workflow for investigating fault roughness. Starting from a fault surface (1), the scan is cleaned and orientated (2), then profiles are taken, detrended and filtered (3), so that the power spectra can be calculated (4). The power spectra are then stacked to give an average perpendicular to slip and parallel to slip (5).

into account uncertainties in x and y coordinates, as well as z (*Bistacchi et al.*, 2011). Orientating in the slip parallel/perpendicular direction relies upon features such as striations (*Renard et al.*, 2006, *Sagy et al.*, 2007), grooves, corrugations or slickenslides (*Dascher-Cousineau et al.*, 2018), or using PCA (*Bistacchi et al.*, 2011), or finding the smallest relative power spectra (*Brodsky et al.*, 2011).

Numerous profiles are then taken perpendicular and parallel to slip. Fourier analysis is a suitable tool for analysing fault roughness surfaces, as long as enough profiles are used and averaged, to eliminate noise (*Simonsen et al.*, 1998). A Fourier transform decomposes a signal into different frequencies and calculates the strength (power) of each signal. A Fourier transform requires that a signal does not have a trend and the ends of the signal taper, in order to prevent artifacts being created. To ensure this, each profile must be detrended and a taper removed, frequently a 3% or 5% cosine taper function (e.g. *Candela et al.* 2012). The Fourier transform gives power of topography at each lengthscale, in order to investigate if the topography is fractal and exactly what fractal properties it shows. By stacking and averaging the profiles, average properties of a fault surface can be determined.

Other power spectral methods include the Welch method (*Welch*, 1967) or Thomson Multitaper method (*Thomson*, 1982), which have been found to be more stable for this kind of analysis (*Bistacchi et al.*, 2011). Instead of power spectral methods, RMS roughness could be calculated directly, or can be calculated from power spectral density using Parseval's Theorem (see *Brodsky et al.* 2011).

1.1.3 Features of fractal fault roughness

From the power spectra, $P(k)$, two numbers can help quantify the fractal properties of the fault surface: the Hurst parameter, H and 'pre-factor', C, (*Sagy et al.*, 2007) by:

$$P(k) = Ck^{-1-2H} \tag{1.1}$$

The Hurst parameter is inversely proportional to the gradient of power against wavenumber, k, in log-log space and is a measure of the long-term memory of a system. It describes, in this context, whether an observed topography trend along a profile is likely to continue or not. Hurst parameters in the range $0.5 < H < 1$ show persistent behaviour, in that a trend is likely to continue whereas Hurst parameters in the range $0 < H < 0.5$ show antipersistent behaviour, with a trend likely to change, resulting in an oscillating profile (*Simonsen et al.*, 1998) (Figure 1.3).

Since fault topography is fractal, the magnitude of topography changes depending on the scale of observation. Thus the pre-factor, C, is a useful parameter as it gives magnitude at a given lengthscale, enabling comparison between faults and scan sites.

These two parameters help to quantify the smoothness of a fault surface, and consequently how a fault may fail in an earthquake.

1.1.4 Implications for earthquake slip

Measurements of the self-similar nature of fault surfaces can be used to better inform earthquake models. Fault roughness has been incorporated into many different earthquake models and experiments. These include investigations on the effect on nucleation (*Harbord et al.*, 2017, *Tal et al.*, 2018), dynamic rupture models (*Bruhat et al.*, 2016, *Fang and Dunham*, 2013, *Parsons and Minasian*, 2015, *Shi and Day*, 2013), ground-motion simulations (*Mai et al.*, 2017) and stress-drop and strain numerical models (*Zielke and Mai*, 2016, *Zielke et al.*, 2017). It is suggested that faults smooth with maturity (*Sagy et al.*, 2007, *Brodsky et al.*, 2011), with implications for Gutenberg-Richter b values (*Goebel et al.*, 2017) and seismic hazard (*Zielke et al.*, 2017).

Surfaces with fractal roughness are predicted to cause fractal stress drops and coseismic slip distributions (*Candela et al.*, 2011b). Fractal distribution of coseismic slip has been observed in surface slip in the Landers earthquake (*Milliner et al.*, 2015, 2016). In addition, an investigation into published seismological slip distributions demonstrated these distributions have fractal properties (*Mai and Beroza*, 2002).

These observations imply that fractal slip properties should be incorporated into models of earthquake slip inversions.

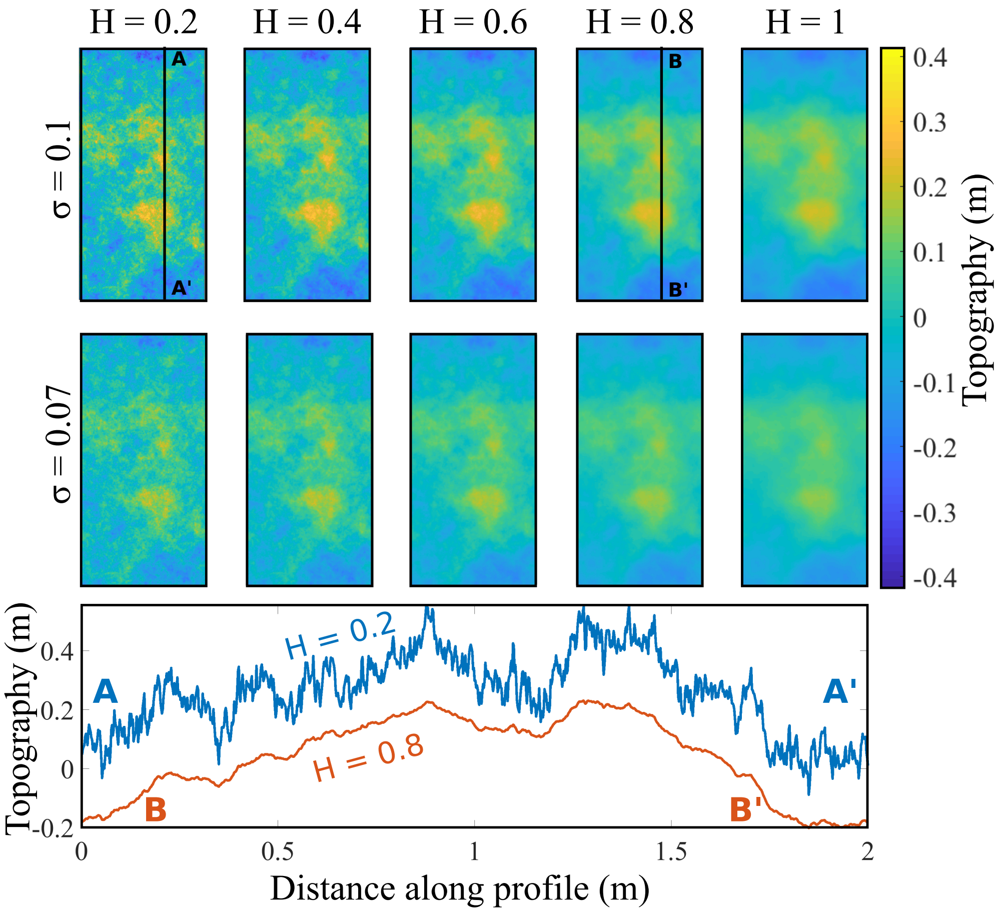

Figure 1.3: Some examples of generated fractal surfaces. The root-mean-square roughness (σ) defines the magnitude of topography and the Hurst parameter, H, defines the long-term trend of a signal. Profiles with $H < 0.5$ have high-frequency oscillations (antipersistent behaviour) compared to profiles where $H > 0.5$, which show persistent behaviour. The topography of profiles A and B have been vertically offset from each other for clarity.

1.1.5 Incorporating fractal properties into slip inversions through von Karman regularisation

The meta-analysis by *Mai and Beroza* (2002) investigated the autocorrelation (correlation between slip magnitude on patches as a function of distance between them) for various published slip inversion solutions. They looked mostly at seismological finite-fault inversions and investigated which of four types of autocorrelation function best described the slip distributions: Gaussian, exponential, fractal and von Karman. The von Karman autocorrelation best matched the power spectral density of slip correlation, particularly the gradual roll-off of the power spectral density at small wavenumbers (large wavelengths).

The von Karman correlation was first used to describe turbulence in fluids (*von*

Kármán, 1948). The von Karman correlation, $C(r)$, is given by:

$$C(r) = \frac{G_H(r/a)}{G_H(0)} \tag{1.2}$$

Where $G_H(r/a) = (r/a)^H K_H(r/a)$, where K_H is a modified Bessel function of the second kind of order H, H is the Hurst parameter and r is the separation distanced, scaled by a.

The Hurst parameter, as described above, controls the fractal properties and is related to the fractal dimension, D, by $D = (\textit{Euclidian dimension}) + 1 - H$. Whereas a fractal correlation only has one term to describe its correlation (fractal dimension, D) the von Karman correlation has multiple terms, the Hurst parameter H and correlation lengths along strike, a_{as} and down dip, a_{dd}. This allows for different properties along-strike and down-dip, which is useful for capturing the self-affine earthquake slip properties: differences in scaling along-strike and down-dip.

The von Karman autocorrelation function is similar to an exponential decay function (Figure 1.4; for $H = 0.5$ the von Karman autocorrelation is equal to exponential decay). It is a way of defining the expected decay of similarity between slip patches as a function of the distance between them, scaled by the correlation lengths. This can be incorporated into the slip inversion using a Bayesian approach.

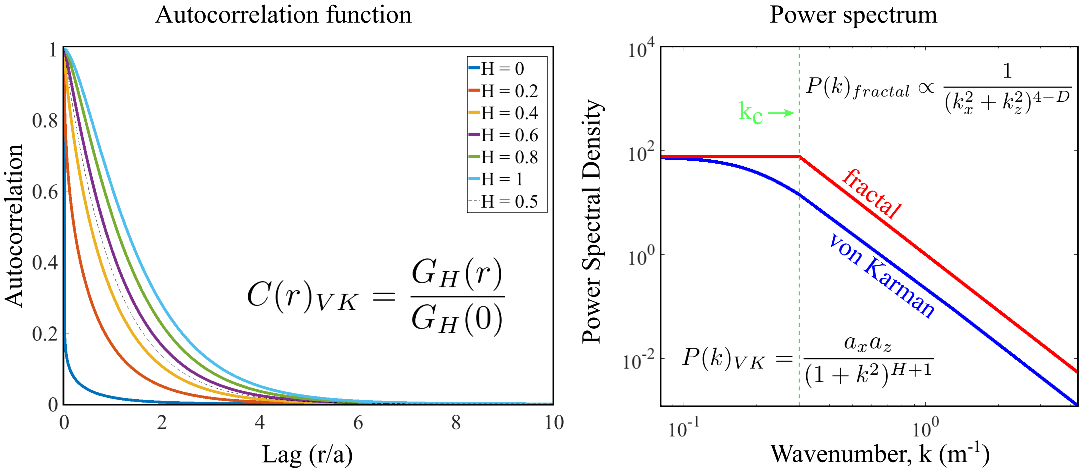

Figure 1.4: The autocorrelation function (left) and power spectrum (right) of the von Karman autocorrelation function. The autocorrelation decays as a function of lag, with the exact relationship defined by the Hurst parameter, H. For $H = 0.5$, the autocorrelation function is equal to an exponential decay. The power spectrum of a von Karman function is similar to a fractal spectrum, but the von Karman power spectrum decays more slowly at small wavenumbers, whereas a fractal medium is controlled by corner wave number, k_c, related to the characteristic source dimension. Adapted from *Mai and Beroza* 2002.

1.2 Slip inversions

Modelling the magnitude and direction of slip that occurs during an earthquake has become a standard procedure during an earthquake investigation (*Elliott et al.*, 2016). By using observations of ground displacements from geodetic data such as Interferometric Synthetic Aperture Radar (InSAR) or Global Navigation Satellite System (GNSS), or seismological data, we can create a model of how much slip occurred underground, along the fault plane, where we cannot directly measure it. The early seismological slip inversions used the finite-fault inversion method, which relied on waveform matching synthetic seismograms for each patch on the fault plane with observed waveform data (*Olson and Apsel*, 1982, *Hartzell and Heaton*, 1983).

Producing a slip solution is achieved using inverse methods; by using observations we work backwards to solve for parameters of interest, using some assumed knowledge of the Earth that relates the parameters we can observe to those we cannot. The standard set-up of inverse methods is:

$$\mathbf{d} = \mathbf{g}(\mathbf{m}) \tag{1.3}$$

Or, for a linear inverse problem:

$$\mathbf{d} = \mathbf{G}\mathbf{m} \tag{1.4}$$

Where **d** is data, **m** are the model parameters (values for which you are solving, such as slip, rake) and **G** is a mapping function that relates the model parameters to the data. In this thesis I used geodetic data, and so will focus on it here.

The most popular inversion method is a linear least-squares method (*Fukuda and Johnson*, 2008). This is because the slip inversion can be written as a linear problem for a known fault geometry, and least-squares methods are quick and computationally cheap. For a distributed slip model, as is used here, the aim is to quantify how slip varies in magnitude and location along a fault plane. The problem is set up such that a fault plane is broken down into discrete elements, such as commonly used rectangular patches (e.g. *Wright* 2003) or triangular patches (e.g. *Barnhart et al.* 2011) of the same size or of different sizes (e.g. *Jolivet et al.* 2014a). The choice of size of these elements is driven by data sensitivity. A high concentration of surface observations means that smaller elements can be used to resolve slip at higher detail, but if too many patches are used there is the risk of over-fitting noise. In contrast, the use of fewer patches averages noise contributions, but potentially resolvable slip is unnecessarily averaged, too. The size of patches is frequently chosen in advance or can be solved for (*Barnhart and Lohman*, 2010, *Atzori and Antonioli*, 2011).

The mapping function, **G** that relates slip at depth on a fault plane to observable surface displacements is frequently formulated using *Okada* (1985). This models the fault as a rectangular dislocation in an elastic half space, and with Lamé parameters, λ (Lamé's first parameter) and μ (Lamé's second parameter, shear modulus), can be used to predict the surface displacements due to elastic motion at depth. Some approaches include varying elastic parameters with depth, particularly joint geodetic-seismic methods (*Simons*, 2002, *Jolivet et al.*, 2014a). The matrix $\mathbf{G}$ must be correctly formulated using the strike and dip of the fault plane, the locations of the discrete fault patches and the rake (direction of earthquake slip). By calculating $\mathbf{G}$ for unit slip, when $\mathbf{G}$ is multiplied by column vector $\mathbf{m}$, which contains the value of slip, this produces the predicted observations $\mathbf{d}$ for that magnitude of slip.

1.2.1 InSAR and GNSS

InSAR and GNSS are invaluable tools for investigating earthquake surface displacements. GNSS provides high temporal resolution but a sparse spatial distribution, which can instead be provided by InSAR.

In-depth descriptions of InSAR processing are provided by works such as *Hanssen* (2001) and *Grandin et al.* (2016) and the application to tectonic settings are provided by reviews such as *Wright* (2002) and *Elliott et al.* (2016). Briefly, by interfering two radar images, taken before and after the earthquake, and correcting for parameters such as topography, geometry and atmospheric delays, a map of surface displacements incurred during an earthquake can be obtained. These measurements give wide ground coverage, provided the area is coherent between InSAR acquisitions. Originally used for topographic mapping (*Gabriel et al.*, 1989), InSAR was first applied in a tectonic setting on the 1992 Landers earthquake (*Massonnet et al.*, 1993). The displacement measurement is in the 'line-of-sight' of the satellite, meaning that the satellite can only distinguish movement in the look direction of the satellite, and is blind to other movement. The number of datapoints provided by InSAR is unnecessarily high for modelling purposes, and if all used would make a calculation very computationally expensive. Thus InSAR scenes are downsampled, frequently using a quadtree downsample method (*Jónsson et al.*, 2002, *Lohman and Simons*, 2005) or by uniform downsampling, to provide enough detail in areas where displacement magnitudes change quickly, but without slowing down computation too much.

In contrast, GNSS measurements provide higher temporal resolution and can be used to determine displacements over a matter of days (e.g. *Floyd et al.* 2016). By triangulating between at least four satellites, the exact ground location can be determined. A site can then be re-occupied (campaign GNSS) or continuously monitored to give displacements through time. Unlike InSAR, GNSS gives North, East and vertical displacements.

By using InSAR and GNSS measurements before and after an earthquake, the coseismic surface displacements can be calculated to a high degree of accuracy. These can then be used to calculate slip at depth in slip inversions.

1.2.2 Regularisation in slip inversions

If a forward model of surface displacements is created from an input slip distribution using *Okada* (1985) by $\mathbf{d} = \mathbf{Gm}$ and then the same surface displacements are inverted for slip, then the exact solution will be returned.

Unfortunately in the real world the InSAR and GNSS measurements of surface displacement are affected by noise, including spatially correlated noise and model errors. The data coverage depends upon the location of GNSS receivers and by areas of coherence in interferograms. This means that slip inversions do not have a unique solution (they are ill posed), or that there is a unique solution but the inversion is too close to singular and the solution will attempt to fit noise, which can cause oscillations in the solution (the solution is unstable). To attempt to find a unique, stable solution, frequently some form of regularisation is used. In the geodetic community, Laplacian smoothing is the commonly adopted approach (*Harris and Segall*, 1987, *Wright*, 2003, *Funning et al.*, 2005). Laplacian smoothing minimises the sum of the second spatial derivatives, thereby seeking to keep the difference in slip between patches small. The weight of this smoothing is controlled by a scalar smoothing factor, the value of which is often chosen by repeating the inversion for different smoothing factors, calculating the misfit and then generating an ‘L-curve’ of smoothing factor against mistfit (*Jónsson et al.*, 2002, *Wright*, 2003, *Walters et al.*, 2009). The smoothing factor is then chosen to balance the misfit and roughness, generally chosen to be near the bend in the L-curve, but a limitation of this is that the bend is often not sharp and the position of the bend changes with the scale of the graph (*Fukuda and Johnson*, 2008). The smoothing parameter can be chosen objectively with methods such as ABIC (Akaike’s Bayesian Information Criterion) (*Yabuki and Matsu’ura*, 1992) or cross-validation (*Johnson et al.*, 2001, *Hreinsdóttir*, 2003) but most frequently the trade-off approach is used, and commonly little or no justification is given at all. This can result in a range of possible solutions (Figure 1.5).

Laplacian smoothing is beneficial in that by minimising the difference in slip between patches it stops unrealistic stress drops in slip solutions, but this does not mean it is necessarily the best regularisation to use. Indeed there are many other regularisations, including methods that promote spatially compact solutions (*Evans and Meade*, 2012) or those that include no regularization at all if resolution allows (*Minson et al.*, 2013, *Jolivet et al.*, 2014b).

This thesis is concerned with incorporating a more realistic regularisation into earthquake slip inversions. As discussed previously, many avenues of research have shown that earthquake slip shows self-similar properties. Since this is an observed and measured feature of earthquake slip this suggests that it is a more realistic prior assumption to bring into earthquake slip inversions. In this thesis I incorporate fractal slip as a regularization into slip inversions, after *Hooper* (2012). This is done using Bayesian

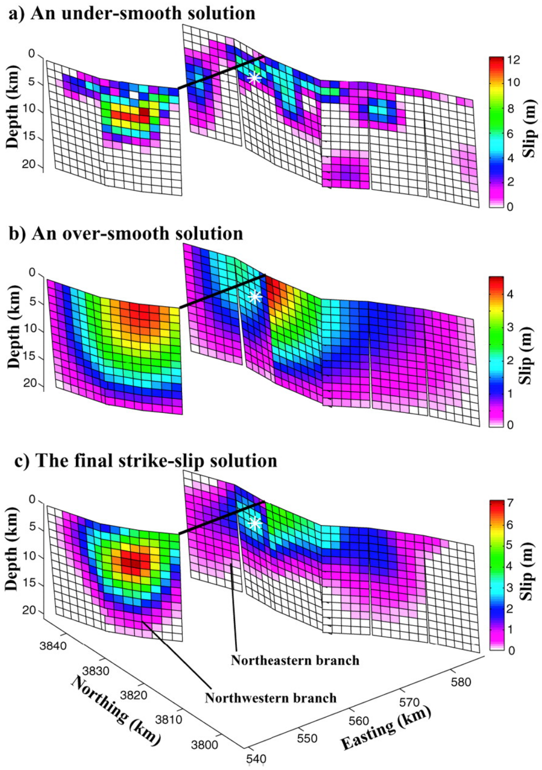

Figure 1.5: Three different smoothing parameters used in a Laplacian smoothed solution for the M_w 7.1 Hector Mine Earthquake. Figure from *Jónsson et al.* (2002).

methods (Section 1.2.3), after *Fukuda and Johnson* (2008), *Hooper and Wright* (2009), *Hooper et al.* (2013), *Minson et al.* (2013), through the von Karman function (Section 1.1.5). In Chapter 3 I fully introduce the method. Upon finding some limitations to it I further refine this method in Chapter 4.

1.2.3 Bayesian methods

In recent years there has been a move towards Bayesian slip inversions in the geophysical community (*Hooper et al.*, 2013, *Minson et al.*, 2013). Unlike a least-squares solution, which presents an answer and a Gaussian distribution through propagation of errors, a Bayesian approach allows the full exploration of the range of values that parameters can take that both fit the data and our prior assumptions about them. It is also a very flexible approach, so constraints can be easily incorporated through the prior probability density function (PDF) and additionally hyperparameters, such as smoothing parameters (discussed in section 1.2.2), can be fit within the inversion. The full solution is a PDF for each model parameter (posterior PDF) that captures the full range of values suitable for that model parameter, as well as an indication of the value it is most likely to be. A fundamental assumption in Bayesian inversions is that our prior knowledge about all the model parameters (the unknowns for which we are solving) can be expressed as a probability.

Bayes theorem states:

$$p(\mathbf{m}|\mathbf{d}) = \frac{p(\mathbf{d}|\mathbf{m})p(\mathbf{m})}{\int_{-\infty}^{\infty} p(\mathbf{d}|\mathbf{m})p(\mathbf{m})d\mathbf{m}} \tag{1.5}$$

Where the posterior distribution, $p(\mathbf{m}|\mathbf{d})$, is comprised of how well the model fits the observed data (the likelihood, $p(\mathbf{d}|\mathbf{m})$) and how well a model fits prior assumptions (the prior, $p(\mathbf{m})$). The denominator is referred to as the 'evidence' and is a normalising constant, so is frequently ignored. Throughout the inversion our prior knowledge, $p(\mathbf{m})$, about the model parameters is updated by the data, $\mathbf{d}$, to give the posterior distribution.

Some Bayesian solutions can be solved analytically, but if this is not possible (e.g. if solving for hyperparameters) then frequently Bayesian methods are paired with MCMC (Markov chain Monte Carlo) methods. This is a sampling method so that instead of attempting to evaluate Equation 1.5 for all possible values of every parameter, which would quickly become impractical for a problem with a large number of parameters, it allows an efficient search of parameter space.

A Markov chain is a memoryless chain in which a trial is generated as a perturbation of the current state. By accepting or rejecting new trials based on the ratio of their probability to the probability of the current state, the Markov chain preferentially samples in areas of high probability, thus building the posterior PDF. The flexible Bayesian framework allows us to incorporate prior assumptions such as fractal slip, prevent unphysical features such as backslip and solve for hyperparameters within the inversion.

I implement the Bayesian framework using two steps, as described by *Tarantola* (2005). I use the first step to sample the prior: a slip distribution consistent with the von Karman prior, which is non-trivial to directly generate using a random walk. Whilst generating a von Karman slip distribution is simple, the MCMC sampling requires a perturbation from the current distribution, and so we select von Karman trials using the first sampling step instead of attempting to produce von Karman trials directly. The second step then samples the posterior, by calculating the likelihoods. There is an efficiency benefit to performing this in two steps, since the likelihood is computationally expensive and this calculation need not be performed for trials that would have been rejected for low prior probability anyway.

Our method for incorporating the von Karman correlation is developed and described in Chapter 3.

1.2.4 Trans-dimensional approaches

If the number of unknowns within an inversion is itself unknown, this becomes a trans-dimensional inversion.

Geyer and Møller (1994) and *Green* (1995) introduced a method of sampling trans-dimensional posteriors. *Green* (1995) termed the method 'reversible-jump MCMC' methods, in which the chain is able to 'jump' between differently-sized parameter spaces as the number of model parameters changes. Trans-dimensional Bayesian approaches have been applied to many geophysical problems (*Sambridge et al.*, 2006), including parameterising the number, thickness and geophysical properties in a layered Earth model (*Malinverno et al.*, 2002), tomography (*Bodin and Sambridge*, 2009) and recently finite-fault inversions (*Dettmer et al.*, 2014).

In Chapter 4 I use trans-dimensional methods to solve for the number of slipping patches within an inversion, so that the inversion is not biased by initial assumptions on fault size.

1.3 Faults and earthquakes in this study

1.3.1 Campo Felice fault, Italian Apennines

The Italian Apennines are a northeast-southwest striking mountain belt consisting of many normal faults that are accommodating the current ∼3 mm/yr extension (*Malinverno and Ryan*, 1986, *D'Agostino et al.*, 2014) (Figure 1.6).

The Campo Felice fault in the Italian Apennines offers an excellent opportunity to conduct an along-strike fault roughness study, as its bedrock fault scarp is well exposed along its ∼5 km length. This provides suitable scanning sites along its length, enabling the quantification of differences between the fault surface properties over a small (tens of meters to hundreds of meters) scale. Using this data I will examine any systematic variation along the fault, and the relationship between fault roughness and rupture propagation and termination.

A previous study of the limestone fault scarp divided the fault into three different morphological units up-dip but the roughness measurements did not distinguish any differences in weathering up the fault scarp, that could have related to seismic events (*Giaccio et al.*, 2003). A terrestrial laser scanner study identified a prominent bend that links across a former left-stepping relay zone, with increased throw rates in the vicinity of the bend (*Wilkinson et al.*, 2015).

1.3.2 The Napa Valley earthquake

The M_w 6.0 Napa Valley, California earthquake, also called the South Napa earthquake, happened on the 24th August 2014 (Figure 1.7). This was the first earthquake imaged by Sentinel-1a, with the image before the earthquake taken on the first day it reached its operation orbit. It was also the largest earthquake in the San Francisco Bay area for twenty-five years, so attracted a lot of scientific interest (*Hudnut et al.*, 2014, *Parsons et al.*, 2014, *Grapenthin et al.*, 2014, *Dreger et al.*, 2015, *Elliott et al.*, 2015, *Ji et al.*,

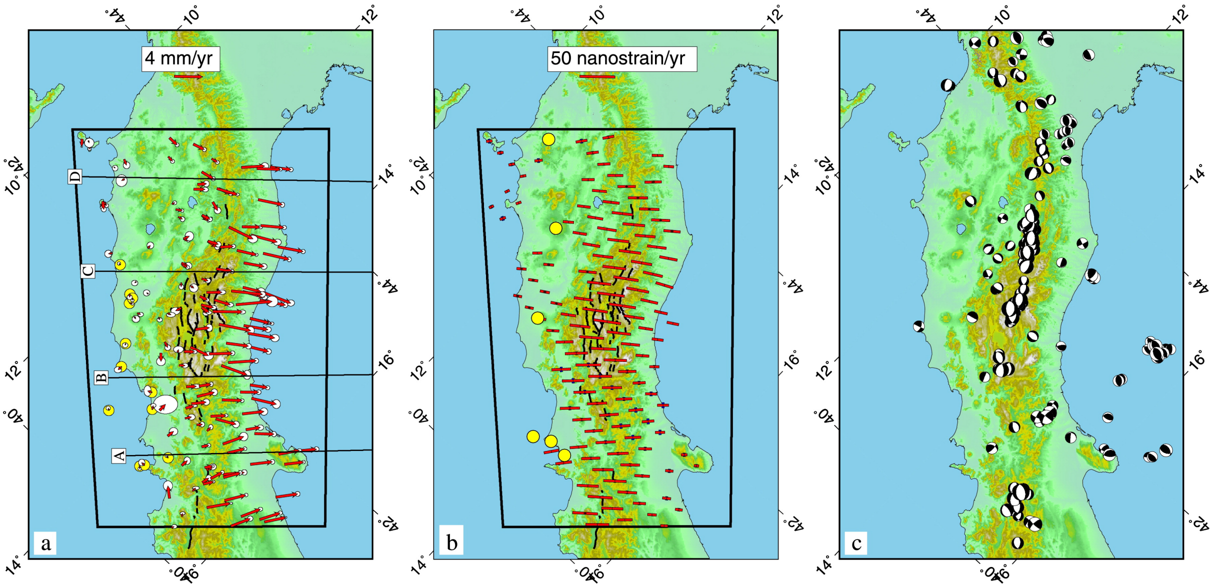

Figure 1.6: Continuous GNSS observations (panel *a*), strain rates (panel *b*) and earthquakes <30 km depth across the Italian Apennines. Figure from *D'Agostino et al.* (2014)

2015, *Guangcai et al.*, 2015, *Barnhart et al.*, 2015, *Zhang et al.*, 2015, *Langbein*, 2015, *Taira et al.*, 2015, *Melgar et al.*, 2015, *DeLong et al.*, 2016, *Floyd et al.*, 2016). It had right-lateral strike-slip sense of motion and occurred on the West Napa Fault and the surface ruptures were extensively mapped (*Hudnut et al.*, 2014) which provided excellent detail to constrain the fault plane.

1.3.3 The Central Tottori earthquake

The Central Tottori earthquake occurred in the Tottori prefecture of the Chugoku region, Japan, 2016 (Figure 1.8). It had a left-lateral strike-slip sense of motion and occurred in the Northern Chugoku shear zone, in a region in which there has been several large magnitude earthquakes including a magnitude 7.2 in 1943 (*Kanamori*, 1972), a magnitude 6.2 in 1983 (*Tsukuda*, 1988) and magnitude 6.6 in 2000 (*Semmane et al.*, 2005, *Monelli et al.*, 2009).

At the time of writing, no geodetic investigation of this earthquake had been undertaken, though two seismology investigations had performed slip inversions to which I could compare my results.

One benefit of this earthquake is that it presented simpler fault geometry than Napa, for testing our new method. Whereas for Napa the mapped surface rupture and complicated InSAR pattern suggested multiple faults may be necessary, here the deformation pattern suggests modelling as one fault may be more reasonable.

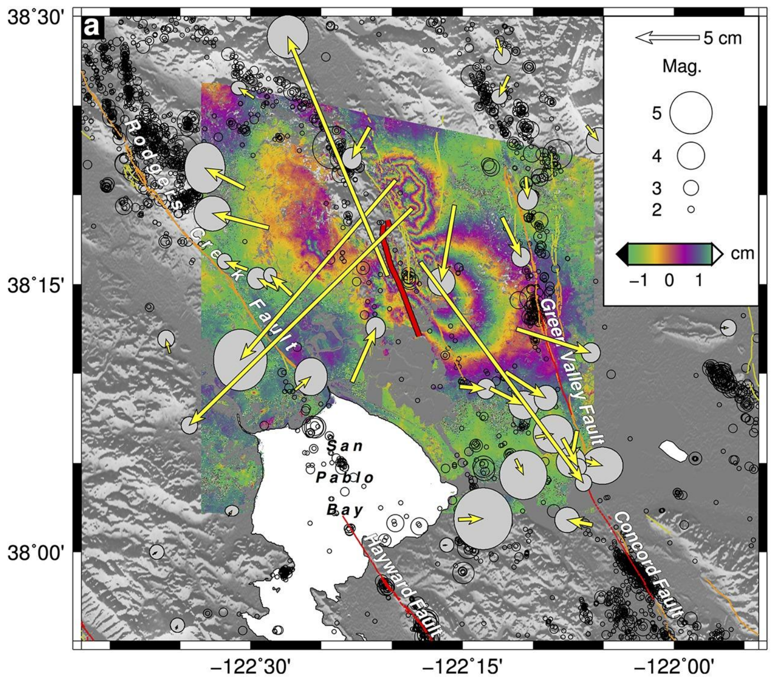

Figure 1.7: Coseismic InSAR and GPS surface displacements for the Napa Valley earthquake. Pre earthquake seismicity shown in black (*Waldhauser*, 2009), mapped surface rupture shown in red (*Morelan et al.*, 2015), GPS vectors in yellow with grey 95% confidence ellipses. Figure from (*Floyd et al.*, 2016)

.

1.4 Aims and objectives

In this work I aim to further explore the fractal properties of fault surfaces and fault slip, to confirm that these properties can be incorporated into earthquake slip inversions and introduce this new method of regularisation. In doing so I aim to present a viable new methodology that the scientific community can adopt for slip inversions, or at the very least cause the community to question its default regularisation choice.

My specific objectives are:

1. Investigate properties of fractal slip and incorporate them into multiple earthquake scenarios

2. Explore how the fractal properties of fault surfaces change along-strike of a fault and the link to fault structure

3. Develop a Bayesian method to efficiently and reliably solve for earthquake slip from InSAR and GNSS data on a multi-fault model, incorporating fractal properties

4. Further refine the method of incorporating fractal slip to make the inversion as unbiased as possible, by solving for the number of slip patches within the inversion

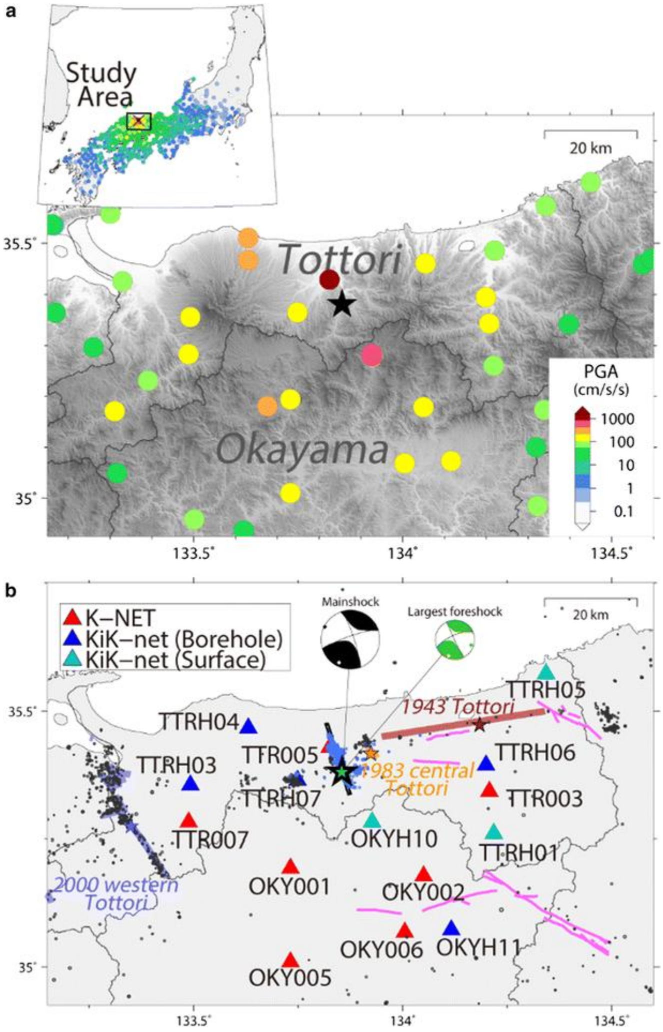

Figure 1.8: The Central Tottori earthquake occurred in the Chugoku region of Japan (Figure a). Panel b shows the peak ground acceleration (PGA) during the earthquake as measured by K-NET and KiK-net. Panel b shows the 2016 earthquake (green star), focal mechanism and fault plane as well as aftershocks and approximate fault planes from other recent earthquakes in the region. Figure from (*Kubo et al.*, 2017).

1.5 Thesis roadmap

In Chapter 2, I investigate how the fractal properties of fault roughness vary along the Campo Felice fault in the Italian Apennines and relate this to fault structure.

In Chapter 3, I develop a method for incorporating self-affine properties into earthquake slip inversions. I do this using a Bayesian inversion, incorporating several measures for efficiency. I test this on several synthetic tests to show that this regularization is as good if not better than current methods and then apply this method to the Napa Valley earthquake.

In Chapter 4, I further refine this method, making it trans-dimensional to remove the bias caused by choosing fault size in advance.

In Chapter 5, I discuss this work in the wider context of understanding earthquake slip and its importance and use to the tectonics community, as well as future work.

References

Amey, R. M. J., A. Hooper, and R. J. Walters (2018), A Bayesian Method for Incorporating Self-Similarity into Earthquake Slip Inversions, *Journal of Geophysical Research: Solid Earth*, *123*, doi:10.1029/2017JB015316. 1

Atzori, S., and A. Antonioli (2011), Optimal fault resolution in geodetic inversion of coseismic data, *Geophysical Journal International*, *185*(1), 529–538, doi:10.1111/j.1365-246X.2011.04955.x. 1.2

Barnhart, W. D., and R. B. Lohman (2010), Automated fault model discretization for inversions for coseismic slip distributions, *Journal of Geophysical Research*, *115*(B10), B10,419, doi:10.1029/2010JB007545. 1.2

Barnhart, W. D., M. J. Willis, R. B. Lohman, and M. Andrew K. (2011), InSAR and Optical Constraints on Fault Slip during the 20102011 New Zealand Earthquake Sequence, *82*(6), 815–823, doi:10.1785/gssrl.82.6.815. 1.2

Barnhart, W. D., J. R. Murray, S. Yun, J. L. Svarc, S. V. Samsonov, E. J. Fielding, B. A. Brooks, and P. Milillo (2015), Geodetic Constraints on the 2014 M 6.0 South Napa Earthquake, *Seismological Research Letters*, *86*(2), 335–343, doi:10.1785/0220140210. 1.3.2

Ben-Zion, Y. (2008), Collective behavior of earthquakes and faults: Continuum-discrete transitions, progressive evolutionary changes, and different dynamic regimes, *Reviews of Geophysics*, *46*(4), RG4006, doi:10.1029/2008RG000260. 1, 1.1.1

Biegel, R. L., W. Wang, C. H. Scholz, G. N. Boitnott, and N. Yoshioka (1992), Micromechanics of rock friction 1. Effects of surface roughness on initial friction and slip hardening in westerly granite, *Journal of Geophysical Research: Solid Earth*, *97*(B6), 8951–8964, doi:10.1029/92JB00042. 1

Bilham, R. (2013), Societal and observational problems in earthquake risk assessments and their delivery to those most at risk, *Tectonophysics*, *584*, 166–173, doi:10.1016/j.tecto.2012.03.023. 1, 1.1

Bistacchi, A., W. A. Griffith, S. A. F. Smith, G. Di Toro, R. Jones, and S. Nielsen (2011), Fault Roughness at Seismogenic Depths from LIDAR and Photogrammetric Analysis, *Pure and Applied Geophysics*, *168*(12), 2345–2363, doi:10.1007/s00024-011-0301-7. 1.1.2, 1.1.2

Bodin, T., and M. Sambridge (2009), Seismic tomography with the reversible jump algorithm, *Geophysical Journal International*, *178*(3), 1411–1436, doi:10.1111/j.1365-246X.2009.04226.x. 1.2.4

Brodsky, E. E., J. J. Gilchrist, A. Sagy, and C. Collettini (2011), Faults smooth gradually as a function of slip, doi:10.1016/j.epsl.2010.12.010. 1.1.1, 1.1.2, 1.1.2, 1.1.4

Brodsky, E. E., J. D. Kirkpatrick, and T. Candela (2016), Constraints from fault roughness on the scale-dependent strength of rocks, *Geology*, *44*(1), 19–22, doi:10.1130/G37206.1. 1.1.2

Brown, S. R., and C. H. Scholz (1985), Broad Bandwidth Study of the Topography of Natural Rock Surfaces, *Journal of Geophysical Research*, *90*(B14), 12,575, doi:10.1029/JB090iB14p12575. 1.1.1

Bruhat, L., Z. Fang, and E. M. Dunham (2016), Rupture complexity and the supershear transition on rough faults, *Journal of Geophysical Research: Solid Earth*, *121*(1), 210–224, doi:10.1002/2015JB012512. 1, 1.1.4

Candela, T., and E. E. Brodsky (2016), The minimum scale of grooving on faults, *Geology*, *44*(8), 603–606, doi:10.1130/G37934.1. 1.1.2

Candela, T., F. Renard, M. Bouchon, A. Brouste, D. Marsan, J. Schmittbuhl, and C. Voisin (2009), Characterization of Fault Roughness at Various Scales: Implications of Three-Dimensional High Resolution Topography Measurements, *Pure and Applied Geophysics*, *166*(10-11), 1817–1851, doi:10.1007/s00024-009-0521-2. 1.1.2

Candela, T., F. Renard, J. Schmittbuhl, M. Bouchon, and E. E. Brodsky (2011a), Fault slip distribution and fault roughness, *Geophysical Journal International*, *187*(2), 959–968. 1

Candela, T., F. Renard, M. Bouchon, J. Schmittbuhl, and E. E. Brodsky (2011b), Stress Drop during Earthquakes: Effect of Fault Roughness Scaling, *Bulletin of the Seismological Society of America*, *101*(5), 2369–2387, doi:10.1785/0120100298. 1.1.4

Candela, T., F. Renard, Y. Klinger, K. Mair, J. Schmittbuhl, and E. E. Brodsky (2012), Roughness of Fault Surfaces over Nine Decades of Length Scales, *Journal of Geophysical Research*, *117*(B8), B08,409, doi:10.1029/2011JB009041. 1.1.1, 1.1.2

Corradetti, A., K. McCaffrey, N. D. Paola, and S. Tavani (2017), Evaluating roughness scaling properties of natural active fault surfaces by means of multi-view photogrammetry, *Tectonophysics*, *717*, 599–606, doi:10.1016/j.tecto.2017.08.023. 1.1.2

D'Agostino, N., P. England, I. Hunstad, and G. Selvaggi (2014), Gravitational potential energy and active deformation in the Apennines, *Earth and Planetary Science Letters*, *397*, 121–132, doi:10.1016/j.epsl.2014.04.013. 1.3.1, 1.6

Dascher-Cousineau, K., J. D. Kirkpatrick, and M. L. Cooke (2018), Smoothing of Fault Slip Surfaces by Scale-Invariant Wear, *Journal of Geophysical Research: Solid Earth*, doi:10.1029/2018JB015638. 1.1.2

DeLong, S. B., A. Donnellan, D. J. Ponti, R. S. Rubin, J. J. Lienkaemper, C. S. Prentice, T. E. Dawson, G. Seitz, D. P. Schwartz, K. W. Hudnut, C. Rosa, A. Pickering, and J. W. Parker (2016), Tearing the terroir: Details and implications of surface rupture and deformation from the 24 August 2014 <i>M</i> 6.0 South Napa earthquake, California, *Earth and Space Science*, doi:10.1002/2016EA000176. 1.3.2

Dettmer, J., R. Benavente, P. R. Cummins, and M. Sambridge (2014), Trans-dimensional finite-fault inversion, *GJI Seismology*, *199*, 735–751, doi:10.1093/gji/ggu280. 1.2.4

Dreger, D. S., M.-H. Huang, A. Rodgers, T. Taira, and K. Wooddell (2015), Kinematic Finite-Source Model for the 24 August 2014 South Napa, California, Earthquake from Joint Inversion of Seismic, GPS, and InSAR Data, *Seismological Research Letters*, *86*(2A), 327–334, doi:10.1785/0220140244. 1.3.2

Elliott, J. R., A. J. Elliott, A. J. Hooper, Y. Larsen, P. Marinkovic, and T. J. Wright (2015), Earthquake Monitoring Gets Boost from New Satellite, *EOS*, *96*, doi:10.1029/2015EO023967. 1.3.2

Elliott, J. R., R. J. Walters, and T. J. Wright (2016), The role of space-based observation in understanding and responding to active tectonics and earthquakes, *Nature Communications*, *7*(13844), doi:10.1038/ncomms13844. 1, 1.2, 1.2.1

Evans, E. L., and B. J. Meade (2012), Geodetic Imaging of Coseismic Slip and Postseismic Afterslip: Sparsity Promoting Methods Applied to the Great Tohoku Earthquake, *Geophysical Research Letters*, *39*(11), doi:10.1029/2012GL051990. 1.2.2

Fang, Z., and E. M. Dunham (2013), Additional shear resistance from fault roughness and stress levels on geometrically complex faults, *Journal of Geophysical Research: Solid Earth*, *118*(7), 3642–3654, doi:10.1002/jgrb.50262. 1, 1.1.1, 1.1.4

Floyd, M. A., R. J. Walters, J. R. Elliott, G. J. Funning, J. L. Svarc, J. R. Murray, A. J. Hooper, Y. Larsen, P. Marinkovic, R. Bürgmann, I. A. Johanson, and T. J. Wright (2016), Spatial variations in fault friction related to lithology from rupture and afterslip of the 2014 South Napa, California, earthquake, *Geophysical Research Letters*, *43*(13), 6808–6816, doi:10.1002/2016GL069428. 1.2.1, 1.3.2, 1.7

Fukuda, J., and K. M. Johnson (2008), A Fully Bayesian Inversion for Spatial Distribution of Fault Slip with Objective Smoothing, *Bulletin of the Seismological Society of America*, *98*(3), 1128–1146, doi:10.1785/0120070194. 1.2, 1.2.2, 1.2.2

Funning, G. J., R. M. Barke, S. H. Lamb, E. Minaya, B. Parsons, and T. J. Wright (2005), The 1998 Aiquile, Bolivia earthquake: A seismically Active Fault Revealed with InSAR, *Earth and Planetary Science Letters*, *232*(1-2), 39–49, doi:10.1016/j.epsl.2005.01.013. 1.2.2

Gabriel, A. K., R. M. Goldstein, and H. A. Zebker (1989), Mapping small elevation changes over large areas: Differential radar interferometry, *Journal of Geophysical Research: Solid Earth*, *94*(B7), 9183–9191, doi:10.1029/JB094iB07p09183. 1.2.1

Geyer, C. J., and J. Møller (1994), Simulation Procedures and Likelihood Inference for Spatial Point Processes, *Scandinavian Journal of Statistics*, *21*(4), 359–373. 1.2.4

Giaccio, B., F. Galadini, A. Sposato, P. Messina, M. Moro, M. Zreda, A. Cittadini, S. Salvi, and A. Todero (2003), Image processing and roughness analysis of exposed bedrock fault planes as a tool for paleoseismological analysis: results from the Campo Felice fault (central Apennines, Italy), *Geomorphology*, *49*(3-4), 281–301, doi:10.1016/S0169-555X(02)00191-5. 1.3.1

Goebel, T. H., G. Kwiatek, T. W. Becker, E. E. Brodsky, and G. Dresen (2017), What allows seismic events to grow big?: Insights from b-value and fault roughness analysis in laboratory stick-slip experiments, *Geology*, *45*(9), 815–818, doi:10.1130/G39147.1. 1.1.4

Grandin, R., E. Klein, M. Métois, and C. Vigny (2016), 3D displacement field of the 2015 M w 8.3 Illapel earthquake (Chile) from across- and along-track Sentinel-1 TOPS interferometry, *Geophysical Research Letters*, *43*, 2552–2561, doi:10.1002/2016GL067954. 1.2.1

Grapenthin, R., I. Johanson, and R. M. Allen (2014), The 2014 M w 6.0 Napa earthquake, California: Observations from Real-time GPS-enhanced Earthquake Early Warning, *Geophysical Research Letters*, *41*, 8269–8276, doi:10.1002/2014GL061923. 1.3.2

Green, P. J. (1995), Reversible jump Markov chain Monte Carlo computation and Bayesian model determination, *Biometrika*, *82*(4), 711–732, doi:10.1093/biomet/82.4.711. 1.2.4

Guangcai, F., L. Zhiwei, S. Xinjian, X. Bing, and D. Yanan (2015), Source parameters of the 2014 Mw 6.1 South Napa earthquake estimated from the Sentinel 1A , COSMO-SkyMed and GPS data, *Tectonophysics*, *655*, 139–146, doi:10.1016/j.tecto.2015.05.018. 1.3.2

Gutenberg, B., and C. F. Richter (1955), Magnitude and Energy of Earthquakes, *Nature*, *176*, 795, doi:10.1038/176795a0. 1.1.1

Hanssen, R. F. (2001), *Radar interferometry : data interpretation and error analysis*, 140–141 pp., Kluwer Academic. 1.2.1

Harbord, C. W. A., S. B. Nielsen, N. De Paola, and R. E. Holdsworth (2017), Earthquake nucleation on rough faults, *GEOLOGY*, *45*(10), doi:10.1130/G39181.1. 1, 1.1.4

Harris, R. A., and P. Segall (1987), Detection of a Locked Zone at Depth on the Parkfield, California, Segment of the San Andreas Fault, *Journal of Geophysical Research*, *92*(B8), 7945, doi:10.1029/JB092iB08p07945. 1.2.2

Hartzell, S. H., and T. H. Heaton (1983), Inversion of Strong Ground Motion and Teleseismic Waveform Data for the Fault Rupture History of the 1979 Imperial Valley, California, Earthquake, *Bulletin of the Seismological Society of America*, *73*(6A), 1553–1583. 1.2

Hooper, A., and T. J. Wright (2009), Comparison of Monte Carlo Methods for Model Probability Distribution Determination in SAR Interferometry, *'Fringe 2009 Workshop'*. 1.2.2

Hooper, A. J. (2012), Earthquake Slip Distribution Estimation, using a Random Vector Approach, *AGU Fall Meeting Abstracts*, *-1*, 08. 1.2.2

Hooper, A. J., J. Pietrzak, W. Simons, H. Cui, R. Riva, M. Naeije, A. Terwisscha van Scheltinga, E. Schrama, G. Stelling, and A. Socquet (2013), Importance of Horizontal Seafloor Motion on Tsunami Height for the 2011 Mw=9.0 Tohoku-Oki Earthquake, *Earth and Planetary Science Letters*, *361*, 469–479, doi:10.1016/j.epsl.2012.11.013. 1.2.2, 1.2.3

Hreinsdóttir, S. (2003), Coseismic Slip Distribution of the 2002 M W 7.9 Denali Fault Earthquake, Alaska, Determined from GPS Measurements, *Geophysical Research Letters*, *30*(13), 1670, doi:10.1029/2003GL017447. 1.2.2

Hudnut, K., T. Brocher, C. Prentice, J. Boatwright, B. Brooks, B. T. Aagaard, J. Blair, J. Fletcher, J. Erdem, C. Wicks, J. Murray, F. Pollitz, J. Langbein, J. Svarc, D. Schwartz, D. Ponti, S. Hecker, S. DeLong, C. Rosa, B. Jones, R. Lamb, A. Rosinski, T. McCrink, T. Dawson, G. Seitz, R. Rubin, C. Glennie, D. Hauser, T. Ericksen, D. Mardock, D. Hoirup, and J. Bray (2014), Key Recovery Factors for the August 24, 2014, South Napa Earthquake, *Tech. rep.*, U.S. Geological Survey Open-File Report 2014-1249, doi:2331-1258 (online). 1.3.2

Ingleby, T., and T. J. Wright (2017), Omorilike decay of postseismic velocities following continental earthquakes, *Geophysical Research Letters*, *44*, 3119–3130, doi:10.1002/2017GL072865. 1.1.1

Ji, C., R. J. Archuleta, and C. Twardzik (2015), Rupture History of 2014 M w 6.0 South Napa Earthquake Inferred from Near-fault Strong Motion Data and its Impact to the Practice of Ground Strong Motion Prediction, *Geophysical Research Letters*, *42*(7), 2149–2156, doi:10.1002/2015GL063335. 1.3.2

Johnson, K. M., Y.-J. Hsu, P. Segall, and S.-B. Yu (2001), Fault Geometry and Slip Distribution of the 1999 Chi-Chi, Taiwan Earthquake Imaged from Inversion of GPS Data, *Geophysical Research Letters*, *28*(11), 2285–2288, doi:10.1029/2000GL012761. 1.2.2

Jolivet, R., M. Simons, P. S. Agram, Z. Duputel, and Z. Shen (2014a), Aseismic Slip and Seismogenic Coupling Along the Central San Andreas Fault, *Geophysical Research Letters*, pp. 1–10, doi:10.1002/2014GL062222.We. 1.2

Jolivet, R., Z. Duputel, B. Riel, M. Simons, L. Rivera, S. E. Minson, H. Zhang, M. A. G. Aivazis, F. Ayoub, S. Leprince, S. Samsonov, M. Motagh, and E. J. Fielding (2014b), The 2013 Mw 7.7 Balochistan Earthquake: Seismic Potential of an Accretionary Wedge, *Bulletin of the Seismological Society of America*, *104*(2), 1020–1030, doi:10.1785/0120130313. 1.2.2

Jónsson, S., H. Zebker, P. Segall, and F. Amelung (2002), Fault Slip Distribution of the 1999 Mw 7.1 Hector Mine, California, Earthquake, Estimated from Satellite Radar and GPS Measurements, *Bulletin of the Seismological Society of America*, *92*(4), 1377–1389, doi:10.1785/0120000922. 1.2.1, 1.2.2, 1.5

Kanamori, H. (1972), Determination of effective tectonic stress associated with earthquake faulting. The Tottori earthquake of 1943, *Physics of the Earth and Planetary Interiors*, *5*, 426–434, doi:10.1016/0031-9201(72)90114-8. 1.3.3

Kanamori, H., and D. L. Anderson (1975), Theoretical Basis of Some Empirical Relations in Seismology, *Bulletin of the Seismological Society of America*, *65*(5), 1073–1095. 1.1.1

Klinger, Y. (2010), Relation between continental strike-slip earthquake segmentation and thickness of the crust, *Journal of Geophysical Research: Solid Earth*, *115*(B7), doi:10.1029/2009JB006550. 1.1.2

Kubo, H., W. Suzuki, S. Aoi, and H. Sekiguchi (2017), Source rupture process of the 2016 central Tottori, Japan, earthquake (MJMA 6.6) inferred from strong motion waveforms, *Earth, Planets and Space*, *69*, doi:10.1186/s40623-017-0714-3. 1.8

Langbein, J. (2015), Borehole strainmeter measurements spanning the 2014, M w 6.0 South Napa Earthquake, California: The effect from instrument calibration, *Journal of Geophysical Research: Solid Earth*, *120*, 7190–7202, doi:10.1002/2015JB012278. 1.3.2

Lohman, R. B., and M. Simons (2005), Some Thoughts on the use of InSAR Data to Constrain Models of Surface Deformation: Noise Structure and Data Downsampling, *Geochemistry, Geophysics, Geosystems*, *6*(1), doi:10.1029/2004GC000841. 1.2.1

Mai, P. M., and G. C. Beroza (2002), A Spatial Random Field Model to Characterize Complexity in Earthquake Slip, *Journal of Geophysical Research*, *107*(B11), 2308, doi:10.1029/2001JB000588. 1, 1.1.4, 1.1.5, 1.4

Mai, P. M., M. Galis, K. K. S. Thingbaijam, J. C. Vyas, and E. M. Dunham (2017), Accounting for Fault Roughness in Pseudo-Dynamic Ground-Motion Simulations, *Pure and Applied Geophysics*, *174*(9), 3419–3450, doi:10.1007/s00024-017-1536-8. 1.1.4

Malinverno, A., and W. B. F. Ryan (1986), Extension in the Tyrrhenian Sea and shortening in the Apennines as result of arc migration driven by sinking of the lithosphere, *Tectonics*, *5*(2), 227–245, doi:10.1029/TC005i002p00227. 1.3.1

Malinverno, A., M. Sacchi, A. Woodbury, M. Roussignol, E. Teller, A. Dawid, and A. Smith (2002), Parsimonious Bayesian Markov chain Monte Carlo inversion in a nonlinear geophysical problem, *Geophysical Journal International*, *151*(3), 675–688, doi:10.1046/j.1365-246X.2002.01847.x. 1.2.4

Mandelbrot, B. B. (1967), How Long is the Coast of Britain? Statistical Self-similarity and Fractional Dimension., *Science (New York, N.Y.)*, *156*(3775), 636–8, doi:10.1126/science.156.3775.636. 1, 1.1.1

Massonnet, D., M. Rossi, and C. Carmona (1993), The Displacement Field of the Landers Earthquake Mapped by Radar Interferometry, *Nature*. 1.2.1

Melgar, D., J. Geng, B. W. Crowell, J. S. Haase, Y. Bock, W. C. Hammond, and R. M. Allen (2015), Seismogeodesy of the 2014 M w 6.1 Napa Earthquake, California: Rapid Response and Modeling of Fast Rupture on a Dipping Strike-slip Fault, *Journal of Geophysical Research: Solid Earth*, *120*(7), 5012–5033, doi:10.1002/2015JB011921. 1.3.2

Milliner, C. W., J. F. Dolan, J. Hollingsworth, S. Leprince, F. Ayoub, and C. Sammis (2015), Quantifying Near-field and Off-fault Deformation Patterns of the 1992 M w 7.3 Landers Earthquake, *Geochemistry, Geophysics, Geosystems*, *16*(5), 1525–2027, doi:10.1002/2014GC005693. 1, 1.1.4

Milliner, C. W. D., C. Sammis, A. A. Allam, J. F. Dolan, J. Hollingsworth, S. Leprince, and F. Ayoub (2016), Resolving Fine-Scale Heterogeneity of Co-seismic Slip and the Relation to Fault Structure, *Scientific Reports*, *6*, 27,201, doi:10.1038/srep27201. 1.1.4

Minson, S. E., M. Simons, and J. L. Beck (2013), Bayesian Inversion for Finite Fault Earthquake Source Models I–Theory and Algorithm, *Geophysical Journal International*, *194*(3), 1701–1726, doi:10.1093/gji/ggt180. 1, 1.2.2, 1.2.2, 1.2.3

Monelli, D., P. M. Mai, S. Jónsson, and D. Giardini (2009), Bayesian imaging of the 2000 Western Tottori (Japan) earthquake through fitting of strong motion and GPS data, *Geophysical Journal International*, *176*(1), 135–170. 1.3.3

Morelan, A. E., C. C. Trexler, and M. E. Oskin (2015), SurfaceRupture and Slip Observations on the Day of the 24 August 2014 South Napa Earthquake, *Seismological Research Letters*, *86*(4), 1119–1127, doi:10.1785/0220140235. 1.7

Okada, Y. (1985), Surface Deformation Due to Shear and Tensile Faults in a Half-space, *Bulletin of the Seismological Society of America*, *75*(4), 1135–1154. 1.2, 1.2.2

Olson, A. H., and R. J. Apsel (1982), Finite Faults and Inverse Theory with Applications to the 1979 Imperial Valley Earthquake, *Bulletin of the Seismological Society of America*, *72*(6A), 1969–2001. 1.2

Omori, F. (1894), On the aftershocks of earthquakes, *J. Coll. Sci. Imp. Univ. Tokyo*, *7*, 111 – 200. 1.1.1

Parsons, T., and D. L. Minasian (2015), Earthquake rupture process recreated from a natural fault surface, *Journal of Geophysical Research: Solid Earth*, *120*(11), 7852–7862, doi:10.1002/2015JB012448. 1, 1.1.4

Parsons, T., M. Segou, V. Sevilgen, K. Milner, E. Field, S. Toda, and R. S. Stein (2014), Stress-based aftershock forecasts made within 24 h postmain shock: Expected north San Francisco Bay area seismicity changes after the 2014 M = 6.0 West Napa earthquake, *Geophysical Research Letters*, *41*(24), 8792–8799, doi:10.1002/2014GL062379. 1.3.2

Poon, C. Y., R. S. Sayles, and T. A. Jones (1992), Surface Measurement and Fractal Characterization of Naturally Fractured Rocks, *Journal of Physics D: Applied Physics*, *25*(8), 1269–1275, doi:10.1088/0022-3727/25/8/019. 1.1.1

Power, W. L., and T. E. Tullis (1995), Review of the Fractal Character of Natural Fault Surfaces with Implications for Friction and the Evolution of Fault Zones, in *Fractals in the Earth Sciences*, edited by C. C. Barton and P. R. La Pointe, pp. 89–105, Springer US, Boston, MA, doi:10.1007/978-1-4899-1397-5. 1.1.1

Renard, F., C. Voisin, D. Marsan, and J. Schmittbuhl (2006), High resolution 3D Laser Scanner Measurements of a Strike-slip Fault Quantify its Morphological Anisotropy at all Scales, *Geophysical Research Letters*, *33*(4), L04,305, doi:10.1029/2005GL025038. 1.1.1, 1.1.2

Sagy, A., E. E. Brodsky, and G. J. Axen (2007), Evolution of Fault-surface Roughness with Slip, *Geology*, *35*(3), 283, doi:10.1130/G23235A.1. 1, 1.1.1, 1.1.2, 1.1.3, 1.1.4

Sambridge, M., K. Gallagher, A. Jackson, P. Rickwood, and W. R. (2006), Trans-dimensional inverse problems, model comparison and the evidence, *Geophysical Journal International*, *167*(2), 528–542, doi:10.1111/j.1365-246X.2006.03155.x. 1.2.4

Schneiderbauer, S., and D. Ehrlich (2004), Risk, Hazard and People's Vulnerability to Natural Hazards: a Review of Definitions, Concepts and Data., *Joint Research Centre, European Commission, EUR 21410*. 1

Semmane, F., F. Cotton, and M. Campillo (2005), The 2000 Tottori earthquake: A shallow earthquake with no surface rupture and slip properties controlled by depth, *Journal of Geophysical Research*, *110*(B3), B03,306, doi:10.1029/2004JB003194. 1.3.3

Shi, Z., and S. M. Day (2013), Rupture dynamics and ground motion from 3-D rough-fault simulations, *Journal of Geophysical Research: Solid Earth*, *118*(3), 1122–1141, doi:10.1002/jgrb.50094. 1, 1.1.4

Simons, M. (2002), Coseismic Deformation from the 1999 Mw 7.1 Hector Mine, California, Earthquake as Inferred from InSAR and GPS Observations, *Bulletin of the Seismological Society of America*, *92*(4), 1390–1402, doi:10.1785/0120000933. 1.2

Simonsen, I., A. Hansen, and O. Nes (1998), Determination of the Hurst Exponent by use of Wavelet Transforms, *Physical Review E.* 1.1.2, 1.1.3

Taira, T., F. Brenguier, and Q. Kong (2015), Ambient noise-based monitoring of seismic velocity changes associated with the 2014 M w 6.0 South Napa earthquake, *Geophysical Research Letters*, *42*, 6997–7004, doi:10.1002/2015GL065308. 1.3.2

Tal, Y., B. H. Hager, and J. P. Ampuero (2018), The Effects of Fault Roughness on the Earthquake Nucleation Process, *Journal of Geophysical Research: Solid Earth*, doi:10.1002/2017JB014746. 1, 1.1.4

Tarantola, A. (2005), *Inverse Problem Theory and Methods for Model Parameter Estimation*, chap. 2, pp. 50–52, Society for Industrial and Applied Mathematics, Philadelphia, doi:10.1137/1.9780898717921.ch2. 1.2.3

Thomson, D. (1982), Spectrum estimation and harmonic analysis, *Proceedings of the IEEE*, *70*(9), 1055–1096, doi:10.1109/PROC.1982.12433. 1.1.2

Tsukuda, T. (1988), Coda-Q before and after the 1983 Misasa earthquake of M 6.2, Tottori Prefecture, Japan, *Pure and Applied Geophysics PAGEOPH*, *128*(1-2), 261–279, doi:10.1007/BF01772600. 1.3.3

von Kármán, T. (1948), Progress in the Statistical Theory of Turbulence, *Proceedings of the National Academy of Sciences of the United States of America*, *34*(11), 530–9. 1.1.5

Waldhauser, F. (2009), Nearrealtime doubledifference event location using longterm seismic archives, with application to northern California, *Bull. Seismol. Soc. Amer.*, *99*, 2736–2748, doi:10.1785/0120080294. 1.7

Walters, R. J., J. R. Elliott, N. D'Agostino, P. C. England, I. Hunstad, J. A. Jackson, B. Parsons, R. J. Phillips, and G. Roberts (2009), The 2009 L'Aquila Earthquake (Central Italy): A Source Mechanism and Implications for Seismic Hazard, *Geophysical Research Letters*, *36*(17), L17,312, doi:10.1029/2009GL039337. 1, 1.2.2

Welch, P. D. (1967), The Use of Fast Fourier Transform for the Estimation of Power Spectra: A Method Based on Time Averaging Over Short, Modified Periodograms, *Audio and Electroacoustics, IEEE Transactions on*, *15*, 70–73. 1.1.2

Wilkinson, M., G. P. Roberts, K. McCaffrey, P. A. Cowie, J. P. Faure Walker, I. Papanikolaou, R. J. Phillips, A. M. Michetti, E. Vittori, L. Gregory, L. Wedmore, and Z. K. Watson (2015), Slip distributions on active normal faults measured from LiDAR and field mapping of geomorphic offsets: an example from L'Aquila, Italy, and implications for modelling seismic moment release, *Geomorphology*, *237*, 130–141, doi:10.1016/j.geomorph.2014.04.026. 1.3.1

Wright, T. J. (2002), Remote monitoring of the earthquake cycle using satellite radar interferometry., *Philosophical transactions. Series A, Mathematical, physical, and engineering sciences*, *360*(1801), 2873–88, doi:10.1098/rsta.2002.1094. 1.2.1

Wright, T. J. (2003), Source Model for the M w 6.7, 23 October 2002, Nenana Mountain Earthquake (Alaska) from InSAR, *Geophysical Research Letters*, *30*(18), 1974, doi:10.1029/2003GL018014. 1.2, 1.2.2

Yabuki, T., and M. Matsu'ura (1992), Geodetic Data inversion using a Bayesian Information Criterion for Spatial Distribution of Fault Slip, *Geophysical Journal International*, *109*(2), 363–375, doi:10.1111/j.1365-246X.1992.tb00102.x. 1.2.2

Zhang, Y., R. Wang, and Y.-T. Chen (2015), Stability of rapid finite-fault inversion for the 2014 Mw6.1 South Napa earthquake, *Geophysical Research Letters*, *42*(23), 10,263–10,272, doi:10.1002/2015GL066244. 1.3.2

Zielke, O., and P. M. Mai (2016), Sub-Patch Roughness in Earthquake Rupture Investigations, *Geophysical Research Letters*, *43*, 1893–1900, doi:10.1002/2015GL067084. 1.1.4

Zielke, O., M. Galis, and P. M. Mai (2017), Fault roughness and strength heterogeneity control earthquake size and stress drop, *Geophysical Research Letters*, doi:10.1002/2016GL071700. 1, 1.1.4

Chapter 2

Fractal Properties of the Campo Felice Fault

2.1 Abstract

The roughness of fault surfaces has fractal properties: there is a power-law relationship between the topography of a fault and the wavelength of this topography. This understanding of the behaviour of fault surfaces over many spatial scales gives vital information for studying earthquake friction, nucleation, slip behaviour and fault mechanics, but no previous study has addressed how fractal properties vary along strike in an individual fault. Here we present our investigation of how fault roughness varies along-strike of the Campo Felice fault in the Italian Apennines. Using a combination of measurements from terrestrial laser scanners and a laser profilometer we have created 3D point clouds of the fault surfaces, with scales ranging from submillimeter up to over 1 km. We show results from 14 locations along the fault, with multiple samples taken to investigate in the lab using a laser profilometer at two locations, as well as a scan covering several hundred meters along the length of the fault. We find that the Campo Felice fault shows fractal properties over six orders of magnitude in length in the slip perpendicular direction (along strike), and at least three orders of magnitude in the slip parallel direction. The Hurst parameter, which constrains self-similarity, varies considerably along the length of the fault. We speculate this variation is due to structural complexity, and that the fault surface may be recording variations in slip direction along the fault, or that the variation is due to different asperities on the fault experiencing different faulting histories or stress conditions. Our measurements of the self-similar nature of the faults will enable us to better inform earthquake models, in particular modelling of coseismic slip.

2.2 Introduction

Understanding the nature of fault surfaces is vital to understanding how faults and earthquakes nucleate, propagate and terminate as the slip surfaces record these processes as they evolve over time. Fault surfaces have long been known to be rough and early work showed that this roughness is not random but shows fractal properties (*Brown and Scholz*, 1985, *Power et al.*, 1987), meaning that a feature is similar at all scales, often used interchangeably with 'self-similarity'. In the context of fault surfaces, this means that the geometric pattern of topography is replicated at every length scale (*Bistacchi et al.*, 2011). In other words, *Power and Tullis* (1995) say 'if both an elephant and an ant were to walk on a self-similar surface, they would observe the same type of topography relative to their respective body size'. Mathematically fractal behaviour means that a feature can be described by a power law, i.e. in this case that the root-mean-square fluctuations of fault topography are proportional to the length of the profile (*Fang and Dunham*, 2013). Earthquake surface ruptures have also been shown to be fractal (*Rockwell and Klinger*, 2013, *Candela et al.*, 2012) as has coseismic surface slip (*Milliner et al.*, 2015, 2016).

This study quantifies for the first time how the fault roughness varies along-strike of a fault. We provide details at multiple scales, with sampling sites spaced within tens or hundreds of meters along-strike. These measurements can help inform earthquake models, which frequently parameterise the fault into minimum 1 km elements, without any consideration for how the fault properties may change at distances less than this.

Roughness affects nucleation (*Tal et al.*, 2018) and the minimum scale of grooving may be linked to the transition in deformation mechanism of the fault (*Brodsky et al.*, 2016). It has been suggested that faults smooth gradually with maturity (*Brodsky et al.*, 2016) and that this may affect Gutenberg-Richter b values (*Goebel et al.*, 2017). Fault roughness has been incorporated into ground-motion simulations (*Mai et al.*, 2017) as well as into dynamic rupture models (*Fang and Dunham*, 2013, *Shi and Day*, 2013, *Parsons and Minasian*, 2015, *Bruhat et al.*, 2016) and fractal properties have been incorporated into earthquake slip inversions (*Amey et al.*, 2018). Thus it is vital to properly quantify fractal nature of fault roughness to better inform these models, which in turn help estimate magnitude of shaking and stress transfer that can help inform seismic hazard analysis.

In recent years investigations of fault surfaces have been conducted at a full range of scales, using white light interferometers and laser profilometers at the shortest scale to measure μm roughness (*Candela et al.*, 2009, 2012, *Candela and Brodsky*, 2016) up to LiDAR and photogrammetry scans at the longest scale to measure hundreds of meters (*Renard et al.*, 2006, *Sagy et al.*, 2007, *Candela et al.*, 2009, *Bistacchi et al.*, 2011, *Candela et al.*, 2012, *Corradetti et al.*, 2017). This enables the quantification of the fractal properties of a fault over several orders of magnitude.

One method to determine the roughness of the fault from laser scans is to calculate the average deviation of the profile from planarity (RMS, root-mean-square, roughness; *Tal et al.* 2018), but instead of measuring the roughness directly, we calculate the power spectrum of the scan to constrain the power of each oscillation for each wavelength. From the power spectra we can calculate the Hurst parameter (*Candela et al.*, 2012). The Hurst parameter is related to the fractal dimension and quantifies the power of a feature as a function of the scale at which the feature is observed (Figure 2.1). It was first defined by *Hurst et al.* (1965) who showed that the flow through the River Nile on a particular year correlated to the rainfall in subsequent years with a long-term trend. In the context of fault roughness, it gives a measure of the long-term trend of the topography of the fault (Figure 2.1), and it quantifies the change in power as a function of lengthscale. Hurst parameters in the range $0.5 < H < 1$ have a positive autocorrelation, meaning that the observed trend is likely to continue (persistent behaviour) (*Simonsen et al.*, 1998). In these instances the profile is dominated by long wavelength signals, and the profile is smoother at small wavelengths, because the topographic trend is continuing instead of oscillating, as in Figure 2.1. In contrast, if H is in the range $0 < H < 0.5$ then an observed trend is likely to reverse (antipersistent behaviour) (*Simonsen et al.*, 1998), resulting in oscillating fault topography that alternates between high and low values along a profile. The Hurst parameter is only valid in the range $0 - 1$, as the upper limit ensures the fault tends to a flat surface, and the lower limit ensures topography increases at increasing scale (*Simonsen et al.*, 1998). Figure 2.1 highlights the difficulty in defining ‘smoothness’ of a fault, as a higher Hurst parameter with the same RMS roughness is smoother, but lower RMS roughness represents a lower deviation from a planar surface and therefore is also smoother. In this paper we use ‘smoother’ to mean lower magnitude of topography, i.e. lower RMS roughness; lower power topography.

Recent higher-resolution studies of fault topography (e.g. *Sagy et al.* 2007) find that faults are self-affine, rather than self-similar. This implies that whereas a self-similar feature will appear statistically identical on small and large scales, a self-affine feature requires scaling in one direction (*Poon et al.*, 1992). As the length scale of observation of a self-similar fault surface increased the magnitude of topography would increase by the same factor, that is if the length, δx, increased by a factor of γ then the topography δz would increase by γ also, by $\delta x \rightarrow \gamma \delta x, \delta z \rightarrow \gamma^H \delta z$ (*Candela et al.*, 2012). These studies also showed a difference in the Hurst parameter parallel to slip and perpendicular to slip (*Sagy et al.*, 2007), demonstrating a relationship between the direction of slip and the roughness of a fault. The Hurst parameter is thus a useful scaling for understanding the variations across many scales of fault roughness. We can also calculate a ‘pre-factor’ term that gives an estimation of the inherent roughness of the fault (*Sagy et al.*, 2007), i.e. a measure of the magnitude of the fault topography, related to $\text{RMS}_{roughness}$ (σ in Figure 2.1).

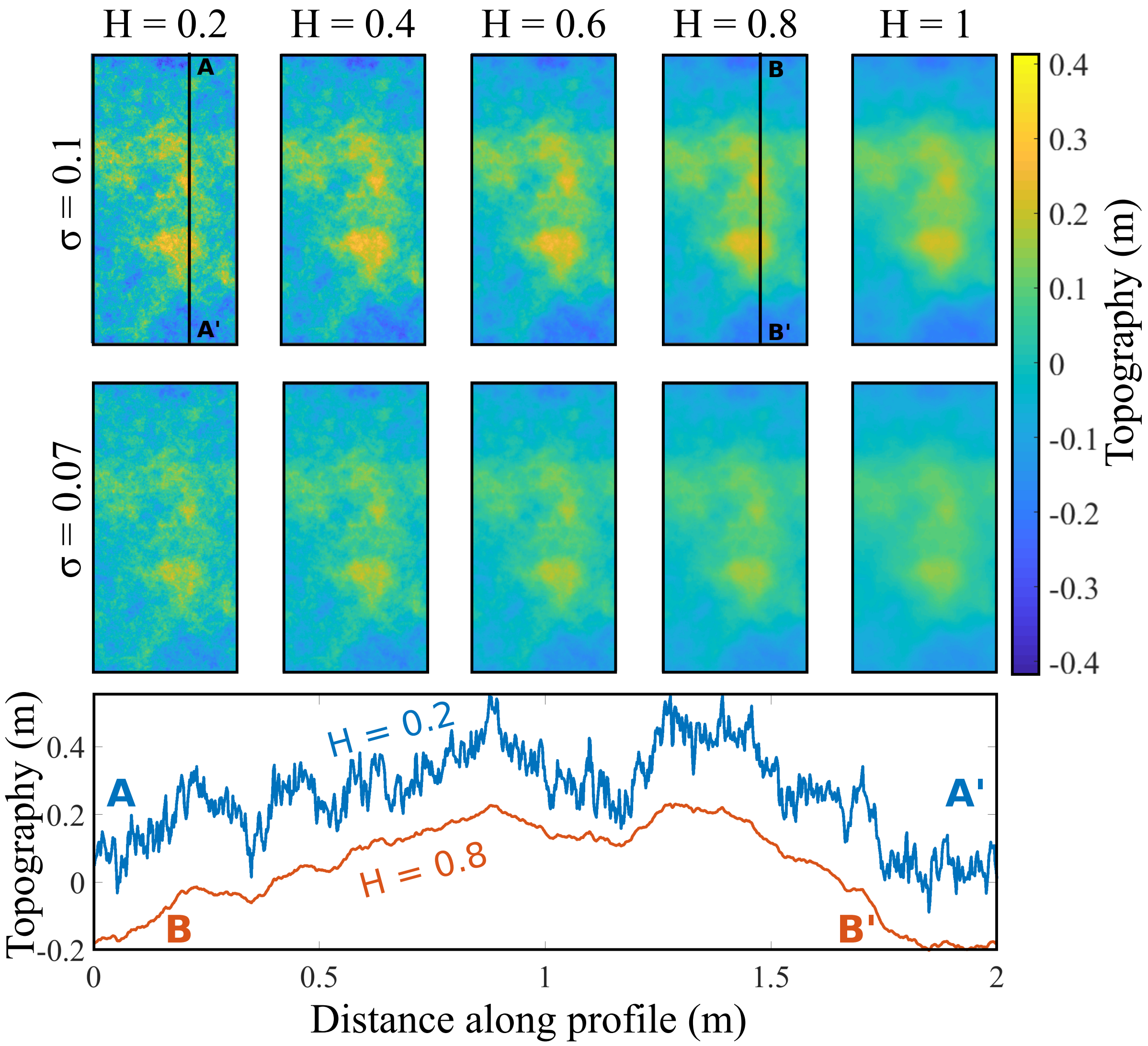

Figure 2.1: Generated fractal surfaces and profiles along the surfaces, illustrating the effect of Hurst parameter, H and RMS roughness, σ. The Hurst parameter defines the relative contribution of long-wavelength and small-wavelength topography features. A surface with Hurst parameter in the range $0 < H < 0.5$ is antipersistent, meaning an observed trend unlikely to continue, resulting in oscillations (profile A-A'). In contrast, Hurst parameters in the range $0.5 < H < 1$ are persistent, and observed trends are likely to continue (profile B-B'), meaning the surface has fewer topographic highs and lows, and is instead dominated by the long wavelength signal. The topographic profiles have been vertically offset for clarity. Note that these are isotropic surfaces, with the same Hurst parameter in both the x and y directions, whereas natural fault surfaces are observed to have different Hurst parameters parallel to slip and perpendicular to slip.

Here we present an in-depth study along several hundreds meters of the Campo Felice fault in the Italian Apennines, measured using a terrestrial laser scanner and a laser profilometer, ranging from millimetre to several hundred meter scale. We present our findings for the Campo Felice fault and discuss the implications for earthquake mechanisms, rupture dynamics and seismic hazard. We find the fault shows fractal properties, and that the exact scaling of this parameter values along-strike.

2.3 Laser scanning data from the Campo Felice fault

2.3.1 Campo Felice fault

The Campo Felice fault is a normal fault within the central Italian Apennines (Figure 2.2). The Apennines are a northwest-southeast striking mountain range that have been undergoing extension for the past 2-3 Myr and are currently extending at ∼3 mm/yr (*Malinverno and Ryan*, 1986, *D'Agostino et al.*, 2014). The basins are bounded by young, segmented, normal faults that accommodate this extension in medium to large ($> \mathrm{M}_w$ 6) earthquakes, which have devastated towns and cities in the Apennines (recent earthquakes shown in Figure 2.2).

The Campo Felice fault is a northwest-southeast striking fault with a nearly continuous exposed limestone bedrock scarp for much of its ∼5km length. The lowest part of the fault scarp is a clean, largely unbroken surface, which has been suggested to be almost unweathered apart from a low level of biokarst (*Giaccio et al.*, 2003). The fault surface was previously investigated using a microroughness-meter on transects along the fault but did not define any observable roughness variation relating to palaeoseismic events (*Giaccio et al.*, 2003). A detailed study using a terrestrial laser scan of the fault surface has shown that a bend in the fault (Figure 2.2*d*) produces local maxima in Quaternary throw-rates (*Wilkinson et al.*, 2015). We will investigate the effect of this structural complexity upon the fault roughness.

We sampled the central section of the fault where it is best exposed and preserved, focusing on two main areas: from hereafter denoted as the northwest and southeast localities. The northwest locality is close to the center of the fault, and the southeast locality is just north of prominent change in strike or relay zone (Figure 2.2*d*) (*Wilkinson et al.*, 2015).

Details, field photographs and figures of the gridded scans can be found in Appendix A, Table A.1 and Figures A.1 - A.7.

2.3.2 Terrestrial Laser Scanner

We scanned the fault surface using a range of different scanning equipment, with details summarised in Table 2.1.

For the largest scales we used terrestrial laser scanners (TLS). The full-length scan

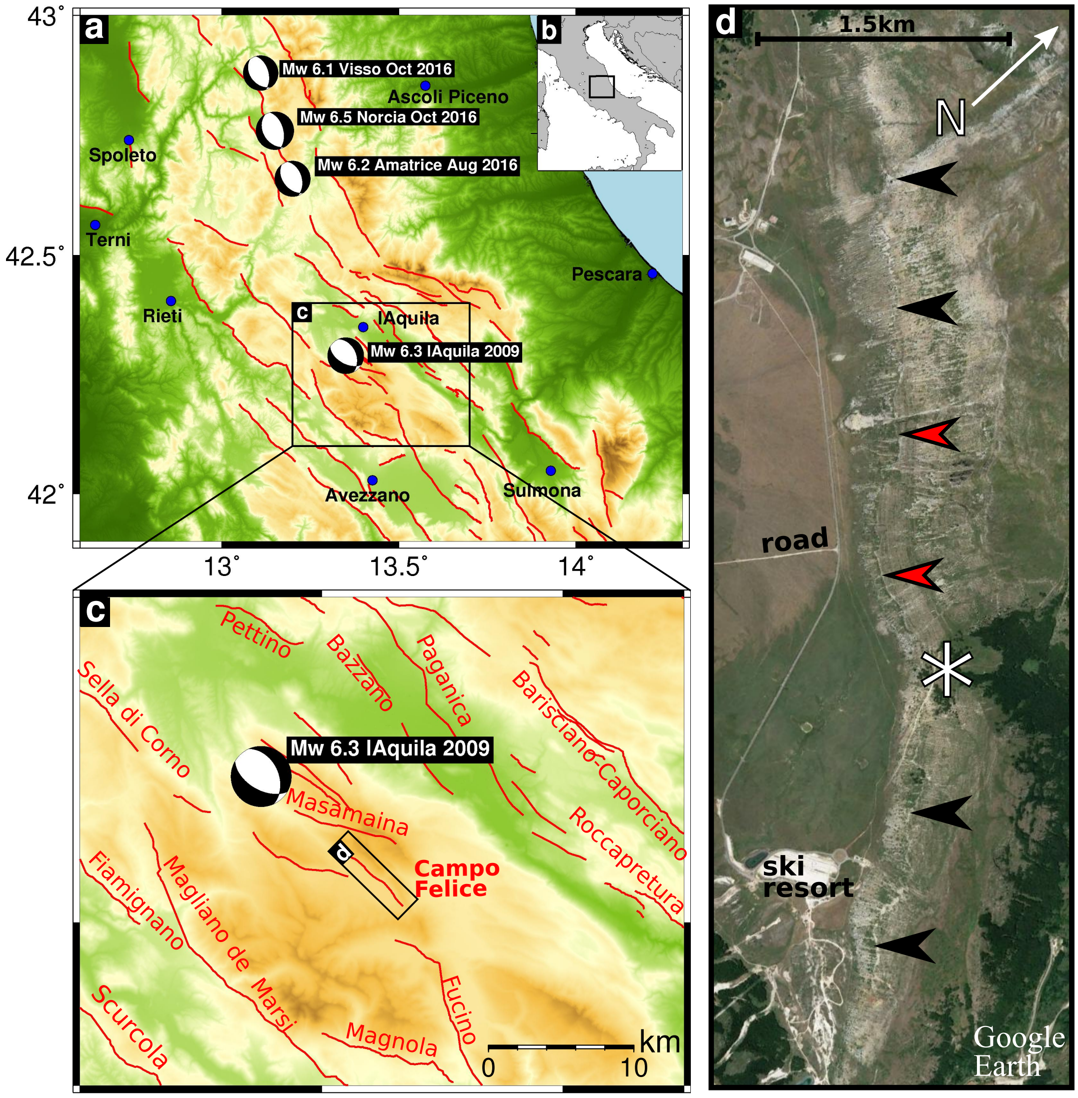

Figure 2.2: Italian Apennines fault system. This northwest-southeast trending system of normal faults is accommodating extension across Italy and has been the source of many devastating earthquakes, with recent ones indicated by their focal mechanisms in panel *a*. The location of the Campo Felice fault and its neighbouring faults is shown in panel *c*, with a birds-eye Google Earth image in panel *d* showing the fault trace (black arrows), two scanning localities used in this study (red arrows) and location of a change in strike of the fault (white star). Panel *a* and *c* plotted on SRTM topography (*Farr et al.*, 2007)

of the fault was acquired using a Riegl LMS-z420i laser scanner, consisting of 6 scan positions from at a range of ~400 m to cover a 5 km length of the fault (*Wilkinson et al.*, 2015). Detailed scans were acquired within a couple of meters of the fault to capture surface sections of up to 4 m perpendicular to slip by 10 m parallel to slip. The first five scans were taken in 2014 using a Leica C10 and the next nine scans were taken in 2017 using a Riegl VZ-1000.

2.3.3 Laser profilometer

We acquired topographical scans of 14 cm slip perpendicular x 10 cm slip parallel sample blocks using a NextEngine 2020i laser profilometer. Scans were obtained with a capture density of 40,000 points/cm^2, and dimensional accuracy of ± 100 μm. The laser profilometer scans were taken parallel to the slip direction at approximately 200 μm intervals.

Type of instrument	**Site**	**Name of scanner**	**Precision**	**Accuracy**
Terrestrial laser scanner	A,B,C,D,E,F,G, J, N	Riegl VZ-1000	8 mm	5 mm
Terrestrial laser scanner	H,I,K,L,M	Leica C10	2 mm	6 mm
Terrestrial laser scanner	Whole fault	Riegl LMS-z420i	8 mm	10 mm
Laser profilometer	D, J	NextEngine 2020i		100 μm

Table 2.1: Details of the different scanner used in this study. The sites correspond to the locations on the fault at which scans were performed, see Figure 2.5. Laser profilometer scans were taken at the same locations as terrestrial laser scans, D and J.

2.4 Method

We broadly follow the methodology of *Candela et al.* (2012), shown in Figure 2.3.

The fault surface scans give raw point clouds of x, y, z data. Starting from the point clouds, we first remove features such as shrubs, bushes and areas of weathering from the point cloud based on field photos using the CloudCompare software. We then orientate the fault such that the x axis is perpendicular to slip, the y axis is parallel to slip and the z axis is fault topography. This is achieved by performing principal component analysis on the pointcloud in MatLab to identify the vector normal to the plane and use this to rotate the pointcloud into the xy plane, with z being topography. The benefit of principal component analysis is that it accounts for errors in x, y in addition to accounting for z errors as with linear-least squares (*Bistacchi et al.*, 2011). Once this is achieved, for the small and medium-scale datasets we manually pick grooves in the fault surfaces and use this vector to orientate the plane so that y is parallel to the slip direction as indicated by the grooves. For the scan of the whole fault, the slip parallel direction is assumed to coincide with the fault dip.

When the pointcloud has been fully orientated we crop it to a rectangle and grid

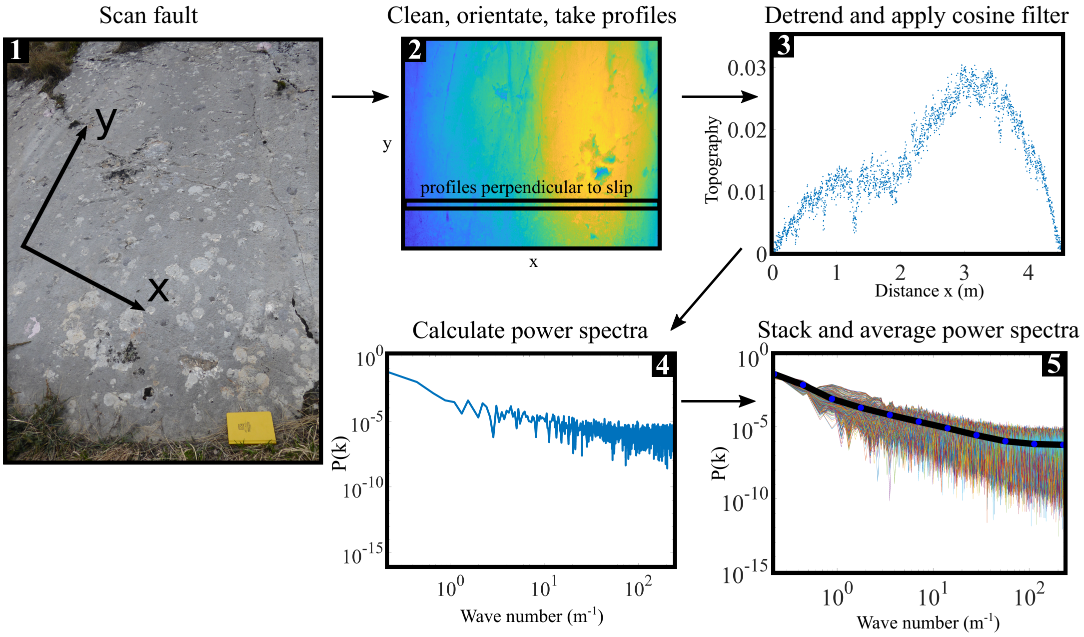

Figure 2.3: Methodology employed to estimate power spectra. Panel *1* shows the fault surface, with notebook for scale. This is then scanned and orientated to give a point cloud as shown in panel *2*. We take profiles parallel and perpendicular to slip to gain profiles which we detrend and apply a taper function as in panel *3*. We calculate the power spectra of the profile (panel *4*) and stack the power spectra for all the profiles (panel *5*) to get an average.

it. For the laser profilometer we choose the gridsize to be twice the average separation distance between points in the cropped pointcloud. For the terrestrial laser scan of the whole fault we vertically average up-dip and then grid every 1 m, giving only one profile along the length of the fault, with 1 m spacing between datapoints. For the meter-scale terrestrial laser scans we grid the data where either the gridsize is twice the average separation distance between points in the cropped pointcloud, or 1 mm, whichever is larger. Due to areas of grass there may be some gaps in the pointcloud between which we interpolate during gridding, but *Candela et al.* (2009) found that this analysis is not biased by randomly distributed absent data.

Fourier spectral analysis can be used to quantify roughness, as long as many profiles are available, to stack and allow signal to dominate over noise (*Simonsen et al.*, 1998). Therefore we compute spectral analysis by taking profiles parallel to slip and perpendicular to slip from the gridded pointcloud. The Fourier transform requires that each profile be detrended, and that the profile starts and ends at the same value, to remove artifacts in the power calculation caused by topography at the edge of the profiles. We achieve this by fitting a line through the first and last point in the profile and then using a 3% cosine taper (*Candela et al.*, 2012). We found that this method gave fewer topographic artifacts at the end of the profile than either fitting a linear trend to the data or using principal component analysis. We then compute the Fourier transform and calculate the power, $P(k)$ as a function of wavenumber, k, by squaring the modulus of the Fourier transform. Since we use the fast Fourier transform, which is a discrete sum, it must be multiplied by the sampling distance, dx to produce the fourier transform as an integral quantity. Thus $power = (FFT \times \delta x)^2$. The power is then normalised by dividing by the length of the profile multiplied by the sampling distance ($N\delta x$). This gives the power spectral density calculated at each wavenumber, k, with units m^3 (*Sagy et al.*, 2007).

To stack the profiles we calculate the mean of all the profiles at wavenumbers in geometric progression, to which we fit a best-fit line. This reduces noise associated with each individual profile. From this the 'pre-factor', C, and Hurst parameter, H, can be calculated, as:

$$P(k) = Ck^{-1-2H} \tag{2.1}$$

Where the Hurst parameter quantifies the power of a feature as a function of scale at which the feature is observed and is inversely proportional to the gradient of the line, in log-log space. The pre-factor is a measure of the magnitude of the fault roughness at a given wavelength.

2.5 Results

The Campo Felice fault shows fractal properties over six orders of magnitude in the slip perpendicular direction (along strike), and at least three orders of magnitude in the slip parallel direction (Figure 2.4). This is demonstrated by the straight line of the power spectra in log-log space, from the millimeter scale up to 1.5 km along the length of the entire fault.

The spectra taken at different scales are offset vertically from each other in Figure 2.4. This is likely due to the bias introduced by the necessity of choosing un-cracked hand samples to measure in the laboratory and choosing smoother, unweathered sections of fault plane to scan. Whereas the natural fault surfaces are cross-cut by numerous cracks and pits, formed during earthquakes (*Dascher-Cousineau et al.*, 2018), when choosing samples to cut from the rock it is necessary to choose areas where these features are not present. The same is true when picking smoother areas of the fault to scan with the terrestrial laser scanner.

The terrestrial laser scanner measurements at meter to centimeter scale (warm colours in Figure 2.4) show high variability at low wavenumbers due to fewer profiles of this length being available in the power spectra, so there are fewer available data points to remove noise by stacking. We also note that at this scale the power spectra flatten at the highest wavenumbers. We attribute this to the power spectra intersecting the noise spectrum, as it occurs at approximately similar wavelengths in the spectra

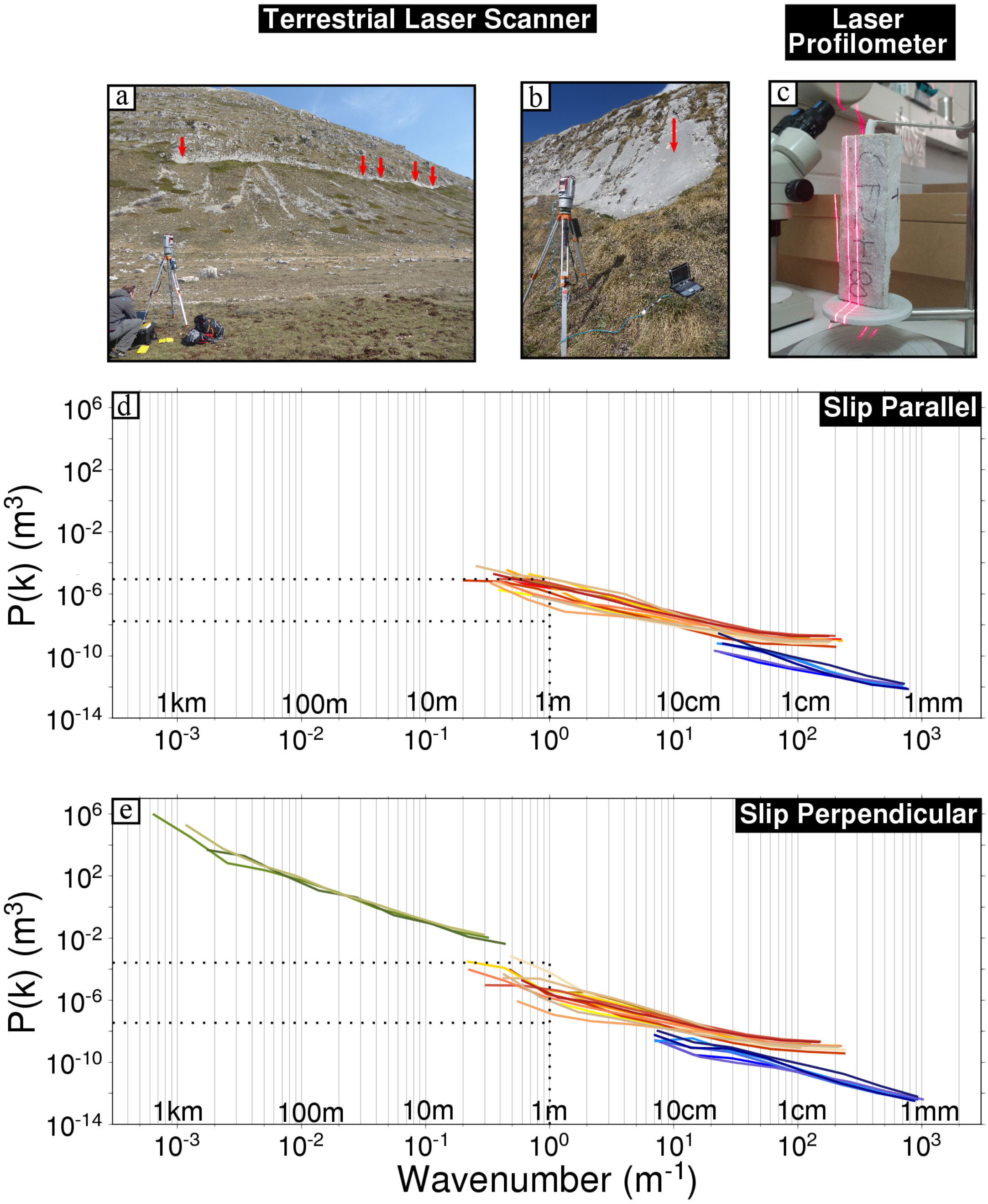

Figure 2.4: Power spectra parallel to slip and perpendicular to slip, with photos indicating how the topography was measured. Green indicates terrestrial laser scan of the entire fault *Wilkinson et al.* 2015, panel *a*), warm colours are meter scale measurements taken by the terrestrial laser scanner (panel *b*) and cold colours are measurements from the laser profilometer (panel *c*). The full-length scan means we have power spectra at much larger wavelengths perpendicular to slip (along strike) than parallel to slip (up-dip), where there are only a few meters available. Dotted lines indicate the minimum and maximum pre-factors (y-intercepts) at 1 m wavelength, where the minimum values are calculated from extrapolating the lower power laser profilometer profile and the maximum value is calculated from the maximum power terrestrial laser scanner profile. The Hurst parameters are inversely proportional to the gradient of the line (a steeper negative slope is a higher Hurst parameter).

for all the different medium-scale terrestrial laser scans, at ~1-2 cm, and not for the laser profilometer scans.

We also calculated the pre-factors (y-axis intercept, Figure 2.4) at 1 m wavelength, to give a measure of roughness magnitude. Since the topography is fractal, the magnitude of the topography depends upon the scale of observation, but calculating the pre-factor at a given wavelength enables comparison between different faults or sites. In the slip parallel direction the maximum prefactor is 1.5×10^{-6} (from a terrestrial laser scan) and the minimum prefactor is 1.7×10^{-8} (from a laser profilometer scan). In the slip perpendicular direction the maximum prefactor is 8.8×10^{-6} (from the terrestrial laser scan of the entire fault) and the minimum prefactor is 3.5×10^{-8} (from a laser profilometer scan).

Using the power spectra, we calculated the Hurst parameters for each using Equation 2.1. A steeper slope of the power spectra represents a higher Hurst parameter, results shown in Figure 2.5. Our scans give mean and standard deviation values of $H_{\perp} = 0.50 \pm 0.21$ and $H_{\|} = 0.40 \pm 0.14$.

We find that the Campo Felice fault displays a broad range of Hurst parameters. Figure 2.5 shows that there is not an observable trend of Hurst parameters as a function of distance along the fault from the centre or the ends. In the slip perpendicular direction, different measurements taken at the same location (D and J) show similar Hurst values, with a range of ~0.2, but in the slip parallel direction the variation for measurements at the same site is much larger, of ~0.3.

We find the highest value of 0.9 for the Hurst parameter perpendicular to slip at scanning site F. Whereas most exposed fault surfaces we scanned were approximately planar, this fault surface was extremely curved, with topography of 8 cm across a 2 m scan. This accounts for the higher Hurst number: its power spectra has a steeper slope in log-log space, indicating that the signal is dominated by the large wavelength corrugation and is lacking in low wavelength topography. The power spectra still shows a fractal relationship: it is a straight line in log-log space down to the noise level, but the slope is steeper.

Scanning site E displays very low Hurst parameters in both the slip parallel and slip perpendicular direction. The fault scarp at this site had a large density of pink lichen covering it, which could not be removed during the data cleaning. This may mean that the signal from the fault surface is being obscured, leading to a similar topography power at higher and lower wavelengths.

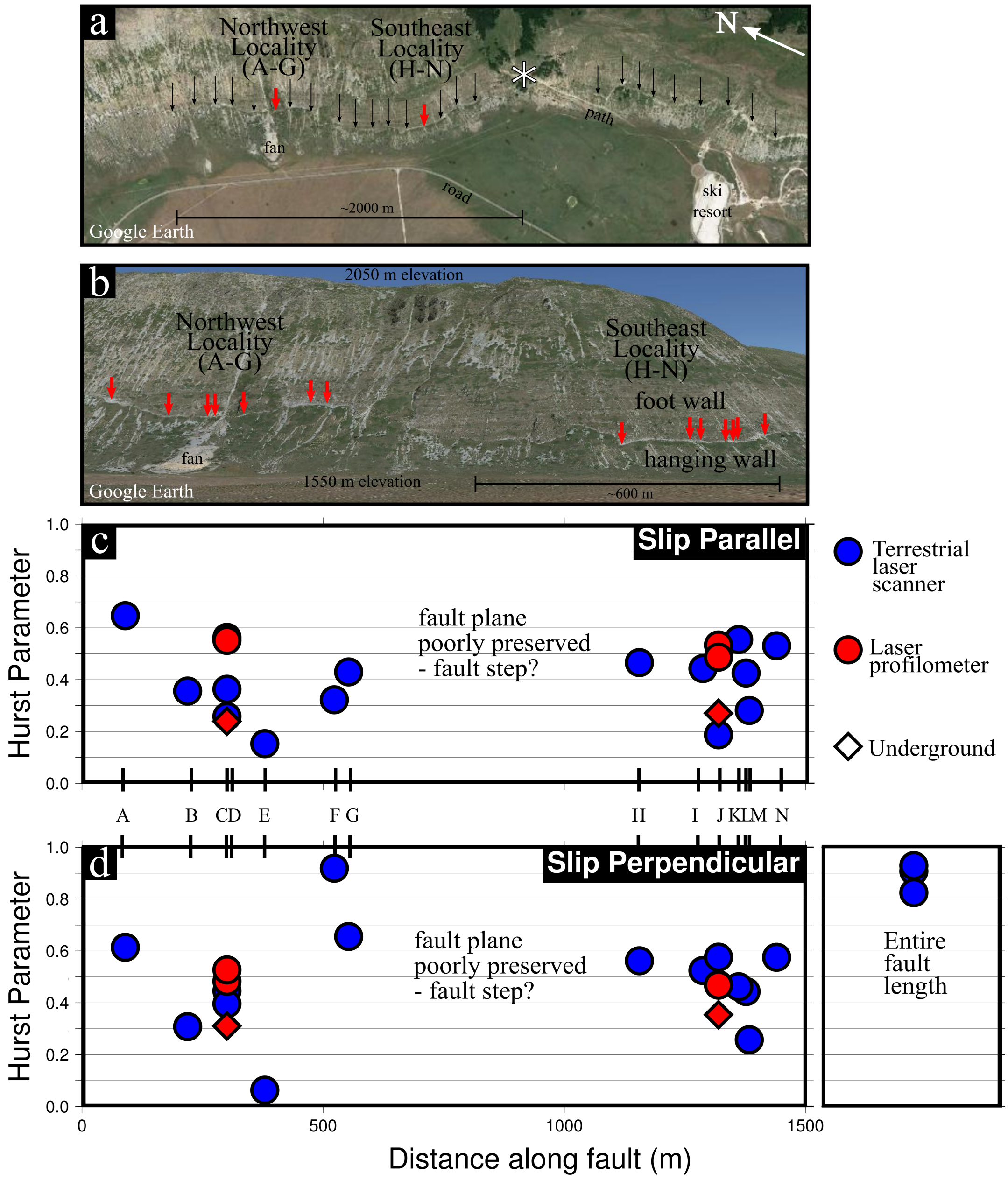

Figure 2.5: Hurst parameters plotted as a function of distance along the Campo Felice fault. Panel *a* shows a bird-eye Google Earth image of the fault with black arrows showing fault trace, red arrows showing rough location of the scanning localities and the star (*) showing the location of a suggested fault bend (*Wilkinson et al.*, 2015). Panel *b* shows Google Earth image looking at the uplifted footwall as if standing in the basin, with red arrows indicating locations that scans have been taken. Panel *c* and *d* show the Hurst parameters parallel to slip and perpendicular to slip respectively, as a function of distance along the fault, with the measurement sites labelled A to N. Circles indicate readings taken above the ground and diamonds indicate readings below the ground, where we have dug a trench and then sampled the fault surface. Blue symbols are measurements taken by terrestrial laser scanner and red symbols are taken by laser profilometer, where all laser profilometer samples were taken at a site that we also scanned with the terrestrial laser scanner. The slip perpendicular direction has the additional scan of the entire fault length, which is on the right of panel d.

2.6 Discussion on the relationship between roughness and fault structure

Fault rupture and asperities

Previous work has shown faults of different lithology and tectonic regime to have a remarkably constant Hurst parameter of ∼0.8 in the slip perpendicular direction, and ∼0.6 in the slip parallel direction (*Bistacchi et al.*, 2011, *Candela et al.*, 2012), with the exception of *Dascher-Cousineau et al.* (2018). Here we find, generally, lower values of Hurst parameter. In the slip parallel direction only two sites are within the one sigma range found by *Candela et al.* (2012). This lower Hurst parameter is consistent with Campo Felice being a young (‘immature’), short and segmented fault, meaning that small wavelength topography has not eroded. We also find a higher variability in the Hurst parameters along the same fault than has been found in previous studies for datasets consisting of numerous faults (*Candela et al.*, 2012), suggesting that conclusions drawn from fault roughness, including its relationship with fault displacement (*Brodsky et al.*, 2011), must be based on a representative sample of the fault has been scanned, to ensure apparent differences between faults are not instead due to natural variations along a fault.

Of the two distinct scan groups, the samples in the northwest group (towards the center of the fault) display increased variability to those in the southeast group (towards the fault tip). Considering only the northwest region gives a mean of $H_{\perp} = 0.42 \pm 0.17$ and $H_{\|} = 0.40 \pm 0.18$, where the southeast group gives a mean of $H_{\perp} = 0.46 \pm 0.10$ and $H_{\|} = 0.40 \pm 0.13$. Whilst the means are similar the higher standard deviation in the northwest is of interest. We also calculated the power and Hurst parameters separately on the entire northwest fault section and entire southeast fault section down to 1 m and found $H_{northwest} = 0.82$ and $H_{southeast} = 0.93$, both perpendicular to slip direction. It’s worth noting that the scanning sites in the southeast are located closer together than those in the northwest: spread over 463 m in the north-west compared to 228 m in the south-east, which may play a part in the decreased variability.

These two areas could have experienced different conditions in a number of ways. *Wilkinson et al.* (2015) found that whilst the strike, dip and plunge were constant between the two fault areas, the throw and strain rate (since 15±3 ka) decreases from the northwest to the southeast along the fault, with an anomalous decrease between our two scanning areas. They suggest that a bend in the fault, which is very prominent in the continuation of the fault to the south-east (not sampled here, shown as a star in Figure 2.5*a*), begins in the region of the south-eastern group of fault scans. Fault bends frequently arrest or stop earthquake rupture (*Wesnousky*, 1988), so it could be that these two slip areas have experienced a different number of earthquakes, and presumably a different amount of slip, because the rupture may have stopped between them. Indeed, Campo Felice must have grown from smaller segments and linked to form the long fault strand currently exposed, so it's reasonable to assume that as the relay zone developed, the area in this zone (the southeast locality) would have experienced fewer earthquakes. Thus even if more recently the southeast and northwest localities have experienced similar earthquake histories, before linking the southeast would have experienced a drastically different slip history from the rest of the Campo Felice fault.

Alternatively, even if most recently these two localities failed in the same earthquakes as a result of fault bend complexity, they could have experienced different stress conditions due to their location on an asperity. If one locality was positioned where rupture is frequently stopped or slowed-down, due to the fault bend, and the other locality were frequently in the center of an asperity that rupture goes through, then different stress drops may lead to different imprints onto the fault surface. We speculate that potentially, the variability in Hurst parameters could be used to determine the size of asperities. If areas of the fault within an asperity experience similar conditions within an earthquake, then they may have more similar Hurst parameters than an area of a fault not within the asperity, or on its edge. Alternatively, by assessing the changes in Hurst parameters along strike, potentially different asperities or long-standing asperities could be identified and investigated.

Whatever its cause, the variability in the fault surface over a scale of a few hundreds meters could have important implications for modeling. The roughness of a fault surface affects ground-motion (*Mai et al.*, 2017) and stress drop (*Zielke et al.*, 2017) in an earthquake, yet many static or dynamic slip models parameterise fault planes into patches much larger than the scale over which we observe variability. This will be averaged over the fault patch, thus losing some of the intrinsic complexity of earthquake processes (e.g. *Zielke and Mai* 2016).

Permissible earthquake mechanisms

We find that half (9 out of the 18) Hurst parameters were larger in the slip perpendicular direction than the slip parallel direction, whereas previous results have reported consistently larger values in the slip perpendicular directions (*Candela et al.*, 2012). Larger Hurst parameters in the slip perpendicular direction suggest that long wavelength signals (grooves, corrugations) dominate over short wavelength signals. Sites where the fault visibly curved did show higher values in the slip perpendicular direction, but many surfaces and hand samples that we scanned were remarkably flat and lacking in prominent grooves or striations to distinguish the slip perpendicular and slip parallel directions. As well as having implications for earthquake size, this lack of difference between the slip parallel and slip perpendicular directions could mean that a larger range of focal mechanisms is possible for the Campo Felice fault. Whereas a highly corrugated fault plane with grooves on the order of typical slip would strongly arrest rupture perpendicular to the axis of these grooves, the smoothness (small power deviation from a planar surface) of the Campo Felice fault surface may mean that a wide range of slip vector is possible without being stopped by the friction associated with corrugations. This is consistent with the significant variation (up to 10 degrees) of slip plunge between measurement sites that are up to only 100 m apart (*Wilkinson et al.*, 2015). This may be the consequence of multiple ruptures producing different generations of slickenslides at individual locations, or may be capturing the variation in the direction of slip during one event, or the imprint of segment linkage that's not been masked.

2.6.1 Implications for seismic hazard

We consider the pre-factor (y-intercept) at 1 m, using the minimum values from the laser profilometer and maximum values from the laser scan of the whole fault, as shown in Figure 2.4, to compare with measurements in *Candela et al.* (2012). We find that in the slip parallel direction the maximum pre-factor we measured (1.5×10^{-6}) is one or two orders of magnitude lower (at 1 m) than the five faults *Candela et al.* (2012) measured, including the Magnola fault, which is another limestone normal fault in the Italian Apennines, ∼12 km south of Campo Felice (see Figure 2.2). The minimum pre-factor we measured slip parallel (1.7×10^{-8}) is on the same order, or an order of magnitude lower than their measurements. In the slip perpendicular direction, our minimum prefactor of (3.5×10^{-8}) is up to three orders of magnitude lower than the faults measured by *Candela et al.* (2012), and the maximum prefactor of (8.8×10^{-6}) two orders of magnitude lower, though we note our measurement of the entire fault is not directly comparable to a meter scale scan. This shows that Campo Felice has lower power topography deviations from a planar surface than the faults in the study by *Candela et al.* (2012) (Figure 2.1 lower panel compared to the top panel). This has implications for seismic hazard, as the seismic moment release in an earthquake is modelled to be strongly affected by fault roughness: smoother faults, with a lower deviation from a planar surface, are capable of generating larger earthquakes than rougher faults, in the same loading conditions (*Zielke et al.*, 2017).

2.6.2 Limitations and caveats

Availability of well-preserved fault plane

All roughness studies are biased by the necessity of scanning well preserved fault plane. This means that, whilst we have a large number of scanned sites, it is hard to get a representative survey along the entire Campo Felice fault. In particular, it is unfortunate that the exposed fault scarp in the continuation of the fault to the southeast, across the suggested relay zone (*Wilkinson et al.*, 2015), is largely poorly preserved with a high degree of vegetation, and lacking in large areas of exposed fault that would make this area suitable for analysis.

Scanner noise

Noise must be considered as a factor in leading to low Hurst parameters. Increased noise in the data would mean increased power at small wavelengths, artificially inflating the power and thus decreasing the difference between the power at low wavelengths and high wavelengths, which decreases the Hurst parameter. However we do not believe this to be the case, as the generally lower Hurst parameters are measured using four different instruments (three different laser scanners and the laser profilometer). We also find that the minimum and maximum pre-factor at $k = 1$ is lower than other scanned faults, whilst we expect noise in a scanner to artificially increase the minimum pre-factor. We do find however that estimates of Hurst parameter from the Riegl VZ-1000 laser scanner show larger scatter in Hurst parameters than the other laser scanner or the laser profilometer (Figure 2.6), as well as having the largest scanner errors (Table 2.1). This scanner was used measuring all the northwestern scanning sites (pentagons in Figure 2.6), as well as two south-eastern scanning locations (squares in Figure 2.6). It is therefore difficult to say for sure if the sites measured by this scanner are recording true differences between the localities. But we note that all scanners revealed a range in Hurst parameter of at least 0.2, suggesting there is a lot of variability in the Campo Felice fault, compared to others that have been scanned (*Candela et al.*, 2012).

Depth

The depth at which the fault surface features gains its fractal topography affects its relevance to faulting processes. Previous studies have suggested fault surfaces such as the one we measured may have been exhumed from depths of 5 km (*Sagy et al.*, 2007), whilst others have focussed on outcrops exhumed from deeper, up to 10 km depths (*Bistacchi et al.*, 2011).

The surfaces that we are measuring are unlikely to preserve any of the features from depths any greater than a few kilometers, and so could only preserve nucleation information for earthquakes that nucleated at very shallow depths. But we speculate that in the brittle crust similar fracturing processes occur and may leave a similar roughness signature, so roughness observed at the surface could potentially be a reasonable estimate of roughness at depth.

2.7 Conclusion

In this study we find that the roughness of the Campo Felice fault surface displays self-similar properties over six orders of magnitude in the slip perpendicular direction and at least three orders of magnitude in the slip parallel direction, as is shown by the power spectra of the topography of the fault surface. The Hurst parameter, which records this self-similarity is variable along the length of the fault, with increased variability in the

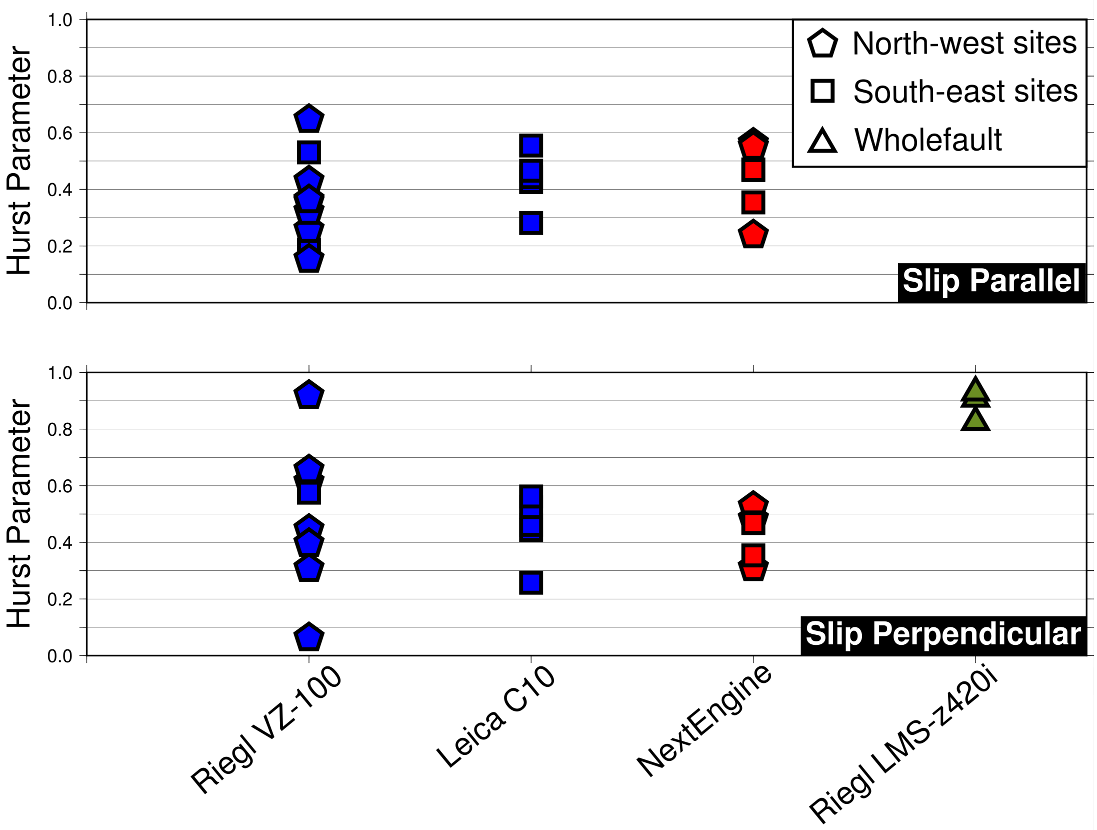

Figure 2.6: Hurst parameters calculated from scans taken by four different scanners. The blue and green measurement points are terrestrial laser scanners, and the red is a laser profilometer. The Riegl VZ-1000 has the largest variability in the calculated Hurst parameters.

northwestern scans compared to the southeastern scans. We hypothesise that the variability could be attributed to 1) the variability of slip vector along a fault plane in one earthquake or 2) a fault bend arresting rupture, meaning the two localities experienced a different number of earthquakes, and consequently different slip histories or 3) the fault bend creating long-standing asperities, with one locality experiencing the center of the asperity through which rupture always propagates and the other experiencing the edge of the asperity, where rupture is frequently stalled or stopped. The small scale (few hundred meters) over which variability occurs also has important implications for fault modelling, where regularly earthquake slip models are parameterised into >1 km fault patches. Finally, the low pre-factors displayed by the fault surface suggest that the Campo Felice fault is particularly smooth (low magnitude deviations from a planar surface) which implies that it may be at risk from larger earthquakes than faults that are rougher.

2.8 Acknowledgements

This work was support by NERC (Natural Environment Research Countil), grant numbers: NE/L002574/1, NE/E016545/1, NE/I026715/1, NE/P018858/1, NE/H003266/1, NE/E01545X/1, NE/B504165/1, GR9/02995, NE/I024127/1 and EPSRC UKRI Studentship 1652177. The authors are grateful to Emily Brodsky and Andrea Bistacchi for their help and advice. Some figures were made using the Generic Mapping Tools (GMT) (*Wessel and Smith*, 1991).

References

Amey, R. M. J., A. Hooper, and R. J. Walters (2018), A Bayesian Method for Incorporating Self-Similarity into Earthquake Slip Inversions, *Journal of Geophysical Research: Solid Earth*, *123*, doi:10.1029/2017JB015316. 2.2

Bistacchi, A., W. A. Griffith, S. A. F. Smith, G. Di Toro, R. Jones, and S. Nielsen (2011), Fault Roughness at Seismogenic Depths from LIDAR and Photogrammetric Analysis, *Pure and Applied Geophysics*, *168*(12), 2345–2363, doi:10.1007/s00024-011-0301-7. 2.2, 2.4, 2.6, 2.6.2

Brodsky, E. E., J. J. Gilchrist, A. Sagy, and C. Collettini (2011), Faults smooth gradually as a function of slip, doi:10.1016/j.epsl.2010.12.010. 2.6

Brodsky, E. E., J. D. Kirkpatrick, and T. Candela (2016), Constraints from fault roughness on the scale-dependent strength of rocks, *Geology*, *44*(1), 19–22, doi:10.1130/G37206.1. 2.2

Brown, S. R., and C. H. Scholz (1985), Broad Bandwidth Study of the Topography of Natural Rock Surfaces, *Journal of Geophysical Research*, *90*(B14), 12,575, doi:10.1029/JB090iB14p12575. 2.2

Bruhat, L., Z. Fang, and E. M. Dunham (2016), Rupture complexity and the supershear transition on rough faults, *Journal of Geophysical Research: Solid Earth*, *121*(1), 210–224, doi:10.1002/2015JB012512. 2.2

Candela, T., and E. E. Brodsky (2016), The minimum scale of grooving on faults, *Geology*, *44*(8), 603–606, doi:10.1130/G37934.1. 2.2

Candela, T., F. Renard, M. Bouchon, A. Brouste, D. Marsan, J. Schmittbuhl, and C. Voisin (2009), Characterization of Fault Roughness at Various Scales: Implications of Three-Dimensional High Resolution Topography Measurements, *Pure and Applied Geophysics*, *166*(10-11), 1817–1851, doi:10.1007/s00024-009-0521-2. 2.2, 2.4

Candela, T., F. Renard, Y. Klinger, K. Mair, J. Schmittbuhl, and E. E. Brodsky (2012), Roughness of Fault Surfaces over Nine Decades of Length Scales, *Journal of Geophysical Research*, *117*(B8), B08,409, doi:10.1029/2011JB009041. 2.2, 2.2, 2.4, 2.4, 2.6, 2.6, 2.6.1, 2.6.2

Corradetti, A., K. McCaffrey, N. D. Paola, and S. Tavani (2017), Evaluating roughness scaling properties of natural active fault surfaces by means of multi-view photogrammetry, *Tectonophysics*, *717*, 599–606, doi:10.1016/j.tecto.2017.08.023. 2.2

D'Agostino, N., P. England, I. Hunstad, and G. Selvaggi (2014), Gravitational potential energy and active deformation in the Apennines, *Earth and Planetary Science Letters*, *397*, 121–132, doi:10.1016/j.epsl.2014.04.013. 2.3.1

Dascher-Cousineau, K., J. D. Kirkpatrick, and M. L. Cooke (2018), Smoothing of Fault Slip Surfaces by Scale-Invariant Wear, *Journal of Geophysical Research: Solid Earth*, doi:10.1029/2018JB015638. 2.5, 2.6

Fang, Z., and E. M. Dunham (2013), Additional shear resistance from fault roughness and stress levels on geometrically complex faults, *Journal of Geophysical Research: Solid Earth*, *118*(7), 3642–3654, doi:10.1002/jgrb.50262. 2.2

Farr, T. G., P. A. Rosen, R. Caro, Edward Crippen, R. Duren, S. Hensley, M. Kobrick, M. Paller, E. Rodriguez, and L. Roth (2007), The Shuttle Radar Topography Mission, *Review of Geophysics*, *45*(2). 2.2

Giaccio, B., F. Galadini, A. Sposato, P. Messina, M. Moro, M. Zreda, A. Cittadini, S. Salvi, and A. Todero (2003), Image processing and roughness analysis of exposed bedrock fault planes as a tool for paleoseismological analysis: results from the Campo Felice fault (central Apennines, Italy), *Geomorphology*, *49*(3-4), 281–301, doi:10.1016/S0169-555X(02)00191-5. 2.3.1

Goebel, T. H., G. Kwiatek, T. W. Becker, E. E. Brodsky, and G. Dresen (2017), What allows seismic events to grow big?: Insights from b-value and fault roughness analysis in laboratory stick-slip experiments, *Geology*, *45*(9), 815–818, doi:10.1130/G39147.1. 2.2

Hurst, H., R. Black, and Y. Simaika (1965), Long-term Storage: An Experimental Study. 2.2

Mai, P. M., M. Galis, K. K. S. Thingbaijam, J. C. Vyas, and E. M. Dunham (2017), Accounting for Fault Roughness in Pseudo-Dynamic Ground-Motion Simulations, *Pure and Applied Geophysics*, *174*(9), 3419–3450, doi:10.1007/s00024-017-1536-8. 2.2, 2.6

Malinverno, A., and W. B. F. Ryan (1986), Extension in the Tyrrhenian Sea and shortening in the Apennines as result of arc migration driven by sinking of the lithosphere, *Tectonics*, *5*(2), 227–245, doi:10.1029/TC005i002p00227. 2.3.1

Milliner, C. W., J. F. Dolan, J. Hollingsworth, S. Leprince, F. Ayoub, and C. Sammis (2015), Quantifying Near-field and Off-fault Deformation Patterns of the 1992 M w 7.3 Landers Earthquake, *Geochemistry, Geophysics, Geosystems*, *16*(5), 1525–2027, doi:10.1002/2014GC005693. 2.2

Milliner, C. W. D., C. Sammis, A. A. Allam, J. F. Dolan, J. Hollingsworth, S. Leprince, and F. Ayoub (2016), Resolving Fine-Scale Heterogeneity of Co-seismic Slip and the Relation to Fault Structure, *Scientific Reports*, *6*, 27,201, doi:10.1038/srep27201. 2.2

Parsons, T., and D. L. Minasian (2015), Earthquake rupture process recreated from a natural fault surface, *Journal of Geophysical Research: Solid Earth*, *120*(11), 7852–7862, doi:10.1002/2015JB012448. 2.2

Poon, C. Y., R. S. Sayles, and T. A. Jones (1992), Surface Measurement and Fractal Characterization of Naturally Fractured Rocks, *Journal of Physics D: Applied Physics*, *25*(8), 1269–1275, doi:10.1088/0022-3727/25/8/019. 2.2

Power, W. L., and T. E. Tullis (1995), Review of the Fractal Character of Natural Fault Surfaces with Implications for Friction and the Evolution of Fault Zones, in *Fractals in the Earth Sciences*, edited by C. C. Barton and P. R. La Pointe, pp. 89–105, Springer US, Boston, MA, doi:10.1007/978-1-4899-1397-5. 2.2

Power, W. L., T. E. Tullis, S. R. Brown, G. N. Boitnott, and C. H. Scholz (1987), Roughness of Natural Fault Surfaces, *Geophysical Research Letters*, *14*(1), 29–32, doi:10.1029/GL014i001p00029. 2.2

Renard, F., C. Voisin, D. Marsan, and J. Schmittbuhl (2006), High resolution 3D Laser Scanner Measurements of a Strike-slip Fault Quantify its Morphological Anisotropy at all Scales, *Geophysical Research Letters*, *33*(4), L04,305, doi:10.1029/2005GL025038. 2.2

Rockwell, T. K., and Y. Klinger (2013), Surface Rupture and Slip Distribution of the 1940 Imperial Valley Earthquake, Imperial Fault, Southern California: Implications for Rupture Segmentation and Dynamics, *Bulletin of the Seismological Society of America*, *103*(2A), 629–640, doi:10.1785/0120120192. 2.2

Sagy, A., E. E. Brodsky, and G. J. Axen (2007), Evolution of Fault-surface Roughness with Slip, *Geology*, *35*(3), 283, doi:10.1130/G23235A.1. 2.2, 2.2, 2.4, 2.6.2

Shi, Z., and S. M. Day (2013), Rupture dynamics and ground motion from 3-D rough-fault simulations, *Journal of Geophysical Research: Solid Earth*, *118*(3), 1122–1141, doi:10.1002/jgrb.50094. 2.2

Simonsen, I., A. Hansen, and O. Nes (1998), Determination of the Hurst Exponent by use of Wavelet Transforms, *Physical Review E.* 2.2, 2.4

Tal, Y., B. H. Hager, and J. P. Ampuero (2018), The Effects of Fault Roughness on the Earthquake Nucleation Process, *Journal of Geophysical Research: Solid Earth*, doi:10.1002/2017JB014746. 2.2

Wesnousky, S. (1988), Seismological and structural evolution of strike-slip faults, *Nature*, *335*, 340–343, doi:10.1038/335340a0. 2.6

Wessel, P., and W. H. F. Smith (1991), Free Software Helps Map and Display Data, *EOS Trans. AGU*, *72*, 441. 2.8

Wilkinson, M., G. P. Roberts, K. McCaffrey, P. A. Cowie, J. P. Faure Walker, I. Papanikolaou, R. J. Phillips, A. M. Michetti, E. Vittori, L. Gregory, L. Wedmore, and Z. K. Watson (2015), Slip distributions on active normal faults measured from LiDAR and field mapping of geomorphic offsets: an example from L'Aquila, Italy, and implications for modelling seismic moment release, *Geomorphology*, *237*, 130–141, doi:10.1016/j.geomorph.2014.04.026. 2.3.1, 2.3.2, 2.4, 2.5, 2.6, 2.6, 2.6.2

Zielke, O., and P. M. Mai (2016), Sub-Patch Roughness in Earthquake Rupture Investigations, *Geophysical Research Letters*, *43*, 1893–1900, doi:10.1002/2015GL067084. 2.6

Zielke, O., M. Galis, and P. M. Mai (2017), Fault roughness and strength heterogeneity control earthquake size and stress drop, *Geophysical Research Letters*, doi:10.1002/2016GL071700. 2.6, 2.6.1

Chapter 3

Incorporating Fractal Properties into Geodetic Slip Inversions

An edited version of Chapter 3 was published by AGU, Copyright (2018) American Geophysical Union:
Amey, R.M.J., A.J. Hooper, and R. Walters (2018), *A Bayesian Method for Incorporating Self-Similarity into Earthquake Slip Inversions*, Journal of Geophysical Research Solid Earth, 123, `doi:10.1029/2017JB015316`

3.1 Abstract

Distributions of coseismic slip help illuminate many properties of earthquakes, including fault geometry, stress changes, frictional properties and potential future hazard. Slip inversions take observations and calculate slip at depth, but there are a number of commonly-adopted assumptions such as minimizing the second spatial derivative of slip (the Laplacian), that have little physical basis and potentially bias the result. In light of growing evidence that fault slip shows fractal properties, we suggest that this information should be incorporated into slip inversions as a form of regularization, instead of Laplacian smoothing. We have developed a Bayesian approach to efficiently solve for slip incorporating von Karman regularization. In synthetic tests, our approach retrieves fractal slip better than Laplacian regularization, as expected, but even performs comparably, or better, when the input slip is not fractal. We apply this to the 2014 M_w 6.0 Napa Valley earthquake on a two-segment fault using InSAR and GPS data. We find the von Karman and Laplacian inversions give similar slip magnitude but in different locations and the von Karman solution has much tighter confidence bounds on slip than the Laplacian solution. Differences in earthquake slip due to the regularization technique could have important implications for the interpretation and modeling of stress changes on the causative and neighbouring faults. We therefore recommend that choice of regularization method should be routinely made explicit and

justified and that von Karman regularization is a better default than Laplacian.

3.2 Introduction

Determining the magnitude and distribution of slip along a fault plane is an essential component of earthquake investigations. Coseismic slip can help elucidate the geometry, strength and frictional properties of active faults (*Milliner et al.*, 2015, *Perrin et al.*, 2016) and can be used to estimate where stress has been partially released and where it remains or has increased, which may indicate areas of the fault or neighbouring faults that have been brought closer to or further from failure (*Walters et al.*, 2009, *Lorito et al.*, 2011, *Avouac et al.*, 2015). The same inversion methods can also be used to monitor postseismic and interseismic slip (e.g. *Floyd et al.* 2016) and to help deduce the distribution and proportion of off-fault deformation, giving insight into the earthquake cycle (*Wang et al.*, 2015, *Lindsey and Fialko*, 2016). Values of slip are also used extensively in palaeoseismic studies to estimate the magnitude of pre-instrumental earthquakes (*Campbell et al.*, 2015).

By combining satellite acquisitions before and after an earthquake, InSAR (Interferometric Synthetic Aperture Radar) provides spatially dense measurements of surface displacement which along with GPS measurements can be used to invert for the magnitude, location and direction of earthquake slip along a fault plane (*Wright*, 2003). With the new European Space Agency (ESA) satellites Sentinel-1A and B providing unprecedented ground repeat times, the scientific community is now in a position to routinely investigate all large continental earthquakes using InSAR (*Elliott et al.*, 2015), and inverting for slip is a crucial part of that procedure. However, in order for slip inversions to be useful we need to ensure that the inversion processes give results that adequately represent the true slip distribution.

Slip inversions are usually ill-posed and unstable, meaning that the solution is non-unique and small amounts of data noise lead to slip oscillations in least-squares solutions. Because of this inversions are usually regularized, with Laplacian smoothing being the most common approach (*Harris and Segall*, 1987, *Wright*, 2003, *Funning et al.*, 2005). This regularization approach minimizes the second derivative of slip with the importance of this constraint relative to minimizing data misfit controlled by a scalar smoothing factor. The choice of smoothing factor is often subjective and often not stated at all in the literature but can result in major differences between solutions derived from the same data. There is no specific justification for the use of Laplacian smoothing in slip inversions, other than that a rough or oscillating slip distribution would produce unrealistically large stress-drops. Whilst Laplacian smoothing can prevent such large stress-drops this does not mean it is the best function to describe the nature of slip; it is just a mathematical constraint rather than being based on any observed fundamental feature of slip distributions.

Other regularization techniques promote sparse solutions (*Evans and Meade*, 2012) or impose little regularization (*Minson et al.*, 2013, *Jolivet et al.*, 2014), and these approaches, together with smoothness-promoting methods produce a huge range in solutions for the same earthquake. We argue that whichever regularization method is used, it should have a physical justification based on some observed behaviour of earthquakes and faulting.

Many features of earthquakes and faults show self-similar (fractal) properties, meaning that a feature is similar at all scales, or mathematically that a behaviour can be described by a power law (*Mandelbrot*, 1983). Features that show this relationship include the Gutenberg-Richter frequency magnitude scale (*Gutenberg and Richter*, 1955, *Kanamori and Anderson*, 1975), the Omori aftershock frequency law (*Omori*, 1894), seismicity distribution across faults (*Powers and Jordan*, 2010), spatial structure of faults (*Aviles et al.*, 1987, *Okubo and Aki*, 1987), spatial distribution of earthquake hypocentres (*Robertson et al.*, 1995), fault gouge texture (*Rice and Cocco*, 2007, *Muto et al.*, 2015), fracture energy (*Passelègue et al.*, 2016) and many others (see *Ben-Zion* 2008).

Fault surfaces are naturally rough and early work found this roughness is self-similar (*Brown and Scholz*, 1985, *Power et al.*, 1988, *Poon et al.*, 1992), meaning that the root-mean-square height fluctuations are proportional to the profile length (*Fang and Dunham*, 2013). Recent higher-resolution studies of exhumed faults (*Renard et al.*, 2006, *Sagy et al.*, 2007, *Brodsky et al.*, 2011, *Candela et al.*, 2012) support these initial observations but find that roughness is self-affine rather than self-similar. Self-affine systems require different scaling in the x and z direction to maintain their similarity, where self-similar systems have the same scaling. In the context of fault roughness, a profile of fault topography is self-affine if it remains statistically invariant if the x (along-strike) and z (topography) coordinates are subject to the scaling transformation $\delta x \rightarrow \gamma \delta x$, $\delta z \rightarrow \gamma^H \delta z$, where H is the Hurst parameter (*Candela et al.*, 2012). For a self-similar system, the scaling is instead γ in both directions. Different values of H are found along-strike and down-dip directions, giving rise to different properties perpendicular and parallel to the slip vector.

Modeling of slip on a surface with fractal roughness predicts that both the distribution of stress drop and coseismic slip should also have a fractal distribution (*Candela et al.*, 2011). *Milliner et al.* (2015, 2016) observed this in their field investigations of surface slip of the Landers earthquake rupture, where a power-law describes the relationship between slip amplitude and wavelength. Models that produce power-law frequency magnitude statistics of earthquake occurrence, in keeping with the Gutenberg-Richter law, also produce fractal slip distributions (*Fisher et al.*, 1997).

Additionally, *Mai and Beroza* (2002) found that seismological slip solutions show fractal properties, a feature that was robust irrespective of the regularization imposed upon the inversions. They tested various autocorrelation functions to assess how the magnitude of slip varied as a function of distance and found that the von Karman autocorrelation function best describes slip distributions. This function has a similar power law relationship as a fractal distribution at high spatial frequencies, but the power decays more slowly for small wavenumbers (large wavelength).

These studies imply that a better and more realistic alternative to regularization by Laplacian smoothing is regularization by constraining the slip distribution to be self-affine. By using a regularization technique that does not capture the fractal nature of slip we may be biasing slip solutions, and therefore also any conclusions drawn from them. Fractal fault roughness is now incorporated into many numerical models of dynamic rupture (*Fang and Dunham*, 2013, *Shi and Day*, 2013, *Parsons and Minasian*, 2015, *Bruhat et al.*, 2016) and ground-motion simulations (*Mai et al.*, 2017) and in this paper we incorporate the von Karman autocorrelation function into a geodetic slip inversion as a prior assumption, using Bayesian methods.

The von Karman correlation was first introduced in fluid dynamics to describe turbulence (*von Kármán*, 1948). Unlike a fractal correlation, that has only a single term to describe its power (the fractal dimension, D), the von Karman distribution also has correlation lengths, which define the cut off lengths of fractal behaviour (*Dolan et al.*, 1998) and allow for different scalings down-dip and along-strike, which is useful for capturing the nature of slip.

Here we use the von Karman distribution to describe the expected similarity of magnitude of slip between all patches of the fault. This correlation function, $C(r)$ is given by:

$$C(r) = \frac{G_H(r/a)}{G_H(0)} \tag{3.1}$$

Where $G_H(r/a) = (r/a)^H K_H(r/a)$ where K_H is a modified Bessel function of the second kind, of order H, r is the distance between slip patches, a is the correlation length used to scale this distance and H is the Hurst parameter (*Mai and Beroza*, 2002). The Hurst parameter describes the fractal properties of the correlation and controls the decay of this correlation (Figure 3.1). For self-affine profiles the Hurst parameter is linked to the fractal dimension, D, by D = (Euclidian dimension *+ 1 - H*) and is a measure of the long-term memory of a system.

In form, the von Karman correlation decays as a function of lag (scaled distance), and for $H = 0.5$ the von Karman function is identical to an exponential decay function. The von Karman correlation decays quicker for either decreased Hurst parameter or decreased correlation lengths. Thus the correlation between the magnitude of slip on two patches decays as a function of the distance between them, and the nature of this decay is controlled by the Hurst parameter and correlation lengths.

The von Karman correlation can be added as a prior assumption into a slip inversion,

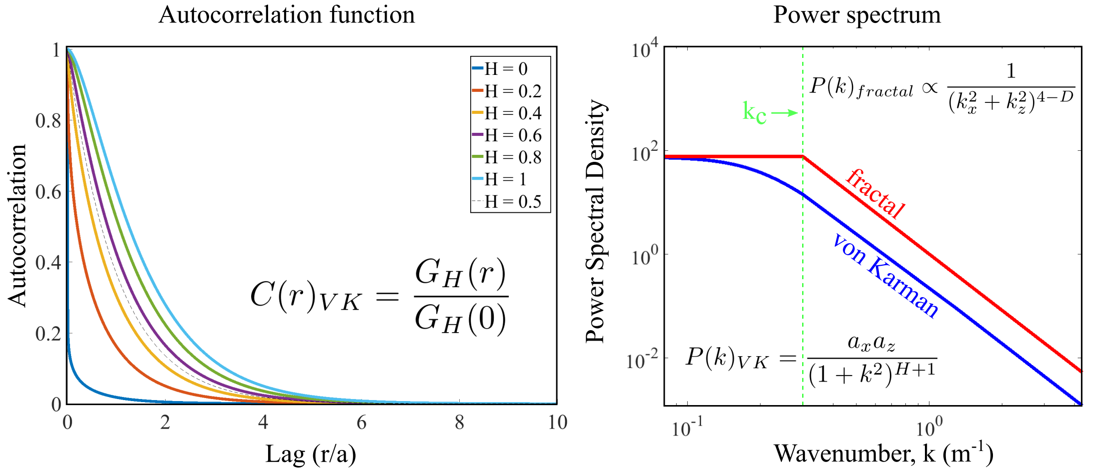

Figure 3.1: Left = The von Karman autoccorelation function, $C(r)$. The autocorrelation (similarity) between two functions decays with lag (scaled distance) between them. The exact shape of the drop-off is controlled by the Hurst parameter, H, where $H = 0.5$ is equivalent to an exponential decay function. Right = von Karman power spectrum, $P(k)$, using $a_x = 5$, $a_z = 15$ and $H = 0.8$ at $k_z = 0$. Also plotted at $k_z = 0$ is the fractal power spectrum, again using $H = 0.8$, giving a fractal dimension $D = E + 1 - H = 2.2$. For high wavenumbers both are a straight line on the log-log graph, displaying characteristic self-similar properties. The fractal power spectrum decays beyond a corner wave number, $k_c = 0.3$, which is related to the characteristic source dimension (*Mai and Beroza*, 2002) whereas the von Karman shows a more gradual roll-off, the start of which is related to the correlation lengths, a_x and a_z. Here a_x and a_z were chosen to align the two functions at small wavenumbers. Adapted from (*Mai and Beroza*, 2002).

so that a slip solution has a joint probability based upon how well a slip distribution fits the observed data and how well the slip distribution fits the von Karman autocorrelation function. The parameters describing the von Karman distribution (H, a) could themselves be solved for as hyperparameters, with their prior probability distributions determined by the seismic study meta-analysis from *Mai and Beroza* (2002). These parameters differ depending on fault type (normal, reverse or strike-slip) and also differ in the along-strike and down-dip directions.

In this study we present a method to invert for slip incorporating von Karman regularization, using a Bayesian approach and implemented using a Markov chain Monte Carlo (MCMC) algorithm. A Bayesian approach allows us to fully explore the range of parameters that fit the data, incorporate constraints (e.g. on rake to avoid unphysical features such as back-slip), and solve for a hyperparameter which represents the variance of the slip (discussed more in Section 3.3.3). This means that instead of having to assume in advance the variance of slip we are able to search the range of slip magnitudes and rakes for a range of permitted variances. This flexible approach, whilst computationally expensive, allows us to be more objective and explore the full range of possible solutions in more detail.

We test this method on synthetic data, and then apply it to the M$_w$ 6.0 Napa Valley, California, 2014 earthquake. For comparison we also invert for slip with Laplacian smoothing implemented using the same Bayesian approach.

3.3 Method and Data

3.3.1 Bayesian inversion

In Bayesian inversions each parameter to be solved for (e.g. slip, rake) is treated as a random variable with a prior PDF (probability density function) that is updated by the inversion process. The result is the full joint posterior PDF for every model parameter, giving an ensemble of all possible models that fit the data reasonably, as well as providing a good understanding of the uncertainties on parameters and the covariance between them. This approach also allows us to solve for hyperparameters within the inversion.

Following *Fukuda and Johnson* (2008) and *Hooper et al.* (2013)'s incorporation of Laplacian smoothing into slip inversions using a non-linear Bayesian approach, here we present our method for incorporating a von Karman prior assumption, after (*Hooper*, 2012).

The posterior probability is built from the prior and likelihood function using Bayes' theorem. The prior probability describes how well the model parameters fit a prior assumption. The likelihood function describes how well the forward model calculated using these model parameters fits the observed data.

Bayes' theorem states:

$$p(\mathbf{m}|\mathbf{d}) = \frac{p(\mathbf{d}|\mathbf{m})p(\mathbf{m})}{\int_{-\infty}^{\infty} p(\mathbf{d}|\mathbf{m})p(\mathbf{m})d\mathbf{m}} \tag{3.2}$$

Meaning that the posterior probability, $p(\mathbf{m}|\mathbf{d})$, of a model, $\mathbf{m}$, given a set of data, $\mathbf{d}$, is the product of the prior probability of the model, $p(\mathbf{m})$ and the fit to data $p(\mathbf{d}|\mathbf{m})$, where the denominator is a normalizing constant.

We use an MCMC method incorporating the Metropolis-Hastings algorithm (*Metropolis et al.*, 1953, *Hastings*, 1970) to generate samples of the prior probability density and also to sample the parameter space and thus approximate the posterior PDF. The algorithm samples parameter space in such a way that more models are drawn in areas of high probability. We adapt the approach of *Fukuda and Johnson* (2008) to include multiple Metropolis steps and sensitivity tests.

An MCMC chain is a memoryless system in which parameter space is sampled using random walks, with each random step depending only upon the previous step (in contrast to methods such as the neighbourhood algorithm (*Sambridge et al.*, 1999)). The MCMC chain samples parameter space to provide an estimation of the posterior PDF (*Tarantola* (2005), *Chapter 2, Pg 50*).

3.3.2 Our MCMC approach

In an MCMC chain each parameter is perturbed at the start of each iteration, meaning a random number is added to each model parameter giving a new 'trial' value. The new trial is drawn from the prior distribution, then the likelihood is calculated. The trial is then accepted or rejecting using the 'Metropolis rule'. This acceptance rule states that if the trial likelihood is greater than that of the current model it is accepted. If the trial likelihood is lower, then the probability of acceptance is calculated: the ratio of the two likelihoods. This ratio is compared to a randomly drawn number between 0 and 1. If the probability of acceptance is greater than this random number, the trial is accepted. Otherwise it is rejected. This means that sometimes trials that have lower likelihood are accepted, which allows the chain to not get stuck in local minima. If a trial is accepted it is saved; the next random step is taken from those model parameters.

At the end of the inversion the first B iterations which constitute the 'burn-in' are removed. These are the early steps which do not properly sample the posterior as they may be influenced by starting state (*Fukuda and Johnson*, 2008). The rest of the saved trials represent the posterior, giving the full range of models which adequately fit the data and prior assumptions. This posterior can be represented by some statistical representation of the distribution, which is discussed further in Section 3.5.3.

Here we implement the MCMC chain in two separate steps for efficiency, as described by (*Tarantola* (2005), *Chapter 2, Pg 52*). The first step generates samples of the prior probability density: a von Karman trial. We draw random slip trials for each patch from their prior distribution (Section 3.3.4) and use the Metropolis-Hastings algorithm to accept/reject these trials based on their von Karman probability. The slip trials are generated by adding a random number from a boxcar distribution between ± each parameters' 'step size'. The second step is to sample the posterior probability distribution, which is achieved by comparing the likelihoods of the current trial to the previous trial (*Tarantola* (2005) *Chapter 2, Pg 52*). This implementation reduces the number of times the particularly computationally-expensive likelihood calculation is made, since it avoids making the calculation for most models that already have a low posterior probability due to their slip distribution having very low von Karman probability. Also for efficiency we periodically perform a sensitivity test to adapt the step sizes being taken, which is discussed in detail in Section 3.3.6. In Section 3.3.4 we describe how we sample the prior and in Section 3.3.5 we describe how we sample the posterior, using the likelihood; these two steps together comprise one iteration of our algorithm.

3.3.3 Model parameterisation

We divide the fault into M slip patches and solve for magnitude of slip and rake (the direction of slip) separately for each patch, as well as a hyperparameter α^2 for each separate fault. The physical meaning of the hyperparameter α^2 is the variance of the slip. The correlation matrix calculated using Equation 3.2 defines the desired von Karman correlation between slipping patches and the hyperparameter α^2 acts on this to dictate the magnitude of the slip, in effect converting correlation to variance-covariance. It is necessary to solve for α^2 in order to explore the full plethora of slip and rake solutions that fit a range of permitted variances. If a model contains multiple faults that are assumed to be uncorrelated in terms of their slip, then we would calculate separate von Karman prior probabilities for each fault and consequently we assign one α^2 parameter per fault. Slip and α^2 are the only parameters used in the von Karman prior probability calculation.

3.3.4 First MCMC step - sampling the prior

The prior probability describes how well a slip distribution fits the prior assumptions. Here the prior is the product of prior distributions of slip magnitude and rake for individual patches, α^2 for each separate fault, the von Karman probability of slip and a moment regularization (if this option is used).

Model parameter priors

We solve for slip magnitude and rake using boxcar priors and we solve for α^2 using a logarithmic prior. This means that for slip and rake the new trials are generated with uniform probability between a given range i.e. slip is given uniform probability between 0 meters and x meters, and the probability is zero outside of this range. For α^2 we implement a logarithmic prior. This means that we solve for a model parameter, q, and then calculate α^2 by $\alpha^2 = 10^q$, thus transforming a uniform prior for q into a logarithmic prior for α^2.

Von Karman prior

Once each model parameter has been drawn from its prior, we apply the von Karman prior using the Metropolis-Hastings algorithm, since it is difficult to directly generate von Karman distributions directly with a random walk.

The von Karman autocorrelation is given by:

$$p(\mathbf{s}) = (2\pi\alpha^2)^{-M/2}|\mathbf{\Sigma_s}|^{-1/2}e^{\frac{-1}{2\alpha^2}\mathbf{s}^T\mathbf{\Sigma_s}^{-1}\mathbf{s}} \tag{3.3}$$

Where:

$p(\mathbf{s})$ = probability of this slip distribution
$\alpha^{\mathbf{2}}$ = a hyperparameter controlling the slip variance
M = number of slip patches in a fault strand

$|\mathbf{\Sigma_s}|$ = the determinant of the slip patch autocorrelation matrix
$\mathbf{s}$ = vector of slip magnitudes

We calculate the probability for each separate fault using a corresponding α^2 term for that strand. The product of the prior probabilities for all the faults gives the the joint probability of the overall distribution of slip conforming to the von Karman correlation function.

The autocorrelation, $\mathbf{\Sigma_s}$ is calculated for a particular fault strand from the von Karman correlation function given in Equation 3.2. In MATLAB, $G_H(0)$ gives an infinite value, so we investigated the $lim_{r \to 0}$ of $G_H(r) = (r)^H K_H(r)$. We found any values smaller than $r = 10^{-4}$ changed the value of $G_H(r)$ significantly less than 1% so we therefore used a value of $r = 10^{-10}$ to approximate $r = 0$.

We calculate the scaled distance, r/a, by calculating the along-strike and down-dip separation distance between each fault patch, then dividing this by the along-strike, a_{as}, or down-dip, a_{dd}, correlation value respectively. We then used these scaled along-strike and down-dip separation distances to calculate the scaled separation distance between each patch. We used the correlation values from *Mai and Beroza* (2002) for strike-slip faults:

$$a_{as} = 1860 + 0.34 \times (fault\ length) \quad (meters) \tag{3.4}$$

$$a_{dd} = -390 + 0.44 \times (fault\ width) \quad (meters) \tag{3.5}$$

We also used Hurst parameter values, H, from *Mai and Beroza* (2002) for along-strike, $H_{as} = 0.71$, and down-dip, $H_{dd} = 0.77$ and scaled them appropriately for angles between purely along-strike and down-dip. These values are calculated in the meta-analysis performed by *Mai and Beroza* (2002) and have uncertainties associated with them, which we have not accounted for here. These correlation lengths and Hurst parameters could be solved for as hyperparameters as part of the inversion in future studies, using the distribution from *Mai and Beroza* (2002).

Moment regularization prior

Geodetic slip inversions have poor depth resolution since all the data are acquired at the surface. Consequently deep slip makes very little difference to the likelihood; it is almost in the null space. To attempt to limit the amount of slip being put in the null space we optionally include moment regularization in the inversion such that slip trials with a moment very different to that of the seismological moment are more likely to be rejected. We use a Gaussian prior for moment: it is calculated with the standard equation for calculating the probability from a Gaussian distribution given a mean (moment from the USGS page) and standard deviation (standard deviation of the different moment calculations on the USGS page). The prior probability is then the von Karman prior multiplied by the moment regularization prior.

However, we prefer to avoid this regularization where possible, since many geodetic measurements also include surface displacements from postseismic slip or aftershocks, and there are often systematic differences between geodetically and seismologically-derived seismic moments (*Weston et al.*, 2011). It is not clear whether this is predominantly due to real differences from aseismic slip, errors in the seismic estimate or errors in the geodetic estimate, or some combination of these. In this study moment regularization is not applied unless specifically mentioned.

Prior acceptance rule

We use the Metropolis rule to decide if a temporary trial is accepted, as discussed in Section 3.3.2. If it is accepted then it is a representative draw from the von Karman distribution and the other prior distributions; therefore we move onto the second step.

3.3.5 Second MCMC step - sampling the posterior

Once we have drawn a sample from the prior using the first MCMC step, we sample the posterior by calculating the likelihood.

A forward model of surface displacements is calculated from the trial model parameters, using the formulation for rectangular dislocations in an elastic half-space (*Okada*, 1985). This is calculated by multiplying the current slip model, $\mathbf{s}$, by a kernel $\mathbf{G}$, which gives predicted surface displacements, $\hat{\mathbf{d}}$, at each of the locations of our InSAR and GPS data for unit slip on each fault patch and the appropriate rake:

$$\hat{\mathbf{d}} = \mathbf{G}\mathbf{s} \tag{3.6}$$

Because we solve for slip magnitude and rake, the kernel $\mathbf{G}$ needs to be updated for the current rake value during each iteration. For a linear case in which fault geometry is held fixed (i.e. not changing dip), $\mathbf{G}$ matrices for purely left-lateral strike-slip, $\mathbf{G}_{ss}$, and purely thrust dip-slip, $\mathbf{G}_{ds}$, movement can be calculated before commencing the inversion. Then the $\mathbf{G}$ matrix for the current iteration is calculated using the current values of rake by:

$$\mathbf{G} = \mathbf{G_{ss}} \times cos(rake) + \mathbf{G_{ds}} \times sin(rake) \tag{3.7}$$

Where $cos(rake)$ and $sin(rake)$ are diagonal matrices.

The likelihood is calculated using the weighted misfit of a forward model to the observed data. The misfit is weighted by the inverse of the variance-covariance matrix, $\mathbf{\Sigma_d}$, which represents data uncertainty. The likelihood is given by:

$$p(\mathbf{d}|\mathbf{s}) = (2\pi)^{-N/2}|\mathbf{\Sigma_d}|^{-1/2}e^{\frac{-1}{2}(\mathbf{d}-\mathbf{Gs})^T\mathbf{\Sigma_d}^{-1}(\mathbf{d}-\mathbf{Gs})} \tag{3.8}$$

Where:

$p(\mathbf{d}|\mathbf{s})$ = the probability of the observation, given the slip and rake distribution
N = total number of data points
$\mathbf{\Sigma_d}$ = variance-covariance of the data
$\mathbf{d}$ = data (e.g. InSAR, GPS, vertical displacement of coral atolls)
$\mathbf{s}$ = magnitude of slip
$\mathbf{G}$ = kernel, calculated for the appropriate rake and dip values

We then once again use the Metropolis rule on the ratio of the trial likelihood to current model likelihood. If the trial passes this test, then it is saved as the current model and future trials will be drawn as a step from this trial, until another more likely trial is drawn. If the trial is rejected, the previous model is saved and next trial is initiated from this trial.

The inversion results in a joint probability from which we can calculate a histogram of the posterior for each model parameter. We can also calculate the 2D PDFs, which show the joint PDF of each pair of parameters.

3.3.6 Efficiency

Bayesian inversions are computationally expensive and so methods are employed to improve the efficiency of the parameter search, such as the use of multiple MCMC chains e.g. (*Minson et al.*, 2013). Here we improve efficiency by using two steps within one MCMC chain as discussed in Section 3.3.2 and by modifying the step size for each parameter within the MCMC chain, in a manner similar to that used by *Hooper et al.* (2013) and also *Minson et al.* (2013) between chains.

We modify the step size for each parameter to achieve an optimal acceptance rate of 0.234 (*Roberts et al.*, 1997). Acceptance rates that are higher or lower than this give an inefficient search of parameter space. For the sensitivity tests we use a 'rejection' to mean either a rejection at the prior or likelihood stage.

In order to ensure we achieve this ideal rejection ratio whilst properly exploring parameter space, we perform sensitivity tests at regular intervals throughout the inversion, with the first sensitivity test, $j = 1$, starting at $i = 100$ where i is the iteration, then at $i = 500$ and every 1000 iterations up until 10,000 and then every 10,000 iterations for higher values of i. We use a 'probability target' parameter to adjust the step sizes, so that perturbation of each model parameter results in the same amount of change to the posterior probability. This probability target is the expected ratio of the posterior probability after perturbing a single model parameter, to the current posterior probability. Changing step sizes to match this probability target ensures no parameter is having too great or too little an effect on the posterior probability. Adapting the probability target with the rejection rate forces step sizes to increase or decrease to optimise efficiency. At the start of a sensitivity test we first adjust the probability target at the current sensitivity test, j, using the probability target from the previous sensitivity test, $j-1$, by:

$$Ptarget_j = Ptarget_{j-1} \times \frac{r_{ideal}}{r_j} \tag{3.9}$$

This means if too many trials are being rejected (i.e. the rejection ratio since last sensitivity test, r_j, is larger than the ideal rejection ratio, r_{ideal}) then the previous probability target, $Ptarget_{j-1}$, will be decreased. We then adjust step sizes of each model parameter using this new probability target. This is done during a sensitivity test by calculating the posterior probability, perturbing each parameter by half a step size in turn and recalculating the posterior probability. The ratio of posterior-before-perturbation to posterior-after-perturbation is calculated and subtracted from the probability target to give the difference, D. If the perturbation is such that model parameter's contribution to the posterior probability is more than the probability target ($D < 0$) then the step size is having too large an effect, which means the step size must be decreased. We decrease or increase step sizes using the empirical formula:

$$stepsize_j = stepsize_{j-1} \times e^{\frac{D}{Ptarget_j \times C_1}} \qquad \text{for } D > 0 \text{ (step sizes too small)} \tag{3.10}$$

$$stepsize_j = stepsize_{j-1} \times e^{\frac{D}{(1-Ptarget_j) \times C_2}} \qquad \text{for } D < 0 \text{ (step sizes too big)} \tag{3.11}$$

Where the constants, $C1$ and $C2$, are arbitrarily chosen to control how quickly step sizes increase or decrease in size; increasing C_1 decreases the amount by which step size increases, increasing C_2 increases the amount by which a step size decreases. These values were chosen after experimentation as they resulted in gradual changes in rejection rates in synthetic tests. Different values may work better in different situations, depending on the number of model parameters. For a von Karman regularized inversion we use $C_1 = 16$ and $C_2 = 2$, although we find higher values of C_1 work better for Laplacian and moment regularized inversions. If we are re-running an inversion we optionally use the idealised step sizes from a previous run. A simple test demonstrates that an inversion scheme with changing step sizes correctly samples the posterior (Appendix B, Figure B.1); a mathematical proof of this is beyond the scope of the current paper would be a valuable avenue of future work.

3.4 Synthetic tests

3.4.1 Synthetic test set up

We first tested our slip inversion code on three synthetic cases. Each consists of a strike-slip fault modeled as two connected strands, and the simulated surface displacements are created using our forward model described by Equation 3.6, shown in Figure 3.2. The three synthetic slip distributions created are:

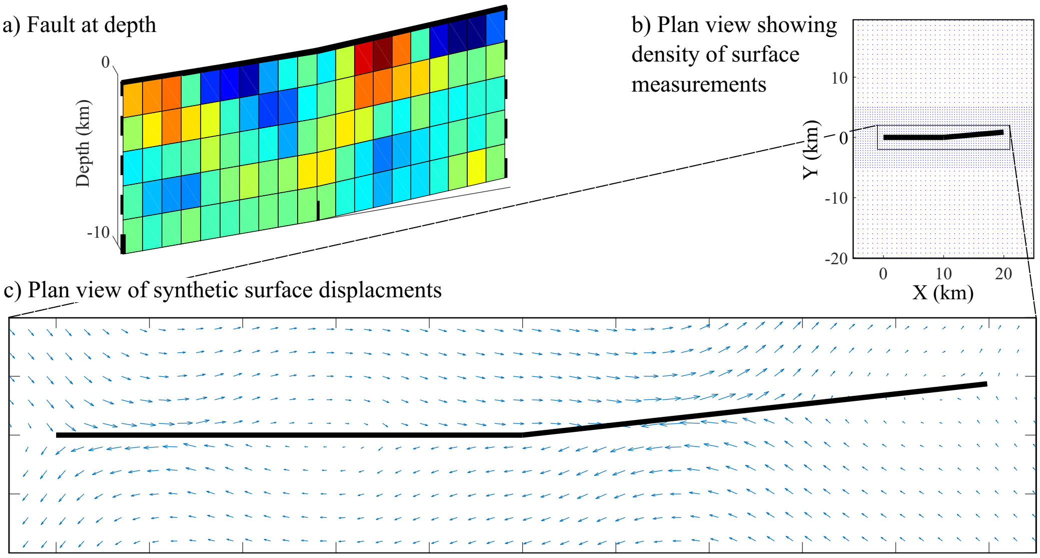

Figure 3.2: Setup of synthetic tests. *a*) Fault plane, with two joining strands, with example slip distribution indicated by colour. Thick black line shows top of fault, at the surface. *b*) Plan view of location of surface displacements caused by this right-lateral fault, indicated by a black line *c*) Zoomed in on box shown in *b*), showing the surface displacements around the fault.

1. Uniform, pure strike-slip motion that ruptures the surface down to ∼6km depth.
2. Laplacian smoothed slip.
3. Slip displaying von Karman autocorrelation.

The Laplacian smoothed slip is created using a matrix of discretised Laplacians appropriate for this fault geometry, the inverse of which is multiplied by normally-distributed random numbers.

The von Karman consistent synthetic test is created by transforming a random slip distribution into a correlated distribution using the appropriate correlation matrix (e.g. *Lohman and Simons* 2005), for a fault of given dimensions.

To investigate the differences caused by regularization alone we conducted the synthetic tests on noise-free synthetic data. We used a high density of 3D surface displacements, spaced every 400 m within 5 km of the fault and every 2 km up to a distance of 20 km from the center of the fault.

We then inverted for slip for these three separate synthetic tests using three modes of the Bayesian inversion: with no regularization, Laplacian regularization and von Karman regularization.

Each was performed with the correct fault geometry, with a prior rake within ±30 degrees of the true value, adding no further regularization than that specified above. For Laplacian regularization we solved for the hyperparameter that controls the strength of the smoothing within the inversion.

3.4.2 Synthetic test results

The results are shown in Figures 3.3 and 3.4, Appendix B Figures B.2 - B.3 and the fit to the data for each model shown in Appendix B Figures B.4 - B.12.

It is not simple to display the results from a Bayesian inversion since the inversion produces a multidimensional joint PDF for all model parameters. All saved models formulate the solution, which would best be displayed as a video. However to present the results in a 2D image, in Figure 3.3 we have plotted the 'mode' solution for each slip patch. This slip distribution itself has not been drawn as a trial in the Bayesian inversion, but gives an indication of where slip is likely to have occurred from all the saved trials. We calculate the joint slip mode and rake mode for each patch by finding the value of the peak of the highest bar in the 2D histogram of slip against rake.

All solutions fit the data very well; however low data residuals do not ensure a correct source model, as the Earthquake-Source Inversion Validation project has previously shown (*Mai et al.*, 2016). The smoothed solutions give a less oscillatory result than the unsmoothed solutions, and also the unsmoothed solutions add additional high slip at depth; no moment regularization was applied to any of the synthetic test inversions. This illustrates the unstable nature of an unsmoothed inversion. Neither the Laplacian nor von Karman regularised inversions fit the distribution of uniform slip adequately, as is to be expected, but are equally biased.

These tests show that a von Karman correlation constraint retrieves a von Karman slip distribution better than a Laplacian or no constraint, as might be expected. However von Karman also adequately resolves a slip solution that is not von Karman. The von Karman regularization outperforms both Laplacian regularized and unsmoothed inversions for uniform slip, as is shown by the lower RMS (text under each solution in Figure 3.3). For the Laplacian slip input model and von Karman slip input model the RMS for von Karman regularization and Laplacian smoothing is similar enough to suggest they have the same resolving power for these slip distributions ($RMS_{Laplacian} = 0.182$ and $RMS_{vonKarman} = 0.187$ for Laplacian slip, and $RMS_{Laplacian} = 0.252$ and $RMS_{vonKarman} = 0.241$ for von Karman slip.

Further comparisons using the method outlined by (*Zhang et al.*, 2015a) confirm this, shown in Appendix B Figure B.13. We find that the von Karman solution outperforms Laplacian and unsmoothed solutions in matching the magnitude of slip and correlation of slip for all three input slip distributions, though for Laplacian input slip the von Karman is only marginally better than the Laplacian.

The histograms in Figure 3.3 show the posterior PDF for a single slip patch, indicated by the black box, for each of the different inversion methods. An unsmoothed inversion has a very high standard deviation in the histogram, showing that the slip is poorly constrained. In comparison, the smoothed solutions have much lower standard deviations, meaning they have a much tighter constraint. This is apparent in Figure

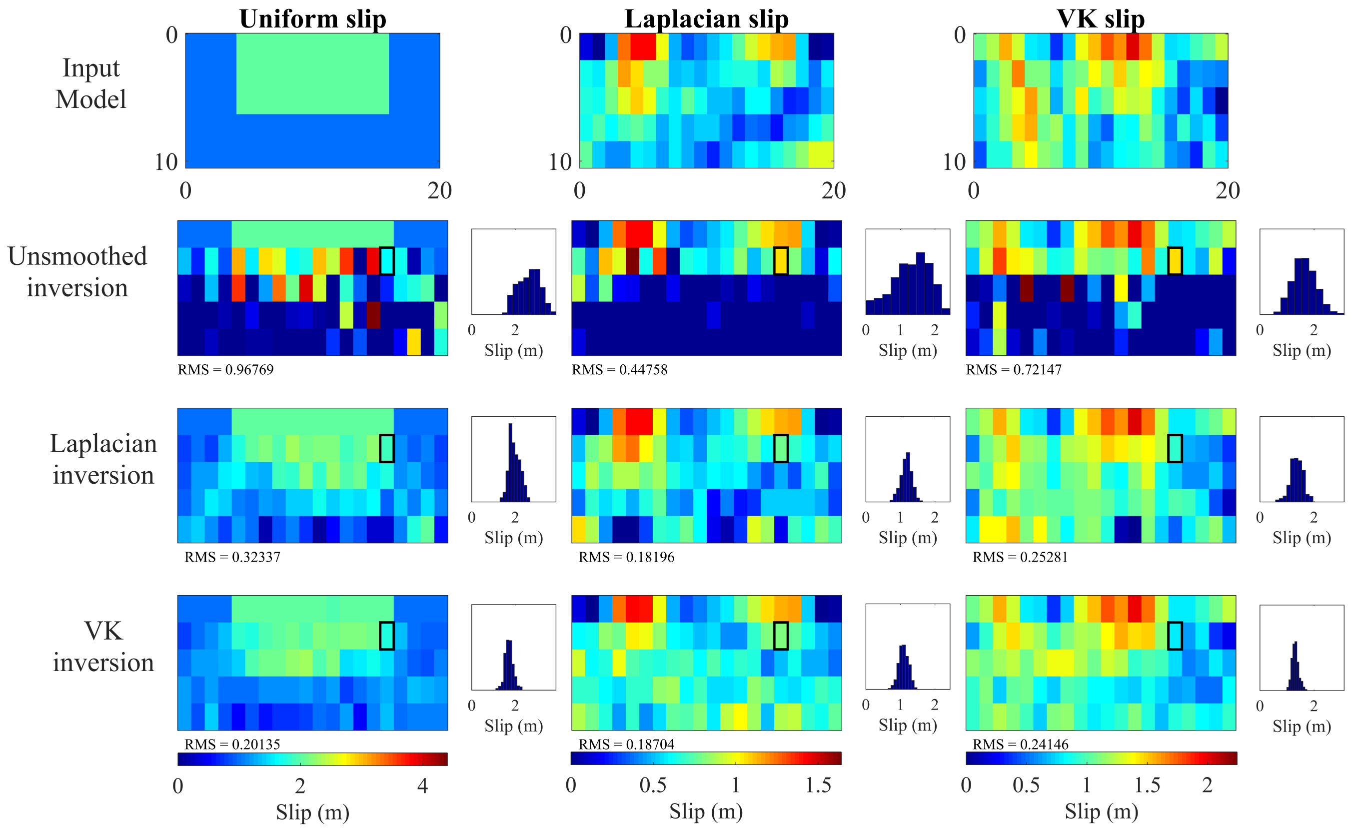

Figure 3.3: Results of slip inversions for synthetic tests, each with the fault planes shown as a flat surface and colour indicating magnitude of slip. Top row show shows input slip distribution, which is then solved using a Bayesian inversion with no smoothing (row 2), with Laplacian smoothing (row 3) and von Karman smoothing (row 4). All distributions displayed give the mode result for each patch, and are displayed with the same color scale as the corresponding model. Note that the colorbar for column 3 (VK slip) is saturated for one value in the unsmoothed solution. The RMS is the sum of the square of the misfit between the true slip (input model) and the mode of each patch (not data misfit). Also shown is the PDF for patch 77, indicated by a box, showing how smoothed solutions give a much tighter constraint than unsmoothed versions. Note that the unsmoothed results just serve to show the unstable nature of an unsmoothed inversion, and additionally that it is not expected that either a Laplacian or a von Karman regularised inverison should be able to well resolve the uniform slip solution.

3.4 for von Karman slip and Appendix B Figures B.2 and B.3 for surface slip and Laplacian slip, which show that the smoothed inversions yield much tighter confidence intervals than for the unsmoothed inversion. For von Karman slip the true value of slip lies within the 95% confidence intervals for 94 out of 100 patches using von Karman regularization and 99 out of 100 patches for Laplacian regularization.

3.4.3 InSAR/GPS synthetic test

We explored the effects that data-type (InSAR and or GPS) may have on the ability for a regularization style to resolve an input slip distribution. InSAR has the benefit of high spatial resolution, but the displacement field is only measured in one dimension (satellite line of sight, or LOS). In contrast GPS provides 3D measurements of displacement but at a spatially sparser set of discrete locations.

We created a synthetic test with noise-free InSAR data spaced every 400 m within 5 km of the fault, and every 2 km up to a distance of 20 km away from the fault, with the same LOS vector as for the Sentinel-1 interferograms in the Napa earthquake. To simulate loss of coherence we randomly remove 800 data points, which also serves to reduce the time to calculate the likelihood. We randomly scattered thirty noise-free 3D GPS measurements around the fault.

We simulated von Karman slip on a strike-slip fault consisting of two connected segments and solved for this with von Karman regularization and Laplacian smoothing.

We find that the von Karman regularization consistently matches the magnitude of input slip and spatial distribution of input slip better than Laplacian, regardless of datatype used in the inversion (Appendix B Figures B.14 and B.15).

3.4.4 Synthetic test summary

These tests demonstrate that our method is working as expected and that inversions incorporating von Karman regularization can successfully recover the distribution of slip from geodetic data.

Our new method of regularization not only outperforms Laplacian smoothing when the slip has a fractal distribution, but also does better for uniform slip and performs comparably when slip is smooth. This suggests that incorporating von Karman regularization into slip inversions is likely to produce solutions that are at least as accurate than those generated by inversions incorporating Laplacian smoothing, and if the true slip conforms to the von Karman correlation function our method is significantly more accurate. Therefore is a better default regularization approach to use than Laplacian.

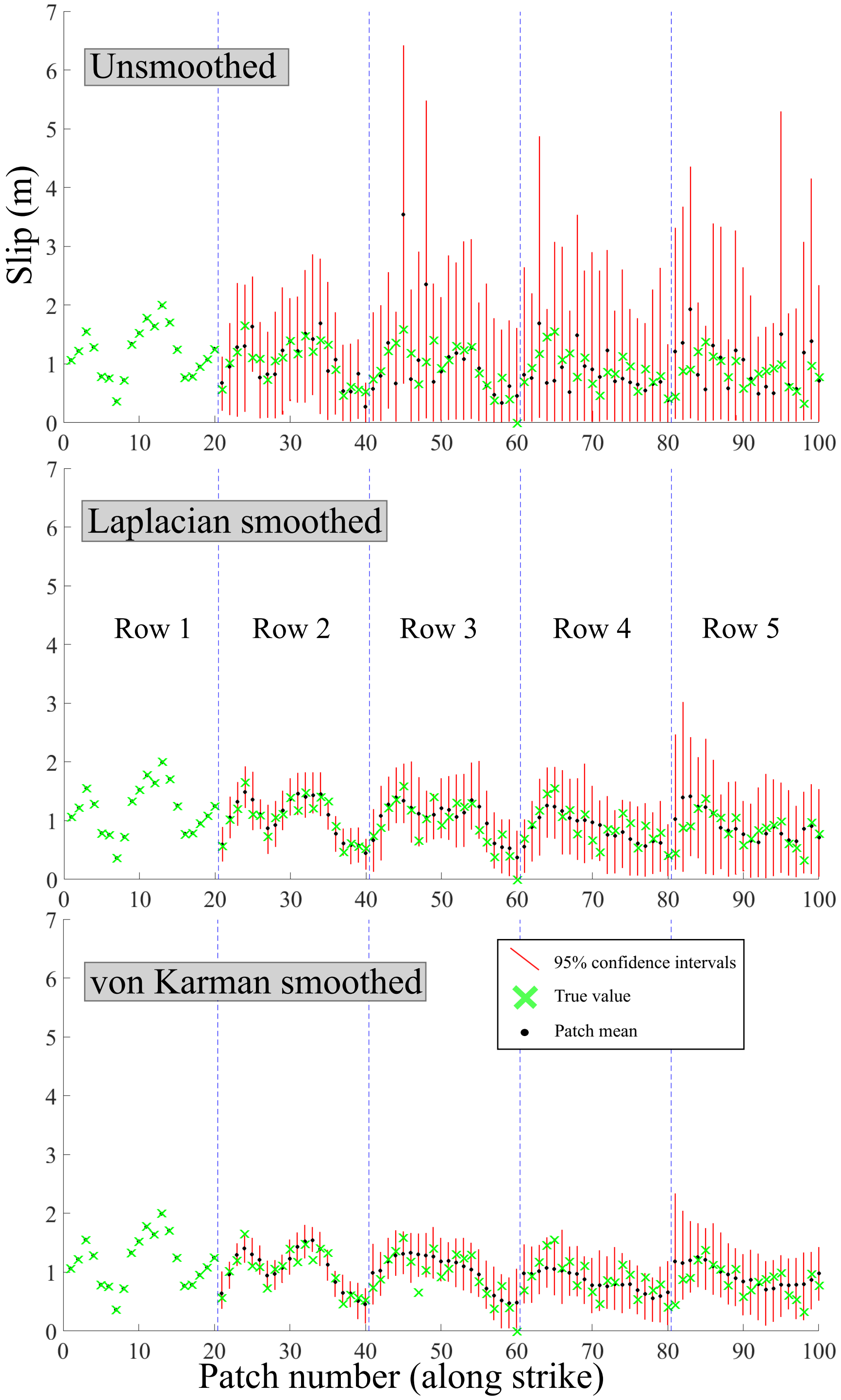

Figure 3.4: Top: 95% confidence intervals (red line) for each slip patch, patch mean (black circle) and the true value for that slip patch (green cross) for von Karman slip solved for with no smoothing (top), Laplacian smoothing (middle) and von Karman smoothing (bottom). For von Karman regularization 94% of patches had the true value of slip within the 95% confidence intervals, compared to 99% for Laplacian smoothing. Note that Row 1 (the surface) has significantly smaller confidence intervals due to better resolving power nearer to the data, which means the patch mean and true slip are plotting in very similar locations, and confidence intervals are too small to see.

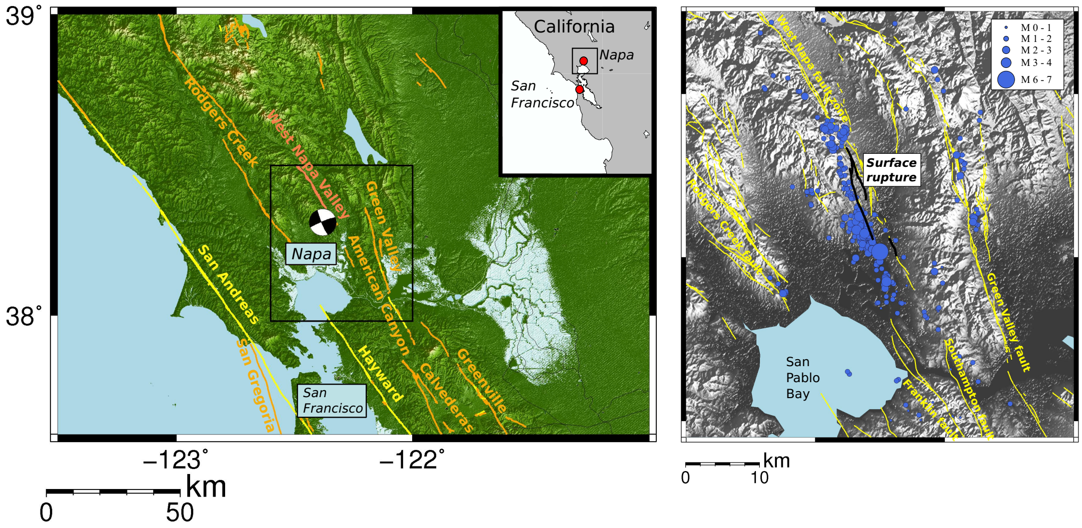

Figure 3.5: Regional setting of the Napa Valley earthquake. Left: Focal mechanism was almost entirely strike slip with a strike of 345 degrees. Historical (yellow), Holocene (orange) and selected Quaternary (coral) faults (*USGS*, 2006). Right: surface rupture of Napa earthquake from (*Hudnut et al.*, 2014) and aftershocks from August to February shown in blue, with size indicating magnitude. Yellow shows faults of all ages (*USGS*, 2006).

3.5 M$_w$ 6.0 Napa Valley earthquake, 2014

We applied our method to the M$_w$ 6.0 Napa Valley, California earthquake of August 24th 2014. This was the first earthquake imaged by Sentinel-1A, with the pre-earthquake image acquired on the first day that the satellite reached its operational orbit. The earthquake occurred on the West Napa Fault (*Hudnut et al.*, 2014) which is part of the San Andreas fault system; the broad region of faults that accommodates right-lateral movement between the Pacific and North American plates (Figure 3.5).

3.5.1 InSAR and GPS data

The details of the acquisition and processing of the InSAR and GPS data are given in *Floyd et al.* (2016). The earthquake happened on 24th August 2014 and the second Sentinel-1 acquisition was on the 31st August, meaning that the interferogram contains 7 days of postseismic displacement in addition to the coseismic signal. We use GPS displacements calculated between the day before the earthquake and the 31st August, for continuity between the two datasets. We do not weight either dataset above the other, though there are more InSAR datapoints than GPS datapoints.

Spatio-temporal variation in propagation path properties through the atmosphere adds noise to InSAR scenes that is spatially correlated. To account for the covariance of this noise we calculate the variance-covariance matrix by selecting an undeforming region of the interferogram and computing the 1D semivariogram (e.g. *Lohman and Simons* 2005, *Oliver and Webster* 2014), which is a function of variance with distance that describes the spatial dependence in a data set (*Foody and Atkinson*, 2002). This model gives us three values: the sill, nugget and range, which are indicated on our semi-variogram shown in Appendix Figure B.16 and that can be used to estimate the spatially-correlated error in the InSAR data. The nugget indicates the level of spatially independent noise present and the sill is the maximum value of the semi-variance as the range tends to infinity (*Foody and Atkinson*, 2002). The range is the distance at which the semi-variance reaches approximately 95% of the sill (*Curran*, 1988) and is the distance over which we expect data points to be spatially correlated. We calculate a sill of 5×10^{-4} m^2, nugget of 1×10^{-5} m^2 and a range of 12.8 km from the semi-variogram, which we use to calculate the variance-covariance matrix using the exponential function:

$$\mathbf{\Sigma_d} = (sill - nugget) \times e^{\frac{-3 \times x}{r}} \tag{3.12}$$

Where x is the distance between each InSAR data point, r is the range, and $\mathbf{\Sigma_d}$ has dimensions $N \times N$ where N is the number of data points. At $r = 0$ the variance of a datapoint is equal to the sill.

A larger range would mean that covariance between datapoints extends over a larger distance (e.g. larger wavelength atmospheric signals). A larger sill would mean a higher variance for individual datapoints (at $r = 0$), i.e. greater uncertainty on individual datapoints and also higher covariance between datapoints. A larger nugget indicates decreased covariance if the sill remains the same. Many studies find the range for an interferogram to be > 10 km, the standard deviation ($\sqrt{variance}$) of the sill to be a couple of centimeters, and the nugget to be significantly smaller than the sill (e.g. *Hanssen* 2001, *Bekaert et al.* 2016). The values we estimate for these parameters are indeed in accordance with these previous studies.

3.5.2 Model parameters

We constrained the surface fault using the rupture map of *Hudnut et al.* (2014). Based on this we modeled the fault as two vertical strands, one with three sections to capture the fault curve, and one straight (details given in Table 3.1). We assumed slip correlation did not continue between the two separate fault strands.

Correlation lengths for the two faults were calculated based upon the length and width of the faults using Equations 3.4 and 3.5, giving the correlation down-dip as $a_{dd} = 5330$ meters and along-strike as $a_{as} = 5070$ meters for the north-eastern fault strand and $a_{dd} = 5330$ meters and $a_{as} = 6040$ meters for the separate segments on the most south-western fault strand. We note that ideally these parameters would be drawn from their prior distributions, discussed more in Section 3.6.4. The Lamé parameters used in the Okada Green's function calculation were $\lambda = \mu = 3.23\ GPa$. The initial probability target (later used in sensitivity tests to adjust step sizes) was 10^{-4}.

Strike	**Dip**	**Rake**	**Center (UTM x)**	**Center (UTM y)**	**Length (km)**	**Top depth (km)**	**Bottom depth (km)**
337	90	180	559561	4232632	6.88	0	13
343	90	180	557784	4237229	2.99	0	13
4	90	180	557434	4239865	2.42	0	13
337	90	180	557850	4240305	9.45	0	13

Table 3.1: Details of the fault geometry. The first three lines are one fault (south-western fault) modeled as three separate rectangles to capture the curve in the fault geometry, and the forth line is a separate fault segment (north-eastern fault). The center refers to the up-dip surface projection of the fault and the UTM zone is 10S. This fault setup can be seen in Figure 3.7.

The InSAR and GPS data were only weighted according to their variance-covariance. In this case an offset and ramp has been removed from the InSAR before the inversion.

To ensure the inversion had reached convergence we check four criteria:

1. Smoothness of histograms for each model parameter.
2. Smoothness of 2D histograms of the six patches with the most slip.
3. Posterior probability is no longer increasing.
4. The value of each parameter through the inversion has reached stability and does not have an increasing or decreasing trend.

As standard we remove the first 2000 saved trials to remove the burn-in. We then check if the posterior probability is stable, and the form of the joint PDFs. An increase in the posterior probability for the first saved-trials or a visible tail in the joint PDFs implies that the burn-in has not been fully removed, and we increase the burn-in period so as to remove these two effects.

Examples of unconverged and converged solutions with burn-in present are shown in Figure 3.6.

Priors

For the slip prior we used a uniform probability density between 0 and 50 meters. The upper bound slip prior was set arbitrarily high, but we found that slip at no point explored values higher than 1.8 meters, so this choice of high upper bound made no difference to the efficiency of our inversion. For rake we used a uniform probability density between 135 and 225 degrees on the south-western fault and 135 and 270 on the north-eastern fault where previous studies have found normal motion on a releasing step-over of the S. Napa fault (*Floyd et al.*, 2016). The probability outside of the ranges given for slip and rake is 0, so model parameters were only drawn from within these ranges. We used a logarithmic prior for α as discussed in Section 3.3.3.

3.5.3 Napa von Karman results

As discussed previously, the solution of a Bayesian inversion is a multidimensional probability density function, which is difficult to visualize. A video is an appropriate method of showing a selection of the saved results (Supplementary materials in **?**). To illustrate this with static images we have used statistical parameters estimated from the model parameters' PDFs. These are shown in Figure 3.7, for a Bayesian inversion with von Karman smoothing. The 'mode' for each patch is shown in 3D to show fault geometry and as for the synthetic tests, we calculate the joint slip mode and rake mode for each patch by finding the value of the peak of the highest bar in the 2D histogram of slip against rake. The mode, mean and median have not been drawn as trials, but

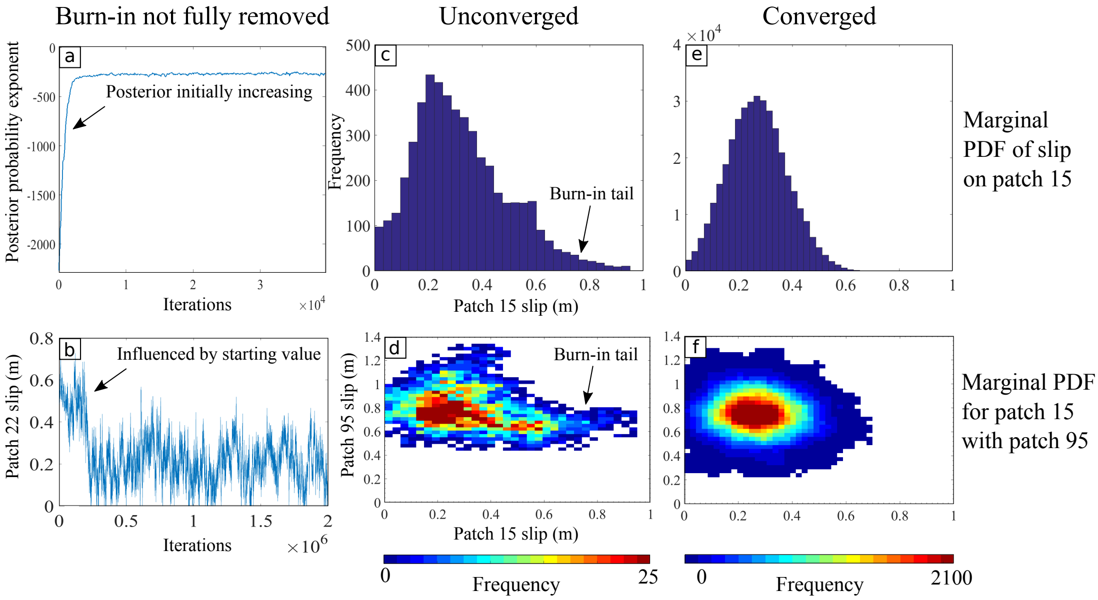

Figure 3.6: Illustrating converged and unconverged solutions and those with the burn-in not fully removed. Panels *a* and *b* show the posterior probability and value of one of the model slip on fault patch 22 respectively; in this case they are both still influenced by the starting parameters because some of the burn-in remains. Note the difference in x-axis between *a* and *b*, because we have zoomed in on *a* for clarity. Panels *c* and *d* show unconverged inversion: the PDF is not filled out and the joint PDF is rough. In this example we have also left the burn-in present, which is shown by an elongate tail extending from the starting value of ∼0.9m. Panels *e* and *f* show converged solutions of *c* and *d*: both PDFs are smooth. Note that the frequency shown by the colour bar for the joint PDFs is not plotted on the same scale, to illustrate how the PDF would look at the end of the unconverged inversion, rather than in comparison to the later one.

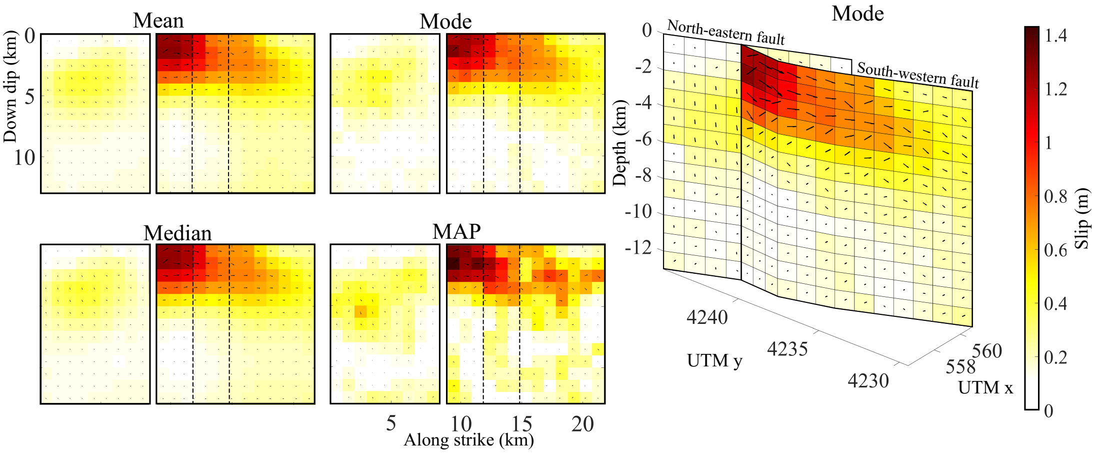

Figure 3.7: Results of inversion for the Napa Valley earthquake incorporating a von Karman prior. All five show the same fault plane, which is in two strands, and dotted vertical lines indicate the bends on the south-western fault. The first three are different statistical parameters to visually capture the full PDF, whereas the MAP solution is the saved trial with the maximum *a posteriori* result. The MAP is the multi-dimensional mode solution; the single solution that maximises the posterior PDF (i.e. that maximises both the prior and the likelihood). Peak slip is around ~1.2m and at a depth of 2km. The right hand figure shows the mode solution shown in 3D, showing the fault geometry of the two separate strands more clearly. Note that the rake display oscillatory features, discussed further in Section 5.5.

by plotting them all we hope to give an indication of where slip is most probable and the probable direction of rake.

These results show that the majority of slip occurred as strike-slip motion on the south-western fault, near to the surface. We found peak magnitude of slip of ~1.2m at about 2km depth. This is similar in magnitude and location to InSAR and GPS studies by *Guangcai et al.* (2015), *Wei et al.* (2015), *Floyd et al.* (2016) and the strong-motion study by *Zhang et al.* (2015b). Many studies also find a peak magnitude of 1.2 m, though find slip deeper at ~5 km (*Barnhart et al.*, 2015, *Dreger et al.*, 2015, *Melgar et al.*, 2015). On the north-eastern fault there was a component of normal motion between 3 and 6 km depth, as also found by *Wei et al.* (2015), *Floyd et al.* (2016).

The MAP result gives a moment of 2.78×10^{18} Nm which is higher than the seismic moment of 1.33×10^{18} Nm from the USGS event page. Part of this over-estimation of the energy release may be due to the 7 days afterslip included in the InSAR and GPS. We found MAP values of α^2 where 0.05 on the north-eastern strand and 0.26 on the south-western strand.

Figure 3.8 shows the fit of the MAP model to the InSAR and GPS data. The predicted InSAR displacements fit the magnitude and wavelength of the signals in the data, but there are some areas of high residuals. The InSAR misfit on the eastern side of the south-western fault is in part due to displacements on a separate, third fault which ruptured at the surface in this earthquake but which we have not modeled here (*Hudnut et al.*, 2014). The three GPS points nearest to the fault are not fit within the

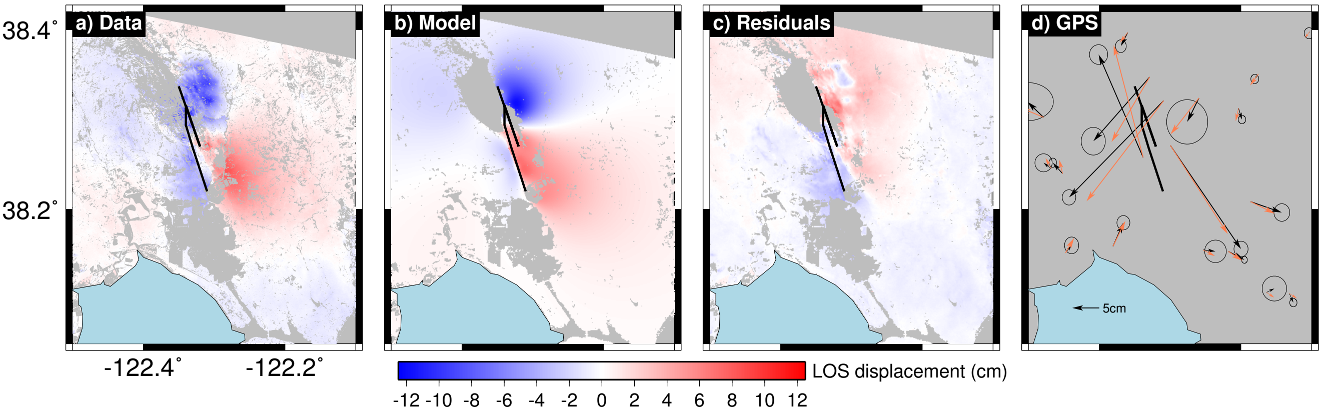

Figure 3.8: The InSAR data (*a*), model fit (*b*) and residuals (*c*) for the von Karman regularized MAP slip solution on selected patches for the Napa earthquake. Panel (*d*) shows the closest GPS data (black) to the fault, with model vector (orange) and 95% confidence intervals.

95% error ellipses and show a very similar misfit as found by *Floyd et al.* (2016) using the same data. The complexity of surface deformation in the north-east, where two GPS points are poorly fit, is shown in the InSAR data (panel *a* of Figure 3.8). This could be due to an unmodeled fault as suggested by *Guangcai et al.* (2015) or due to local surface effects and changes in elastic properties in the north-east due to a change in lithology to Quaternary sediments. The modeling of these complexities is beyond the scope of this paper.

3.6 Discussion

3.6.1 Comparison of VK and Laplacian result for Napa

For comparison we also solved for slip in a Bayesian fashion using a Laplacian prior, in which we solved simultaneously for the model fit to the data and for the fit of the model to a Laplacian distribution as well as for the Laplacian smoothing hyperparameter. In the Laplacian solution we assume all the edges are free surfaces, so the solution is not constrained to tend to 0 m of slip at any edge. The results of the mode solutions are shown in Figure 3.9 and fit to the data for the Laplacian solution is shown in Appendix B Figure B.17. Both put more slip on the south-western fault (shown on the right in Figure 3.9) than the north-eastern fault and find a peak slip of just over 1 m, however the Laplacian solution has a slightly higher peak slip and extends this slip further along the south-western fault. The standard deviation on the south-western fault is significantly larger than for the von Karman regularized inversion, showing the larger uncertainty for the Laplacian solution in this area. This is not unexpected as the von Karman prior provides a tighter constraint than the Laplacian prior, but it is an important result, as the tighter constraint is based upon observed features of fault slip. The von Karman solution puts a slightly lower magnitude of slip on the north-eastern fault and fits the data better in this region (Appendix Figure B.17).

The moment of the MAP Laplacian solution is 3.04 $\times 10^{18}$ Nm which is significantly larger than the USGS moment of 1.33 $\times$ 10^{18} Nm, and slightly larger than the von Karman MAP moment of 2.78 $\times$ 10^{18} Nm.

We find that the von Karman solution extends high slip right to the surface, in contrast with the Laplacian solution and many other geodetic studies for this earthquake (*Melgar et al.*, 2015, *Guangcai et al.*, 2015, *Wei et al.*, 2015, *Barnhart et al.*, 2015, *Floyd et al.*, 2016). Oversmoothing, as well as non-negativity in the inversion and lack of data near the fault have been found to result in a lack of slip at the surface and apparent shallow-slip deficit (*Xu et al.*, 2016). By solving for the degree of smoothing with the hyperparameter α^2 we speculate that the von Karman regularization could potentially resolve slip at the surface better in the Napa Valley earthquake. However, we note that it is hard to directly compare specifics of slip solutions between published studies since different studies use different fault geometry, including one fault (*Dreger et al.*, 2015, *Barnhart et al.*, 2015, *Zhang et al.*, 2015b, *Melgar et al.*, 2015), two straight faults (*Wei et al.*, 2015, *Ji et al.*, 2015) or a more complicated curved fault geometry such as we used here (*Guangcai et al.*, 2015, *Floyd et al.*, 2016).

These two different results show the bias that a regularization technique can cause.

3.6.2 Trade-offs

We examined trade-offs between different model parameters for the von Karman solution. First we computed the correlation coefficients between all the model parameters, using their full posterior PDFs (Appendix B Figure B.18). This identified some interesting behaviour which we explored further by examining the individual histograms. We find strong positive trade-offs between the five patches with the largest magnitude of slip. This is as expected because they are located close together, at distances smaller than the von Karman correlation lengths (Appendix B Figure B.19). We also examined the spatial distribution of slip and potential correlations. We found that there is no covariance between the patches with the highest slip on the south-western fault and patches with the highest slip on the north-eastern fault as shown in Appendix B Figure B.20. We also found no covariance between the patches with maximum slip on the south-western fault and patches along-strike from them (Appendix B Figure B.21). There is positive correlation between the magnitude of slip of patches down-dip from each other on the north-eastern fault (Appendix B Figure B.22), though not on patches farthest away from each other, indicating that this is largely due to the von Karman correlation.

The von Karman correlation acts on the magnitude of slip but it does not act upon the rake. We found that normal faulting sense of motion was required on the north-eastern fault to fit the InSAR in this area. In light of this, we consider the trade-offs between the normal-faulting sense of motion rake on this fault. We found that near

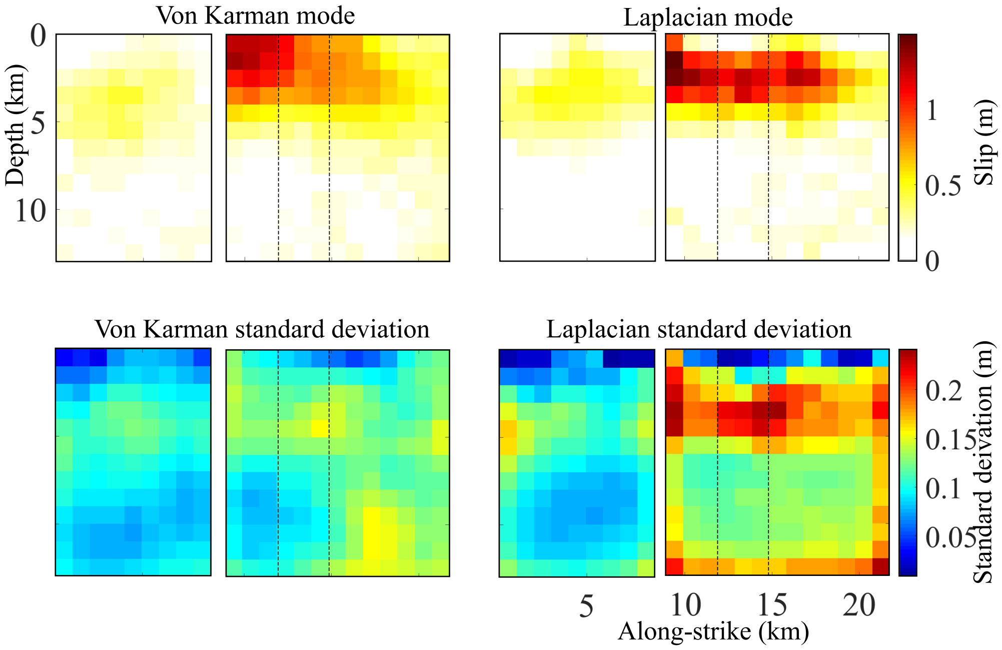

Figure 3.9: Results (mode) of a Bayesian inversion incorporating VK (left) and Laplacian (right) priors. The Laplacian solution has all edges as free; the solution is not forced to 0 m slip at any edge. Below, the standard deviation of each fault patch. The results are broadly similar in magnitude but vary in location, as the Laplacian extends slip along strike for the south-western fault (shown on the right) and puts higher slip on the north-eastern fault. The uncertainties are much higher for the Laplacian solution, as is evident from the higher standard deviations across the fault. For comparison the slip magnitude colourbar is the same as Figure 3.7.

the surface, the rake was well constrained to have normal faulting motion, up to the maximum of the rake prior, 270 degrees (Appendix B Figure B.23). At depth the rake is very poorly constrained and all of parameter space within the rake prior is almost equally searched. On the south-western fault we observed some oscillatory slip along-strike; the histograms in Appendix B Figure B.24 show that many patches display either no correlation or negative correlation with the rake of a patch next to them, but show either no correlation or positive correlation with a patch two along. This indicates that patches next to each other are anti- correlated and so we observe an oscillation in rake along the fault.

From our trade-off analysis, the main influence on magnitude of slip magnitude for any given patch is that of its nearest neighbours, as is to be expected from von Karman regularization. Rake shows some oscillatory behaviour, with the rake of a patch likely to be anticorrelated to the rake of its immediate neighbours along-strike, and positively correlated to rake on those patches that are separated along-strike by a single patch.

3.6.3 Slip at the step-over

Our fault geometry includes a step-over, with the rupture originating at the hypocenter at 11 km depth on the south-western fault and propagating to the northwest (*Wei et al.*, 2015). Strike-slip earthquakes have often been found to stop at such step-overs (*Wesnousky*, 2006), and how earthquake rupture is able to propagate through complicated geometry and across step-overs like these is important in understanding why earthquake ruptures stop, and subsequently for seismic hazard. We investigated the trade-offs at the overlap area of the two faults. The faults overlap by over 5 km but are separated by approximately 1.5 km at the maximum separation, which is in keeping with observations of overlap and separation for echelon strike-slip faults, which are themselves self-similar (*Aydin and Schultz*, 1990). We impose von Karman regularization separately on the two faults, so any form of correlation is independent of regularization. We find that there is a negative correlation between the two fault strands: where there is high slip on the south-western fault there is low slip on the north-eastern strand (Appendix B Figure B.25). There is also a change in rake, with the south-western fault undergoing primarily right-lateral slip motion, whereas the north-eastern fault displays largely normal fault motion, which is required to fit the InSAR to the north-east of the surface rupture.

This negative correlation means that there is a sharp drop in slip from one fault to the other. Observations of slip magnitude at step overs suggests that an abrupt decrease in slip magnitude at the step over makes the rupture more likely to continue to rupture on the other side (*Elliott et al.*, 2009), as does the proximity of two faults (*Wesnousky*, 2006), both of which we observe in this study. This proximity also means that stress may increase or decrease on one fault due to failure of the other, made more complicated by their overlap and curved geometry of the south-western fault. This interaction between the faults affects how fault systems grow (*Cowie*, 1998) and simplify over time (*Wesnousky*, 1988). The significantly lower slip on the north-eastern fault may suggest that whilst the rupture was able to cross this geometrical complexity the earthquake rupture may have been impeded by it, as has frequently been documented and modeled at step overs (*Wesnousky*, 1988, *Harris and Day*, 1993).

We note that this interpretation is affected by our assumption to treat the two faults as independent, and not smooth between them. We have also assumed that they remain as separate faults at depth and do not merge.

3.6.4 Fault parameterisation - fault size

In contrast to the Laplacian smoothness constraint, the von Karman constraint penalises regions of zero slip. If the modeled fault plane is larger than the area that actually slipped, a Laplacian smoothed solution would give a high probability to zero slip in regions that are not well resolved as long as the solution is smooth, whereas the von Karman correlation would give greater probability to non-zero slip in these areas. This is because regions of zero slip have 100% correlation at all distances, which is inconsistent with a VK distribution. This is particularly a problem at depth or when lack of data mean resolution is poor elsewhere. Ideally only areas that actually slipped should be included in a von Karman constrained inversion.

Additionally, choice of fault dimensions in a von Karman slip inversion affects the correlation lengths (empirical Equations 3.4 and 3.5 include fault length and width). In the case of the Napa Valley earthquake we could constrain the fault geometry due to an abundance of mapped surface rupture (*Hudnut et al.*, 2014) but if a rupture does not break the surface then some constraint on length must be adopted, such as the distribution of aftershocks. Any vastly incorrect estimation of fault length and therefore correlation parameters at this initial stage has the potential to bias the results of the inversion.

The correlation lengths themselves are empirical scaling relations with their own uncertainty for any particular fault size, and so ideally these would be drawn from their prior distribution, as discussed in *Mai and Beroza* (2002).

Solving for fault length and correlation parameters during the inversion would solve these issues. This would mean that throughout an MCMC chain the size of the fault would increase or decrease in length and width, and correlation parameters would be drawn from a normal distribution, centered on the value for the current length and width. This would require recalculating the correlation matrix, Σ_s which adds computational expense, and solving for fault size this would transform the inversion into a transdimensional problem (e.g. *Dettmer et al.* 2014). We leave the implementation of this to future work.

3.6.5 Fault parameterisation - number of slip patches

In this paper we have chosen the slip patches to be approximately 1km × 1km in size. In the literature there is very little consistency in choosing the number or dimension of these patches, and they range from being less than 1km in length up to greater than 25km, rectangular or triangular, with up to thousands of patches. The choice of patch size should be based on model resolving power (e.g. *Page et al.* 2009) as determined by the data and, particularly for Bayesian inversions, computational expense.

If a fault is divided into more patches than can be resolved by the data, this model will give an artificial level of detail. But if too few patches are used on a fault, then the data will be poorly fit and the model unrepresentative.

In order to correctly parameterise the model, methods include determining the size of the patches to reflect the resolving power of surface displacements (*Barnhart and Lohman*, 2010, *Atzori and Antonioli*, 2011) before commencing an inversion. Other methods include using self-adapting grids that change patch size and number throughout the inversion (*Dettmer et al.*, 2014).

As a simple test to compare the effect of the number of slip patches, we solved for the Napa earthquake using exactly the same inversion parameters as the von Karman inversion above, but with each patch twice as long and twice as wide. Figure 3.10 shows that the solution has a similar location of peak slip as the von Karman inversion on the full fault, but the moment is 2.77×10^{18} Nm which is also significantly bigger than the USGS moment of 1.33×10^{18} Nm but roughly the same as the von Karman regularized solutions.

We also solve for von Karman regularization across the entire fault with moment regularization, using a Gaussian prior with a mean of the USGS moment of 1.33×10^{18} Nm and a standard deviation of 1.07×10^{17}. Here we found the MAP result gives a moment of 2.43×10^{18} Nm which is still significantly larger than the USGS moment of 1.33×10^{18} Nm, though closer to the USGS value than the von Karman regularization with smaller slip patches. Other geodetic studies also found moments larger than the USGS moment; the study by *Guangcai et al.* (2015) found a value of 2.07×10^{18} Nm and the study by *Floyd et al.* (2016) found a value of 1.67×10^{18} Nm. Some of this difference to the USGS moment may be due to the documented differences between geodetic and seismically derived moment (*Weston et al.*, 2011), as well as to the 7 days of postseismic deformation present in the InSAR and GPS data (e.g. *Floyd et al.* 2016).

3.6.6 Solving for smoothing parameters

The von Karman distribution is determined by three parameters: the Hurst parameter and along-strike and down-dip correlation coefficients. Here we have used the average value for strike slip faults determined by *Mai and Beroza* (2002) rather then solving for them and for the synthetic tests have used the same correlation lengths for generating

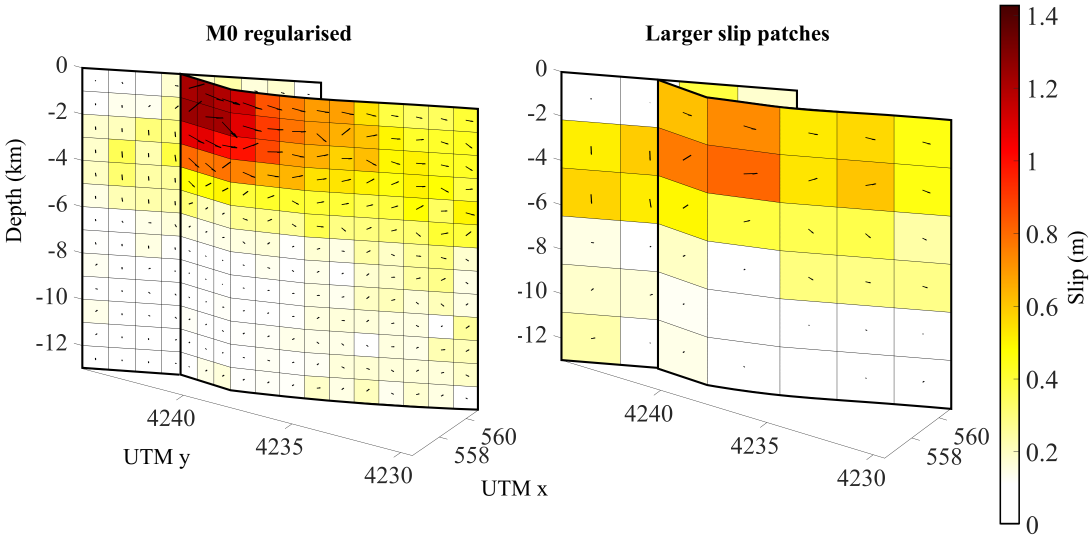

Figure 3.10: The mode results of Bayesian inversions for the Napa earthquake using von Karman regularization and moment regularization (left) or bigger slip patches (right). For direct comparison the scalebar is the same as Figure 3.7.

the input slip distributions and for the inversion. An incorrect assumption of correlation lengths is likely to bias model results, and in future work, to be as objective as possible, we propose to solve for them as hyperparameters with priors constrained by the full distribution determined by *Mai and Beroza* (2002).

There is evidence that faults become smoother with increasing slip (*Sagy et al.*, 2007, *Brodsky et al.*, 2011) due to fault maturity. This can be characterized using the Hurst parameter, which has been carried out for several exhumed fault surfaces (*Candela et al.*, 2011, *Bistacchi et al.*, 2011, *Candela et al.*, 2012). Prior knowledge of the Hurst parameter or the degree of maturity of a particular fault could therefore help constrain the Hurst parameter in slip inversions better. Alternatively, solving for correlation coefficients and the Hurst parameter within the slip inversion could be used to estimate the smoothness of active faults are, and consequently their maturity. This could be tested on faults of known age.

3.7 Conclusion

In light of all the evidence suggesting earthquake slip shows fractal properties we suggest that von Karman regularization should be the default for slip inversions in the future. Our tests show that even if the underlying slip were not fractal, von Karman regularization does at least as well as the commonly-used Laplacian regularization. We have developed a method to solve for earthquake slip inversion in a Bayesian sense, with the capability of incorporating von Karman, Laplacian or no smoothing and with the potential to add other spatial constraints in the future. MCMC models are more computationally expensive than some other inversion algorithms, but enable us to fully capture the plethora of model solutions that fit the prior and data, and characterize the uncertainties and trade-offs between parameters. We have made the search more efficient by using two steps in the MCMC chain and adapting parameter step size as the inversion proceeds. We find that a Laplacian smoothed inversion places slip in different locations to von Karman regularization for the Napa Valley earthquake and and the von Karman solution gives much tighter confidence bounds on slip. We argue that this tighter confidence represents an important improvement on the solution, since the tighter constraint is arises from the self-similar prior we are imposing which is based on observational evidence. We therefore suggest that von Karman regularization is a better constraint since it is capable of capturing the self-affine properties of coseismic slip.

3.8 Acknowledgments

This work was supported by the Leeds-York Doctoral Training Partnership (DTP) of the Natural Environmental Research Council (NERC) and COMET, the NERC Centre for Observation and Modelling of Earthquakes, Volcanoes and Tectonics. Some figures were prepared using the public domain GMT software (*Wessel and Smith*, 1991). We are grateful to Tim Wright, Jessica Hawthorne, Laura Gregory and Tom Ingleby for useful discussions, as well as to Martin Mai, two anonymous reviewers, Editor Yehuda Ben-Zion and Associate Editor Yoshihiro Kaneko for their helpful and constructive reviews that greatly improved this manuscript. Data and scripts available at `https://doi.org/10.5518/444` and `https://doi.org/10.5518/445`

References

Atzori, S., and A. Antonioli (2011), Optimal fault resolution in geodetic inversion of coseismic data, *Geophysical Journal International*, *185*(1), 529–538, doi:10.1111/j.1365-246X.2011.04955.x. 3.6.5

Aviles, C. A., C. H. Scholz, and J. Boatwright (1987), Fractal Analysis Applied to Characteristic Segments of the San Andreas Fault, *Journal of Geophysical Research*, *92*(B1), 331, doi:10.1029/JB092iB01p00331. 3.2

Avouac, J.-P., L. Meng, S. Wei, T. Wang, and J.-P. Ampuero (2015), Lower edge of locked Main Himalayan Thrust unzipped by the 2015 Gorkha earthquake, *Nature Geoscience*, *8*(9), 708–711, doi:10.1038/ngeo2518. 3.2

Aydin, A., and R. Schultz (1990), Effect of mechanical interaction on the development of strike-slip faults with echelon patterns, *Journal of Structural Geology*, *12*(1), 123–129, doi:10.1016/0191-8141(90)90053-2. 3.6.3

Barnhart, W. D., and R. B. Lohman (2010), Automated fault model discretization for inversions for coseismic slip distributions, *Journal of Geophysical Research*, *115*(B10), B10,419, doi:10.1029/2010JB007545. 3.6.5

Barnhart, W. D., J. R. Murray, S. Yun, J. L. Svarc, S. V. Samsonov, E. J. Fielding, B. A. Brooks, and P. Milillo (2015), Geodetic Constraints on the 2014 M 6.0 South Napa Earthquake, *Seismological Research Letters*, *86*(2), 335–343, doi:10.1785/0220140210. 3.5.3, 3.6.1

Bekaert, D. P. S., P. Segall, T. J. Wright, and A. J. Hooper (2016), A Network Inversion Filter combining GNSS and InSAR for tectonic slip modeling, *Journal of Geophysical Research: Solid Earth*, *121*, 2069–2086, doi:10.1002/2015JB012638. 3.5.1

Ben-Zion, Y. (2008), Collective behavior of earthquakes and faults: Continuum-discrete transitions, progressive evolutionary changes, and different dynamic regimes, *Reviews of Geophysics*, *46*(4), RG4006, doi:10.1029/2008RG000260. 3.2

Bistacchi, A., W. A. Griffith, S. A. F. Smith, G. Di Toro, R. Jones, and S. Nielsen (2011), Fault Roughness at Seismogenic Depths from LIDAR and Photogrammetric Analysis, *Pure and Applied Geophysics*, *168*(12), 2345–2363, doi:10.1007/s00024-011-0301-7. 3.6.6

Brodsky, E. E., J. J. Gilchrist, A. Sagy, and C. Collettini (2011), Faults smooth gradually as a function of slip, doi:10.1016/j.epsl.2010.12.010. 3.2, 3.6.6

Brown, S. R., and C. H. Scholz (1985), Broad Bandwidth Study of the Topography of Natural Rock Surfaces, *Journal of Geophysical Research*, *90*(B14), 12,575, doi:10.1029/JB090iB14p12575. 3.2

Bruhat, L., Z. Fang, and E. M. Dunham (2016), Rupture complexity and the supershear transition on rough faults, *Journal of Geophysical Research: Solid Earth*, *121*(1), 210–224, doi:10.1002/2015JB012512. 3.2

Campbell, G. E., R. T. Walker, K. Abdrakhmatov, J. Jackson, J. R. Elliott, D. Mackenzie, T. Middleton, and J. L. Schwenninger (2015), Great Earthquakes in Low-Strain-rate Continental Interiors: an Example from SE Kazakhstan, *Journal of Geophysical Research: Solid Earth*, *120*(8), 5507–5534, doi:10.1002/2015JB011925. 3.2

Candela, T., F. Renard, M. Bouchon, J. Schmittbuhl, and E. E. Brodsky (2011), Stress Drop during Earthquakes: Effect of Fault Roughness Scaling, *Bulletin of the Seismological Society of America*, *101*(5), 2369–2387, doi:10.1785/0120100298. 3.2, 3.6.6

Candela, T., F. Renard, Y. Klinger, K. Mair, J. Schmittbuhl, and E. E. Brodsky (2012), Roughness of Fault Surfaces over Nine Decades of Length Scales, *Journal of Geophysical Research*, *117*(B8), B08,409, doi:10.1029/2011JB009041. 3.2, 3.6.6

Cowie, P. A. (1998), A healingreloading feedback control on the growth rate of seismogenic faults, *Journal of Structural Geology*, *20*(8), 1075–1087, doi:10.1016/S0191-8141(98)00034-0. 3.6.3

Curran, P. (1988), The semivariogram in remote sensing: An introduction, *Remote Sensing of Environment*, *24*(3), 493–507, doi:10.1016/0034-4257(88)90021-1. 3.5.1

Dettmer, J., R. Benavente, P. R. Cummins, and M. Sambridge (2014), Trans-dimensional finite-fault inversion, *GJI Seismology*, *199*, 735–751, doi:10.1093/gji/ggu280. 3.6.4, 3.6.5

Dolan, S., C. Bean, and B. Riollet (1998), The broad-band fractal nature of heterogeneity in the upper crust from petrophysical logs, *Geophysical Journal International*, *132*(3), 489–507, doi:10.1046/j.1365-246X.1998.00410.x. 3.2

Dreger, D. S., M.-H. Huang, A. Rodgers, T. Taira, and K. Wooddell (2015), Kinematic Finite-Source Model for the 24 August 2014 South Napa, California, Earthquake from Joint Inversion of Seismic, GPS, and InSAR Data, *Seismological Research Letters*, *86*(2A), 327–334, doi:10.1785/0220140244. 3.5.3, 3.6.1

Elliott, A. J., J. F. Dolan, and D. D. Oglesby (2009), Evidence from coseismic slip gradients for dynamic control on rupture propagation and arrest through stepovers, *Journal of Geophysical Research*, *114*(B2), B02,313, doi:10.1029/2008JB005969. 3.6.3

Elliott, J. R., A. J. Elliott, A. J. Hooper, Y. Larsen, P. Marinkovic, and T. J. Wright (2015), Earthquake Monitoring Gets Boost from New Satellite, *EOS*, *96*, doi:10.1029/2015EO023967. 3.2

Evans, E. L., and B. J. Meade (2012), Geodetic Imaging of Coseismic Slip and Post-seismic Afterslip: Sparsity Promoting Methods Applied to the Great Tohoku Earthquake, *Geophysical Research Letters*, *39*(11), doi:10.1029/2012GL051990. 3.2

Fang, Z., and E. M. Dunham (2013), Additional shear resistance from fault roughness and stress levels on geometrically complex faults, *Journal of Geophysical Research: Solid Earth*, *118*(7), 3642–3654, doi:10.1002/jgrb.50262. 3.2

Fisher, D. S., K. Dahmen, S. Ramanathan, and Y. Ben-Zion (1997), Statistics of Earthquakes in Simple Models of Heterogeneous Faults, *Physical Review Letters*, *78*(25), 4885–4888, doi:10.1103/PhysRevLett.78.4885. 3.2

Floyd, M. A., R. J. Walters, J. R. Elliott, G. J. Funning, J. L. Svarc, J. R. Murray, A. J. Hooper, Y. Larsen, P. Marinkovic, R. Bürgmann, I. A. Johanson, and T. J. Wright (2016), Spatial variations in fault friction related to lithology from rupture and afterslip of the 2014 South Napa, California, earthquake, *Geophysical Research Letters*, *43*(13), 6808–6816, doi:10.1002/2016GL069428. 3.2, 3.5.1, 3.5.2, 3.5.3, 3.5.3, 3.6.1, 3.6.5

Foody, G., and M. Atkinson (2002), *Uncertainty in Remote Sensing and GIS*, 100–101 pp. 3.5.1

Fukuda, J., and K. M. Johnson (2008), A Fully Bayesian Inversion for Spatial Distribution of Fault Slip with Objective Smoothing, *Bulletin of the Seismological Society of America*, *98*(3), 1128–1146, doi:10.1785/0120070194. 3.3.1, 3.3.1, 3.3.2

Funning, G. J., R. M. Barke, S. H. Lamb, E. Minaya, B. Parsons, and T. J. Wright (2005), The 1998 Aiquile, Bolivia earthquake: A seismically Active Fault Revealed with InSAR, *Earth and Planetary Science Letters*, *232*(1-2), 39–49, doi:10.1016/j.epsl.2005.01.013. 3.2

Guangcai, F., L. Zhiwei, S. Xinjian, X. Bing, and D. Yanan (2015), Source parameters of the 2014 Mw 6.1 South Napa earthquake estimated from the Sentinel 1A , COSMO-SkyMed and GPS data, *Tectonophysics*, *655*, 139–146, doi:10.1016/j.tecto.2015.05.018. 3.5.3, 3.5.3, 3.6.1, 3.6.5

Gutenberg, B., and C. F. Richter (1955), Magnitude and Energy of Earthquakes, *Nature*, *176*, 795, doi:10.1038/176795a0. 3.2

Hanssen, R. F. (2001), *Radar interferometry : data interpretation and error analysis*, 140–141 pp., Kluwer Academic. 3.5.1

Harris, R. A., and S. M. Day (1993), Dynamics of fault interaction: parallel strike-slip faults, *Journal of Geophysical Research: Solid Earth*, *98*(B3), 4461–4472, doi:10.1029/92JB02272. 3.6.3

Harris, R. A., and P. Segall (1987), Detection of a Locked Zone at Depth on the Parkfield, California, Segment of the San Andreas Fault, *Journal of Geophysical Research*, *92*(B8), 7945, doi:10.1029/JB092iB08p07945. 3.2

Hastings, W. (1970), Monte Carlo sampling methods using Markov chains and their applications, *Biometrika*, *57*(1), 97–109, doi:doi.org/10.1093/biomet/57.1.97. 3.3.1

Hooper, A. J. (2012), Earthquake Slip Distribution Estimation, using a Random Vector Approach, *AGU Fall Meeting Abstracts*, *-1*, 08. 3.3.1

Hooper, A. J., J. Pietrzak, W. Simons, H. Cui, R. Riva, M. Naeije, A. Terwisscha van Scheltinga, E. Schrama, G. Stelling, and A. Socquet (2013), Importance of Horizontal Seafloor Motion on Tsunami Height for the 2011 Mw=9.0 Tohoku-Oki Earthquake, *Earth and Planetary Science Letters*, *361*, 469–479, doi:10.1016/j.epsl.2012.11.013. 3.3.1, 3.3.6

Hudnut, K., T. Brocher, C. Prentice, J. Boatwright, B. Brooks, B. T. Aagaard, J. Blair, J. Fletcher, J. Erdem, C. Wicks, J. Murray, F. Pollitz, J. Langbein, J. Svarc, D. Schwartz, D. Ponti, S. Hecker, S. DeLong, C. Rosa, B. Jones, R. Lamb, A. Rosinski, T. McCrink, T. Dawson, G. Seitz, R. Rubin, C. Glennie, D. Hauser, T. Ericksen, D. Mardock, D. Hoirup, and J. Bray (2014), Key Recovery Factors for the August 24, 2014, South Napa Earthquake, *Tech. rep.*, U.S. Geological Survey Open-File Report 2014-1249, doi:2331-1258 (online). 3.5, 3.5, 3.5.2, 3.5.3, 3.6.4

Ji, C., R. J. Archuleta, and C. Twardzik (2015), Rupture History of 2014 M w 6.0 South Napa Earthquake Inferred from Near-fault Strong Motion Data and its Impact to the Practice of Ground Strong Motion Prediction, *Geophysical Research Letters*, *42*(7), 2149–2156, doi:10.1002/2015GL063335. 3.6.1

Jolivet, R., Z. Duputel, B. Riel, M. Simons, L. Rivera, S. E. Minson, H. Zhang, M. A. G. Aivazis, F. Ayoub, S. Leprince, S. Samsonov, M. Motagh, and E. J. Fielding (2014), The 2013 Mw 7.7 Balochistan Earthquake: Seismic Potential of an Accretionary Wedge, *Bulletin of the Seismological Society of America*, *104*(2), 1020–1030, doi:10.1785/0120130313. 3.2

Kanamori, H., and D. L. Anderson (1975), Theoretical Basis of Some Empirical Relations in Seismology, *Bulletin of the Seismological Society of America*, *65*(5), 1073–1095. 3.2

Lindsey, E. O., and Y. Fialko (2016), Geodetic constraints on frictional properties and earthquake hazard in the Imperial Valley, Southern California, *Journal of Geophysical Research: Solid Earth*, *121*(2), 1097–1113, doi:10.1002/2015JB012516. 3.2

Lohman, R. B., and M. Simons (2005), Some Thoughts on the use of InSAR Data to Constrain Models of Surface Deformation: Noise Structure and Data Downsampling, *Geochemistry, Geophysics, Geosystems*, *6*(1), doi:10.1029/2004GC000841. 3.4.1, 3.5.1

Lorito, S., F. Romano, S. Atzori, X. Tong, A. Avallone, J. McCloskey, M. Cocco, E. Boschi, and A. Piatanesi (2011), Limited overlap between the seismic gap and coseismic slip of the great 2010 Chile earthquake, *Nature Geoscience*, *4*(3), 173–177, doi:10.1038/ngeo1073. 3.2

Mai, P. M., and G. C. Beroza (2002), A Spatial Random Field Model to Characterize Complexity in Earthquake Slip, *Journal of Geophysical Research*, *107*(B11), 2308, doi:10.1029/2001JB000588. 3.2, 3.2, 3.1, 3.3.4, 3.3.4, 3.6.4, 3.6.6

Mai, P. M., D. Schorlemmer, M. Page, J. Ampuero, K. Asano, M. Causse, S. Custodio, W. Fan, G. Festa, M. Galis, F. Gallovic, W. Imperatori, M. Käser, D. Malytskyy, R. Okuwaki, F. Pollitz, L. Passone, H. N. T. Razafindrakoto, H. Sekiguchi, S. G. Song, S. N. Somala, K. K. S. Thingbaijam, C. Twardzik, M. van Driel, J. C. Vyas, R. Wang, Y. Yagi, and O. Zielke (2016), The EarthquakeSource Inversion Validation (SIV) Project, *Seismological Research Letters*, *87*(3), 690–708, doi:10.1785/0220150231. 3.4.2

Mai, P. M., M. Galis, K. K. S. Thingbaijam, J. C. Vyas, and E. M. Dunham (2017), Accounting for Fault Roughness in Pseudo-Dynamic Ground-Motion Simulations, *Pure and Applied Geophysics*, *174*(9), 3419–3450, doi:10.1007/s00024-017-1536-8. 3.2

Mandelbrot, B. B. (1983), *The Fractal Geometry of Nature*, Freeman. 3.2

Melgar, D., J. Geng, B. W. Crowell, J. S. Haase, Y. Bock, W. C. Hammond, and R. M. Allen (2015), Seismogeodesy of the 2014 M w 6.1 Napa Earthquake, California: Rapid Response and Modeling of Fast Rupture on a Dipping Strike-slip Fault, *Journal of Geophysical Research: Solid Earth*, *120*(7), 5012–5033, doi:10.1002/2015JB011921. 3.5.3, 3.6.1

Metropolis, N., A. W. Rosenbluth, M. N. Rosenbluth, A. H. Teller, and E. Teller (1953), Equation of State Calculations by Fast Computing Machines, *The Journal of Chemical Physics*, *21*(6), 1087–1092, doi:10.1063/1.1699114. 3.3.1

Milliner, C. W., J. F. Dolan, J. Hollingsworth, S. Leprince, F. Ayoub, and C. Sammis (2015), Quantifying Near-field and Off-fault Deformation Patterns of the 1992 M w 7.3 Landers Earthquake, *Geochemistry, Geophysics, Geosystems*, *16*(5), 1525–2027, doi:10.1002/2014GC005693. 3.2

Milliner, C. W. D., C. Sammis, A. A. Allam, J. F. Dolan, J. Hollingsworth, S. Leprince, and F. Ayoub (2016), Resolving Fine-Scale Heterogeneity of Co-seismic Slip and the Relation to Fault Structure, *Scientific Reports*, *6*, 27,201, doi:10.1038/srep27201. 3.2

Minson, S. E., M. Simons, and J. L. Beck (2013), Bayesian Inversion for Finite Fault Earthquake Source Models I–Theory and Algorithm, *Geophysical Journal International*, *194*(3), 1701–1726, doi:10.1093/gji/ggt180. 3.2, 3.3.6

Muto, J., T. Nakatani, O. Nishikawa, and H. Nagahama (2015), Fractal Particle Size Distribution of Pulverized Fault Rocks as a Function of Distance from the Fault Core, *Geophysical Research Letters*, *42*(10), 3811–3819, doi:10.1002/2015GL064026. 3.2

Okada, Y. (1985), Surface Deformation Due to Shear and Tensile Faults in a Half-space, *Bulletin of the Seismological Society of America*, *75*(4), 1135–1154. 3.3.5

Okubo, P. G., and K. Aki (1987), Fractal Geometry in the San Andreas Fault System, *Journal of Geophysical Research*, *92*(B1), 345, doi:10.1029/JB092iB01p00345. 3.2

Oliver, M., and R. Webster (2014), A tutorial guide to geostatistics: Computing and modelling variograms and kriging, *CATENA*, *113*, 56–69, doi:10.1016/J.CATENA.2013.09.006. 3.5.1

Omori, F. (1894), On the aftershocks of earthquakes, *J. Coll. Sci. Imp. Univ. Tokyo*, *7*, 111 – 200. 3.2

Page, M. T., S. Custódio, R. J. Archuleta, and J. M. Carlson (2009), Constraining earthquake source inversions with GPS data: 1. Resolution-based removal of artifacts, *Journal of Geophysical Research: Solid Earth*, *114*(B1), doi:10.1029/2007JB005449. 3.6.5

Parsons, T., and D. L. Minasian (2015), Earthquake rupture process recreated from a natural fault surface, *Journal of Geophysical Research: Solid Earth*, *120*(11), 7852–7862, doi:10.1002/2015JB012448. 3.2

Passelègue, F. X., A. Schubnel, S. Nielsen, H. S. Bhat, D. Deldicque, and R. Madariaga (2016), Dynamic rupture processes inferred from laboratory micro-earthquakes, *Journal of Geophysical Research: Solid Earth*, doi:10.1002/2015JB012694. 3.2

Perrin, C., I. Manighetti, J.-P. Ampuero, F. Cappa, and Y. Gaudemer (2016), Location of largest earthquake slip and fast rupture controlled by alongstrike change in fault structural maturity due to fault growth, *Journal of Geophysical Research: Solid Earth*, doi:10.1002/2015JB012671. 3.2

Poon, C. Y., R. S. Sayles, and T. A. Jones (1992), Surface Measurement and Fractal Characterization of Naturally Fractured Rocks, *Journal of Physics D: Applied Physics*, *25*(8), 1269–1275, doi:10.1088/0022-3727/25/8/019. 3.2

Power, W. L., T. E. Tullis, and J. D. Weeks (1988), Roughness and Wear During Brittle Faulting, *Journal of Geophysical Research*, *93*(B12), 15,268, doi:10.1029/JB093iB12p15268. 3.2

Powers, P. M., and T. H. Jordan (2010), Distribution of Seismicity Across Strike-slip Faults in California, *Journal of Geophysical Research*, *115*(B5), B05,305, doi:10.1029/2008JB006234. 3.2

Renard, F., C. Voisin, D. Marsan, and J. Schmittbuhl (2006), High resolution 3D Laser Scanner Measurements of a Strike-slip Fault Quantify its Morphological Anisotropy at all Scales, *Geophysical Research Letters*, *33*(4), L04,305, doi:10.1029/2005GL025038. 3.2

Rice, J., and M. Cocco (2007), Seismic Fault Rheology and Earthquake Dynamics, *Tectonic Faults: Agents of Change on a Dynamic Earth*, pp. 99–137. 3.2

Roberts, G. O., A. Gelman, and W. R. Gilks (1997), Weak convergence and optimal scaling of random walk Metropolis algorithms, *The Annals of Applied Probability*, *7*(1), 110–120, doi:10.1214/aoap/1034625254. 3.3.6

Robertson, M. C., C. G. Sammis, M. Sahimi, and A. J. Martin (1995), Fractal Analysis of Three-dimensional Spatial Distributions of Earthquakes with a Percolation Interpretation, *Journal of Geophysical Research*, *100*(B1), 609, doi:10.1029/94JB02463. 3.2

Sagy, A., E. E. Brodsky, and G. J. Axen (2007), Evolution of Fault-surface Roughness with Slip, *Geology*, *35*(3), 283, doi:10.1130/G23235A.1. 3.2, 3.6.6

Sambridge, M., J. L.R., M. E.L., T. A.H., and T. E. (1999), Geophysical inversion with a neighbourhood algorithm-II. Appraising the ensemble, *Geophysical Journal International*, *138*(3), 727–746, doi:10.1046/j.1365-246x.1999.00900.x. 3.3.1

Shi, Z., and S. M. Day (2013), Rupture dynamics and ground motion from 3-D rough-fault simulations, *Journal of Geophysical Research: Solid Earth*, *118*(3), 1122–1141, doi:10.1002/jgrb.50094. 3.2

Tarantola, A. (2005), *Inverse Problem Theory and Methods for Model Parameter Estimation*, chap. 2, pp. 50–52, Society for Industrial and Applied Mathematics, Philadelphia, doi:10.1137/1.9780898717921.ch2. 3.3.1, 3.3.2

USGS (2006), Quaternary Fault and Fold Database for the United States. 3.5

von Kármán, T. (1948), Progress in the Statistical Theory of Turbulence, *Proceedings of the National Academy of Sciences of the United States of America*, *34*(11), 530–9. 3.2

Walters, R. J., J. R. Elliott, N. D'Agostino, P. C. England, I. Hunstad, J. A. Jackson, B. Parsons, R. J. Phillips, and G. Roberts (2009), The 2009 L'Aquila Earthquake (Central Italy): A Source Mechanism and Implications for Seismic Hazard, *Geophysical Research Letters*, *36*(17), L17,312, doi:10.1029/2009GL039337. 3.2

Wang, L., S. Hainzl, and P. M. Mai (2015), Quantifying slip balance in the earthquake cycle: Coseismic slip model constrained by interseismic coupling, *Journal of Geophysical Research: Solid Earth*, *120*(12), 8383–8403, doi:10.1002/2015JB011987. 3.2

Wei, S., S. Barbot, R. Graves, J. J. Lienkaemper, T. Wang, K. Hudnut, Y. Fu, and D. Helmberger (2015), The 2014 Mw 6.1 South Napa Earthquake: A Unilateral Rupture with Shallow Asperity and Rapid Afterslip, *Seismological Research Letters*, *88*(5). 3.5.3, 3.6.1, 3.6.3

Wesnousky, S. (1988), Seismological and structural evolution of strike-slip faults, *Nature*, *335*, 340–343, doi:10.1038/335340a0. 3.6.3

Wesnousky, S. (2006), Predicting the endpoints of earthquake ruptures, *Nature*, *444*, 358–360, doi:10.1038/nature05275. 3.6.3

Wessel, P., and W. H. F. Smith (1991), Free Software Helps Map and Display Data, *EOS Trans. AGU*, *72*, 441. 3.8

Weston, J., A. M. Ferreira, and G. J. Funning (2011), Global compilation of interferometric synthetic aperture radar earthquake source models: 1. Comparisons with seismic catalogs, *Journal of Geophysical Research*, *116*(B8), B08,408, doi:10.1029/2010JB008131. 3.3.4, 3.6.5

Wright, T. J. (2003), Source Model for the M w 6.7, 23 October 2002, Nenana Mountain Earthquake (Alaska) from InSAR, *Geophysical Research Letters*, *30*(18), 1974, doi:10.1029/2003GL018014. 3.2

Xu, X., X. Tong, D. T. Sandwell, C. W. Milliner, J. F. Dolan, J. Hollingsworth, S. Leprince, and F. Ayoub (2016), Refining the shallow slip deficit, *Geophysical Journal International*, *204*(3), 1843–1862, doi:10.1093/gji/ggv563. 3.6.1

Zhang, L., P. M. Mai, K. K. Thingbaijam, H. N. Razafindrakoto, and M. G. Genton (2015a), Analysing earthquake slip models with the spatial prediction comparison test, *Geophysical Journal International*, *200*(1), 185–198, doi:10.1093/gji/ggu383. 3.4.2

Zhang, Y., R. Wang, and Y.-T. Chen (2015b), Stability of rapid finite-fault inversion for the 2014 Mw6.1 South Napa earthquake, *Geophysical Research Letters*, *42*(23), 10,263–10,272, doi:10.1002/2015GL066244. 3.5.3, 3.6.1

Chapter 4

Solving for Fault Size and Fractal Slip in a Bayesian Inversions

The work in this chapter has been submitted for publication in the Journal of Geophysical Research.

4.1 Abstract

Many earthquake properties, including slip, show self-similar (fractal) features. We can incorporate self-similarity into Bayesian slip inversions via von Karman correlation, so that the regularization applied is representative of observed fault features. In von Karman regularisation, each slip patch has a relationship to every other patch. This means that von Karman regularisation only has meaning when applied to patches that actually slipped; if applied to non-slipping patches, spurious slip can be added to meet the von Karman correlation criteria. Additionally the fault size, usually chosen in advance, also affects the von Karman correlation lengths meaning that the final slip solution may be biased by initial geometry choices. Here we present a method for solving for the size of the fault plane during the slip inversion process, as well as slip, rake and a hyperparameter controlling slip variance. We use a trans-dimensional Bayesian inversion scheme constrained by geodetic surface displacements and regularized using von Karman correlation. We use circular harmonics to solve for the size of the slipping area, to allow for a complex shape that is connected and continuous across the fault. We apply this method to the 2016 M$_w$ 6.2 Central Tottori earthquake, Japan, constrained by InSAR (Sentinel-1, ALOS-2) and GNSS data. We find an area of slip at approximately 8 km depth, with the slipping area elongated in the down-dip direction. In contrast to some seismic studies we find slip ruptured most of the seismogenic layer.

4.2 Introduction

Assumptions incorporated into coseismic slip inversions should be realistic and justifiable for resulting slip distributions to be useful. Every prior assumption changes the final slip distribution, which is one of the reasons behind variability between slip results for the same earthquake (*Minson et al.*, 2013). Most commonly used regularization techniques simply satisfy mathematical constraints (e.g. the Laplacian or minimum norm) and have no physical basis in how faults are seen to behave in nature. Consequently they may bias the result.

There are several aspects of earthquakes that display fractal properties, which mathematically equates to a behaviour following a power law function. Many recent papers suggest that earthquake slip also shows fractal properties. This includes measurements of surface coseismic slip e.g. *Milliner et al.* (2015), analysis of published finite fault inversions (*Mai and Beroza*, 2002) and measurements of exhumed fault surface roughness e.g. *Candela et al.* (2012). We therefore suggest that fractal slip properties should be incorporated into slip inversions, as this approach can better capture the physical properties of faults than other regularisation techniques (*Amey et al.*, 2018).

Mai and Beroza (2002)'s meta-analysis showed that the von Karman autocorrelation function best describes the long-order correlation of earthquake slip along a fault plane. Unlike a fractal correlation, which is only described by one variable (fractal dimension, D), the von Karman correlation is controlled by the Hurst parameter, H, which is related to the fractal dimension by $D =$ (Euclidian dimension *+ 1 -* H), and additionally two correlation lengths. The von Karman correlation power decays more slowly at small wavenumbers and also captures the self-affine nature of slip through different correlation lengths in the along-strike and down-dip directions.

We therefore regularise our inversions using von Karman correlation as a prior assumption. The von Karman autocorrelation function is given by:

$$\Sigma_s = \frac{G_H(r/a)}{G_H(0)} \tag{4.1}$$

Where r is the distance between slip patches, a is the correlation length used to scale this distance, H is the Hurst parameter and $G_H(r/a) = (r/a)^H K_H(r/a)$ where K_H is a modified Bessel function of the second kind, of order H (*Mai and Beroza*, 2002).

We have developed a code, *slipBERI* (*slip* from *B*ay*E*sian *R*egularised *I*nversion, with availability detailed in acknowledgments), to solve for slip in a Bayesian sense using von Karman regularisation whilst simultaneously solving for rake and a hyperparameter that controls the degree of regularisation.

A complication with von Karman regularisation is that it is dependent on the choice of fault size in two ways. First, the empirically derived along-strike and down-dip correlation lengths, a_{as} and a_{dd}, which are used to calculate scaled distance r/a, depend on fault length and fault width respectively (*Mai and Beroza*, 2002). Second, unlike in Laplacian smoothing, where each discrete patch only has a relationship with its neighbouring patches, with von Karman regularization each patch has a relationship with every patch. Whilst this can provide a useful constraint for areas of the fault that are more poorly resolved than patches at the surface, it can result in patches that are almost in the model null space being assigned slip just to satisfy the von Karman regularization. This is particularly a problem at depth, where assigning slip may have little effect on the surface observations, and therefore little affect on the likelihood, but can increase the von Karman prior probability. Multiple patches with zero slip do not satisfy von Karman autocorrelation; if a chosen fault is larger than the area that slipped then there should be zero slip around the edges, but this would lead to patches both near and far having 100% correlation, which the von Karman constraint prevents, and so a small amount of slip is placed there instead. This slip at depth is not representative of earthquake processes and instead is an artifact of the regularisation. Consequently the von Karman constraint introduces a bias in the inversion if applied to patches which are not slipping.

Here we present an algorithm for solving for the size of the slipping area within a Bayesian inversion. We do this using a trans-dimensional MCMC (Markov Chain Monte Carlo) approach (*Green*, 1995) that uses circular harmonics to control the shape, size and orientation of the slipping area whilst ensuring it is continuous.

We apply this inversion technique to the Mw 6.2 Central Tottori, Japan, earthquake (Figure 1). This occurred on the 21st October 2016 and was a strike-slip earthquake with a small normal component. We use InSAR (Interferometric Synthetic Aperture Data) data acquired by Sentinel-1 and ALOS-2, and GNSS (Global Navigation Satellite System) data to constrain the surface displacements. Following the earthquake, ALOS-2 acquired extra acquisitions in a left-looking mode in addition to the normal right-looking acquisitions, for both ascending and descending orbits. These data combined with GNSS give high resolution displacement measurements for this earthquake. During the inversion we solve for the size of the fault plane as well as slip and rake of each patch, the reference displacement of every interferogram and a hyperparameter controlling the extent of smoothing. Finally, we present the slip results, and comment on seismic hazard in this region.

4.3 Methods

4.3.1 Model Set Up

Initially we choose a fault size with fixed strike and dip, using InSAR results and aftershock locations, and extend it along-strike and down-dip to make it larger than

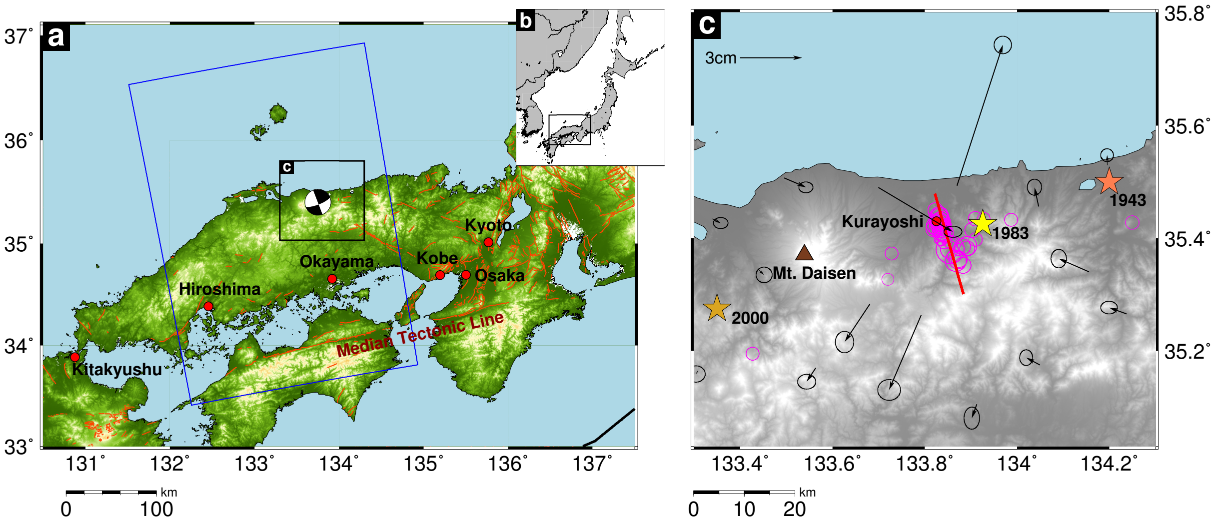

Figure 4.1: Regional setting of the Central Tottori earthquake. Insert *a*) shows tectonic context of this earthquake (area of Japan shown in insert *b*)). Onshore faults in the region shown in dark orange from Research Group for Active Faults of Japan (*RGAFJ*, 1991), and the focal mechanism for the 2016 M_w 6.2 earthquake. Inset *c*) shows aftershocks (open, magenta circles) and GNSS from the earthquake and past large earthquakes in the area (coloured stars). Also shown is Mount Daisen (brown triangle) and the location of the city Kurayoshi (red circle). Our modeled fault is shown in red, based on InSAR and aftershock locations. One month of aftershocks from *NIED (National Research Institute for Earth Science and Disaster Resilience)* (2018) K-NET and KiK-net and GNSS from GEONET.

the likely area that actually slipped. We break the fault-plane down into equally sized rectangular patches and solve separately for slip magnitude and rake for each fault patch. We also solve for a hyperparameter, α^2, which we discuss further in section 4.3.2, a constant offset for each of the InSAR scenes, equivalent to the displacement of the reference point, and circular harmonics terms, which are discussed below. Although we fix strike and dip in the inversions presented here, they can also be solved for as extra model parameters if necessary.

Parameterising fault size with circular harmonics

Having chosen in advance a fault plane that is expected to be too large, we then permit patches to turn ‘on’ or ‘off’ during the inversion. To ensure a continuous slipping area we use circular harmonics, the 2D version of spherical harmonics, to define the area; patches within this area are permitted to slip and those outside are considered to have zero slip. A patch is ‘on’ if its center lies within slipping and area, and ‘off’ otherwise. We use the first four terms of the circular harmonic expansions. For convenience, rather than solving for both positive and negative harmonics, we solve for the coefficient (size) and a rotation parameter, ϕ, for each harmonic. We also solve for the x and y location of the centre of slipping area relative to the top-left of the fault (Figure 4.2).

We calculate the length and width of the slipping area defined by the harmonics,

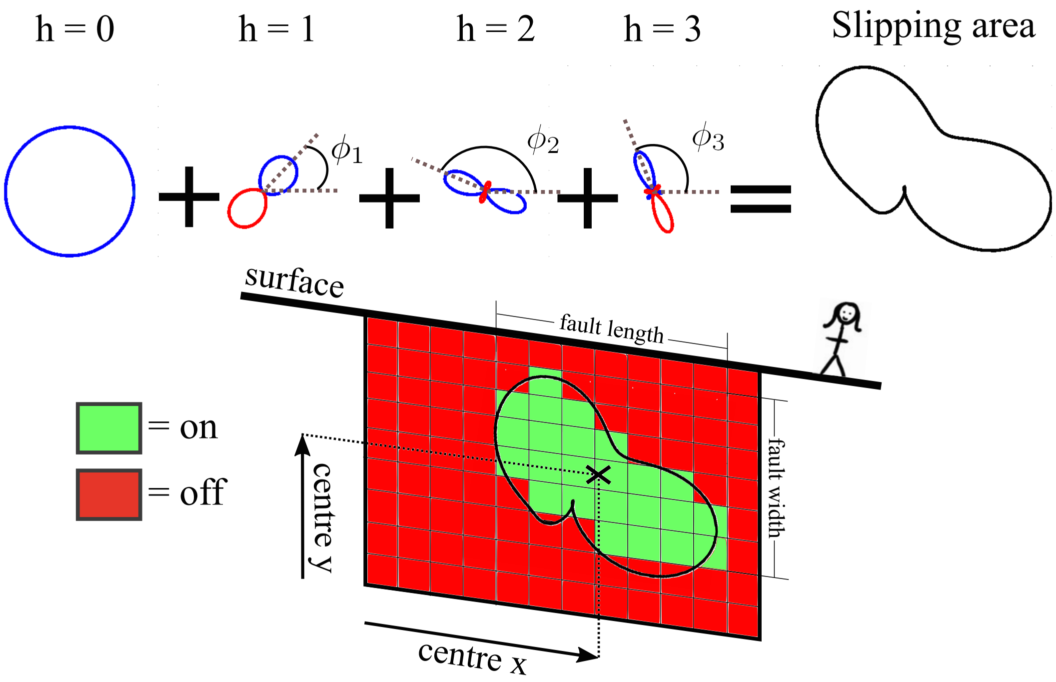

Figure 4.2: We use the first four terms of the circular harmonic expansion to define a slipping area on a fault plane. Patches within this slipping area are 'on' and are permitted to slip, those outside are 'off' and are considered to have zero slip. A patch is 'on' if its centre is within the slipping area. We solve for the coefficients (size) of each harmonic, as well as the rotation, ϕ, and x, y location of the centre of this slipping area on the fault plane.

which feeds into equations used for calculating the von Karman probability, discussed in Section 4.3.2.

We begin our inversion, described below, with the maximum permitted zero-order harmonic, such that the entire fault is ‘on’ at the start of the inversion.

4.3.2 Bayesian slip inversion

We use a Bayesian approach as it allows us to incorporate prior assumptions on the model parameters, including the von Karman nature of slip. Also the solution gives a suite of the models that fit the data within an acceptable level, allowing the quantification of the errors and trade-offs between model parameters. It is also a flexible framework that allows us to easily incorporate features such as solving for the number of model parameters.

We have previously presented our method for solving for slip incorporating the von Karman regularisation (*Amey et al.*, 2018). Here we modify our scheme to allow for a variable number of slipping patches.

A Bayesian inversion aims to update the joint prior probability density function (PDF) for all the model parameters (unknowns) given the data. Our knowledge of what the model parameters should be before commencing the inversion is represented as a joint prior PDF for all of the model parameters. Throughout the inversion, new trials are drawn for each parameter from their prior PDFs, then these prior PDFs are modified based on the likelihood (fit to data) to give the full posterior probability.

By Bayes’ theorem extended to density functions, the posterior probability density, $p(\mathbf{m}|\mathbf{d})$, of a model, $\mathbf{m}$, given a set of data, $\mathbf{d}$, is given by:

$$p(\mathbf{m}|\mathbf{d}) = \frac{p(\mathbf{d}|\mathbf{m})p(\mathbf{m})}{\int_{-\infty}^{\infty} p(\mathbf{d}|\mathbf{m})p(\mathbf{m})d\mathbf{m}} \tag{4.2}$$

Where $p(\mathbf{m})$ is the prior probability density of the model, which is the initial knowledge of the model parameters before commencing an inversion. $p(\mathbf{d}|\mathbf{m})$ is the likelihood density function, which captures how well the data can be fit by a current model (the probability of $\mathbf{d}$ given $\mathbf{m}$). The denominator, sometimes called ‘evidence’, is a normalising constant, as it is independent of the models (*Sambridge et al.*, 2006).

Some posterior PDF solutions can be determined analytically, but we cannot do this here as we solve for a hyperparameter, α^2, representing the variance of slip within the inversion (discussed further in section 4.3.2). Instead we must use some form of sampling to evaluate Equation 4.2 for different models. For a large number of model parameters, uniform sampling quickly becomes impractical and so we use MCMC sampling. MCMC sampling is a way to efficiently sample a target distribution (*Tarantola*, 2005). It is a memoryless chain, in which during each iteration a new trial is generated by perturbing only the current state. We use the Metropolis-Hastings rule (*Metropolis et al.*, 1953), to decide whether to accept each trial; a new trial is accepted if it is more probable, but also less probable new trials are accepted if the ratio of the probabilities (named the acceptance ratio) is greater than a random number drawn between 0 and 1. This allows the chain to extract itself from local maxima. Thus the chain moves and preferentially targets regions of parameter space with higher probabilities. Accepted trials are saved and new trials are drawn from the current model; rejected trials are discarded and the previous state is saved. At the end of the inversion, the initial samples are also discarded as these are still influenced by the starting position and do not properly represent the posterior, but rather the 'burn in'. The full posterior PDF is made up of all the saved trials.

The acceptance ratio, a, which is compared to a random number between 0 and 1 in the Metropolis-Hastings rule, for a new trial m' from perturbing m is given by (*Bodin and Sambridge*, 2009):

$$a(m'|m) = min[1, prior\ ratio \times likelihood\ ratio] \tag{4.3}$$

$$a(m'|m) = min[1, \frac{p(\mathbf{m'})}{p(\mathbf{m})} \times \frac{p(\mathbf{d}|\mathbf{m'})}{p(\mathbf{d}|\mathbf{m})}] \tag{4.4}$$

For a trans-dimensional case, extra terms must be considered in the acceptance ratio, meaning the full acceptance ratio is:

$$a(m'|m) = min[1, prior\ ratio \times likelihood\ ratio \times proposal\ ratio \times Jacobian] \tag{4.5}$$

$$a(m'|m) = min[1, \frac{p(\mathbf{m'})}{p(\mathbf{m})} \times \frac{p(\mathbf{d}|\mathbf{m'})}{p(\mathbf{d}|\mathbf{m})} \times \frac{q(\mathbf{m}|\mathbf{m'})}{q(\mathbf{m'}|\mathbf{m})} \times |J|] \tag{4.6}$$

Where the proposal distribution is the distribution from which a new sample is drawn and the role of the Jacobian, J, is to account for scale changes between m and m' (*Sambridge et al.*, 2006). For non-trans-dimensional inversions, the proposal distribution and Jacobian are equal to 1, but this cannot be assumed for an inversion that changes dimension.

In the following sections we describe each term in the acceptance ratio in turn and how they are calculated.

Prior

In our set-up the prior can be broken down as the product of the independent prior for each model parameter, for example the permitted range each model parameter can take, and the prior imposed by the von Karman constraint, used to ensure that the overall trials drawn represent a von Karman distribution.

Model Parameter Priors We define an independent prior probability distribution for each model parameter from which trials are drawn. We use boxcar priors for slip, rake and InSAR offset, meaning that we assign a constant probability in a permitted range and zero probability outside of that range. For the hyperparameter, α^2, we use a logarithmic prior, discussed above. by solving for a model parameter q with boxcar prior and setting α^2 by $\alpha^2 = 10^q$. For the circular harmonics parameters we also use boxcar priors, and use the dimensions of the fault to set the maximum permitted values, such that the centre x, y coordinates must be on the fault and any one harmonic cannot solely produce a slipping area larger than the fault.

The joint prior is the product of the independent priors for each parameter, and includes a normalising constant. Unlike in *Amey et al.* (2018), this constant cannot be ignored as it depends on the number of patches, which here changes throughout the inversion. For a trans-dimensional case, the prior can be expressed:

$$p(\mathbf{m}) = p(\mathbf{m}|n)p(n) \tag{4.7}$$

Where $p(n)$ is the prior on the number of discrete slip patches, n (*Bodin and Sambridge*, 2009). We assume a constant prior probability for $p(n)$ between 1 and the number of patches in our grid, and so $p(n)$ can be ignored.

The slip and rake for the patch can be separated by:

$$p(\mathbf{m}|n) = p(\mathbf{s}|n)p(\mathbf{r}|n) \tag{4.8}$$

Where $\mathbf{s}$ is slip and $\mathbf{r}$ is rake. As discussed above we use a boxcar for both slip and rake. Thus the prior probability of the patch slip given the number of slip patches is $p(\mathbf{s}|n) = 1/(\Delta s)^n$ when all slips are within the permitted range and zero otherwise, where Δs is the range of permitted slip. The same is true for rake, i.e. $p(\mathbf{r}|n) = 1/(\Delta r)^n$.

Thus the trans-dimensional prior is:

$$p(\mathbf{m}|n) = (\Delta\mathbf{s})^{-n}(\Delta\mathbf{r})^{-n} \tag{4.9}$$

von Karman prior As discussed above, fractal properties of slip are incorporated into the slip inversion using von Karman autocorrelation as a prior.

The von Karman prior probability of a trial slip solution is:

$$p(\mathbf{s}) = (2\pi\alpha^2)^{-n/2}|\mathbf{\Sigma_s}|^{-1/2}e^{\frac{-1}{2\alpha^2}\mathbf{s}^T\mathbf{\Sigma_s}^{-1}\mathbf{s}} \tag{4.10}$$

where:

$p(\mathbf{s})$ = prior probability of this slip distribution
α^2 = a hyperparameter controlling variance of slip
n = number of slip patches currently on

$|\mathbf{\Sigma_s}|$ = determinant of autocorrelation matrix
$\mathbf{s}$ = a vector of slip magnitude

The correlation matrix calculation ($\mathbf{\Sigma_S}$, calculated from Equation 4.2) is dependent on the Hurst parameter H, and the distance between fault patches, normalised by the correlation length. We find that when changing the size of the slipping area, the correlation matrix can become close to singular, so we add a stabilising constant of 0.01 to the diagonal of Σ_s. The normalised distance, r/a, is calculated by scaling the along-strike and down-dip distances between each fault patch by an by an along-strike, a_{as}, or down-dip, a_{dd}, correlation length. We use the scaling relations from *Mai and Beroza* (2002) to calculate the correlation lengths:

$$a_{as} = 1860 + 0.34 \times (fault\ length) \quad (meters) \tag{4.11}$$

$$a_{dd} = -390 + 0.44 \times (fault\ width) \quad (meters) \tag{4.12}$$

These correlation lengths are dependent on length and width of the slipping area, which we recalculate as the size of the slipping area changes (Section 4.3.1).

We use $H_{dd} = 0.77$ and $H_{as} = 0.71$ for down-dip and along-strike Hurst parameters (*Mai and Beroza*, 2002).

The hyperparameter, α^2, represents the variance of the slip distribution; the correlation matrix $\mathbf{\Sigma_s}$ defines the von Karman correlation and the hyperparameter α^2 scales this to produce the appropriate magnitude of slip.

Since we solve for the number of slip patches that are on within the inversion, the scalar n also changes as the slipping area is updated.

Likelihood

On the assumption that the errors are multivariate Gaussian, the likelihood is calculated by the fit of the current model to the observed data, weighted by the variance-covariance matrix and given by:

$$p(\mathbf{d}|\mathbf{m}) = (2\pi)^{-N/2}|\mathbf{\Sigma_d}|^{-1/2}e^{\frac{-1}{2}(\mathbf{d}-\mathbf{Gs}-\mathbf{k})^T\mathbf{\Sigma_d}^{-1}(\mathbf{d}-\mathbf{Gs}-\mathbf{k})} \tag{4.13}$$

where:
$p(\mathbf{d}|\mathbf{m})$ = the probability of the observation for the current model
N = total number of data points
$\mathbf{\Sigma_d}$ = variance-covariance matrix of the data
$\mathbf{d}$ = vector of data (InSAR line-of-sight; GNSS, east, north or up)
$\mathbf{s}$ = vector of magnitude of slip
$\mathbf{G}$ = kernel matrix, calculated for the correct rake values
$\mathbf{k}$ = a vector of constants for InSAR data and zero for GNSS

We use *Okada* (1985) equations for an elastic dislocation in a half space to calculate the kernel **G** for unit slip in LOS (line-of-sight) for InSAR and for east, north or up for GNSS on each fault patch, for the appropriate rake and dip. The product of kernel **G** and slip on each patch, **s**, gives the surface displacements at each InSAR and GNSS measurement for that slip distribution. Before commencing the inversion we calculate kernels with pure strike-slip and dip-slip motion and sum the contribution of these for the current rake values, as we are solving for rake.

The **G** matrix is updated with the constant InSAR offsets, **k**, so that offset is added or subtracted to the data for the appropriate InSAR scene.

Proposal Distribution

By allowing the number of slip patches to change, the problem becomes trans-dimensional; the number of unknowns is itself unknown. This requires an extension of the MCMC methods discussed above in which the algorithm alternates between updating the value of the model parameters (the current state) and the number of model parameters (jumping between state spaces), e.g. the reversible-jump MCMC (*Green*, 1995). In our algorithm we alternate so that on odd iterations we update the values of the model parameters, and on even iterations we update the size of the slipping area (the number of model parameters).

In this case we must consider the potential asymmetry of the proposal distribution, which defines how each parameter is perturbed during the Markov Chain. For a non-trans-dimensional problem the proposal distribution is symmetric; the forward proposal distribution of a step of model $m \rightarrow m'$ is the same as the reverse proposal distribution of model $m' \rightarrow m$ and the ratio of the two proposal distributions is equal to 1 (*Bodin and Sambridge*, 2009). Symmetry cannot however be assumed in a trans-dimensional problem.

For a new model, the proposal ratio can be broken down into:

$$\frac{q(\mathbf{m}|\mathbf{m}')}{q(\mathbf{m}'|\mathbf{m})} = \frac{q(\mathbf{s}|\mathbf{m}')}{q(\mathbf{s}'|\mathbf{m})} \times \frac{q(\mathbf{r}|\mathbf{m}')}{q(\mathbf{r}'|\mathbf{m})} \times \frac{(\boldsymbol{\alpha^2}|\mathbf{m}')}{(\boldsymbol{\alpha^{2\prime}}|\mathbf{m})} \times \frac{(\mathbf{k}|\mathbf{m}')}{(\mathbf{k}'|\mathbf{m})} \times \frac{q(\mathbf{h}|\mathbf{m}')}{q(\mathbf{h}'|\mathbf{m})} \tag{4.14}$$

Where **s** is the slip on the new/removed patch and **r** is rake on all patches, α^2 is a hyperparameter, **k** is the constant InSAR offset and **h** are the harmonic parameters that we use to define the slipping area.

Even though changes to the harmonic parameters can lead to the addition or deletion of patches, the number of harmonic parameters itself does not change and therefore $q(\mathbf{h}|\mathbf{m}') = q(\mathbf{h}|\mathbf{m})$, and the same reasoning can be used for α^2 and **k**.

On addition of a new slip patch, we do not select a new magnitude of slip using a probability distribution, but instead the new patch takes a constant value: its value before being turned off. The probability is thus a delta function, with the probability of its previous value equal to 1 and for all other values equal to 0, meaning that

$q(\mathbf{s}'|\mathbf{m}) = 1$. When this slip patch is removed, the probability of removing the slip magnitude of this patch is $q(\mathbf{s}|\mathbf{m}') = 1$. Thus $q(\mathbf{s}'|\mathbf{m}) = q(\mathbf{s}|\mathbf{m}')$ for the addition of a patch, and likewise for the deletion of a patch. Thus the proposal ratio for slip is always 1, and the same argument can be made for rake. Note that this would not the case if the slip and rake values for a new patch were selected from from a probability distribution, see *Bodin and Sambridge* (2009). The Jacobian, whose role is to account for scale changes between m and m' (*Sambridge et al.*, 2006), is equal to 1 as the bijective transformation $m \rightarrow m'$ involves only constants.

This means that for our formulation of the transdimentional Bayesian method $q(\mathbf{m}|\mathbf{m}') = q(\mathbf{m}'|\mathbf{m})$ and thus the proposal ratio is equal to 1 and can be ignored. This is essentially because the addition of a patch in $m \rightarrow m'$ has the same probability as removal of that patch in $m \rightarrow m'$, unlike adding a new nucleus to a network of Voronoi cells in (*Bodin and Sambridge*, 2009), and the properties for a new patch are constant.

Acceptance ratio

As in *Amey et al.* (2018) we break the algorithm down into two separate Metropolis steps, to first draw a trial that is representative of the prior before calculating the likelihood (*Tarantola* (2005), Chapter 2, Pg 52). The first Metropolis step considers only the prior ratio, in order to draw a von Karman trial, which is non-trivial to directly sample. Then the likelihood is only calculated for trials that pass this prior test, to avoid the unnecessary calculation if a prior probability is low.

At the start of an iteration each model parameter is perturbed from its current state such that a step is taken in parameter space. We generate samples from the individual model priors' directly: boxcar or logarithmic, as discussed above. For a boxcar prior PDF, random numbers are drawn and any that are outside of the permitted range are 'bounced back' into the permitted bounds: if a trial is drawn that is outside of its permitted upper bounds X by x meters (in the example of slip) we move the trial back into permitted bounds by $trial = X - x$.

Once trials have been drawn from each model parameters' prior distribution, we use a prior acceptance ratio to draw a representative transdimensional and von Karman trial. This means that the first step is to apply the Metropolis-Hastings rule to the prior acceptance ratio, a_p:

$$a_p(m'|m) = min[1, prior\ ratio] \tag{4.15}$$

$$a_p(m'|m) = min\left[1, \frac{\Delta\mathbf{s}^{-n'}\Delta\mathbf{r}^{-n'} \times (2\pi\alpha'^2)^{-n'/2}|\mathbf{\Sigma}'_\mathbf{s}|^{-1/2}e^{\frac{-1}{2\alpha'^2}\mathbf{s}'^T\mathbf{\Sigma}'_\mathbf{s}{}^{-1}\mathbf{s}'}}{\Delta\mathbf{s}^{-n}\Delta\mathbf{r}^{-n} \times (2\pi\alpha^2)^{-n/2}|\mathbf{\Sigma}_\mathbf{s}|^{-1/2}e^{\frac{-1}{2\alpha^2}\mathbf{s}^T\mathbf{\Sigma}_\mathbf{s}{}^{-1}\mathbf{s}}}\right] \tag{4.16}$$

If a trial is accepted as a representative sample of the prior, the Metropolis-Hastings rule is applied for the second time to the likelihood acceptance ratio, a_l:

$$a_l(m'|m) = min[1, likelihood\ ratio] \tag{4.17}$$

$$a_l(m'|m) = min\left[1, \frac{(2\pi)^{-N/2}|\mathbf{\Sigma_d}|^{-1/2}e^{\frac{-1}{2}(\mathbf{d}-\mathbf{G's'})^T\mathbf{\Sigma_d}^{-1}(\mathbf{d}-\mathbf{G's'})}}{(2\pi)^{-N/2}|\mathbf{\Sigma_d}|^{-1/2}e^{\frac{-1}{2}(\mathbf{d}-\mathbf{Gs})^T\mathbf{\Sigma_d}^{-1}(\mathbf{d}-\mathbf{Gs})}}\right] \tag{4.18}$$

(4.19)

If accepted the trial model becomes a representative sample of the posterior distribution. If either of the two Metropolis rule applications lead to rejection, the previous saved model becomes the new representative sample.

4.3.3 Simulated annealing initialisation and solving for step size

To save time during burn-in we perform an initial simulated annealing inversion, with all patches 'on', and use the solution to set the initial parameter values for the Bayesian inversion (*Bagnardi and Hooper*, 2018).

Simulated annealing is a direct search method that uses the analogy of annealing (heating and cooling) in its inversion to return the maximum likelihood solution of the posterior PDF (*Tarantola*, 2005). An 'annealing schedule' is chosen prior to starting the inversion and the probability, σ, of a solution as a given temperature, T, is given by the Gibbs-Boltzmann distribution:

$$\sigma = e^{\frac{\phi(m)}{T}} \tag{4.20}$$

Where $\phi(m)$ is the cost function for the model parameters m. In this case the cost function is the exponent part of the posterior. The inversion proceeds in a similar manner to a Bayesian inversion, where new trials are drawn and are accepted or rejected by the Metropolis-Hastings algorithm using a probability ratio, in this case adapted by T.

By reducing T slowly throughout the inversion, probability space is distorted so that the probability of selecting a less likely model gradually decreases. This allows the inversion to search a wide area initially, but hone in on an area of high probability as the inversion proceeds. To lower the chance of the solution converging on a local maxima the annealing schedule should not decrease temperature too quickly. We use a temperature schedule of $T = 1000, 100, 10, 1, 0.1, 0.01, 0.001, 0.0001$ and use 10,000 iterations for each value of T.

We perform sensitivity tests after the simulated annealing initialisation, during the first 20,000 iterations, to tune the proposal distribution. These sensitivity tests increase or decrease the step sizes of each model parameter depending on the rejection ratio (see *Amey et al.* (2018)), aiming to meet an ideal rejection ratio (*Roberts et al.*, 1997). After

10,000 iterations the step sizes are fixed, and these initial iterations are removed with the burn-in.

4.4 Synthetic Tests

We created a synthetic test to verify that our method is able to locate localised slip within a larger fault plane.

The test consists of a single plane, pure strike-slip fault, with one area of slip surrounded by patches of zero slip. The moment, lengthscale and slip are consistent with a magnitude ∼6 earthquake (*Wells and Coppersmith*, 1994). The slipping area has slip that is consistent with von Karman correlation, which we produced by transforming noisy slip into correctly spatially correlated slip (*Lohman and Simons*, 2005). We created synthetic measurements by calculating surface displacements expected for this slip distribution using *Okada* (1985) equations. We then used these surface displacements to invert for slip on a fault with the correct geometry.

We created a synthetic GNSS and InSAR dataset, and added spatially correlated noise to the InSAR data with a sill, nugget and range of 10^{-5} m^2, 10^{-6} m^2 and 15 km respectively. We used InSAR measurements spaced every 400 m within 5 km of the fault and spaced every 2 km within 20 km of the fault. We randomly removed 800 InSAR datapoints (34%) to simulate loss of coherence. We scattered 40 GNSS data points within 20 km of the fault.

We solved for this input using our trans-dimensional inversion scheme detailed in Section 4.3. We used a boxcar prior between 0 m and 10 m for slip and a boxcar prior between 150 and 210 degrees for rake. We used a logarithmic prior for α^2, with a minimum permitted value of 1×10^{-4} m^2 and a maximum permitted value of 10^{-2} m^2. For the circular harmonic coefficients we used a boxcar between 0 and 15,000, for the circular harmonics center coordinates we used a boxcar between 0 and 15,000 m for x, and 0 and 20,559 m for y and for the circular harmonics rotation we use a boxcar between 0 and 100 radians, which is set arbitrarily high.

The results show that the trans-dimensional method is able to resolve the location of slip very well and also does a reasonable job of resolving magnitude (Figure 4.3). Using mean slip of 0.1 m as a threshold, the method correctly identifies 37 patches out of 41 patches, and misidentifies 8 patches that are not slipping. At a 0.2 m threshold, the trans-dimensional approach puts slip on 3 patches that are not slipping. Also shown in Figure 4.3 is von Karman regularisation performed on all patches, which results in smearing of slip over nearly all patches, with mean slip greater than 0.1 m on 82 non-slipping patches; at 0.2 m threshold it puts slip on 13 patches that are not slipping. The latter solution also does not correctly capture the magnitude of slip. The true moment of the synthetic test is $6.95{\times}10^{17}$ Nm (equivalent to a magnitude 5.9) earthquake and the transdimensional approach finds a very similar moment of

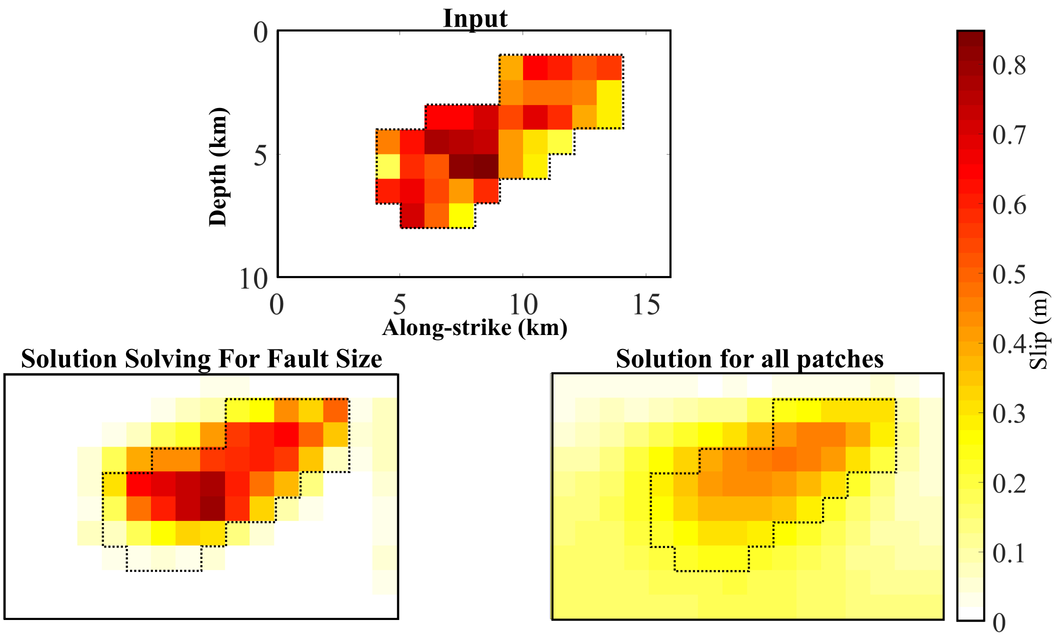

Figure 4.3: Synthetic test of trans-dimensional fault size inversion. Top figure shows the simulated true slip, with a slipping area consistent with von Karman slip surrounded by patches of zero slip. Bottom left shows the mean solution solving for slip and the size of the fault plane with von Karman regularisation. Bottom right shows the inversion performed using von Karman regularisation on all of the patches, for contrast. It is clear that the solution solving for fault size results in less smearing, since it is more likely to put zero slip in areas where the data do not require it.

6.79×10^{17} Nm (equivalent to a magnitude 5.9). The solution for all patches overestimates the moment, with a moment of 9.64×10^{17} Nm, equivalent to a magnitude 6.0 earthquake. The fit to the data for both solutions is shown in Appendix C, Figures C.1 and C.2.

The synthetic test demonstrates that this method is able to identify slipping patches, and better resolves the location and magnitude of slip than von Karman regularisation in a non-trans-dimensional mode.

4.5 Application to the Central Tottori earthquake

4.5.1 Background

The earthquake occurred on the 21st October 2016 in the Tottori prefecture of the Chugoku region of Japan, on Honshu island (Figure 4.1). Estimates of magnitude range from 6.2 (https://earthquake.usgs.gov/earthquakes/eventpage/us20007fta) and 6.6 from the Japan Meteorological Agency (*Earthquake Research Committee*, 2016) but fortunately caused no loss of life, though 30 people were injured and more than 300 houses were completely or partially destroyed (*Kubo et al.*, 2017). It was a left-lateral strike-slip event on a roughly N-S striking fault plane, along which the aftershocks are distributed, 6 km South of the city of Kurayoshi. Peak ground velocities varied between 0.3-1.4 G and the ground motion was widely felt over Southwest Japan (*Kagawa et al.*, 2017).

This earthquake occurred in the Northern Chugoku shear zone, in the area geodetically identified and named San-in shear zone by *Nishimura and Takada* (2017). This shear zone has previously experienced large earthquakes, with a M 7.2 in 1943 (*Kanamori*, 1972), M 6.2 in 1983 (*Tsukuda*, 1988) and Mw 6.6 in 2000 (*Semmane et al.*, 2005, *Monelli et al.*, 2009).

4.5.2 InSAR

We used Sentinel-1 (C-band SAR satellite) Ascending, Track 083, which had a 24 day repeat at this time. We processed Sentinel-1 data using the LiCSAR processing chain (*Gonzalez et al.*, 2016). The SAR images for master (20161012) and slave (20161105) were downloaded from ESA's (European Space Agency) Copernicus Open Access Hub. Within LiCSAR the images were coregistered, multilooked twice in azimuth and ten times in range, filtered, unwrapped and geocoded. We found that the descending track was too decorrelated for the earthquake to be identified, which we put down to the large amount of vegetation and larger perpendicular baseline than the ascending track (82.1 m compared to 30.8 m).

We also used L-band ALOS-2 data; ultrafine-mode SAR data (spatial resolution of 3 m) from four different viewing directions (i.e., a combination of ascending/descending and right/left looking) were acquired by ALOS-2 within five days of the earthquake. A 10-m mesh DEM (*GSI*, 2014) was used to remove the effect of topography. We applied tropospheric noise reduction using a numerical weather model provided by Japan Meterological Agency (JMA) (*Kobayashi et al.*, 2014). To reduce long wavelength sources (i.e., caused by orbital errors, residual tropospheric delay, and ionospheric delay), InSAR displacements were fitted to the GNSS displacements using spline interpolation (*Fukushima*, 2013, *Morishita*, 2016).

We used a nested uniform downsampling approach to downsample the data for modelling. The region within approximately 25 km of the epicenter was downsampled 800 times and outside this region was downsampled 2500 times.

Variance-covariance matrix

Due to atmospheric changes between satellite acquisitions that are correlated in space, we calculated a variance-covariance matrix, Σ_d for each InSAR scene. We did this using the semi-variogram method, details given in *Amey et al.* (2018).

4.5.3 Model set up

We fixed the fault geometry as given in Appendix C, Table C.1 (see figures 4.4 and 4.6 for geometry). We used the InSAR surface displacements to determine a fault strike, and assumed a vertical fault plane. The priors used in this study are given in Table 4.1.

	Min	**Max**
Slip (m)	0	10
Rake (degrees)	-40	20
InSAR offset (m)	-1	1
α^2 **(m^2)**	1×10^{-5}	20
Circular harmonic coefficient	0	15000
Along-strike circular harmonic center (m)	0	20559
Down-dip circular harmonic center (m)	0	15000
Circular harmonic rotation (radians)	0	2π

Table 4.1: Permitted bounds for the boxcar prior PDFs used in this inversion. The probability for each model parameter is 1 between these bounds, and 0 otherwise.

4.5.4 GNSS

We used the data from continuous GNSS stations of the GNSS Earth Observation Network (GEONET) operated by the Geospatial Information Authority of Japan (GSI) (*Sagiya*, 2004, *Nakagawa*, 2009). The site of 960640 was selected as a reference station, which is located >100km ENE from the epicenter, where the coseismic displacement can be ignored. The coseismic displacements were calculated as the difference in the averages of the daily solutions between October 6th to 20th and October 22nd to November 5th, 2016. We also calculated the standard deviations of the daily relative coordinates and assigned them as data uncertainties.

The GNSS shows up to a maximum of 6.8 cm movement at the GNSS stations nearest to the fault and is consistent with left-lateral motion (Figure 4.1).

We do not weight either geodetic dataset above the other, though there are more InSAR datapoints than GNSS measurements.

4.5.5 Results

We chose fault dimensions to be longer and deeper than the area of slip for an earthquake of this magnitude and the lengthscale of deformation from the InSAR.

The mean slip for each patch, including solving for fault size, is shown in Figure 4.4, panel *a*. From the spatial pattern of time spent 'on' by each patch (Figure 4.5) and the slip distribution, the earthquake slipped significantly from depths of approximately 1.5 km down to depths of approximately 10 km. There is a large patch with maximum average of approximately 1.6 m slip that lies of slip at a depth of 8 km. We repeated

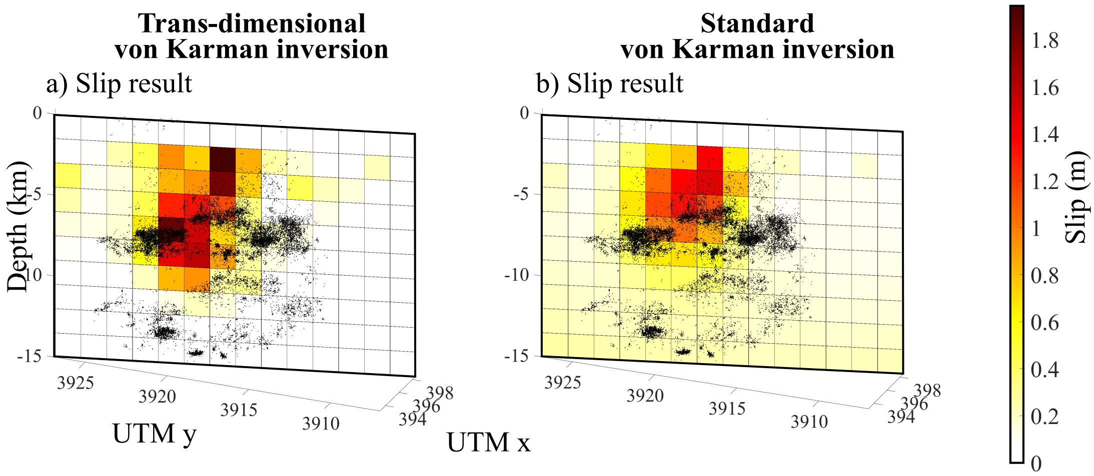

Figure 4.4: Mean slip for every patch from a von Karman regularised inversion for the Central Tottori 2016 earthquake. Panel a shows results for a trans-dimensional inversion using circular harmonics. Panel b shows von Karman regularisation applied to the whole fault, where smearing has occurred. Black circles show 10 days of aftershocks from *Ross et al.* (2018) projected onto fault plane. Note that the aftershocks span a different time period to the geodetic data used to derive the slip solution, and some aftershocks are up to 20 km away, some on sub-parallel faults.

the inversion without solving for fault size (Figure 4.4, panel *b*). This shows a peak slip is lower, with 1.3 m at a depth of 6 km, but this solution is smeared out, with some slip occurring on all deeper patches. Including solving for fault size in the inversion focuses the slip, leader to a larger area of high slip, extending at least 3 km further down-dip. This solution fits the data well as shown in Figures 4.6 and 4.7, as does the solution applied to all patches, shown in Appendix C, figure C.3 and C.4. We also solved for slip using Laplacian smoothing and found it to give a very similar result to the von Karman solution applied to all patches, but with a slightly higher magnitude of slip (Figure C.5).

The 95% confidence interval of the moment for solving for slipping area is 1.95×10^{18} Nm to 2.66×10^{18} Nm, which is slightly lower than the USGS moment of 2.82 $\times10^{18}$ Nm. The 95% confidence interval for the von Karman MAP solution applied to all patches is higher, with a range of 2.60 $\times10^{18}$ and 2.92 $\times10^{18}$.

4.6 Discussion

4.6.1 Implications for seismic hazard

The tectonics in Southwest Japan is dominated by the Philippine Sea plate subducting below the Eurasian plate at the Nankai trough. 200 km north of the Nankai trough, the Median Tectonic line is a mature shear zone (*Ross et al.*, 2018) as is evident from the topography and orientation of faults (Figure 4.1). But at 350 km north of the

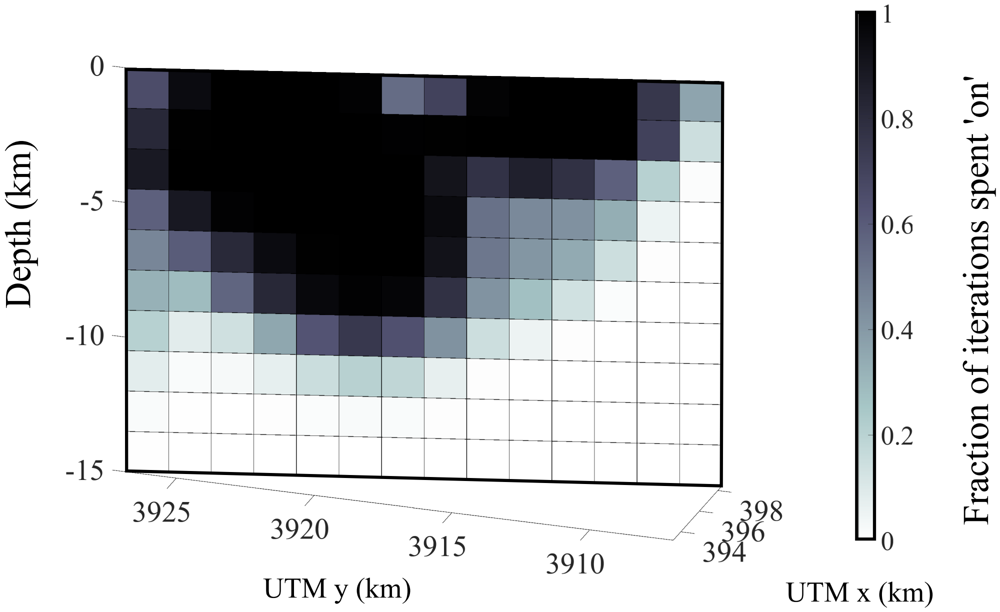

Figure 4.5: Fraction of time each patch is 'on' during the inversion. This indicates that slip is required from the surface to around 10 km. Many other patches are 'off' for the entire inversion, indicating that slip there is not necessary to fit the data. Patches near the surface that have no slip are also 'on', but the inversion is able to resolve these patches as having zero slip, as the data is at the surface.

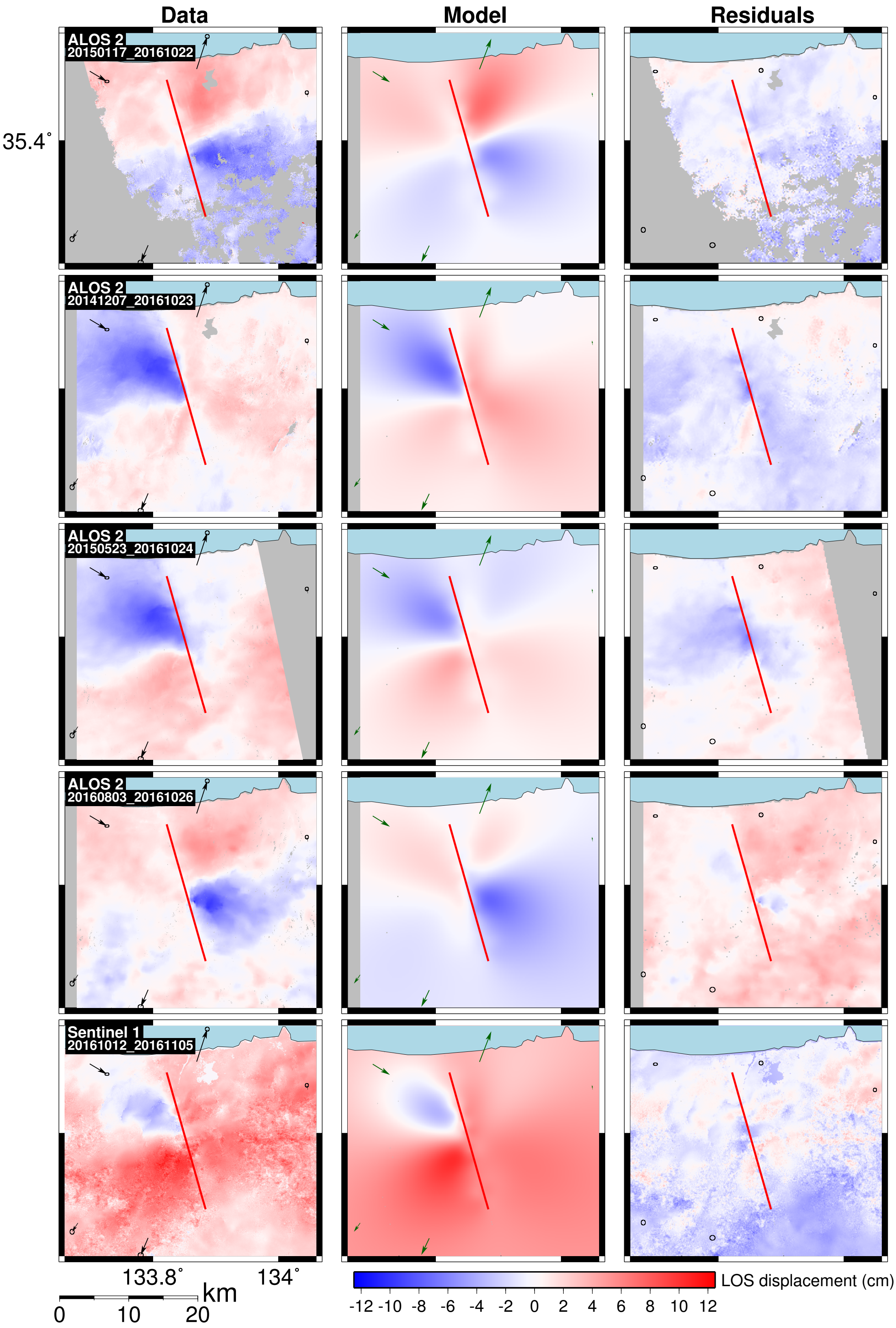

Figure 4.6: InSAR and near-field GNSS results for, from top, ALOS-2 ascending left-looking, ALOS-2 descending left-looking, ALOS-2 ascending right-looking, ALOS-2 descending right-looking, Sentinel-1 ascending. The left hand column shows the unwrapped interferograms, the middle column contains simulated interferograms for the MAP model including solved-for InSAR offset and right-hand column displays residuals between the two. Positive is movement towards the satellite (e.g. uplift). The trace of all candidate fault patches is shown in red. GNSS vectors are shown in black, with 95% confidence intervals. Note that the residual GNSS vectors are too small to be easily seen, see Figure 4.7.

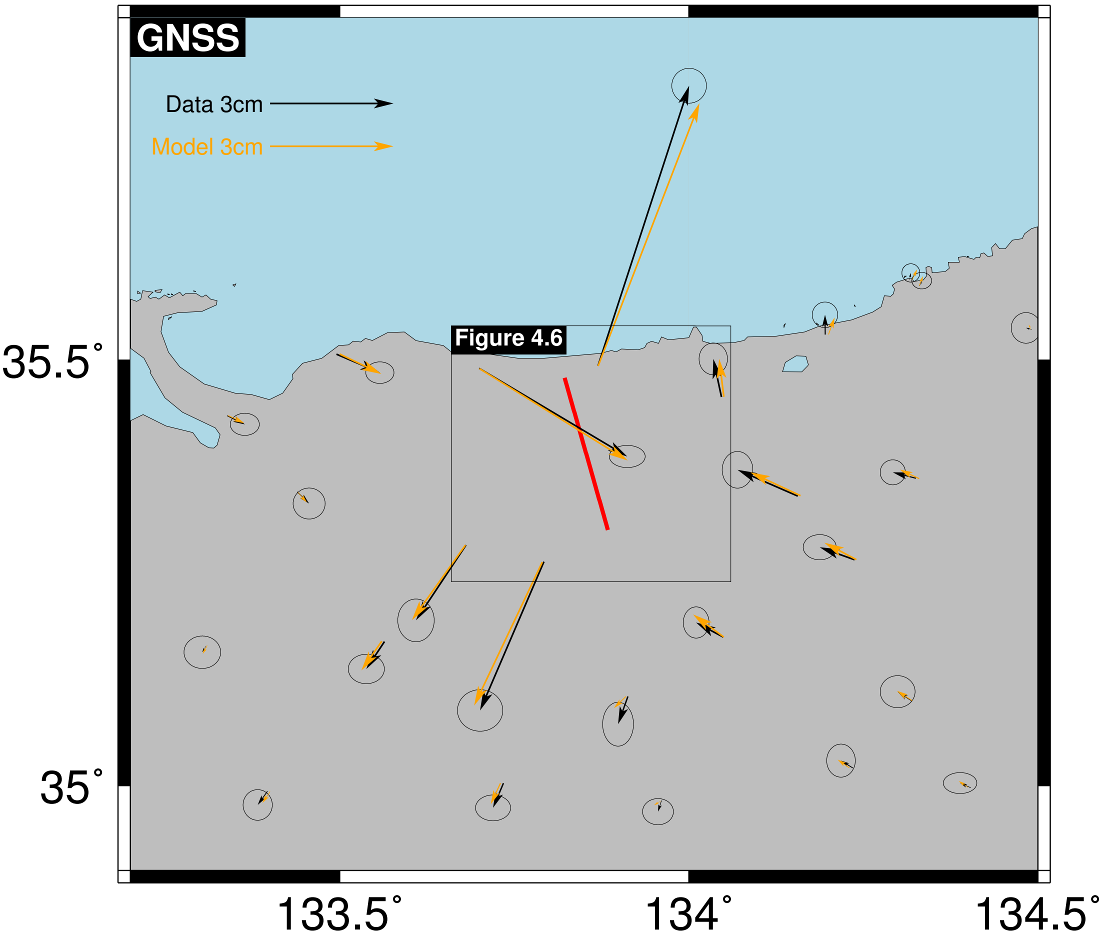

Figure 4.7: GNSS displacements from 6/10/16 to 22/10/16 for the 2016 Central Tottori earthquake, which occurred on the 21/10/16. Black arrows show the observed displacements and green arrows show the fit of the MAP model to the data. The fault trace is shown in red. Ellipses represent the 95% confidence intervals on the data.

Nankai trough, the San-in Shear Zone (*Nishimura and Takada*, 2017) (within the right-lateral Northern Chugoku shear zone (*Gutscher and Lallemand*, 1999)) in which these earthquakes occurred is less developed, without visible surface expressions of active faulting. But there have been several large earthquakes within this zone (*Wesnousky et al.*, 1982), including, in the last century, a M 7.0 in 1943, a M 6.7 in 1943 and a M_w 6.7 in 2000. This region has been geodetically identified as a right-lateral shear zone, but without a main fault along the axis of deformation, and with many conjugate Riedel shears orientated NW-SE left-lateral strike-slip faults instead (*Nishimura and Takada*, 2017), as observed in the 2016 earthquake and the 2000 western Tottori earthquake.

The 2000 and 2016 earthquakes occurred within approximately 30 km of the volcano Mount Daisen (Figure 4.1). In this area *Zhao et al.* (2018) observe significant crustal heterogeneity using seismic tomography, with a low velocity anomaly, that they suggest is linked to fluid and arc magma, related to Mt Daisen. Additionally, they suggest that the subducting Philippine Sea plate is thinner under the Tottori region, leading to higher temperatures and increased slab dehydration reactions, causing hot upwelling in the Tottori region, which may have been the cause of the volcanic activity.

The San-in Shear zone fault zone is immature, as are the faults, which may be the reason for the unusually spatially-extensive off-fault aftershock triggering (*Ross et al.*, 2018). The aftershocks reveal geometric complexity at shallow ($<$ 8 km) depths, with many parallel faults, which may explain why the Tottori mainshock was so dissipative (*Ross et al.*, 2018).

We find the earthquake to have ruptured significantly from depths ~1.5 km beneath the surface down to 10 km, suggesting that most of the seismogenic zone ruptured in this event. This is in contrast to some seismological studies, which suggest significant slip to occur only at depths of ~10-12 km. *Ross et al.* (2018) find a concentrated slip patch of ~ 5 m slip with 93 % of the seismic moment released below 8 km, which would leave the surface at risk from further faulting and considerable seismic hazard. *Kubo et al.* (2017), however, find two distinct slipping patches of 0.6 m slip from 3 km depth down to 12 km depth, supporting our view that most of the seismogenic zone has ruptured. The InSAR data also encompass several days to weeks of activity after the earthquake (up to 4 days for the four ALOS-2 scenes and 15 days for Sentinel-1), which means there could be postseismic and aftershock signal included in our data. All of the InSAR scenes include the 70 foreshocks in the preceding 12 hours, but the largest foreshock, with magnitude M_w 4.2 (*Ross et al.*, 2018), represents only 5×10^{15} Nm of moment, which is less than 1% of the moment of the M_w 6.2 event.

The area around the city of Kurayoshi has experienced many earthquakes greater than M_w 6.2 in the past forty years (Figure 4.1), and due to the ongoing subduction and fluids in the crust, is likely to experience large earthquakes again. Our slip results suggest that stress has been released throughout the seismogenic zone but in a relatively constricted area along-strike, as is particularly evident from the zero slip to the south-

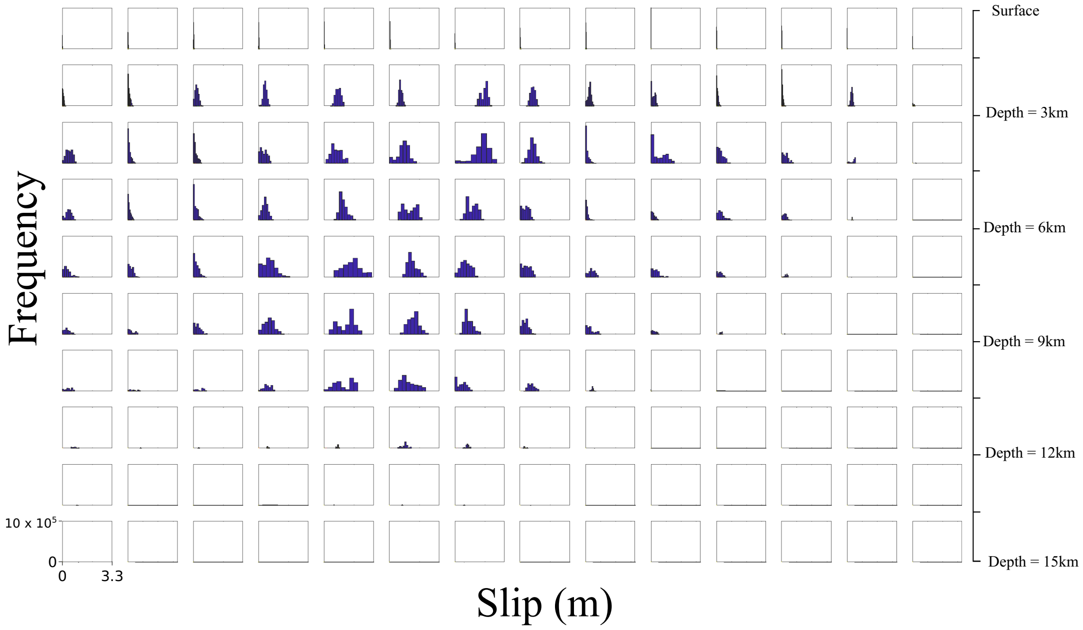

Figure 4.8: Histograms of sampled slip for every fault patch. Every histogram is plotted on the same scale, shown on the bottom left figure, and the histograms are plotted such that each histogram correlates with the patch's position on the fault plane. The patches that are 'on' for the majority of the inversion have smoother, well-filled out histograms, suggesting this inversion has converged. Those that are only on for a small percentage of the time (see Figure 4.5, e.g. the bottom two rows) have fewer samples and are therefore less smooth.

east of the main slipping area in Figure 4.4. This suggests the fault could host another earthquake in the near future. But we note that this modeling is a simplification, as we assume all the slip has occurred on our one modeled fault plane, whereas the aftershocks have shown there to be many sub-parallel fault structures at shallow depths (*Ross et al.*, 2018).

4.6.2 Convergence

Due to the quantised nature of turning patches 'on' and 'off', the histograms of slip on each patch are not all as smooth as we would usually expect to determine convergence. Patches that are off for most iterations are sampled less, leading to rougher histograms (e.g., see bottom f rows of Figure 4.8). Therefore we judge convergence based on the histograms for patches that were on for the majority of the inversion only.

4.6.3 Expansion of work

In this work we have used rectangular patches and have only permitted patches to turn on in pre-determined positions. However the inversion scheme is completely flexible; *Dettmer et al.* (2014), for example, used Voronoi cells in a seismological slip inversion. This approach could be incorporated into our inversion scheme, to determine the size of the patches based on resolution during the inversion, as has been done previously in advance of the inversion (*Atzori and Antonioli*, 2011, *Barnhart and Lohman*, 2010).

4.7 Conclusions

In this study we present a new method for solving for the size of a slipping area within a von Karman regularised inversion. We suggest that von Karman regularisation should be the default for slip inversions, since it is captures the self-similar nature of slip, leading to tighter constraints on slip location. Solving for the size of the slipping area during the inversion removes any bias due to incorrectly choosing the fault length and width in advance. Application to the 2016 Central Tottori earthquake shows the earthquake ruptured the entire seismogenic zone, in contrast to some seismological studies. This implies that an earthquake rupturing the up-dip part of the fault is unlikely in the near future, though the fault could host another along-strike.

4.8 Acknowledgments

This work was supported by the National Environment Research Council (NERC) through the Leeds-York Doctoral Training Programme, grant number NE/L002574/1. ALOS-2 data were provided under a cooperative research contract between GSI and JAXA. All Sentinel-1 data that was used are derived works of Copernicus data (2017) and are available to download through the ESA Copernicus Sentinel programme. The downsampled InSAR and GNSS data is available in the Supplementary materials. The code *slipBERI* is downloadable from https://github.com/ruthamey/slipBERI. We are grateful to Tom Ingleby for many useful discussions and Karsten Spaans for help with LiCSAR.

References

Amey, R. M. J., A. Hooper, and R. J. Walters (2018), A Bayesian Method for Incorporating Self-Similarity into Earthquake Slip Inversions, *Journal of Geophysical Research: Solid Earth*, *123*, doi:10.1029/2017JB015316. 4.2, 4.3.2, 4.3.2, 4.3.2, 4.3.3, 4.5.2

Atzori, S., and A. Antonioli (2011), Optimal fault resolution in geodetic inversion of coseismic data, *Geophysical Journal International*, *185*(1), 529–538, doi:10.1111/j.1365-246X.2011.04955.x. 4.6.3

Bagnardi, M., and A. Hooper (2018), Inversion of surface deformation data for rapid estimates of source parameters and uncertainties: a Bayesian approach, *Geochemistry, Geophysics, Geosystems*, doi:10.1029/2018GC007585. 4.3.3

Barnhart, W. D., and R. B. Lohman (2010), Automated fault model discretization for inversions for coseismic slip distributions, *Journal of Geophysical Research*, *115*(B10), B10,419, doi:10.1029/2010JB007545. 4.6.3

Bodin, T., and M. Sambridge (2009), Seismic tomography with the reversible jump algorithm, *Geophysical Journal International*, *178*(3), 1411–1436, doi:10.1111/j.1365-246X.2009.04226.x. 4.3.2, 4.3.2, 4.3.2, 4.3.2

Candela, T., F. Renard, Y. Klinger, K. Mair, J. Schmittbuhl, and E. E. Brodsky (2012), Roughness of Fault Surfaces over Nine Decades of Length Scales, *Journal of Geophysical Research*, *117*(B8), B08,409, doi:10.1029/2011JB009041. 4.2

Dettmer, J., R. Benavente, P. R. Cummins, and M. Sambridge (2014), Trans-dimensional finite-fault inversion, *GJI Seismology*, *199*, 735–751, doi:10.1093/gji/ggu280. 4.6.3

Earthquake Research Committee (2016), Evaluation of Earthquake in the Central Tottori Prefecture on October 21, 2016, doi:http://www.jishin.go.jp/main/chousa/16nov_tottori/index-e.htm. 4.5.1

Fukushima, Y. (2013), Correction of DInSAR noise using GNSS measurements, in *APSAR2013*, pp. 226–228. 4.5.2

Gonzalez, P., R. Walters, R. Hatton, K. Spaans, McDougill, A. A; Hooper, and T. Wright (2016), LiCSAR: Tools for automated generation of Sentinel-1 frame interferograms, in *AGU Fall Meeting*. 4.5.2

Green, P. J. (1995), Reversible jump Markov chain Monte Carlo computation and Bayesian model determination, *Biometrika*, *82*(4), 711–732, doi:10.1093/biomet/82.4.711. 4.2, 4.3.2

GSI (2014), Overview and types of digital elevation model of fundamental geospatial data. 4.5.2

Gutscher, and Lallemand (1999), Birth of a major strike-slip fault in SW Japan, *Terra Nova*, *11*(5), 203–209, doi:10.1046/j.1365-3121.1999.00247.x. 4.6.1

Kagawa, T., T. Noguchi, S. Yoshida, and S. Yamamoto (2017), Effect of the surface geology on strong ground motions due to the 2016 Central Tottori Earthquake, Japan, *Earth, Planets and Space*, *69*(1), 106, doi:10.1186/s40623-017-0689-0. 4.5.1

Kanamori, H. (1972), Determination of effective tectonic stress associated with earthquake faulting. The Tottori earthquake of 1943, *Physics of the Earth and Planetary Interiors*, *5*, 426–434, doi:10.1016/0031-9201(72)90114-8. 4.5.1

Kobayashi, T., M. Ishimoto, M. Tobita, and H. Yarai (2014), A tool for reduction of atmosphere-related noises included in an InSAR image, incorporating a numerical weather model, *J. GSI (in Japanese)*, *125*, 31–38. 4.5.2

Kubo, H., W. Suzuki, S. Aoi, and H. Sekiguchi (2017), Source rupture process of the 2016 central Tottori, Japan, earthquake (MJMA 6.6) inferred from strong motion waveforms, *Earth, Planets and Space*, *69*, doi:10.1186/s40623-017-0714-3. 4.5.1, 4.6.1

Lohman, R. B., and M. Simons (2005), Some Thoughts on the use of InSAR Data to Constrain Models of Surface Deformation: Noise Structure and Data Downsampling, *Geochemistry, Geophysics, Geosystems*, *6*(1), doi:10.1029/2004GC000841. 4.4

Mai, P. M., and G. C. Beroza (2002), A Spatial Random Field Model to Characterize Complexity in Earthquake Slip, *Journal of Geophysical Research*, *107*(B11), 2308, doi:10.1029/2001JB000588. 4.2, 4.2, 4.3.2, 4.3.2

Metropolis, N., A. W. Rosenbluth, M. N. Rosenbluth, A. H. Teller, and E. Teller (1953), Equation of State Calculations by Fast Computing Machines, *The Journal of Chemical Physics*, *21*(6), 1087–1092, doi:10.1063/1.1699114. 4.3.2

Milliner, C. W., J. F. Dolan, J. Hollingsworth, S. Leprince, F. Ayoub, and C. Sammis (2015), Quantifying Near-field and Off-fault Deformation Patterns of the 1992 M w 7.3 Landers Earthquake, *Geochemistry, Geophysics, Geosystems*, *16*(5), 1525–2027, doi:10.1002/2014GC005693. 4.2

Minson, S. E., M. Simons, and J. L. Beck (2013), Bayesian Inversion for Finite Fault Earthquake Source Models I–Theory and Algorithm, *Geophysical Journal International*, *194*(3), 1701–1726, doi:10.1093/gji/ggt180. 4.2

Monelli, D., P. M. Mai, S. Jónsson, and D. Giardini (2009), Bayesian imaging of the 2000 Western Tottori (Japan) earthquake through fitting of strong motion and GPS data, *Geophysical Journal International*, *176*(1), 135–170. 4.5.1

Morishita, Y. (2016), Reduction of Spatially Long Wavelength Noises in SAR Interferograms Using GNSS Data, *J. Geod. Soc. Jpn. (In Japanese with English abstract)*, *62*(2), 89–100, doi:10.11366/sokuchi.62.89. 4.5.2

Nakagawa, H. (2009), Development and validation of GEONET new analysis strategy (Version 4), *J. Geogr. Surv. Inst. (in Japanese)*, *118*, 1–8. 4.5.4

NIED (National Research Institute for Earth Science and Disaster Resilience) (2018), Strong-motion Seismograph Networks, doi:http://www.kyoshin.bosai.go.jp/. 4.1

Nishimura, T., and Y. Takada (2017), San-in shear zone in southwest Japan, revealed by GNSS observations, *Earth, Planets and Space*, *69*(1), 85, doi:10.1186/s40623-017-0673-8. 4.5.1, 4.6.1

Okada, Y. (1985), Surface Deformation Due to Shear and Tensile Faults in a Half-space, *Bulletin of the Seismological Society of America*, *75*(4), 1135–1154. 4.3.2, 4.4

Onda, S., Y. Sano, N. Takahata, T. Kagoshima, T. Miyajima, T. Shibata, D. L. Pinti, T. Lan, N. K. Kim, M. Kusakabe, and Y. Nishio (2018), Groundwater oxygen isotope anomaly before the M6.6 Tottori earthquake in Southwest Japan, *Scientific Reports*, *8*(1), doi:10.1038/s41598-018-23303-8.

RGAFJ (1991), Active Faults in Japan: Sheet Maps and Inventories, revised edition. 4.1

Roberts, G. O., A. Gelman, and W. R. Gilks (1997), Weak convergence and optimal scaling of random walk Metropolis algorithms, *The Annals of Applied Probability*, *7*(1), 110–120, doi:10.1214/aoap/1034625254. 4.3.3

Ross, Z. E., H. Kanamori, E. Hauksson, and N. Aso (2018), Dissipative intraplate faulting during the 2016 M w 6.2 Tottori, Japan earthquake, *Journal of Geophysical Research: Solid Earth*, *123*(2), 1631–1642, doi:10.1002/2017JB015077. 4.4, 4.6.1

Sagiya, T. (2004), A decade of GEONET: 19942003 The continuous GPS observation in Japan and its impact on earthquake studies, *Earth, Planets and Space*, *56*(8), xxix–xli, doi:10.1186/BF03353077. 4.5.4

Sambridge, M., K. Gallagher, A. Jackson, P. Rickwood, and W. R. (2006), Trans-dimensional inverse problems, model comparison and the evidence, *Geophysical Journal International*, *167*(2), 528–542, doi:10.1111/j.1365-246X.2006.03155.x. 4.3.2, 4.3.2, 4.3.2

Semmane, F., F. Cotton, and M. Campillo (2005), The 2000 Tottori earthquake: A shallow earthquake with no surface rupture and slip properties controlled by depth, *Journal of Geophysical Research*, *110*(B3), B03,306, doi:10.1029/2004JB003194. 4.5.1

Tarantola, A. (2005), *Inverse Problem Theory and Methods for Model Parameter Estimation*, chap. 2, pp. 50–52, Society for Industrial and Applied Mathematics, Philadelphia, doi:10.1137/1.9780898717921.ch2. 4.3.2, 4.3.2, 4.3.3

Tsukuda, T. (1988), Coda-Q before and after the 1983 Misasa earthquake of M 6.2, Tottori Prefecture, Japan, *Pure and Applied Geophysics PAGEOPH*, *128*(1-2), 261–279, doi:10.1007/BF01772600. 4.5.1

Wells, D. L., and K. J. Coppersmith (1994), New empirical relationships among magnitude, rupture length, rupture width, rupture area, and surface displacement., *Bulletin of the Seismological Society of America*, *84*(4), 974–1002. 4.4

Wesnousky, S. G., C. H. Scholz, and K. Shimazaki (1982), Deformation of an island arc: Rates of moment release and crustal shortening in intraplate Japan determined from seismicity and Quaternary fault data, *Journal of Geophysical Research: Solid Earth*, *87*(B8), 6829–6852, doi:10.1029/JB087iB08p06829. 4.6.1

Zhao, D., X. Liu, and Y. Hua (2018), Tottori earthquakes and Daisen volcano: Effects of fluids, slab melting and hot mantle upwelling, *Earth and Planetary Science Letters*, *485*, 121–129, doi:10.1016/J.EPSL.2017.12.040. 4.6.1

Chapter 5

Discussion and Conclusions

5.1 Summary of key findings

My aim in this thesis was to investigate the fractal nature of slip and to incorporate it into earthquake slip models. Here I will summarise my main findings and its importance for the wider scientific community.

5.1.1 Fractal fault roughness

In Chapter 2 I investigated the fault roughness properties of the Campo Felice fault in the Italian Apennines, particularly the along-strike change in roughness. My results show that Campo Felice fault displays fractal properties over at least six orders of magnitude perpendicular to slip and at least three orders of magnitude in the slip parallel direction.

I found that the Hurst parameters, which define the fractal nature of the fault surface, vary considerably along the length of the Campo Felice fault, with no evident trend. Whereas previous work has found surprisingly consistent Hurst parameters across a range of faults, $H_{\perp} \approx 0.8$ and $H_{||} \approx 0.6$, I find a much larger variation along the Campo Felice fault. This is consistent with field observations, where some fault surfaces are remarkably planar and lacking any obvious grooves or corrugations (i.e. long wavelength topography) whereas some fault surfaces are obviously very curved. This suggests that when incorporating fractal properties into earthquake slip inversions, the Hurst parameters cannot be simply assumed to be $H_{\perp} \approx 0.8$ and $H_{||} \approx 0.6$, and that different faults may display different fractal properties, which must be properly considered.

We find that the power spectra are vertically offset from each other between the three different scales at which we observed - the whole fault, meter-sized patches and centimeter samples. We believe this is due to the necessary bias in selecting sites to scan. Whereas the fault naturally has cracks and jumps, when selecting hand samples it's necessary to select areas of the fault without these features.

5.1.2 Incorporating fractal properties into earthquake slip inversions

In light of many strands of my work in Chapter 2 and other strands of evidence that suggest fault slip should be fractal, in Chapter 3 I incorporated fractal properties into earthquake slip inversions through the use of the von Karman autocorrelation function. The von Karman function is partly controlled by the Hurst parameter that controls the long-scale order of a system. It is akin to the fractal dimension and controls the decay of the autocorrelation as a function of distance, thus incorporating fractal features.

Through the development of the MATLAB code *slipBERI* I introduced this autocorrelation as a prior assumption. In the Bayesian inversion this means that how probable a slip solution is depends upon both how well a solution fits the data and how well if fits the von Karman correlation. In other words, the posterior probability is proportional to the likelihood multiplied by the prior probability.

Through synthetic tests I found that a von Karman regularised slip inversion is able to adequately resolve an input slip that is consistent with the von Karman autocorrelation; this is as to be expected. These tests also revealed that a von Karman regularised solution is able to resolve slip solutions as well as, if not better, than an unsmoothed inversion or Laplacian smoothing for slip inputs that are either 'rough' or consistent with Laplacian smoothing. This presents an important result, as whilst I argue the benefit of von Karman regularised slip based upon observable evidence, these tests show that my new method outperforms previously used methods, for slip that is both fractal and otherwise. I also found that since every discrete fault patch has a correlation with every other patch, the regularisation provides a much tighter confidence intervals on the magnitude of slip. This tighter constraint can help in the estimation of seismic hazard, as having better constraints of where slip and therefore stress release has and hasn't occurred helps forecast which areas of a fault may be susceptible to future rupture.

During development of this method I found that there was a noticeable degree of smearing, particularly on fault patches at depth. I attributed this to the von Karman constraint making it favourable to apply slip to patches at depth: whilst this makes little difference to the likelihood, the prior probability will increase due to better fitting of the von Karman correlation. Additionally, patches that have zero slip do not follow the von Karman correlation. If a fault were chosen to be too large, then ideally a solution would put zero slip around all the patches that did not slip. However this does not satisfy the von Karman correlation, as patches at a range of distances would display 100% correlation. Because of this, and their correlation with patches of the fault that slipped a large amount, the inversion will tend to apply slip to satisfy the von Karman correlation, where it is almost in the model null space.

In section 3.6.5, I tested applying a moment regularisation to the inversion to see if this solved the solution, but smearing still occurred. Applying a constraint to a geodetic inversion using the seismically-derived moment introduces its own issues and biases, as there are well documented and systematic differences between them (*Weston et al.*, 2011).

So to solve this problem, in Chapter 4 I adapted my method to solve for the size of the slipping area during the inversion. This way, the von Karman correlation is only applied to patches that are 'on' and patches that are 'off' can have zero slip without this affecting any other patches. In synthetic tests I found that this method can adequately resolve an area of slip embedded in a larger, unslipping fault. Application to the 2016 Central Tottori, Japan, earthquake found that this does change the slip solution. Whereas a standard von Karman regularisation found a patch of approximately 1.3 m slip at a depth of approximately 5 km with evident smearing, a trans-dimensional solution was able to put zero slip on the large majority of our modelled fault plane, with an area of 1.8 m slip extending from 1.5 km depth down to 10 km depth (Figure 4.4. This area of slip was elongated in the down-dip direction compared to the over-smoothed result, and also fitted the data better (Figure 4.6 and 4.7 compared to Figure C.3 and Figure C.4). This solution was also rougher in appearance, as there are no patches with zero slip incorporated into the von Karman correlation that require nearby patches to have low levels of slip, thus introducing smoothing.

This improved trans-dimensional method that I have developed represents another step towards fully objective slip inversions.

5.2 Link between fault roughness and fault structure

I found a lot of variability in Hurst parameters along the length of the Campo Felice fault, which may be controlled by structure. Campo Felice has a prominent bend in the center, and the location of my southeastern scanning site has been suggested to be a left-stepping relay zone as this fault grew (*Wilkinson et al.*, 2015). The change in Hurst parameters along-strike could be reflecting different slip history along the fault. Slip along a fault has been observed to be highly variable (*Milliner et al.*, 2015) and the changes in Hurst parameters over only a few hundred meters may be recording this variation in slip. Alternatively, it could be that, due to structural controls, different areas of the fault have not all failed in the same earthquakes, due to rupture being arrested or stopped at the fault bend. Different areas of the fault may also experience different conditions in the same earthquake. Structurally controlled, long-lasting asperities mean that different stress conditions may be felt along the length of the fault, if that area were located in the center or at the edge of an asperity. If this were to be the case, then potentially measuring the change in Hurst parameters along a fault could constrain the size of asperities. It is most likely the case that the variation in Hurst parameters is a combination of all three factors.

These findings have implications for earthquake slip inversions. When I developed the method in Chapters 3 and 4 I used a consistent Hurst parameter values in the slip parallel and slip perpendicular direction, however the work in Chapter 2 has shown that the Hurst parameters are variable along the fault, even within the size of a discretised fault patch. This implies that using one Hurst parameter for the entire fault may be a simplification.

5.3 Implications for seismic hazard

The roughness of a fault surface is linked to the size of earthquakes that it can accommodate (*Zielke et al.*, 2017). We find, from the pre-factors, that Campo Felice displays lower topography compared to other faults, i.e. that its fault surface topography deviates less from a planar surface. Despite its low Hurst parameters suggesting that its surface is bumpy and has not matured, this is in keeping with field observations that many of the sites we scanned are remarkably planar. This smoothness could imply that it is capable of generating larger earthquakes than a rougher fault in similar conditions (*Zielke et al.*, 2017).

5.4 Implications from slip solutions incorporating fractal smoothing

In both Chapter 3 and Chapter 4 I have found that my new von Karman inversion produced different results to other inversion methods.

In Chapter 3 I found that there were noticeable differences between the solution in which I solved for slip incorporating Laplacian smoothing compared to von Karman regularisation. For both solutions I solved for a hyperparameter controlling the degree of smoothing. I found that the von Karman solution put slip right at the surface, whereas the Laplacian solution found peak slip just below the surface at 2-3 km depth. The Laplacian result would corroborate the shallow-slip-deficit theory (*Fialko et al.*, 2005); that there is a lack of slip at shallow depths during earthquakes. However the von Karman solution suggests that there is no shallow-slip-deficit, and that any appearance of one may be an artifact of the inversion.

In Chapter 4 I compared a von Karman solution applied to the whole fault to a trans-dimensional solution, in which I solved for the number of slip patches. I found that the trans-dimensional solution put slip much deeper, suggesting that most of the seismogenic layer ruptured in this earthquake. This has important implications for seismic hazard, as if the entire seismogenic layer did not rupture it leaves certain depths susceptible to future rupture. Both of these are in contrast to the seismic study by (*Ross et al.*, 2018) that suggested most of the slip occurred at greater then 8 km depth, leaving the surface susceptible to future failure.

5.5 Limitations

One limitation of the method presented in this thesis is that the von Karman regularisation exerts control over the magnitude of slip on patches, as a function of scaled distance to its neighbours, but it does not regularise the rake. This has resulted in some oscillatory rake in the slip distributions, for example Figure 3.7. Patches along-strike from each other show alternating rake or drastically different rake, suggesting that this is not capturing true varying rake along the fault, but instead it is an unstable feature of the inversion. In reality the true rake direction should presumably be an average of the oscillating rake directions. The von Karman regularisation cannot be applied separately to dip-slip motion and strike-slip motion as the inverse of the von Karman correlation matrices is singular if set-up in this way. This implies that some other regularisation of rake should be explored. Here I have used a boxcar distribution for rake between a given range, but a normally distributed prior centered upon the main slip direction may help to regularise rake and minimise oscillations. Another possible suggestion is to apply von Karman regularisation to rake in the same way as we have for slip, though it it not clear if rake should be expected to show a fractal distribution, and so I have not incorporated it here.

Additionally in this thesis I have discretised the fault into equally-sized rectangular patches. But patches increasing in size with depth would better reflect the resolving capability of the model. The von Karman correlation allows such an implementation, since the correlation only depends upon the distance between patches and thus is not affected by the size of the patches.

5.6 Future work

5.6.1 Expanding the Italian Appenines fault roughness dataset

In this thesis I have presented an in-depth study of the Campo Felice fault, but there are many faults in the Italian Appenines with well-preserved bedrock scarps, upon which this analysis could be performed.

In previous work many faults have previously been analysed but from a wide range of places and locations, whereas the Apennines present a unique opportunity for investigating a large number of faults (at least 25) all within the same fault system and under the same tectonic forces, in different lithologies. This presents a unique opportunity to investigate how fractal properties vary across a mountain-range, which can be linked to long-term slip histories and maturities of the faults and how the extension has been distributed between faults.

Additionally, there have been a series of recent earthquakes in Italy (Figure 2.2) and these have exposed fresh fault scarps. These recently exhumed fault surfaces presents an opportunity to further investigate how exposure time affects roughness.

5.6.2 Further improvements to the slip inversion method

There are several improvements that could be made to the code *slipBERI*. Here I shall go through each one in detail.

Solving for dip

Because during this thesis I have largely been concerned with strike-slip faults that I have assumed to be vertical, this was not of key importance. I did incorporate solving for dip within the algorithm, but since this requires re-calculation of the Green's function for every iteration for which the dip is changed, this is very computationally expensive. Since solving for dip was not essential I did not spend time to optimise this solution, but this could be done, particularly if combining with databases of Green's functions such as Pyrocko (*Heimann et al.*, 2017). This would be an important adaptation to make in a situation where dip is poorly constrained.

Solving for strike

Due to the combination of InSAR, aftershocks and surface rupture in this thesis I was able to constrain the fault traces used to an acceptable degree. However, usually the location is not known exactly and in order for an inversion to be objective this should be solved for within the inversion.

Solving for Hurst parameters

The Hurst parameter controls the decay of the von Karman autocorrelation function, and in this thesis I used the averaged values from *Mai and Beroza* (2002)'s meta-analysis. But the results in Chapter 2 have shown that the Hurst parameter is not necessarily consistent across all faults, or indeed along the length of the same fault. This suggests the Hurst parameter should be solved for within the inversion, and that different Hurst parameters may be needed in different areas, perhaps controlled by fault structure.

But for modelling purposes, this small scale variation may not be significant compared to the scale of fault discretisation, and the resolvable scale from the data. Instead larger scale values, such as the measurements of H from several hundred meters along the Campo Felice fault in Chapter 2, may give better estimates of Hurst parameters to include in modelling. Potentially different areas of the fault could be modelled to have different Hurst parameters, but over a scale of kilometers, which is larger than the scale measured in Chapter 2.

Solving for correlation lengths

In both Chapter 3 and 4 I used fixed values of the correlation lengths, a_{as} and a_{dd}, as determined using fault length and fault width using the equations from *Mai and Beroza* (2002). But, as discussed in *Mai and Beroza* (2002), these parameters have their own distributions and uncertainties. These could be solved for within the inversion, drawing directly from their prior distributions as determined by *Mai and Beroza* (2002).

Solving for patch size

A Bayesian inversion is a flexible method, which means that the size of the discrete fault patches could be solved for during this inversion. In many papers the size of the fault patches is increased with depth, to recognise the reduced resolution e.g. *Minson et al.* (2013), or is determined using the data resolution (*Atzori and Antonioli*, 2011, *Barnhart and Lohman*, 2010). Several trans-dimensional methods use self-adapting grids (*Dettmer et al.*, 2014) that change throughout the inversion, so this could be incorporated to limit the effect of choosing patch size in advance of the inversion.

Increasing usage

In order to increase usage and accessibility of the code it could also be integrated it with already established and widely-used software such as GBIS (*Bagnardi and Hooper*, 2018) or re-write it in python.

Benefit of further improvements

Whilst these further improvements represent an ambitious level of software-development, the benefit of their implementation would be to have a significantly more objective method of solving for fault slip, which would hopefully not require the manual tuning that is somewhat essential in Bayesian inversions. In the event of an earthquake we would be able to set an inversion running with fewer biases and allow the inversion to solve for all the required parameters. Thus any conclusions drawn from the final solution would hopefully stand the test of time, with assumptions fully justified and stated.

5.6.3 Assessing fault maturity using slipBERI

The smoothness of a fault affects earthquake nucleation, propagation and termination. Largest slips systematically occur on the most mature half of faults, that are smoother with lower fracture energy (*Perrin et al.*, 2016). This is in keeping with the finding that faults smooth with increasing slip (*Sagy et al.*, 2007, *Brodsky et al.*, 2011), and my results from Chapter 2 that showed Campo Felice, a young fault, shows low Hurst parameters.

A knowledge of the maturity of a fault could be used to set priors of Hurst parameters and correlation lengths for an earthquake that occurs on that fault. Alternatively, we could solve for correlation lengths and Hurst parameters using *slipBERI*, thereby giving an estimate of the smoothness, assuming that the smoothness of a slip distribution relates to the smoothness of a fault, as discussed in Chapter 2 and *Candela et al.* (2011).

Structural maturity, the degree of advancement in the evolution of a fault's structural properties (*Perrin et al.*, 2016), is affected by both fault slip rate but also the rate of healing. Consequently the smoothness of a slip distribution must be based upon both the smoothness of the fault surface and the degree of healing. The age of a fault can be gained from geological evidence, but the healing is difficult to directly compare. By solving for Hurst parameters for earthquakes that occur on faults of known age and known slip rate, we could quantify how the structural maturity of a fault is a trade-off between age and healing.

5.7 Concluding Remarks

In this thesis I have investigated one strand of evidence to suggest that slip should be fractal, as well as presenting a new method to incorporate these fractal properties into earthquake slip inversions. The analysis of fault surfaces in such a detailed way has only been done in the past 12 years (*Renard et al.*, 2006, *Sagy et al.*, 2007), and so investigations like these may yet show many interesting features of fault surfaces. With fault roughness being incorporated into a whole host of earthquake models, we can further target fault roughness investigations with an aim to improve models.

I believe the method of incorporating fractal properties into earthquake slip inversions represents the future of earthquake slip inversions, both in the incorporation of fractal slip and in its Bayesian implementation. By introducing another form of regularisation I hope to make the scientific community question their choice of regularisation, instead of simply using Laplacian smoothing because it is the norm, especially with the rise in observations that fault roughness and fault slip shows fractal properties. By using a Bayesian inversion that solves for the level of smoothing within it I hope that the scientific community will become aware of the bias they may be adding when arbitrarily choosing the level of smoothing. This lack of objectivity means that our slip inversions gradually merge into an accepted idea of what slip solutions should look like. I hope that by incorporating a regularisation based on observed features of fault slip and by solving for smoothing, we can question these solutions and ensure that they are backed up by both the data and observed and quantifiable features of fault slip. Bayesian methods, whilst computationally expensive and undeniably painful, present a wealth of knowledge that I think will be a real benefit to our understanding of earthquakes in the years to come.

References

Atzori, S., and A. Antonioli (2011), Optimal fault resolution in geodetic inversion of coseismic data, *Geophysical Journal International*, *185*(1), 529–538, doi:10.1111/j.1365-246X.2011.04955.x. 5.6.2

Bagnardi, M., and A. Hooper (2018), Inversion of surface deformation data for rapid estimates of source parameters and uncertainties: a Bayesian approach, *Geochemistry, Geophysics, Geosystems*, doi:10.1029/2018GC007585. 5.6.2

Barnhart, W. D., and R. B. Lohman (2010), Automated fault model discretization for inversions for coseismic slip distributions, *Journal of Geophysical Research*, *115*(B10), B10,419, doi:10.1029/2010JB007545. 5.6.2

Brodsky, E. E., J. J. Gilchrist, A. Sagy, and C. Collettini (2011), Faults smooth gradually as a function of slip, doi:10.1016/j.epsl.2010.12.010. 5.6.3

Candela, T., F. Renard, M. Bouchon, J. Schmittbuhl, and E. E. Brodsky (2011), Stress Drop during Earthquakes: Effect of Fault Roughness Scaling, *Bulletin of the Seismological Society of America*, *101*(5), 2369–2387, doi:10.1785/0120100298. 5.6.3

Dettmer, J., R. Benavente, P. R. Cummins, and M. Sambridge (2014), Trans-dimensional finite-fault inversion, *GJI Seismology*, *199*, 735–751, doi:10.1093/gji/ggu280. 5.6.2

Fialko, Y., D. Sandwell, M. Simons, and P. Rosen (2005), Three-dimensional Deformation Caused by the Bam, Iran, Earthquake and the Origin of Shallow Slip Deficit., *Nature*, *435*(7040), 295–9, doi:10.1038/nature03425. 5.4

Foreman-Mackey, D., D. W. Hogg, D. Lang, and J. Goodman (2013), emcee: The MCMC Hammer, *Publications of the Astronomical Society of the Pacific*, *125*, 306–213, doi:10.1086/670067.

Goodman, J., and J. Weare (2010), Ensemble samplers with affine invariance, *Communications in Applied Mathematics and Computational Science*, *5*(1), 65–80, doi:10.2140/camcos.2010.5.65.

Heimann, S., M. Kriegerowski, M. Isken, S. Cesca, S. Daout, F. Grigoli, C. Juretzek, T. Megies, N. Nooshiri, A. Steinberg, H. Sudhaus, H. Vasyura-Bathke, T. Willey, and T. Dahm (2017), Pyrocko - An open-source seismology toolbox and library, *GFZ Data Services*, doi:http://doi.org/10.5880/GFZ.2.1.2017.001. 5.6.2

Mai, P. M., and G. C. Beroza (2002), A Spatial Random Field Model to Characterize Complexity in Earthquake Slip, *Journal of Geophysical Research*, *107*(B11), 2308, doi:10.1029/2001JB000588. 5.6.2, 5.6.2

Milliner, C. W., J. F. Dolan, J. Hollingsworth, S. Leprince, F. Ayoub, and C. Sammis (2015), Quantifying Near-field and Off-fault Deformation Patterns of the 1992 M w 7.3 Landers Earthquake, *Geochemistry, Geophysics, Geosystems*, *16*(5), 1525–2027, doi:10.1002/2014GC005693. 5.2

Minson, S. E., M. Simons, and J. L. Beck (2013), Bayesian Inversion for Finite Fault Earthquake Source Models I–Theory and Algorithm, *Geophysical Journal International*, *194*(3), 1701–1726, doi:10.1093/gji/ggt180. 5.6.2

Perrin, C., I. Manighetti, J.-P. Ampuero, F. Cappa, and Y. Gaudemer (2016), Location of largest earthquake slip and fast rupture controlled by alongstrike change in fault structural maturity due to fault growth, *Journal of Geophysical Research: Solid Earth*, doi:10.1002/2015JB012671. 5.6.3

Renard, F., C. Voisin, D. Marsan, and J. Schmittbuhl (2006), High resolution 3D Laser Scanner Measurements of a Strike-slip Fault Quantify its Morphological Anisotropy at all Scales, *Geophysical Research Letters*, *33*(4), L04,305, doi:10.1029/2005GL025038. 5.7

Ross, Z. E., H. Kanamori, E. Hauksson, and N. Aso (2018), Dissipative intraplate faulting during the 2016 M w 6.2 Tottori, Japan earthquake, *Journal of Geophysical Research: Solid Earth*, *123*(2), 1631–1642, doi:10.1002/2017JB015077. 5.4

Sagy, A., E. E. Brodsky, and G. J. Axen (2007), Evolution of Fault-surface Roughness with Slip, *Geology*, *35*(3), 283, doi:10.1130/G23235A.1. 5.6.3, 5.7

Weston, J., A. M. Ferreira, and G. J. Funning (2011), Global compilation of interferometric synthetic aperture radar earthquake source models: 1. Comparisons with seismic catalogs, *Journal of Geophysical Research*, *116*(B8), B08,408, doi:10.1029/2010JB008131. 5.1.2

Wilkinson, M., G. P. Roberts, K. McCaffrey, P. A. Cowie, J. P. Faure Walker, I. Papanikolaou, R. J. Phillips, A. M. Michetti, E. Vittori, L. Gregory, L. Wedmore, and Z. K. Watson (2015), Slip distributions on active normal faults measured from LiDAR and field mapping of geomorphic offsets: an example from L'Aquila, Italy, and implications for modelling seismic moment release, *Geomorphology*, *237*, 130–141, doi:10.1016/j.geomorph.2014.04.026. 5.2

Zielke, O., M. Galis, and P. M. Mai (2017), Fault roughness and strength heterogeneity control earthquake size and stress drop, *Geophysical Research Letters*, doi:10.1002/2016GL071700. 5.3

Appendix A

Appendix for Chapter 2

Appendix for Chapter 2.

Site	**UTM x**	**UTM y**
A	370863	4677147
B	370930	4677029
C	370993	4676979
D	371006	4676969
E	371048	4676921
F	371175	4676846
G	371198	4676827
H	371536	4676305
I	371661	4676246
J	371692	4676232
K	371735	4676217
L	371746	4676206
M	371753	4676204
N	371823	4676196

Table A.1: Locations of the scanner sites in this study. For approximate location on the fault see Chapter 2 Figure 2.5. UTM Zone 33 T in WGS 84.

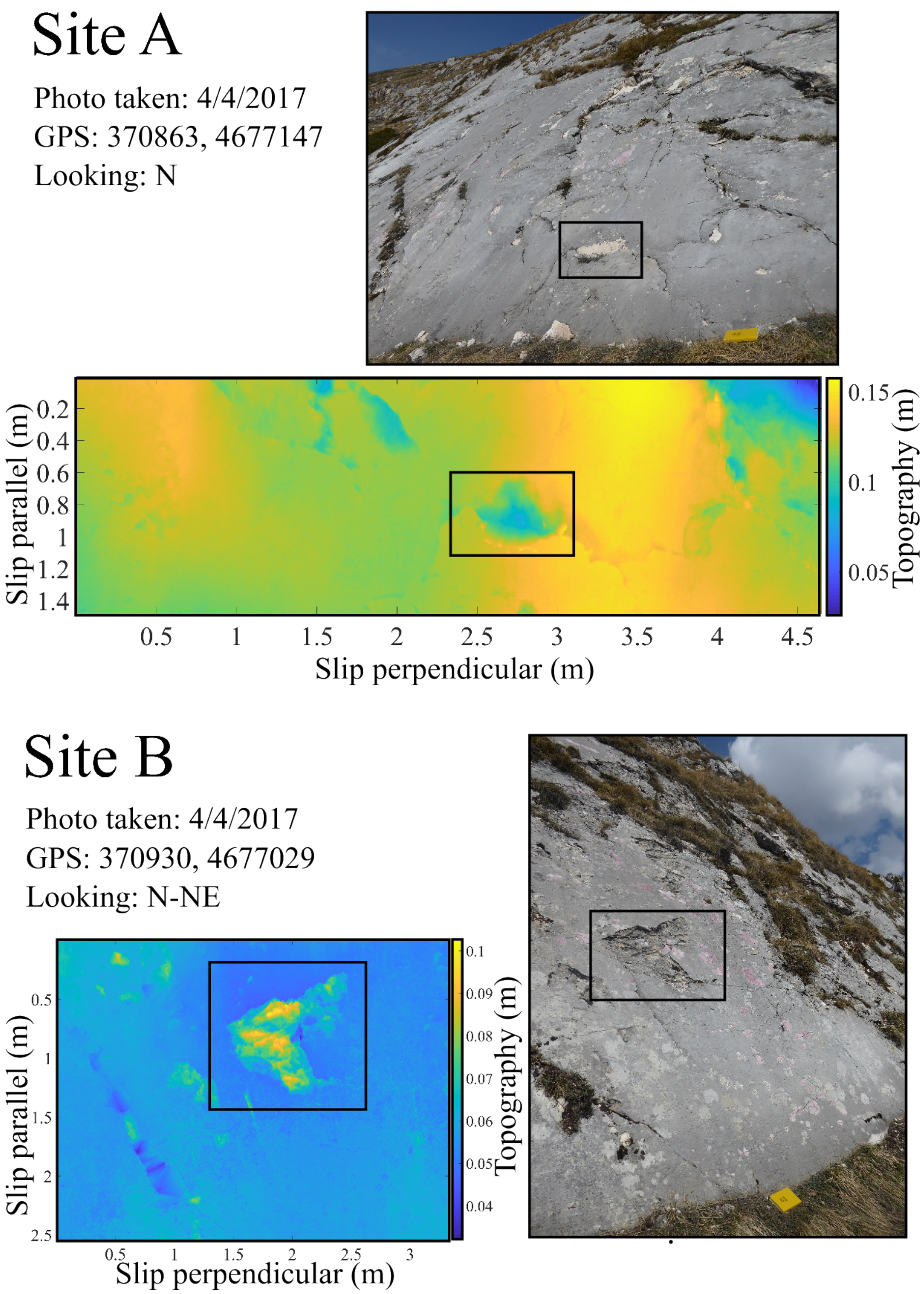

Figure A.1: Field photo and gridded dataset upon which analysis was performed for sites A and B. Boxes show same feature in photograph and scan. Yellow field notebook for scale.

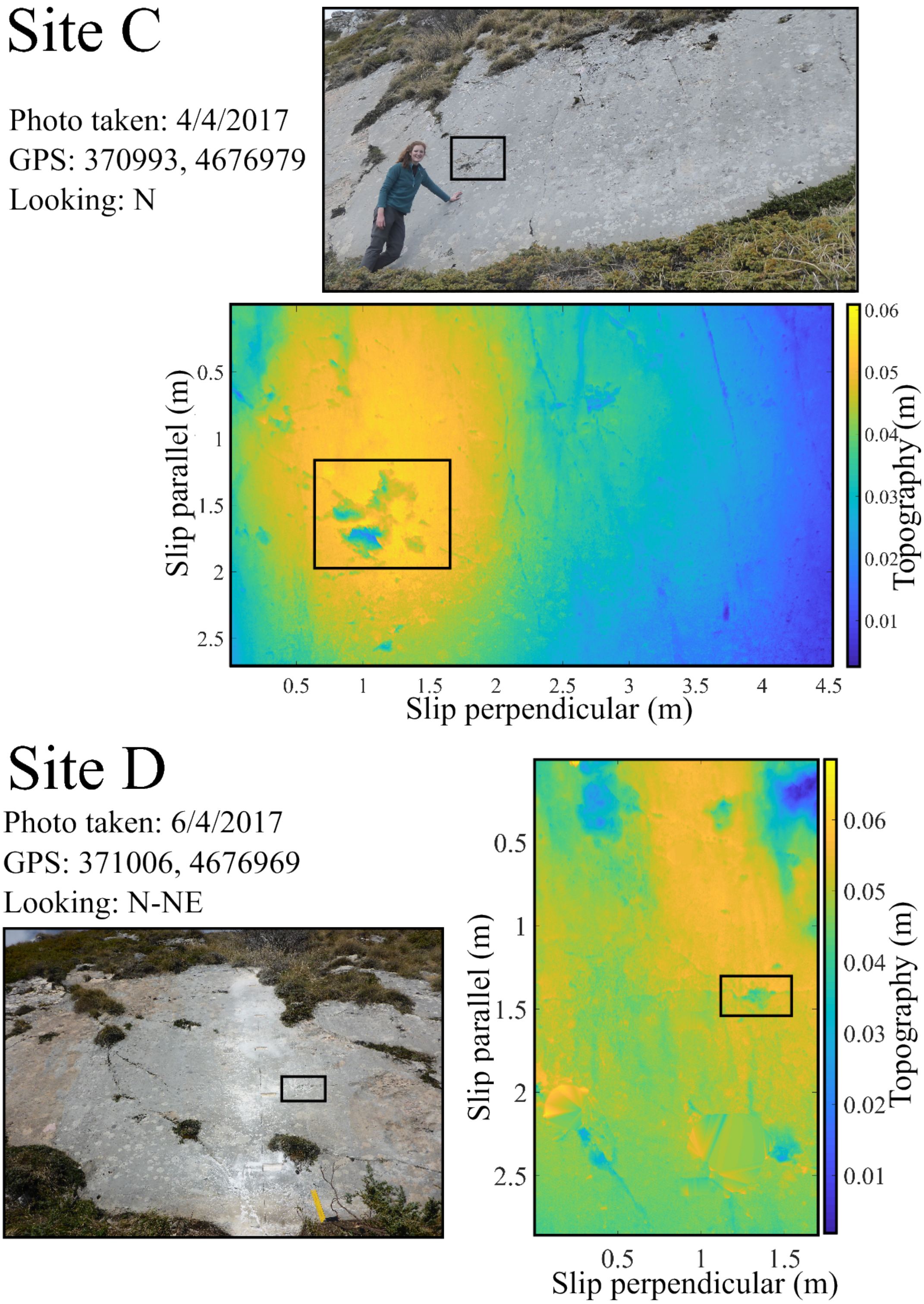

Figure A.2: Field photo and gridded dataset upon which analysis was performed for sites C and D. Boxes show same feature in photograph and scan. Yellow field notebook (bottom) or author (top) for scale.

Site E

Photo taken: 8/4/2017, GPS: 371048, 4676921, Looking: NE

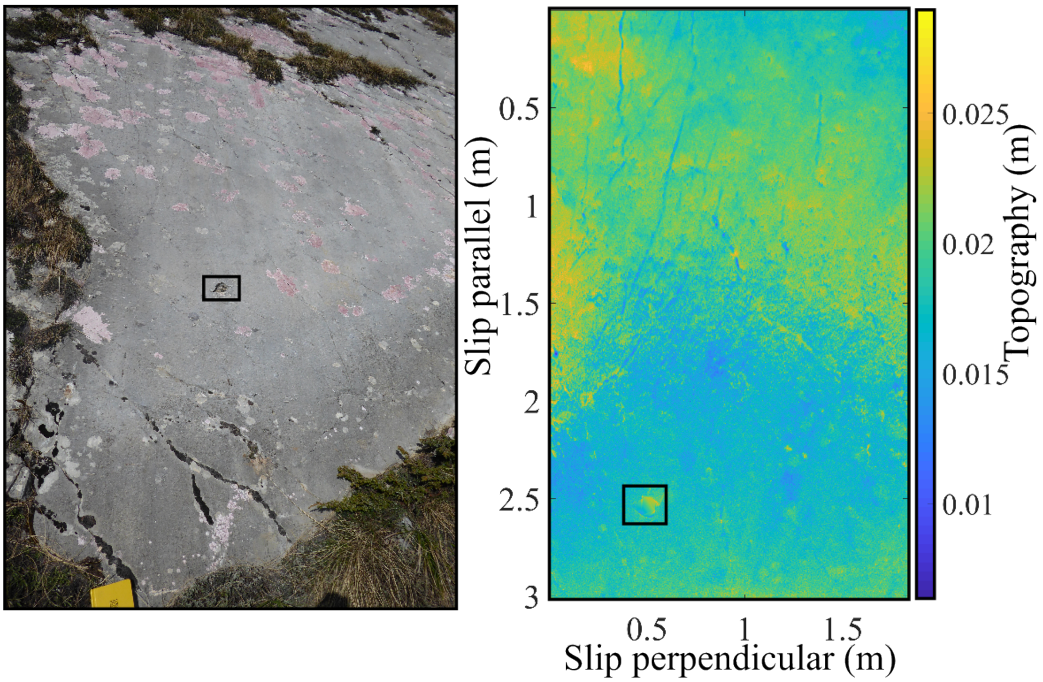

Site F

Photo taken: 8/4/2017, GPS: 371175, 4676846, Looking: N-NE

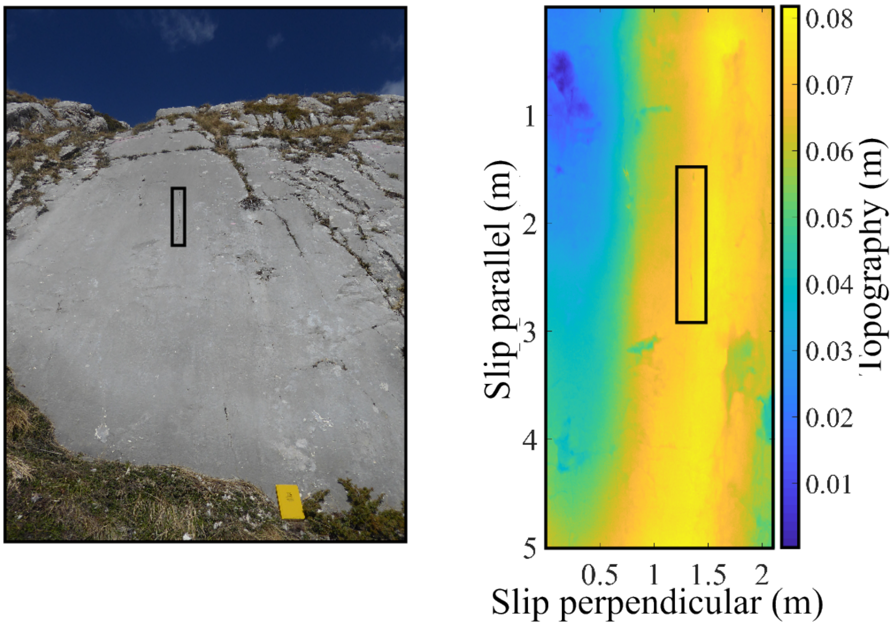

Figure A.3: Field photo and gridded dataset upon which analysis was performed for sites E and F. Boxes show same feature in photograph and scan. Yellow field notebook for scale.

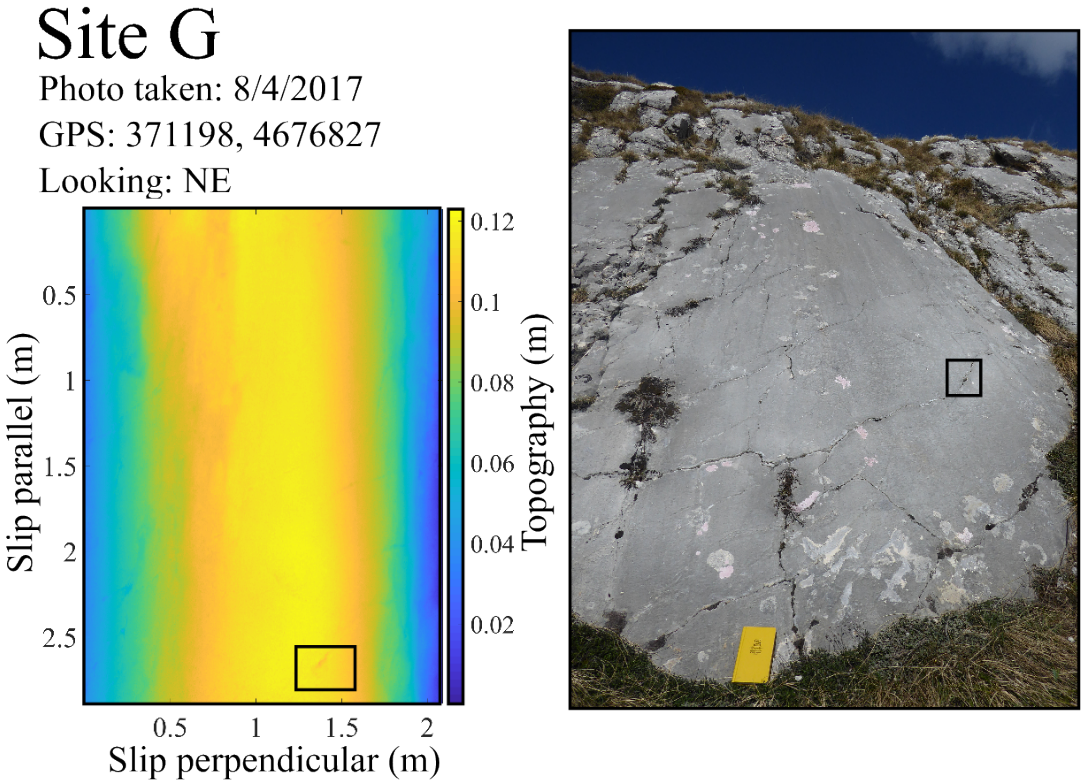

Site G

Photo taken: 8/4/2017

GPS: 371198, 4676827

Looking: NE

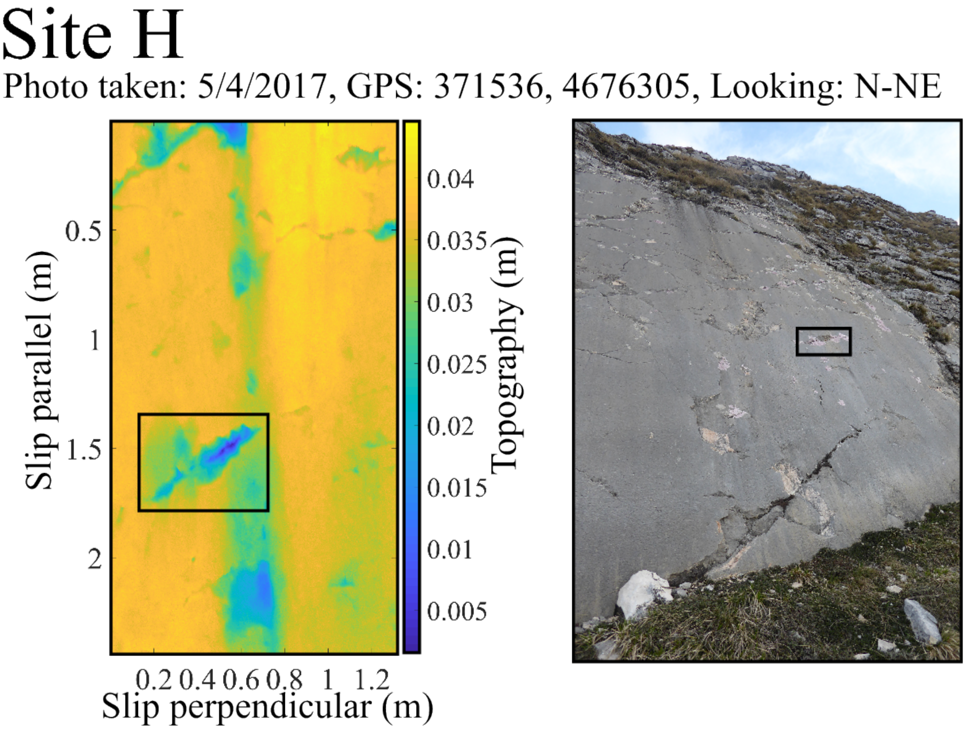

Site H

Photo taken: 5/4/2017, GPS: 371536, 4676305, Looking: N-NE

Figure A.4: Field photo and gridded dataset upon which analysis was performed for sites G and H. Boxes show same feature in photograph and scan. Yellow field notebook for scale.

Site I

Photo taken: 5/4/2017, GPS: 371661, 4676246, Looking : N-NE

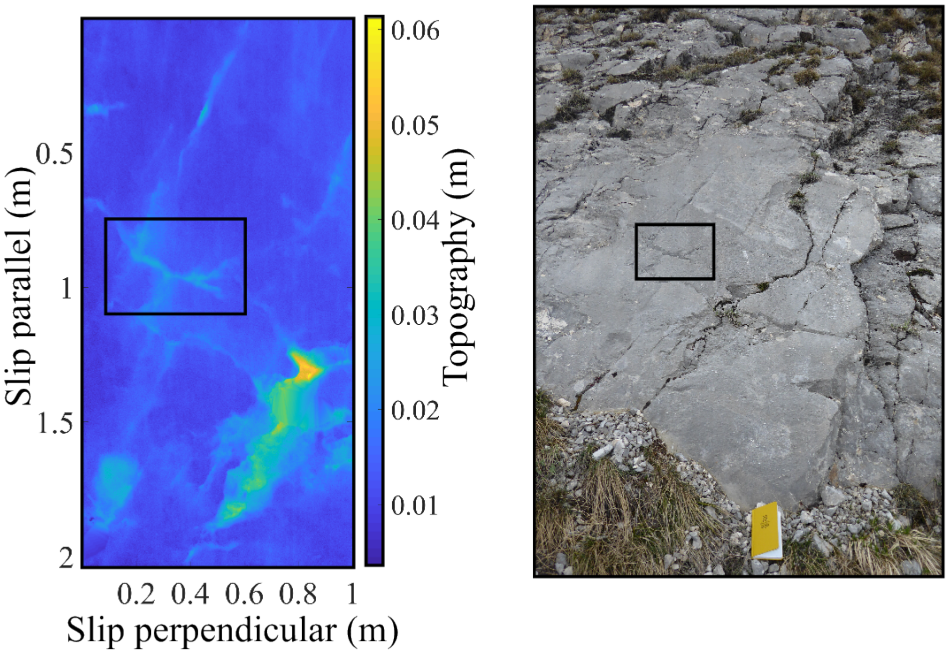

Site J

Photo taken: 5/4/2017

GPS: 371692, 4676232

Looking: N

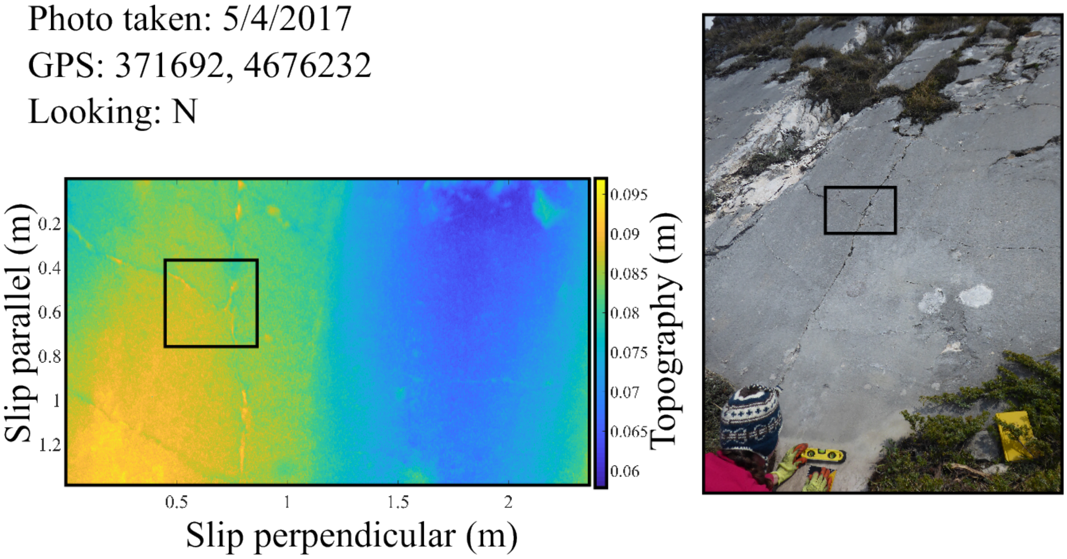

Figure A.5: Field photo and gridded dataset upon which analysis was performed for sites I and J. Boxes show same feature in photograph and scan. Yellow field notebook for scale.

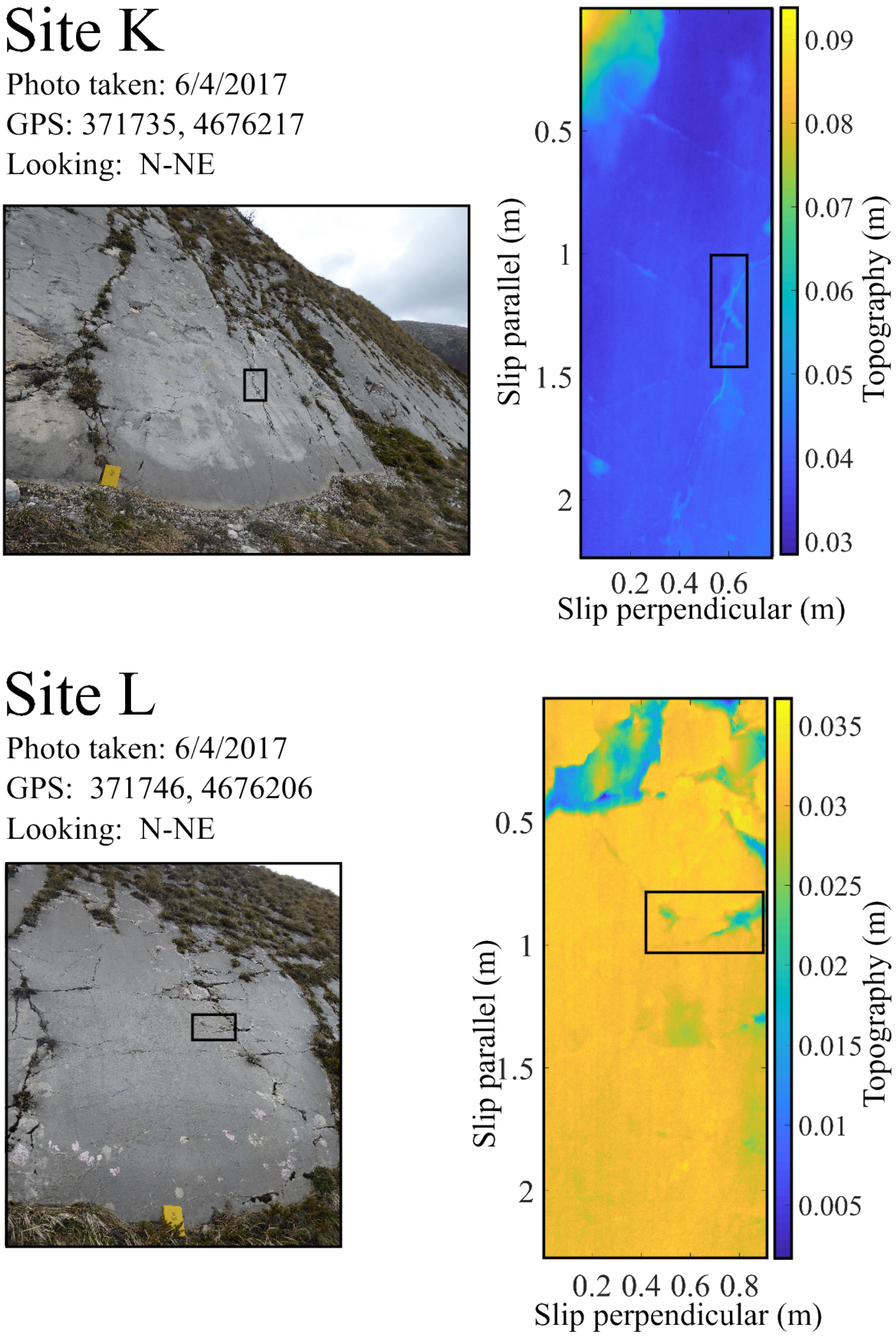

Figure A.6: Field photo and gridded dataset upon which analysis was performed for sites K and L. Boxes show same feature in photograph and scan. Yellow field notebook for scale.

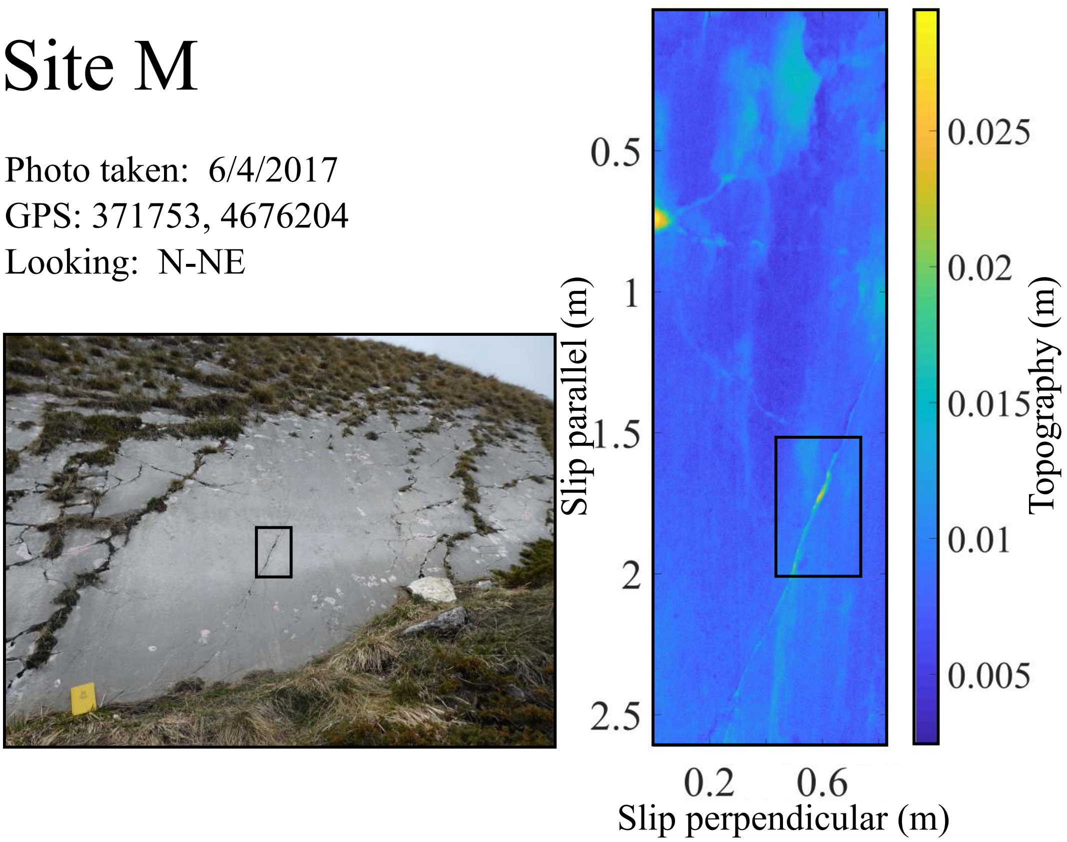

Site M

Photo taken: 6/4/2017
GPS: 371753, 4676204
Looking: N-NE

Site N

Photo taken: 6/4/2017, GPS: 371823, 4676196, Looking: N-NE

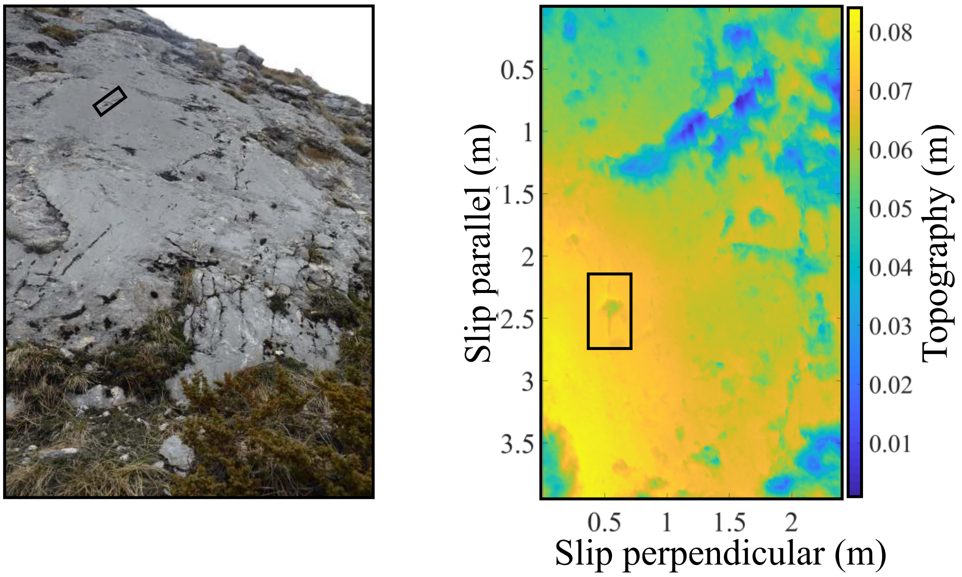

Figure A.7: Field photo and gridded dataset upon which analysis was performed for sites M and N. Boxes show same feature in photograph and scan. Yellow field notebook for scale.

Appendix B

Appendix for Chapter 3

Appendix for Chapter 3. This appears as the Supplementary materials in *Amey et al.* (2018).

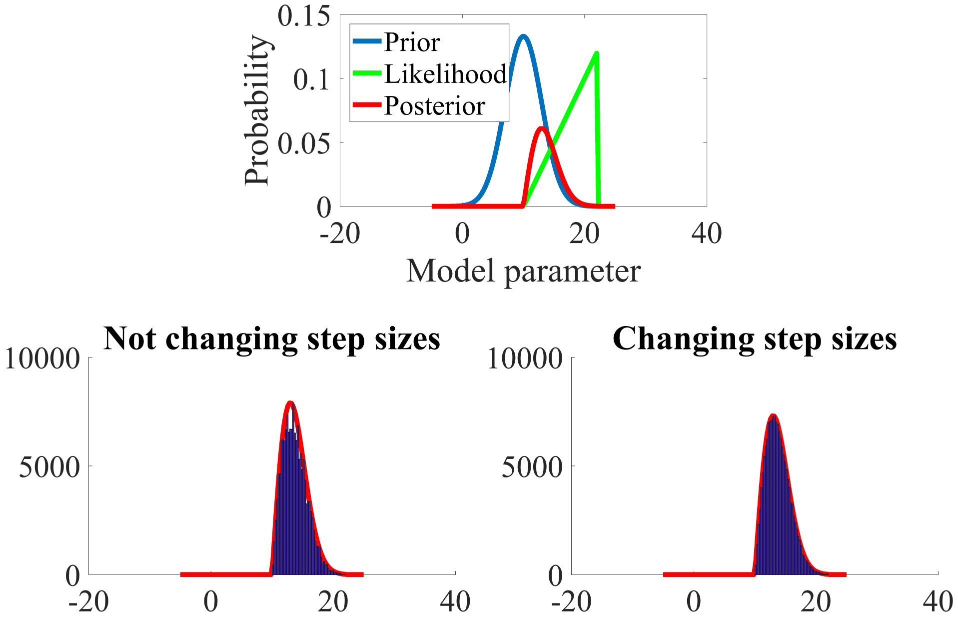

Figure B.1: We perform a 'dummy test' to illustrate that changing step sizes does correctly sample the prior, for one model parameter. We use a Gaussian prior (mean of 10, standard deviation of 3) and a saw-function likelihood to generate the posterior as shown in the top figure. We use a boxcar of ±20 as an inefficiently high starting step-size distribution and compare not changing the step size to an inversion in which the step size is changed. For the same number of iterations (15,0000), the inversion in which step size is permitted to change decreases its step size to $\sim$2 and converges (bottom right), whereas more iterations are needed to converge for the inversion in which step sizes does not change (bottom left). We note that for a simple test like this, unless the step size for the constant step size inversion is chosen to be unreasonably high, the inversion with changing step sizes will converge after approximately the same number of iterations as the inversion with fixed step size. The sensitivity test is also computationally expensive and slows down the inversion. So for very simple situations it may not improve efficiency. But for inversions with several hundred model parameters we find changing step sizes can dramatically reduce the number of iterations needed for convergence, or may be necessary to ensure an MCMC chain does not get stuck.

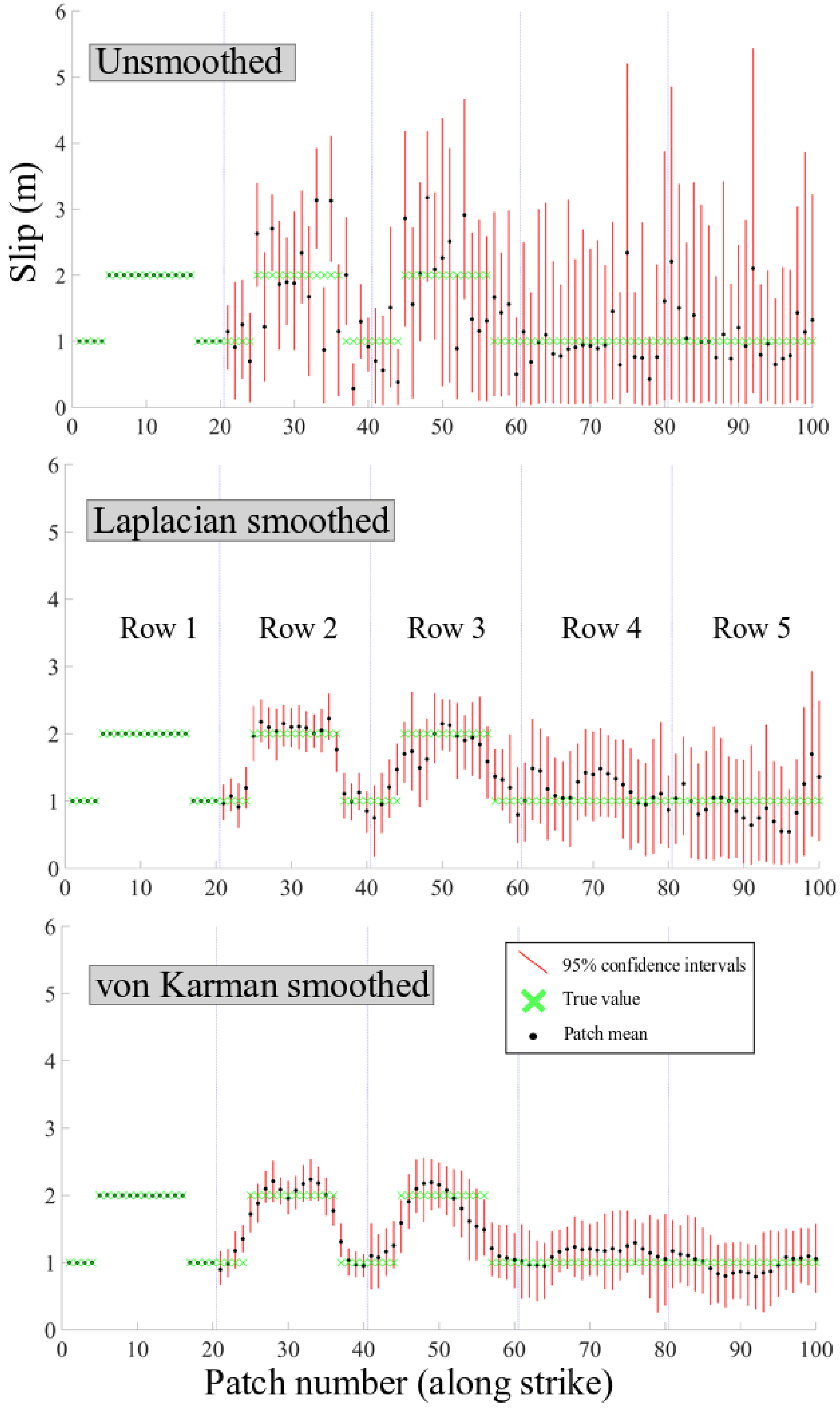

Figure B.2: Confidence intervals (red), true values (green cross) and patch means (black dot) for the three regularization types for uniform surface input slip. Confidence intervals are significantly smaller for von Karman regularization than the other two types.

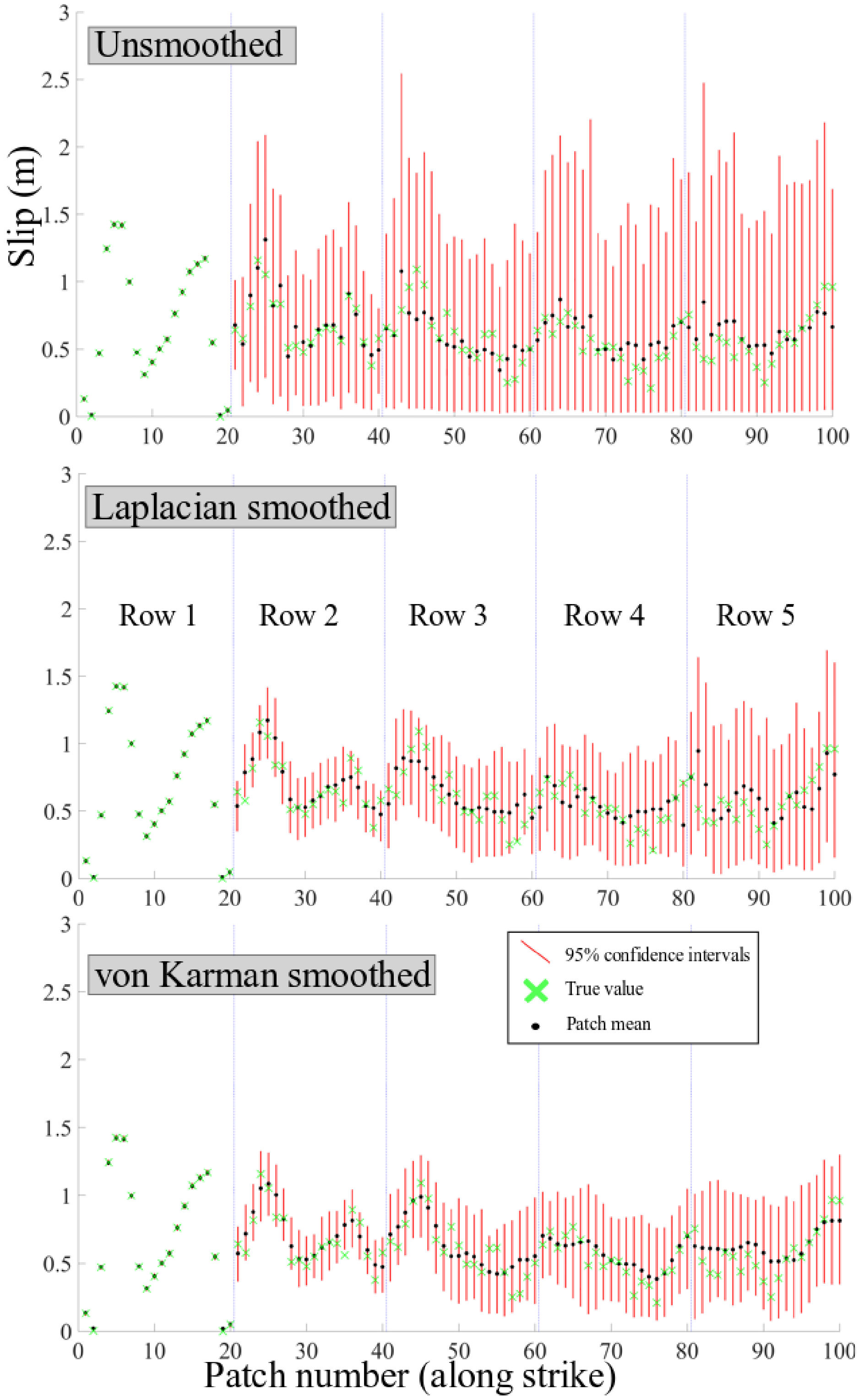

Figure B.3: Confidence intervals (red), true values (green cross) and patch means (black dot) for the three regularization types for Laplacian input slip. Confidence intervals are significantly smaller for von Karman regularization than the other two types.

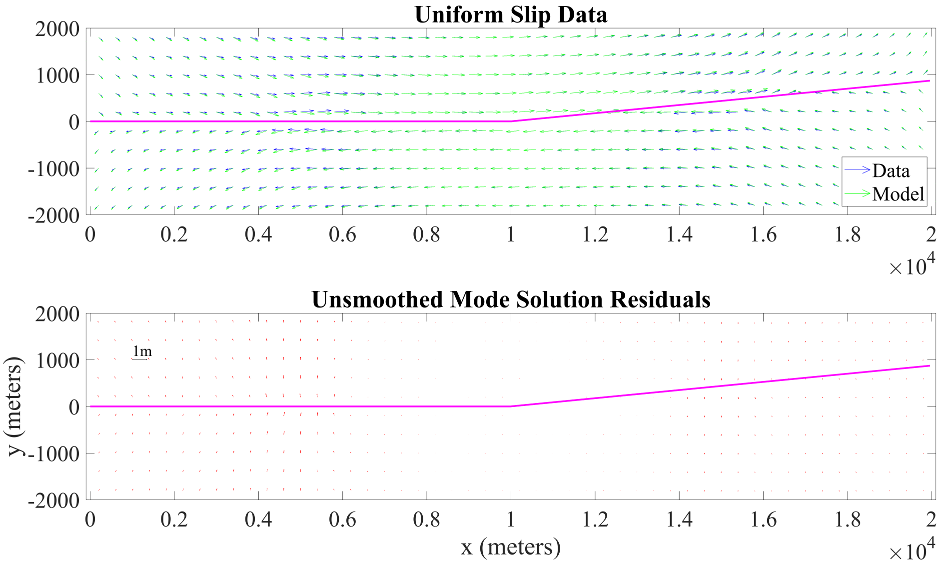

Figure B.4: Data, model and residuals for synthetic test performed with simple uniform slip input data and an unsmoothed inversion. We only show residuals nearest to the fault where they are largest.

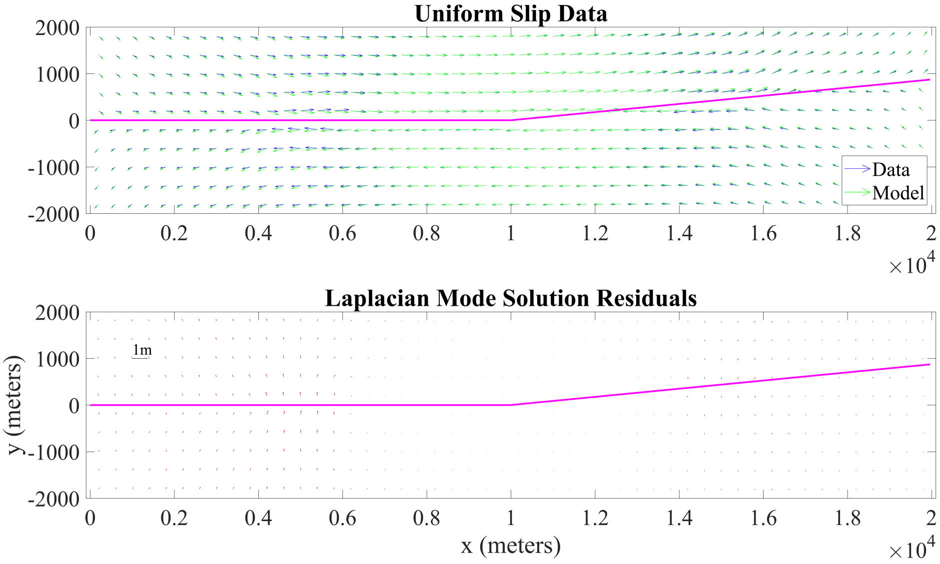

Figure B.5: Data, model and residuals for synthetic test performed with simple uniform slip input data and a Laplacian smoothed inversion. We only show residuals nearest to the fault where they are largest.

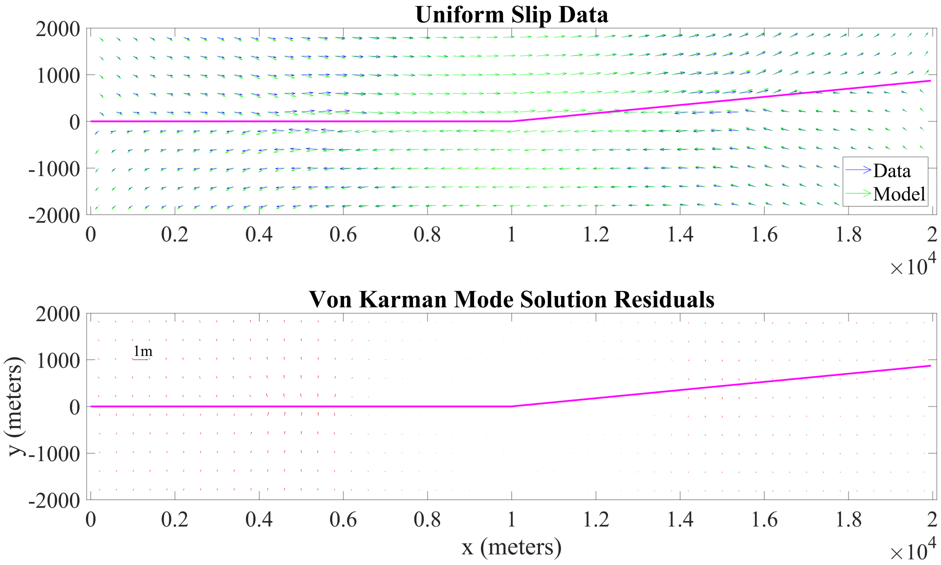

Figure B.6: Data, model and residuals for synthetic test performed with simple uniform slip input data and a von Karman regularized inversion. We only show residuals nearest to the fault where they are largest.

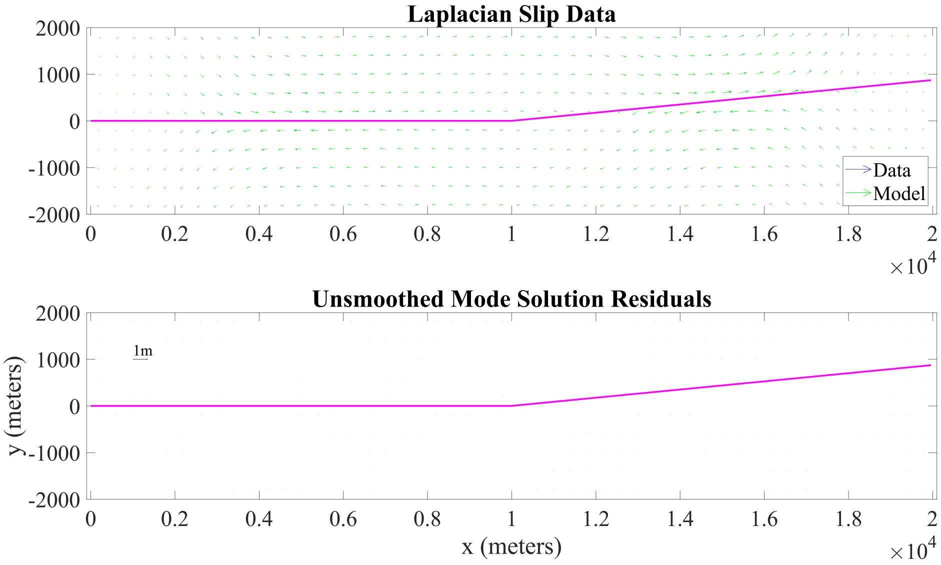

Figure B.7: Data, model and residuals for synthetic test performed with Laplacian slip input data and an unsmoothed regularized inversion. We only show residuals nearest to the fault where they are largest.

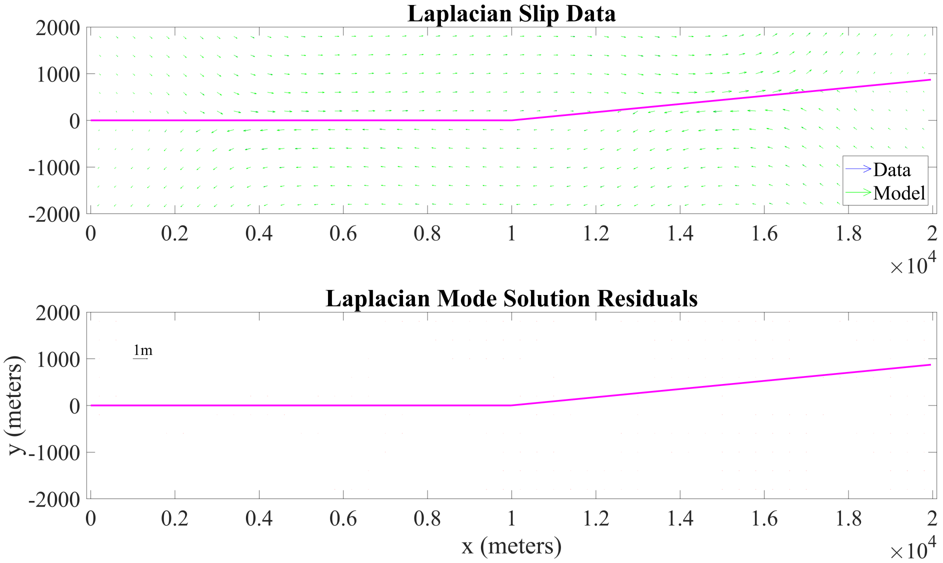

Figure B.8: Data, model and residuals for synthetic test performed with Laplacian slip input data and a Laplacian smoothed inversion. We only show residuals nearest to the fault where they are largest.

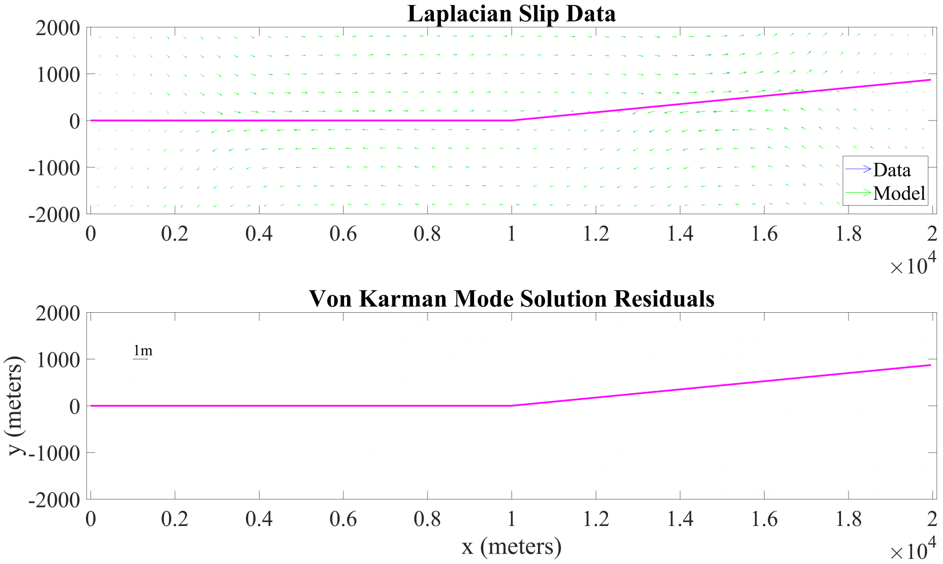

Figure B.9: Data, model and residuals for synthetic test performed with Laplacian slip input data and a von Karman regularized inversion. We only show residuals nearest to the fault where they are largest.

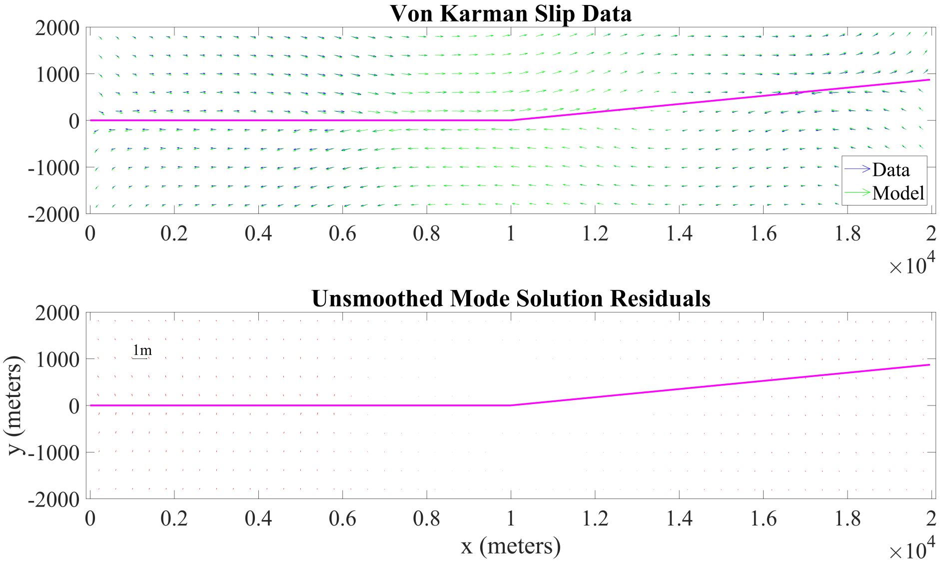

Figure B.10: Data, model and residuals for synthetic test performed with von Karman slip input data and an unsmoothed inversion. We only show residuals nearest to the fault where they are largest.

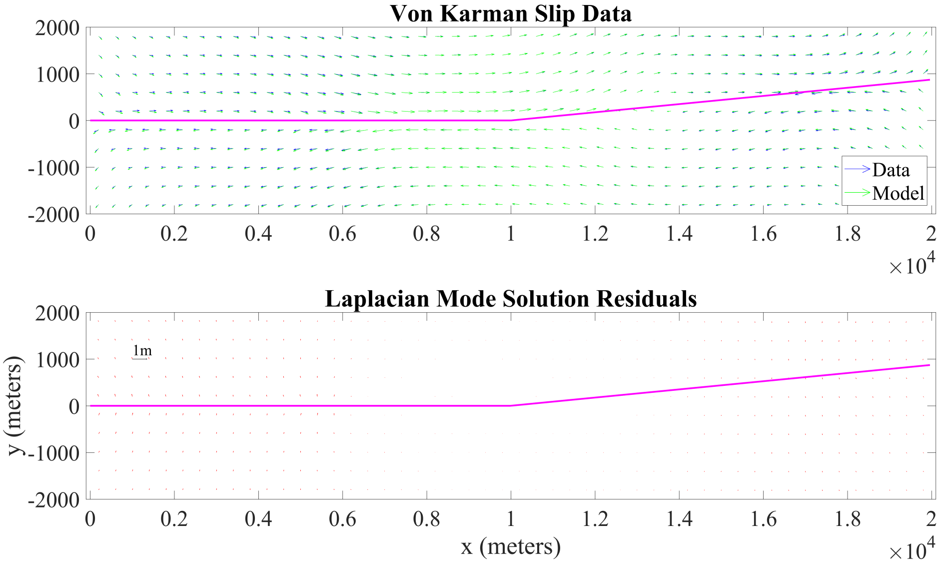

Figure B.11: Data, model and residuals for synthetic test performed with von Karman slip input data and a Laplacian smoothed inversion. We only show residuals nearest to the fault where they are largest.

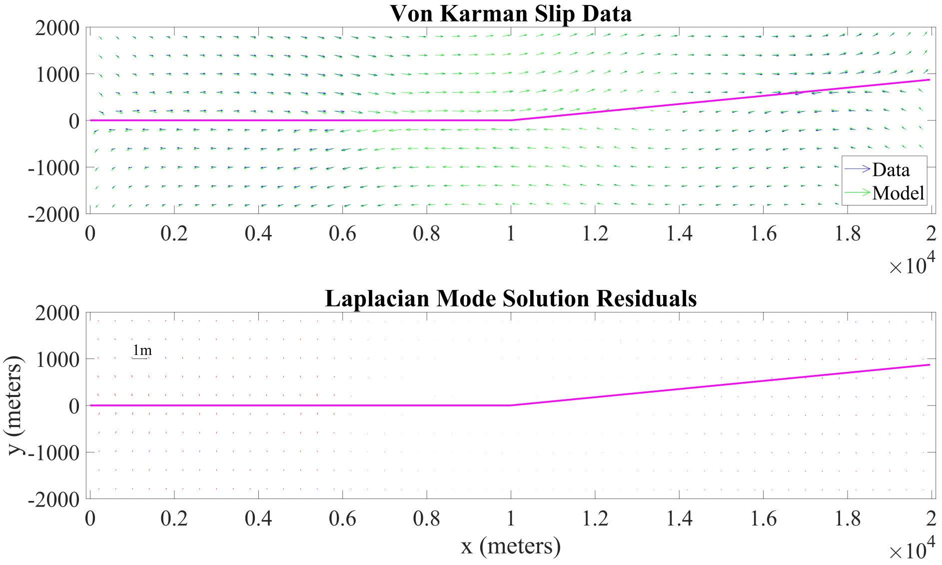

Figure B.12: Data, model and residuals for synthetic test performed with von Karman slip input data and von Karman regularised inversion. We only show residuals nearest to the fault where they are largest.

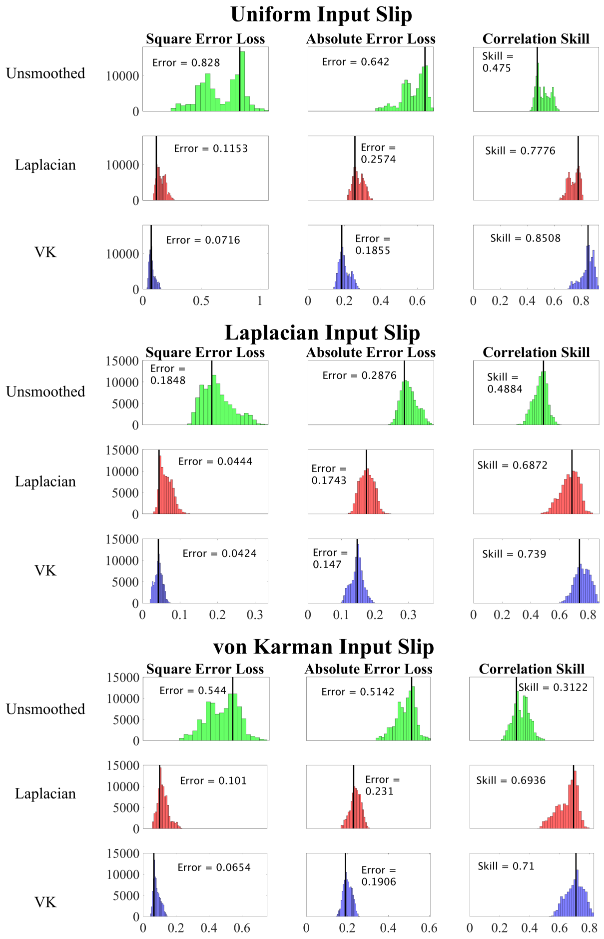

Figure B.13: Three loss functions of the three inversion types (unsmoothed, Laplacian smoothed and von Karman regularized) for three input slip distributions discussed in Figure 3 of the main text. We briefly explain the use of loss functions to compare slip models here, but see *Zhang et al.* (2015) for full details. For each input slip distribution, the x-axis for the plots corresponding to the same loss metric are identical, and for each regularization style the y-axis is the same for the three different metrics. The square error loss function is given by: $g[Z(s_i), \hat{Z}_p(s_i)] = [Z(s_i) - \hat{Z}_p(s_i)]^2$ where $Z(s_i)$ is the model slip on slip patch i and $\hat{Z}_p(s_i)$ is the true slip on slip patch i. The absolute error loss function is given by $g[Z(s_i), \hat{Z}_p(s_i)] = |Z(s_i) - \hat{Z}_p(s_i)$. The correlation skill function is given by $g[Z(s_i), \hat{Z}_p(s_i)] = \frac{n}{(n-1)\hat{\sigma}_z\hat{\sigma}_p}[Z(s_i) - \bar{Z}][\hat{Z}_p(s_i) - \bar{Z}_p]$. Where $\bar{Z}$ is the mean of the model slip across all patches, $\bar{Z}_p$ is the mean of the true slip across all patches, n is the total number of slip patches, $\hat{\sigma}_Z$ is the standard deviation of the model slip patches across all patches and $\hat{\sigma}_p$ is the standard deviation of the true slip across all patches. The mean (for all patches) square error loss and mean absolute error loss give an indication of how well the inversion is matching the magnitude of slip (lower values are better), whereas the mean correlation skill gives an indication of how well the inversion is matching the location of slip (higher values are better).In order to properly compare the Bayesian solutions, we take a representative sample (every 10 saved trials) of each Bayesian solution. For each sample we compute the three mean loss functions and compute the histograms shown in Figure S11. We consider primarily the peak of the histogram, i.e. the modal mean loss function. This Figure shows that the modal mean square error loss and modal mean absolute error loss function for a von Karman regularized result is smaller than for a Laplacian or unsmoothed inversion, for all three input slip distributions, showing that the von Karman solution better matches the magnitude of the input slip. The von Karman solution also has a higher modal mean correlation skill than the Laplacian or unsmoothed solutions for all three input slip distributions, showing that the von Karman better matches the areas of high slip. Therefore the von Karman method is outperforming the Laplacian and unsmoothed inversions in all criteria for uniform slip, Laplacian slip and von Karman slip, though we note that in the case of Laplacian input slip the von Karman method only outperforms the Laplacian by a marginal amount.

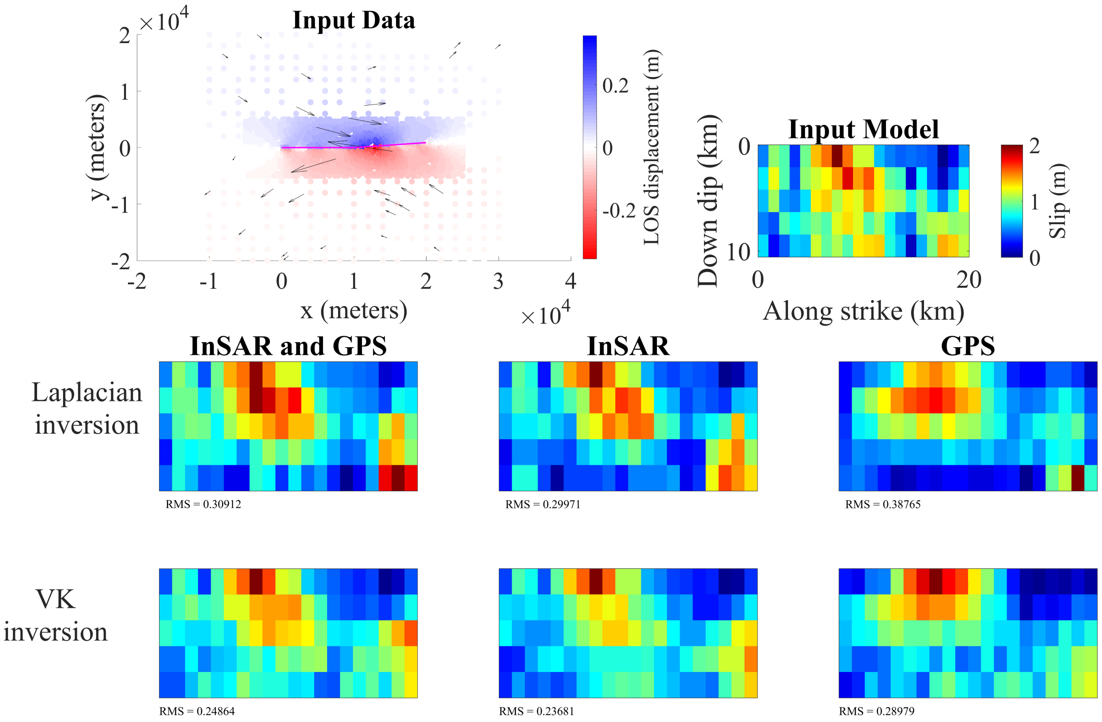

Figure B.14: Slip solutions obtained from von Karman and Laplacian regularized inversions using InSAR synthetic data alone, GPS synthetic data alone and both InSAR- and GPS synthetic data for von Karman input slip. The von Karman regularized solutions (bottom row) fit the input slip model better than the Laplacian smoothed solutions in all cases, as indicated by the lower RMS value, where RMS is the root mean square misfit to the input model. For the GPS-only dataset both solutions are clearly oversmoothed. We perform further comparison between the solutions in Appendix B Figure B.15.

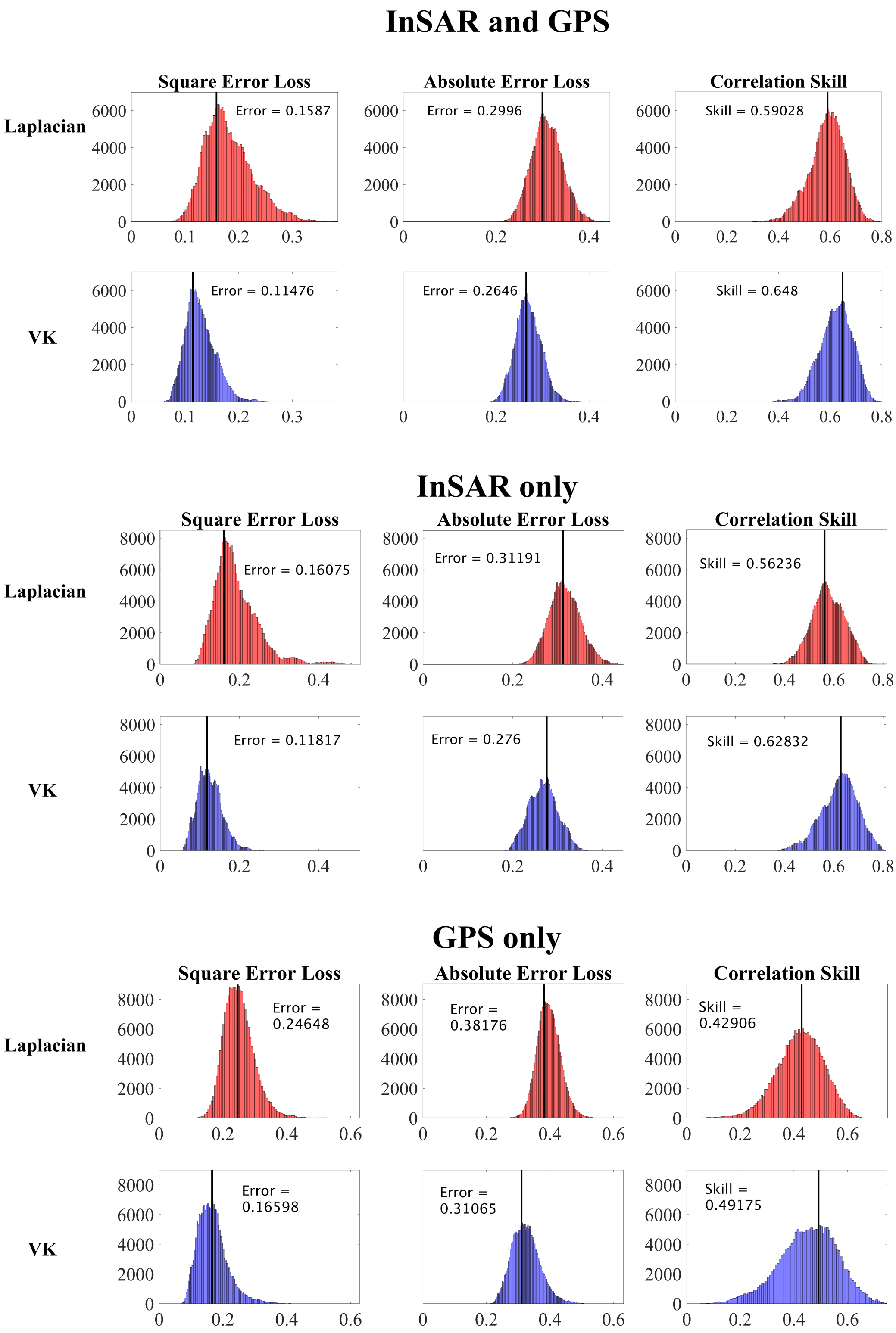

Figure B.15: Comparison of Laplacian and von Karman MAP solutions, using InSAR+GPS, InSAR only and GPS only data for von Karman input slip. We use the same metrics and the same method discussed above in Figure B.15, i.e. calculating the square error loss, absolute error loss and correlation skill for a representative sample of all the saved trials for the von Karman and Laplacian solution. As is evident from the histograms, the mode value for square error loss and absolute error loss is smaller for von Karman than the Laplacian for all three data sets (InSAR and GPS, InSAR only and GPS only). This means that the von Karman is matching the magnitude of slip better in all these cases; the error is lower. The mode value of correlation skill is higher for the von Karman than the Laplacian for all three datasets, meaning that the von Karman captures the location of slip better than the Laplacian regardless of the datatype.

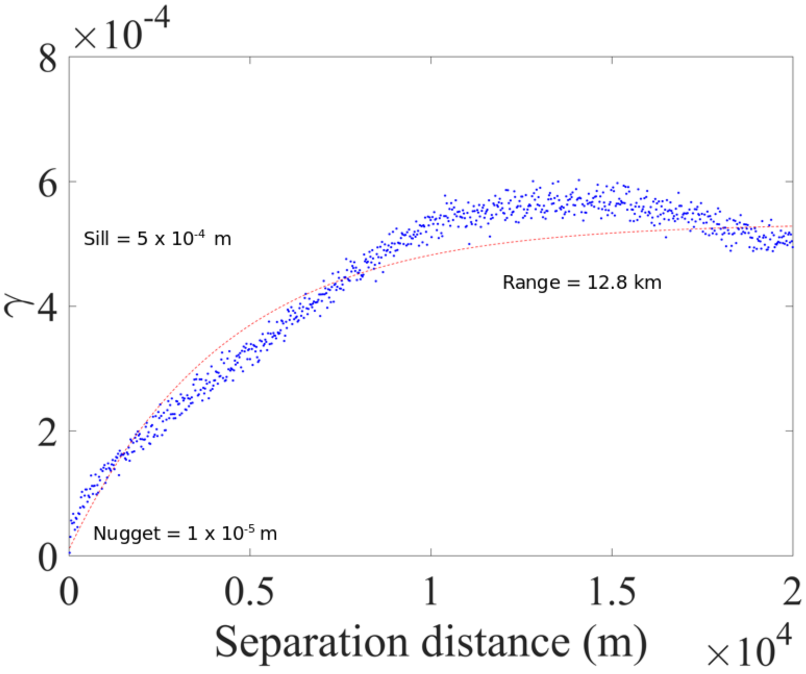

Figure B.16: Semivariogram for an undeforming region of the Napa Valley interferogram. We have indicated the nugget, which is the semivariance at zero lag, the sill, which is the maximum semivariance and the range, which is the distance at which the semivariance reaches 95% of the maximum.

Laplacian

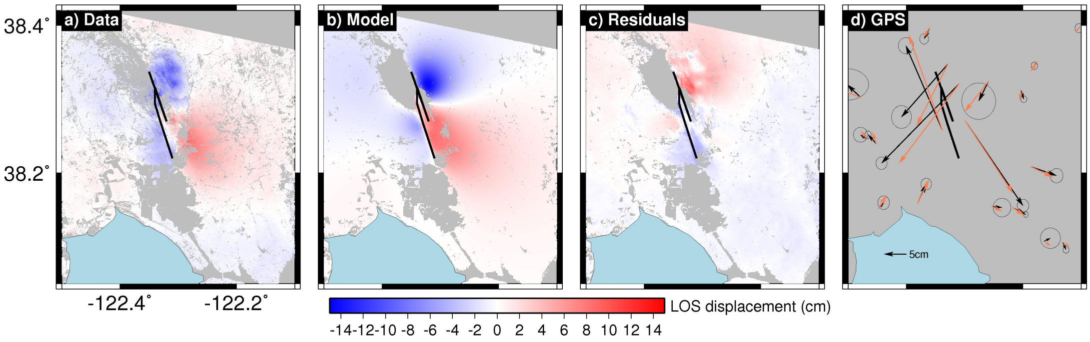

von Karman

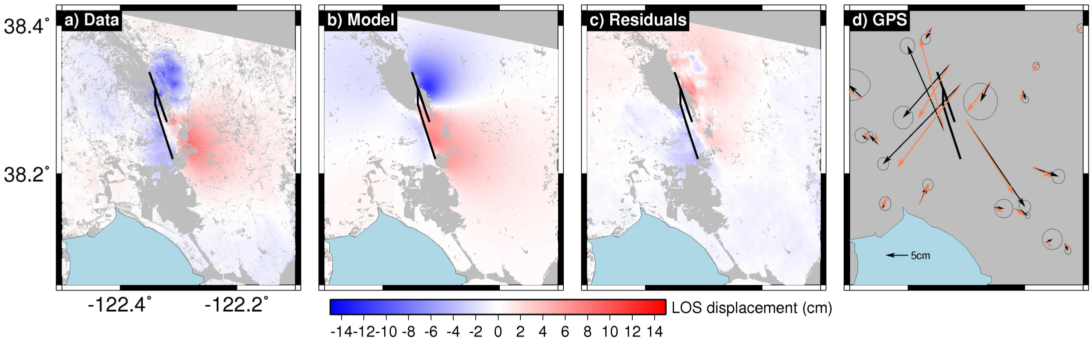

Figure B.17: Top shows fit to data for the Laplacian model shown in Figure 3.9. The residuals are larger than for the von Karman solution shown in Figure 3.8, so below we have replotted the von Karman fit to data on the same scalebar as the Laplacian to allow for direct comparison. The Laplacian model has larger residuals in the north-east of the northern fault and also on the eastern side of the Southern fault than the von Karman solution. Both fit the GPS almost equally as well.

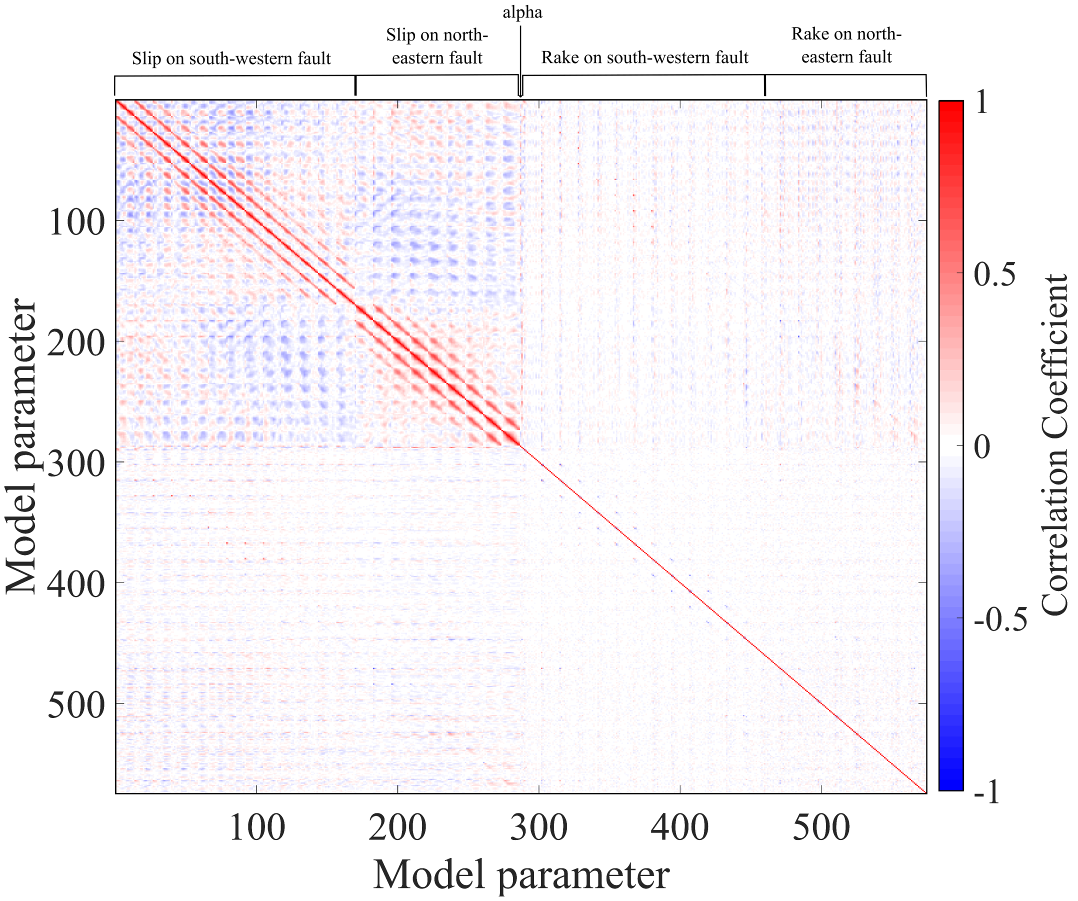

Figure B.18: Correlation coefficients between each model parameter, for their full distributions. Red indicates positive correlation, blue indicates negative correlation. For slip, the signal is largely dominated by the von Karman regularization ensuring patches located close together have similar magnitude slip. In the following figures we explore some of the features identified by this matrix.

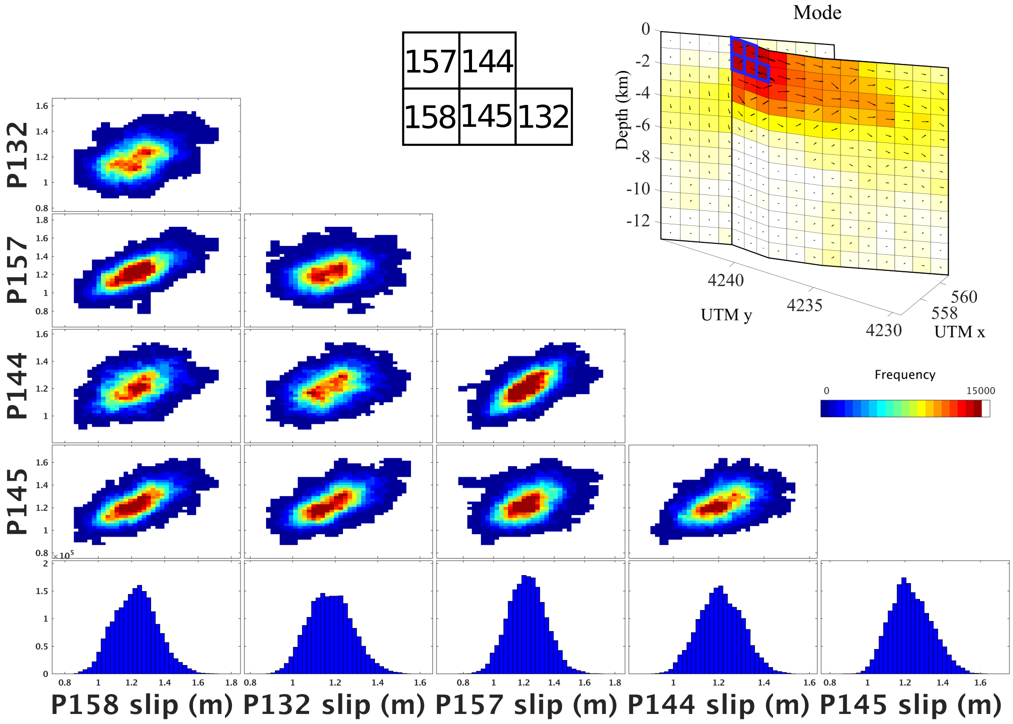

Figure B.19: 2D PDFs to illustrate strong-positive correlation between the magnitude of slip for the five patches with the largest magnitude of slip, indicated by blue squares on fault. This correlation is largely due to the von Karman regularization, since they are all within correlation distances of each other.

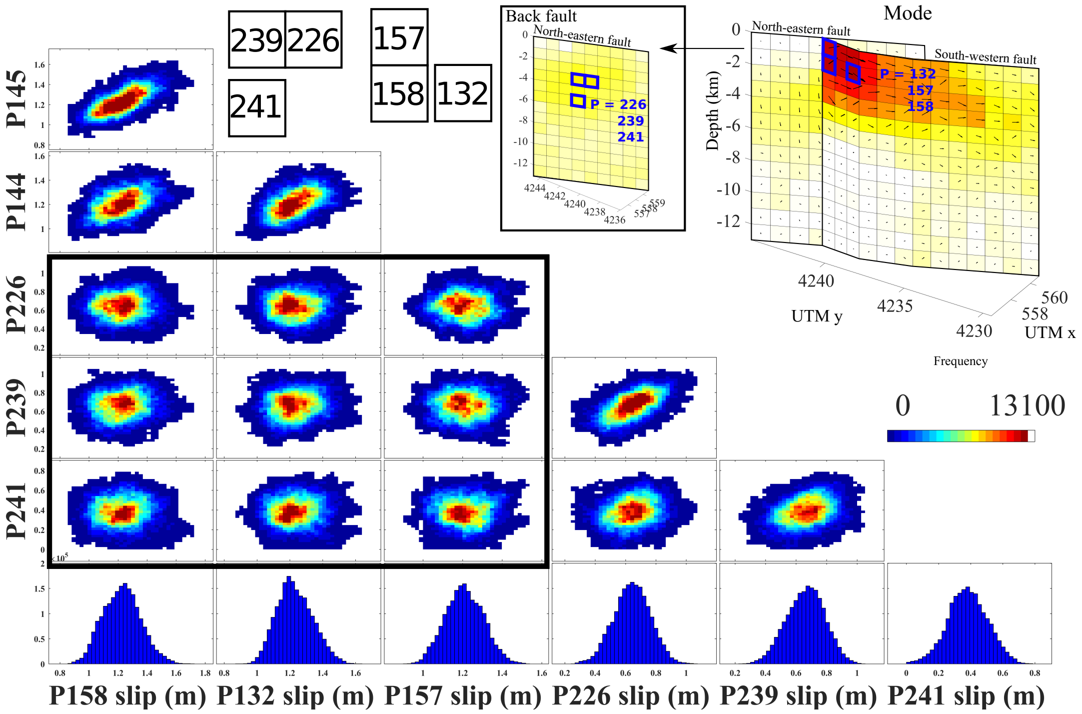

Figure B.20: 2D PDFs indicating that there is no correlation between the magnitude of slip of the patches on the south-eastern fault with maximum slip and the patches on the north-western fault with maximum slip. The histograms for patches from different faults are indicated by the black box: there is observed correlation between slip of patches on the same fault, since they are within correlation length distance of each other.

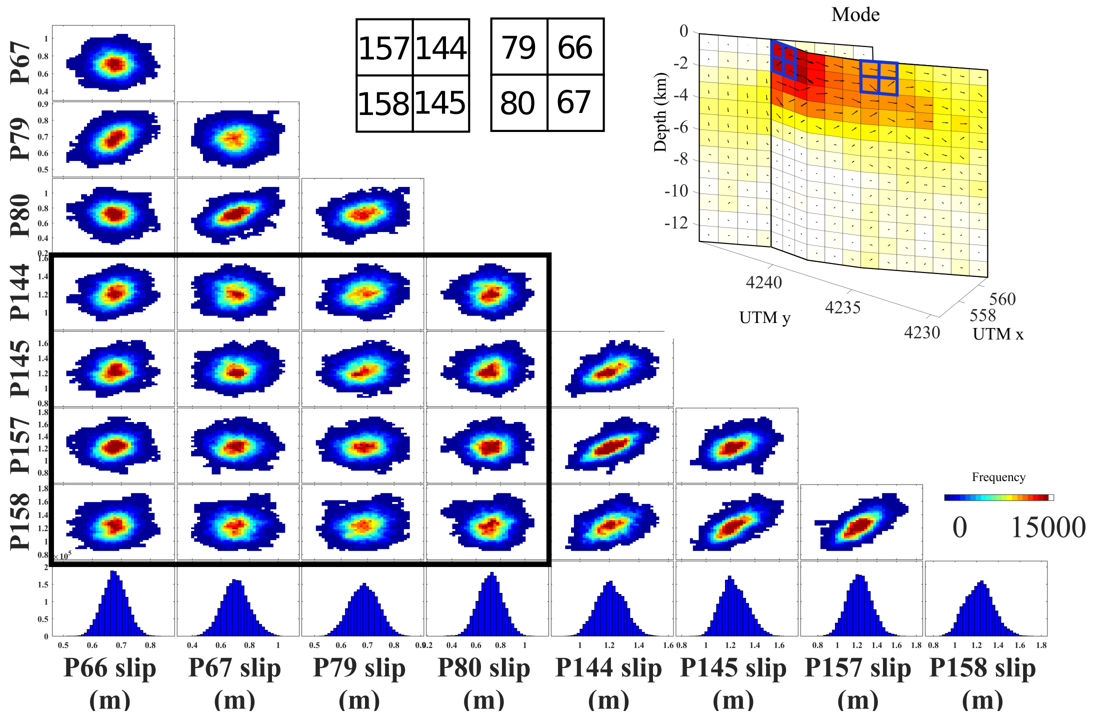

Figure B.21: 2D PDFs of slip magnitude for slip patches along-strike of each other on the south-western fault, indicating that there is no correlation between them.

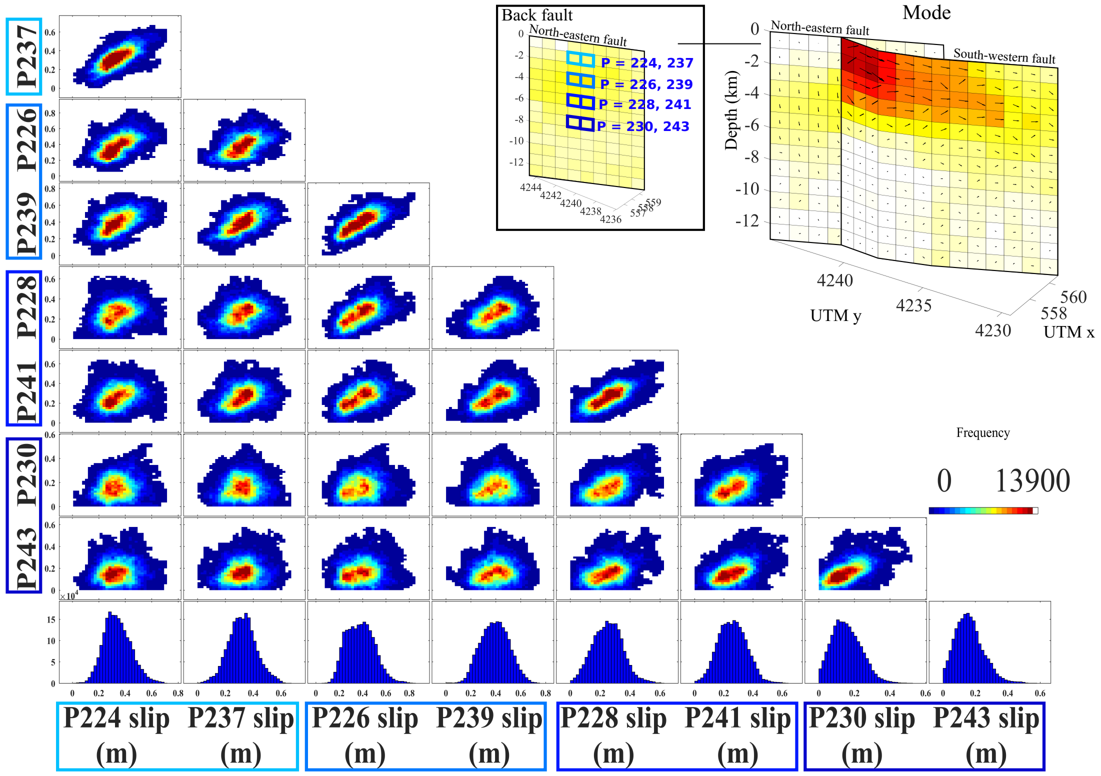

Figure B.22: 2D PDFs exploring whether there is correlation between slip magnitude on patches with increasing depth, on the north-eastern fault. We find that at the largest distance there is no correlation, and that closer patches are correlated, which we deduce to be due to regularization.

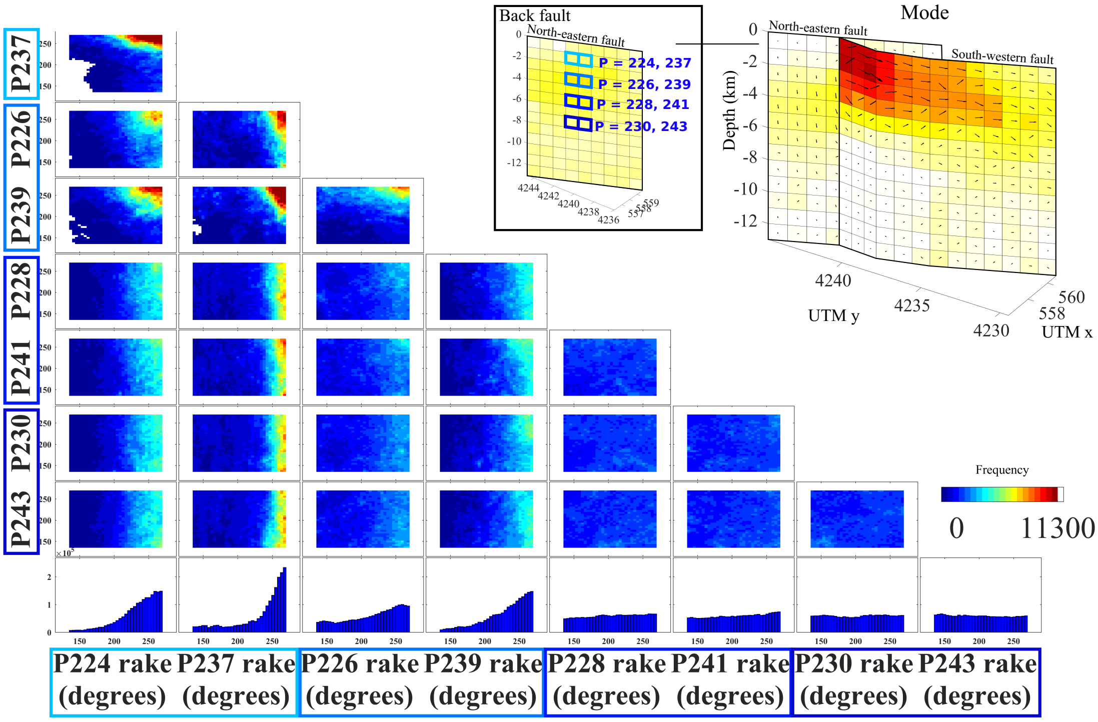

Figure B.23: 2D PDFs of rake with depth on the north-eastern fault. These indicate that rake is well constrained nearer the surface, but beyond 6km depth it is not constrained at all.

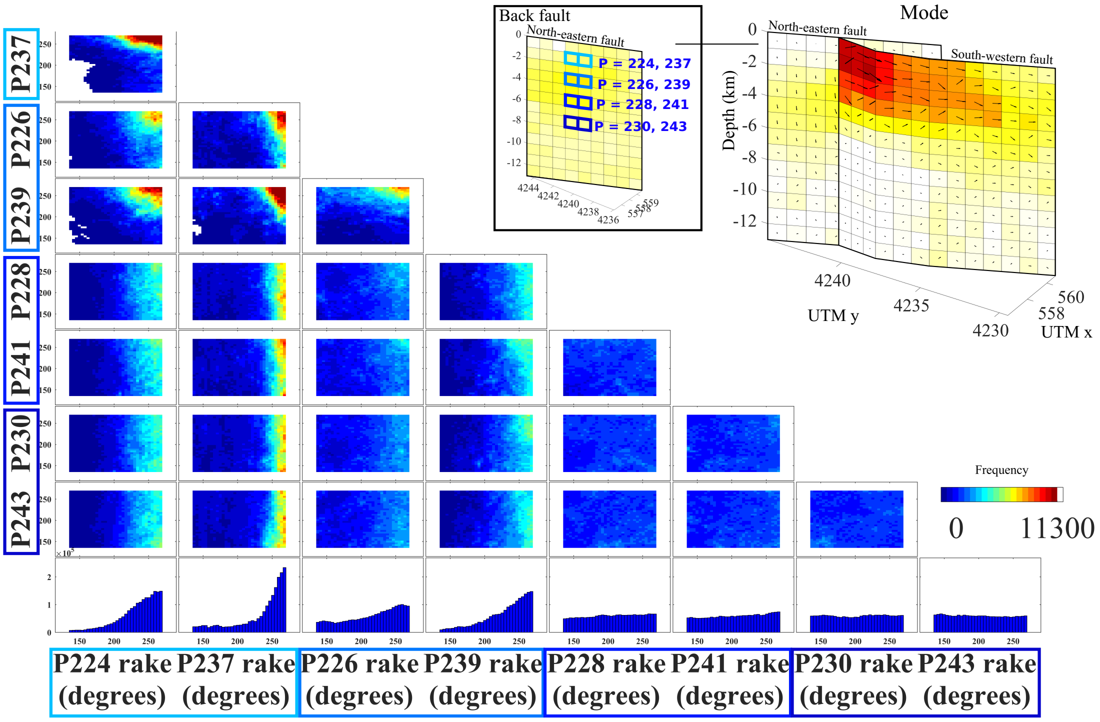

Figure B.24: 2D PDFs of rake with depth on the north-eastern fault. We observe that slip patches next to each other display either no correlation or negative correlation and that slip patches two-along from each other show either no correlation of positive correlation. This is why we observe some oscillatory rake along the fault.

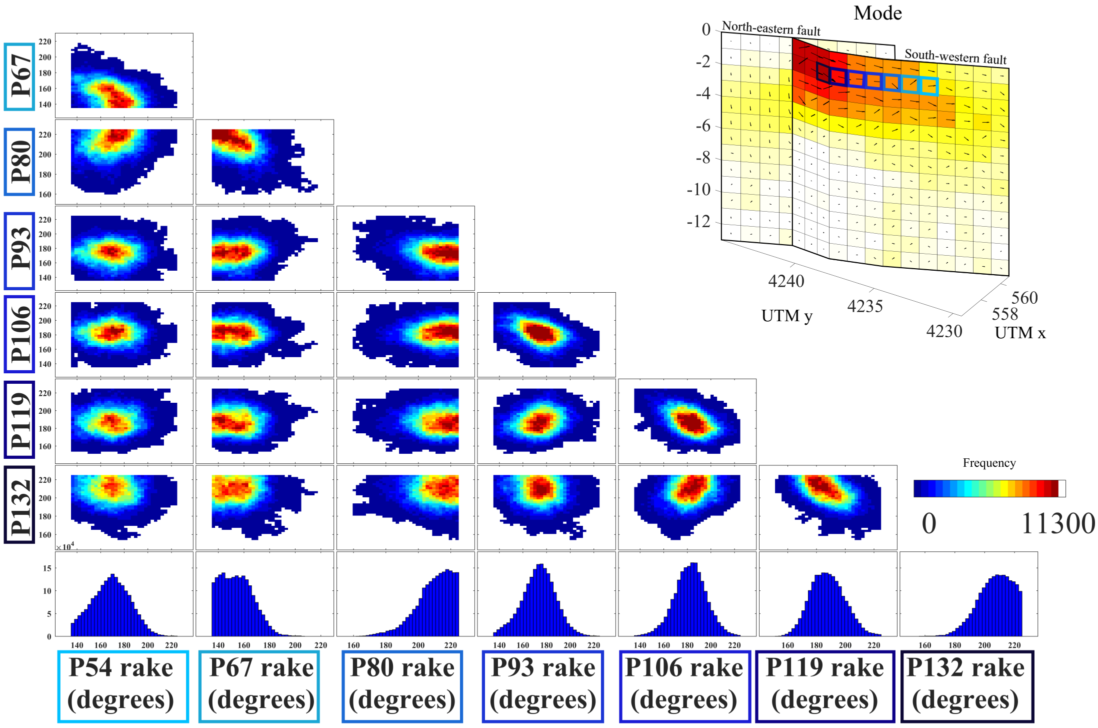

Figure B.25: 2D PDFs of rake along-strike on the south-western fault. We observe that slip patches next to each other display either no correlation or negative correlation and that slip patches two-along from each other show either no correlation of positive correlation. This is why we observe some oscillatory rake along the fault.

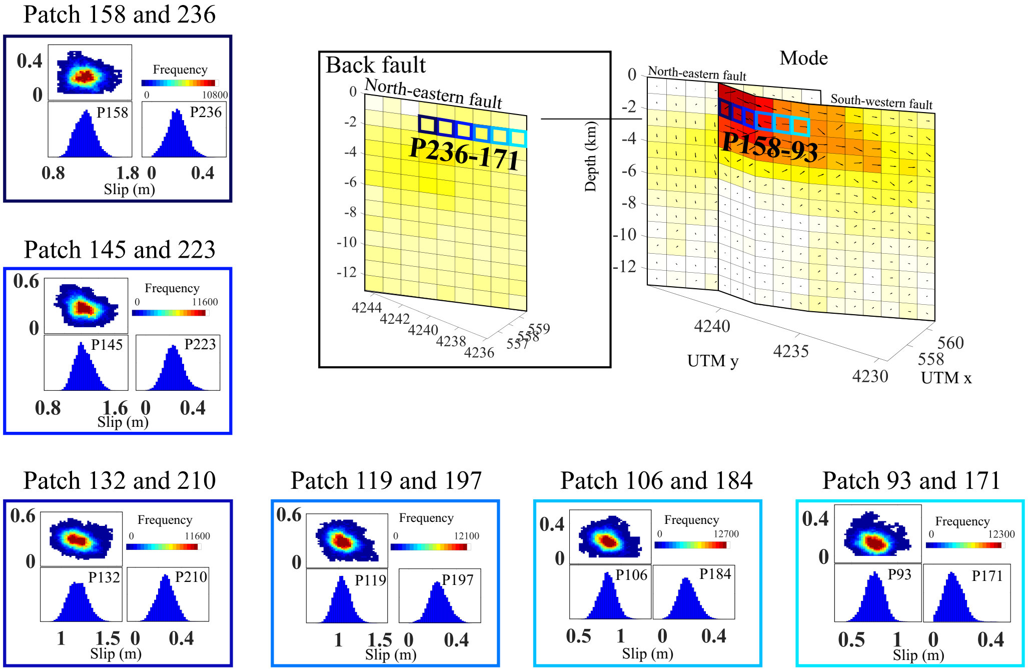

Figure B.26: Trade-offs between slip on different faults at the point at which they overlap. These histograms show that slip is anti-correlated: where slip tends to be high on the south-western fault it tends to be low on the north-eastern fault.

References

Amey, R. M. J., A. Hooper, and R. J. Walters (2018), A Bayesian Method for Incorporating Self-Similarity into Earthquake Slip Inversions, *Journal of Geophysical Research: Solid Earth*, *123*, doi:10.1029/2017JB015316. B

Zhang, L., P. M. Mai, K. K. Thingbaijam, H. N. Razafindrakoto, and M. G. Genton (2015), Analysing earthquake slip models with the spatial prediction comparison test, *Geophysical Journal International*, *200*(1), 185–198, doi:10.1093/gji/ggu383. B.13

Appendix C

Appendix for Chapter 4

Appendix for Chapter 4.

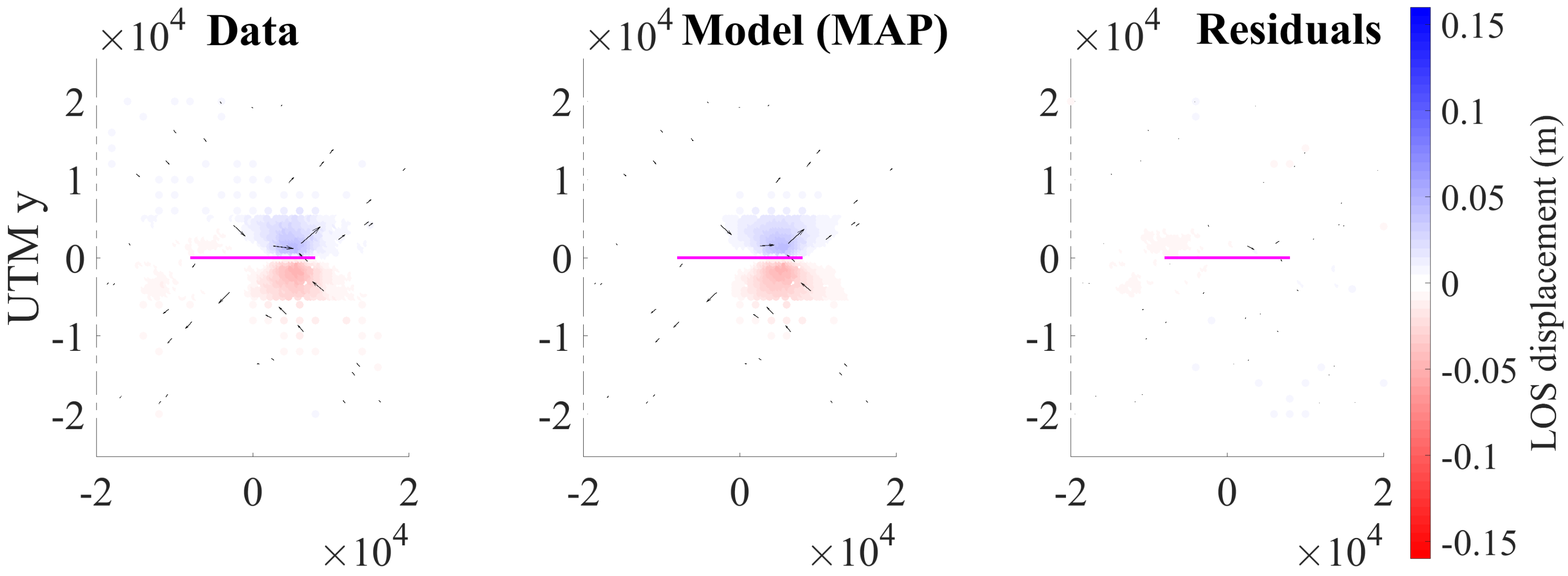

Figure C.1: Fit to data for trans-dimensional synthetic test solution (solution shown in Chapter 4 Figure 4.3).

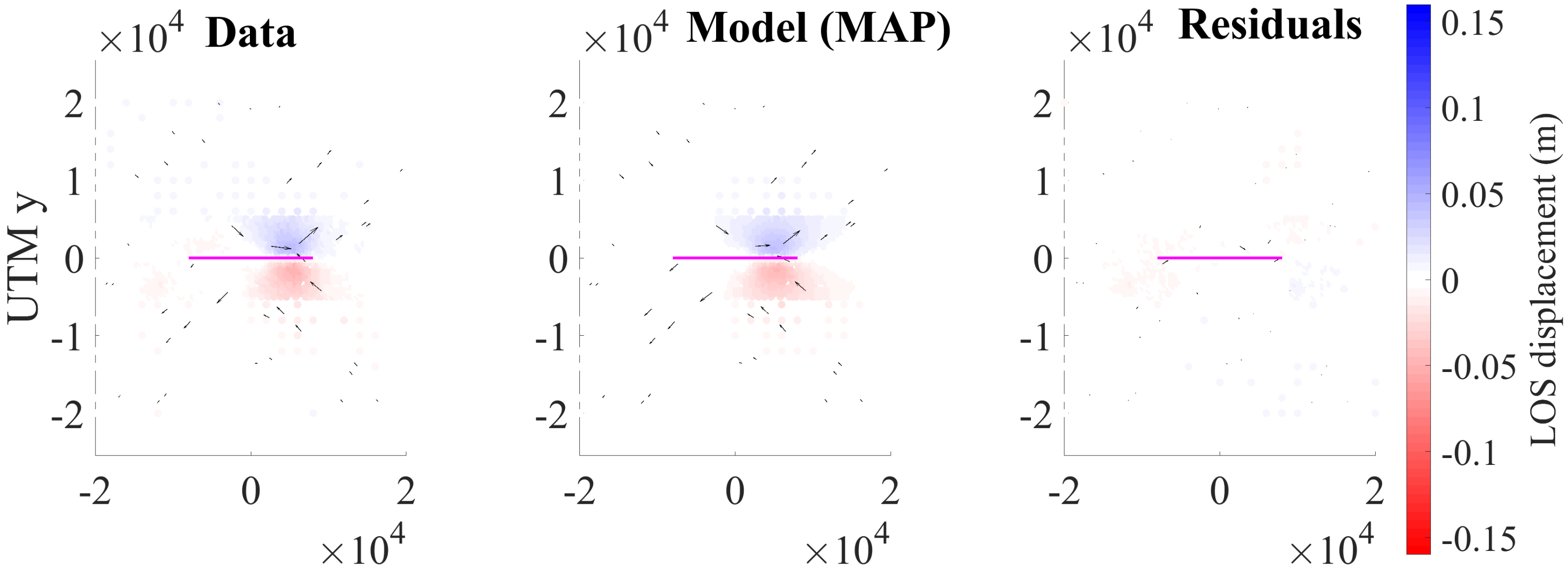

Figure C.2: Fit to data for synthetic test with inversion applied to the whole fault (solution shown in Chapter 4 Figure 4.3).

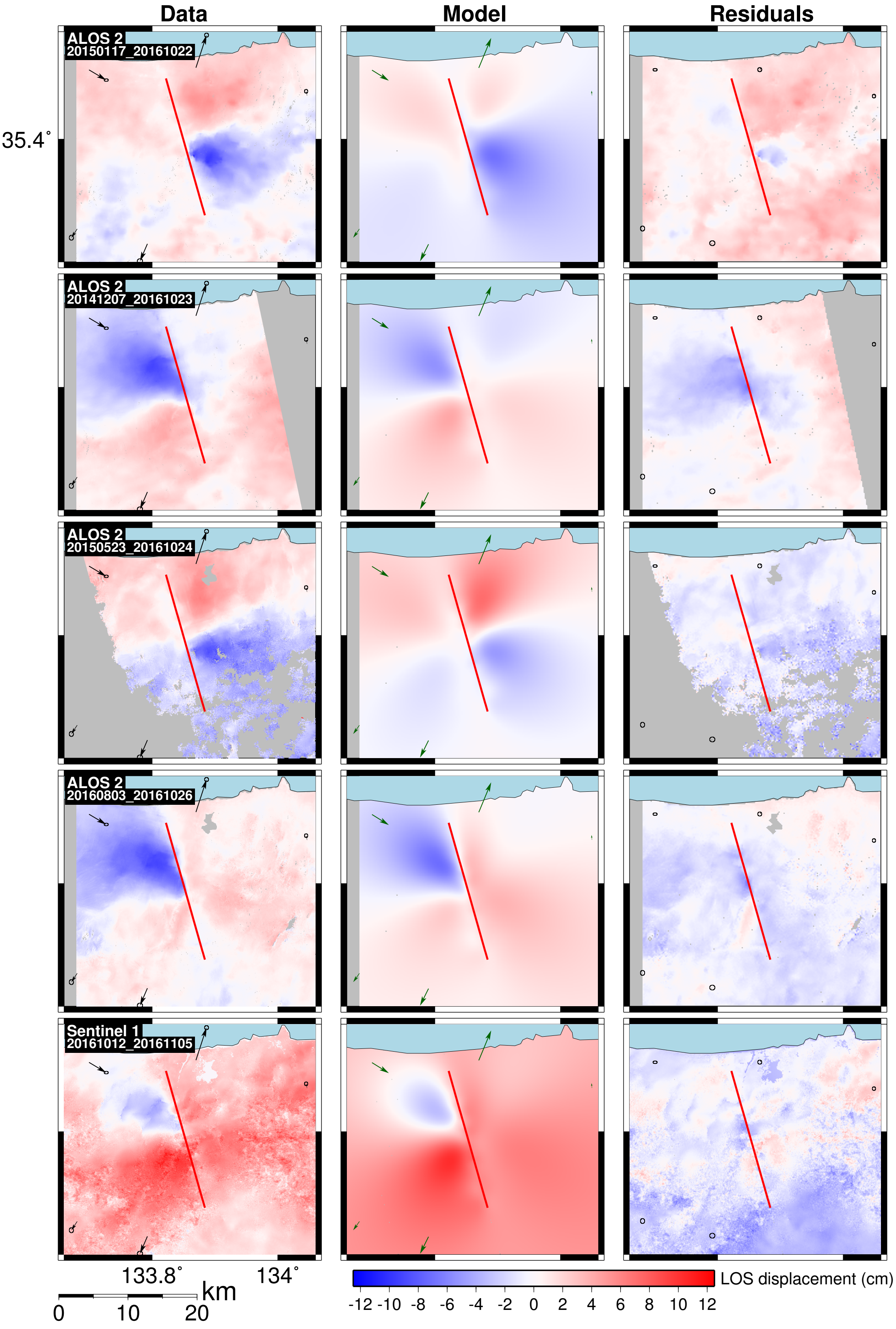

Figure C.3: Data, model and residuals for the MAP solution of an inversion applied to the whole fault (solution shown in Chapter 4 Figure 4.4).

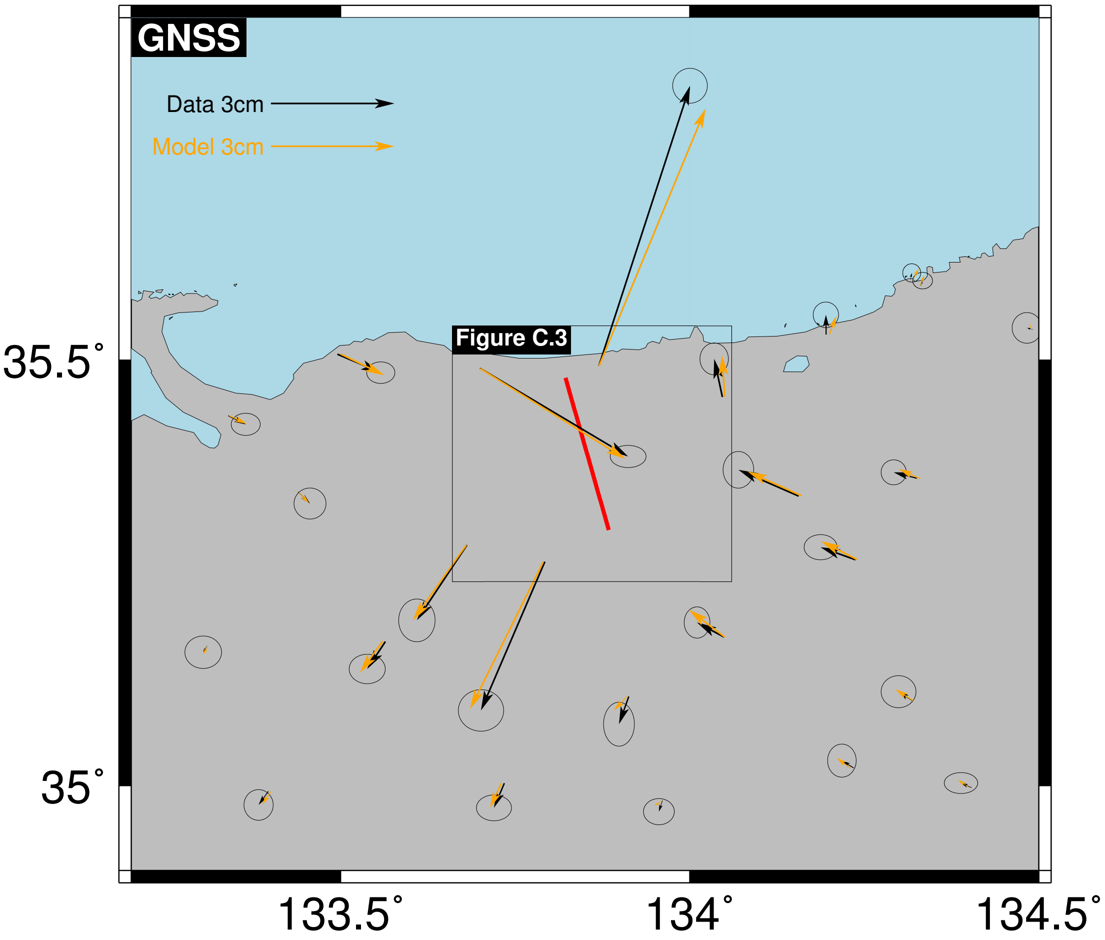

Figure C.4: GNSS displacements from 6/10/16 to 22/10/16 for the 2016 Central Tottori earthquake, which occurred on the 21/10/16. Black arrows show the observed displacements and blue arrows show the fit of the MAP model for the inversion applied to all patches (non trans-dimensional). Solution shown in Chapter 4 Figure 4.4.

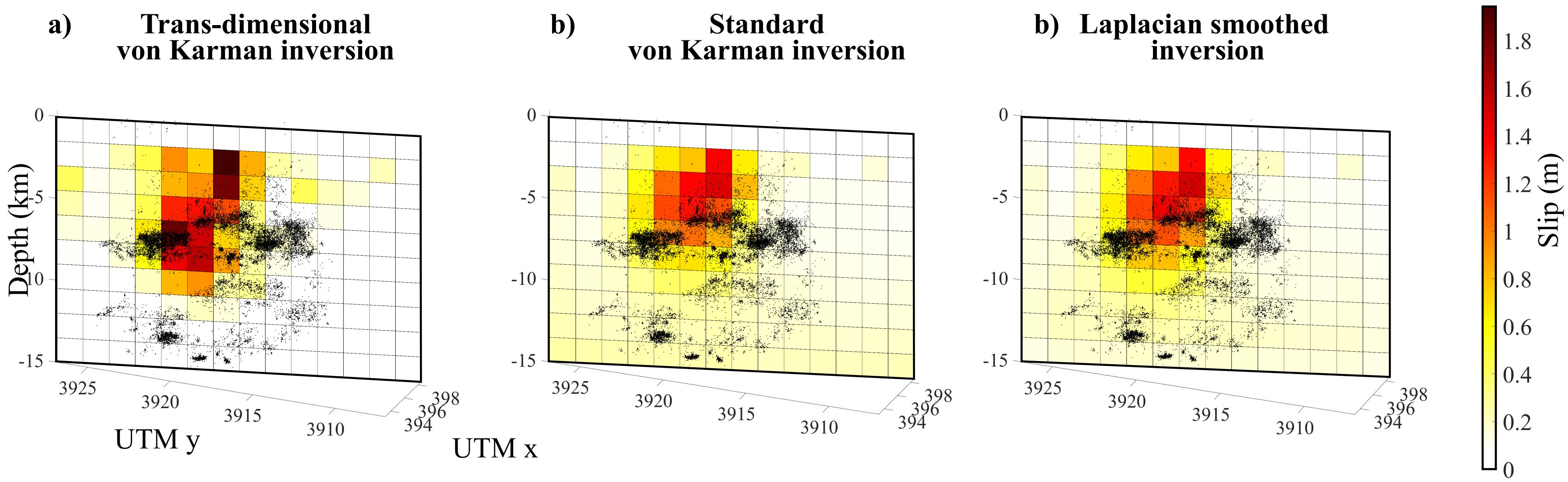

Figure C.5: Mean slip for trans-dimensional (inset a) and standard von Karman solution (inset b) as in Figure 4.4, and additionally a Laplacian solution. The Laplacian solution is very similar to the von Karman solution, but has slightly higher magnitude of slip.

Table C.1: Details of fault used for modelling the 2016 Central Tottori earthquake. The fault was broken into 10 patches down-dip and 14 patches along-strike.

Strike (degrees)	**Dip (degrees)**	**Rake (degrees)**	**Center (UTM x)**	**Center (UTM y)**	**Length (km)**	**Top depth (km)**	**Bottom depth (km)**
345	90	0	395831.1	3916898	20.6	0	15